Multidimensional inversion of transient electromagnetic data for the exploration of clay pans in the Atacama Desert, Chile

Inaugural-Dissertation

zur Erlangung des Doktorgrades
der Mathematisch-Naturwissenschaftlichen Fakultät
der Universität zu Köln

vorgelegt von

Bárbara Nataly Blanco Arrué

aus Arica, Chile

Köln, 2023

1. Gutachter: Prof. Dr. B. Tezkan
2. Gutachter: Prof. Dr. A. Hördt

Tag der mündlichen Prüfung: 05.05.2023

Abstract

This thesis focuses on the geophysical exploration of selected clay pans in northern Chile, the so-called PAG and Paranal clay pans. These sedimentary deposits, are sensitive archives of the Atacama Desert paleoclimate and contain valuable information on the precipitation history. The loop source transient electromagnetic (TEM) method is used to provide the geometry and bedrock topography of each site. In addition to standard 1D inversion techniques, 2D forward modeling approaches are utilized, and a recently published 3D forward modeling and inverse scheme are applied to the TEM data. The investigated sites are study areas of the interdisciplinary Collaborative Research Center, *Earth Evolution at the Dry Limit* (CRC 1211), established at the Universities of Cologne, Bonn, and Aachen. The CRC 1211 contributes to seeking the mutual evolutionary relationships between Earth's surface processes and biota under extreme water limitation. Two extensive geophysical surveys were conducted in both clay pans measuring a total of 181 TEM soundings on a 3D grid. Within the project, other geophysical techniques, such as active seismic and magnetics, were also carried out, complementing the geoscientific integrated interpretation of the subsurface. The presented thesis provides foundations for suitable drilling locations within the CRC 1211 project. The 1D inversion results reveal a three-layered resistivity structure with reliable information down to a depth of 250 m. At the PAG site, the results identify a resistive colluvial sequence increased to high conductive lacustrine sediments followed by a resistive basement. Additionally, at the Paranal clay pan, the results detect a resistive layer of fine sediment succeeded by a conductive sequence of a fluvial conglomerate with a resistive basement beneath. The subsurface models agree with lithology, borehole data, and geological information. In addition, key information is obtained with respect to the sedimentary thickness above the basement, contributing to paleoclimate research in northern Chile. A 2D forward modeling study was performed to validate the 1D interpretation and evaluate possible distortion effects. The analyzed scenarios confirm the presence of 2D effects in the data from both PAG and Paranal TEM data sets, being in the latter more strong. Aiming to obtain a more accurate and independent model, a 3D inversion of the whole Paranal TEM data is derived. The obtained 3D inversion models are in good agreement with the local geology, which validates the geometry and subsurface distribution of the studied clay pan.

Kurzzusammenfassung

Diese Arbeit konzentriert sich auf die geophysikalische Exploration ausgewählter Tonpfannen in Nordchile, die sogenannten PAG- und Paranal-Tonpfannen. Diese Sedimentablagerungen sind empfindlich Archive des Paläoklimas der Atacama-Wüste und enthalten wertvolle Informationen über die Niederschlagsgeschichte. Es wird das transiente elektromagnetische Verfahren (TEM) verwendet um die Geometrie und Topographie des Grundgesteins beider Lokationen zu bestimmen. Neben Standard 1D-Inversionstechniken werden 2D-Vorwärtsmodellierungsansätze und ein kürzlich veröffentlichter 3D-Vorwärts- und Inversionsalgorithmus auf die TEM-Daten angewendet. Die Messgebiete sind Untersuchungsstandorte des interdisziplinären Sonderforschungsbereichs, Evolution der Erde und des Lebens unter extremer Trockenheit (SFB 1211), der Universitäten Köln, Bonn und Aachen. Der SFB 1211 trägt dazu bei, die gemeinsame evolutionäre Beziehung zwischen Oberflächenprozessen der Erde und Biota unter extremer Wasserknappheit zu untersuchen. Auf beiden Tonpfannen wurden zwei umfangreiche geophysikalische Untersuchungen durchgeführt, bei denen insgesamt 181 TEM-Sondierungen auf einem 3D-Raster gemessen wurden. Innerhalb des Projekts werden auch andere geophysikalische Methoden, wie z B. aktive Seismik und Magnetik eingesetzt, um die integrierte geowissenschaftliche Interpretation des Untergrundes zu ergänzen. Die vorgelegte Arbeit liefert Grundlagen zur Auswahl geeigneter Bohrstandorte innerhalb des SFB 1211-Projekts. Die Ergebnisse der 1D-Inversion zeigen eine dreischichtige elektrische Leitfähigkeitsstruktur mit zuverlässigen Informationen bis zu einer Tiefe von 250 m. Für die PAG-Tonpfanne identifizieren die Ergebnisse eine resistive kolluviale Sequenz, gefolgt von einer leitfähigen Sequenz von fluvialem Konglomerat über einem resistiven Grundgestein. Für die Paranal-Tonpfanne zeigen die Ergebnisse eine resistive Schicht aus feinem Sediment, gefolgt von einer leitfähigen Sequenz fluvialen Konglomerats über resistivem Grundgestein. Die abgeleiteten Untergrund Modelle stimmen mit der Lithologie, Bohrlochdaten und geologischen Informationen überein. Zudem werden Information über die Sedimentmächtigkeit über dem Grundgestein gewonnen, die einen Beitrag zur Paläoklimaforschung im Norden Chiles liefern. Um die 1D-Interpretation zu validieren und mögliche Verzerrungseffekte zu bewerten, wurde eine 2D-Vorwärtsmodellierungsstudie durchgeführt. Die analysierten Modellstudien bestätigen das Vorhandensein von 2D-Effekten in den TEM-Datensätzen von

PAG und Paranal, wobei diese in dem letzteren stärker sind. Um ein genaueres und unabhängiges Untergrundmodell abzuleiten wurde eine 3D-Inversion der gesamten Paranal-TEM-Daten durchgeführt. Die abgeleiteten 3D-Inversionsmodelle stimmen gut mit der lokalen Geologie überein, die die Geometrie und Untergrundverteilung der untersuchten Tonpfanne validieren.

Contents

List of Figures

List of Tables

CHAPTER 1

Introduction

In applied geophysics, electromagnetic (EM) methods are widely used, for example, for mining exploration, environmental, hydrogeological, and geothermal studies (Telford et al., 1990; Dentith and Mudge, 2014). Furthermore, particularly in the last decade, the need for better comprehension of the paleoclimate has turned EM methods into relevant tools for interdisciplinary research. Nowadays, the evolution of the Earth in hyperarid areas is still undergoing research. In this context, the Atacama Desert along the Chilean Coastal Cordillera, the driest desert in the world (Clarke, 2006), has become an exceptional landscape for imaging the subsurface affected by extremely limited water availability. Here, clay pans are crucial for providing knowledge of the surface and subsurface processes in areas limited by water availability.

This thesis aims to derive an independent resistivity model using the loop source transient EM method, providing the sedimentary architecture and bedrock topography of two selected clay pans in northern Chile, named PAG and Paranal. In addition to standard 1D inversion techniques, further 2D forward modeling strategies are used, and recently published 3D inverse modeling schemes are applied to the Transient Electromagnetic (TEM) data. The investigated sites are potential study areas of the Collaborative Research Center, *Earth evolution at the dry limit* (CRC 1211), established at the Universities of Cologne, Bonn, and Aachen.

The CRC 1211 investigates the mutual evolutionary relationships between processes on the Earth's surface and the biota affected severely and predominantly by the availability of water (Dunai et al., 2020). The purpose of the subproject A02, *Paleoclimate Proxies: Miocene to Recent Precipitation History of the Atacama Desert*, is to reconstruct the chronology, weathering, and erosion of the basins formed in the Atacama Desert during the Quaternary-Miocene period. Along coastal cordillera, there are a variety of clay pans widespread, mostly formed by tectonic blocking of drainage, creating perfect sediment traps (Ritter et al., 2018a; Diederich et al., 2020). These sites have been archives of the

paleoclimate of Atacama since the Miocene ($\sim$ 10 My) and contain valuable information on the precipitation history (Ritter et al., 2018b). Within the subproject, other geophysical techniques, such as active seismic and magnetics, were also carried out, complementing the geoscientific investigation and providing an interpretation of the internal structure of the subsurface based on other physical properties. The geophysical investigation presented in this thesis provides the basis for determining suitable drilling locations for paleoclimatic research, ensuring reliable results for costly drilling campaigns within the project.

In previous studies, other geophysical methods, such as ground penetration radar (GPR) and horizontal-to-vertical spectral ratios of ambient seismic noise data (H / V), were used in the PAG clay pan, revealing the upper boundary of the clastic sediment successions (Ritter et al., 2019). Furthermore, in 2017 a drilling campaign was conducted in the same clay pan within the CRC 1211 project to recover sediment information to a depth of 52 m (Diederich-Leicher, 2020). However, before the presented thesis, the thickness of the sedimentary deposits was not known in the selected sites. In addition, no spatially dense data based on geophysical techniques were available. Thus, determining the subsurface geometry of clay pans provides essential insight into the depositional regimes, sedimentation rates, and uplift history and is indirectly linked to the period in which the subsurface was exposed to different fluvial or arid periods, contributing to paleoclimate research in northern Chile.

EM methods can be divided into passive, which employ natural fields as incoming plane EM waves as the source, or active, in which a controlled or artificial source is required (Goldman and Neubauer, 1994). Exceptional features of EM methods can be highlighted: the ability to resolve electrical conductors in the ground, the physical response to pore fluids, and the rather fast data acquisition. TEM is an active electromagnetic method that measures the temporal decay of the induced magnetic field (Goldman and Neubauer, 1994). The measurements can be carried out at a rather high survey speed, giving an advantage for the study of conductive sediments located in extreme and hilly conditions. The exponential increase in computational resources, open source EM codes, and new types of devices for data acquisition allow the great potential of active EM methods to be demonstrated.

On a global scale, interesting comprehensive publications related to near- and deep-surface applications of EM methods in the time and frequency domain have been published, e.g. Goldman and Neubauer (1994), Tezkan (1999), Pellerin (2002), Auken et al. (2006), Everett (2012) and Becken et al. (2020). The investigations of shallow sedimentary basins and near-surface structures were carried out using EM methods for different authors (Danielsen et al., 2003; Jørgensen et al., 2003; Yogeshwar, 2014). Several case studies in Chile have recently been presented using TEM techniques to study the hydrogeological processes in the Santiago Basin (Blanco-Arrué et al., 2021) or the El Tatio geothermal geyser fields (Montecinos-Cuadros et al., 2021). Other EM methods, such as deep magnetotellurics, are widely used for deep crustal studies, such as the tectonic evolution of the Andes cordillera or deep geothermal targets (Hoffmann-Rothe et al., 2004; Cordell et al., 2018; Ślzak et al., 2021).

Despite this, loop TEM data is often interpreted by 1D inversion or quasi 2D/3D schemes such as laterally or spatially constrained inversion schemes (Auken et al., 2006; Viezzoli et al., 2008). However, in case of a 2D or 3D conductivity distribution in the subsur-

face, the 1D models cannot explain the field data and therefore distortion effects must be considered (Yogeshwar and Tezkan, 2018). In those cases, a multidimensional algorithm (either 2D or 3D) is required for subsurface reconstruction. Software to perform 2D or 3D TEM modeling and inversion is scarce due to the high computational resources required, so the development of new algorithms is still an ongoing research area. Multidimensional time domain inverse schemes have been published by a few authors (Haber et al., 2007; Commer and Newman, 2008; Oldenburg et al., 2013). Currently, some novel open source codes are available to be used, such as the Python toolbox custEM (Rochlitz et al., 2019; Seidel, 2019; Rochlitz et al., 2021), which performs customizable 3D finite-element modeling of controlled source EM (CSEM), TEM, and natural-source electromagnetic data. Moreover, the Julia package EM3DANI for isotropic/anisotropic 3D forward modeling in frequency-domain data is also convenient. Furthermore, this thesis utilizes the expanded edition of the 3D modeling and inversion algorithm, TEM3DInv, which is designed for time-domain EM data and is developed by the same team (Liu et al., 2019a; Peng et al., 2016; Liu et al., 2017; Peng et al., 2021; Liu et al., 2024).

In the framework of this thesis, two extensive surveys were conducted in the Paranal and PAG clay pans. A total of 181 soundings were carried out, covering a 3D grid on both sites. The TEM data were then processed and analyzed to evaluate the quality of the data set. Subsequently, the 1D inversion algorithm EMU+ (Scholl, 2005) was utilized to derive the electrical resistivity depth models and the uncertainties. In addition, the TEM 1D models were patched together into quasi-2D resistivity-depth sections and complemented with magnetics and active seismics to resolve different subsurface properties at different spatial scales. Furthermore, an interdisciplinary and geoscientific discussion was developed with the available geological information and correlated with lithological borehole data. Afterwards, in order to validate the reliability of our 1D interpretation and to investigate whether our data are affected by 2D distortion effects, a 2D forward modeling study was performed. Several 2D forward modeling studies in time-domain were effectively applied for different source EM configurations (Hördt and Müller, 2000; Goldman et al., 2011; Sudha et al., 2011; Rödder and Tezkan, 2013). Here, the well-tested and established finite difference SLDMem3t algorithm was utilized (Druskin and Knizhnerman, 1988; Hördt et al., 1992; Druskin et al., 1999). In the context of this work, the SLDMem3t was used to model different clay pan scenarios, adapting the slope angle of the conductive layer and their resistivity distributions to the study sites. Subsequently, the 2D synthetic models representative for the Paranal and PAG clay pan were analyzed and studied.

In order to derive a more accurate geometry of the Paranal clay pan and take advantage of the survey design made by covering the site in a 3D grid, the Julia Package for 3D modeling and inversion in time-domain was utilized (Peng et al., 2016; Liu et al., 2024). The 3D algorithm is based on Finite-Volume and uses a Gauss-Newton inversion scheme coupled with a preconditioned conjugate gradient method to avoid explicit Jacobian calculation in each iteration. The algorithm has been applied for 3D forward modeling for an arbitrarily anisotropic Earth and 3D CSEM inversion for marine configurations with excellent convergence rates, highlighting its efficiency and stability (Liu et al., 2019a, 2017). Through the presented work, the 3D modeling and inversion algorithm is utilized and its performance and accuracy were tested using synthetic 1D, 2D, and 3D models representative of the Paranal clay pan. Since the code is implemented for 3D, a very large smoothing in the y-direction is used to force a 2D subsurface reconstruction. Finally, the

subsurface resistivity depth structure in the Paranal clay pan is independently validated by applying the 3D inversion to the TEM field data.

1.1 Structure of this thesis

This thesis manuscript is structured as follows. In Chapter 2, the fundamentals and theoretical background of the TEM method are described, including an explanation of the physical parameters involved in this study. Chapter 3 presents the theoretical framework of the conventional inversion techniques utilized for investigating the subsurface structure. In particular, the Marquardt-Levenberg and the constrained Occam inversion schemes are explained, together with the parameters to assess the uncertainties of the resulting models. In Chapter 4, a detail description of the field surveys and the TEM deployments are presented whereas examples of the collected TEM data at the Paranal and PAG clay pans are shown to describe the data processing and analyses. In this chapter, the geological setting of the surveyed clay pans as well as the specifications of the different surveys (TEM, magnetics and actives seismics) are provided. Subsequently, the 1D inversion results of the TEM data are presented and analyzed in Chapter 5. Here, the 1D models obtained for the PAG and Paranal sites are discussed in terms of the resistivity distribution and the reliability of the derived 1D inversion results is discussed in detail. Furthermore, the 1D model results are validated and interpreted in terms of the available borehole data, the other geophysical surveys and the geological context. Given the analysis of the 1D inversion results, a 2D forward modeling assessment is required in order to understand the presence of anomalous features in the TEM data. This 2D forward modeling study is presented in Chapter 6, which shows the influence of the geometry and resistivity characteristics of the clay pans on possible 2D effects in the observed data. Chapter 7 introduces the theoretical background of the 3D TEM modeling and inversion algorithm that is utilized first to validation the performed with the 1D and 2D subsurface structures. Finally, a 3D inversion of the Paranal TEM data is performed, the subsurface structure is independently validated, and the results are discussed and analyzed. In summary, Chapter 8 describes the main results, findings and implications of this thesis, together with an outlook and future perspectives for the different topics involved in this work.

CHAPTER 2

The TEM method

Induction phenomena are the basis for most EM methods that respond to the electrical and magnetic properties of the subsurface. Inductive methods were originally designed for mining research due to the strong sensitivity of regions with the least inhibited current flow (Telford et al., 1990). These methods are widely used to characterize and deliberate near-surface structures solving exploration, groundwater, hydrocarbon reservoir, paleoclimate, archaeological, geotechnical and environmental problems (Kirsch, 2006). The application of EM techniques in the time and frequency domain can be found in several comprehensive articles (Fitterman and Stewart, 1986; Goldman and Neubauer, 1994; Tezkan, 1999; Pellerin, 2002; Auken et al., 2006).

The TEM applications date from the mid-1980s, considering a relatively young method compared to the frequency domain methods. The TEM method is a suitable deep-sounding technique, among other controlled-source EM methods, which can be helpful in highly urban noise environments (Blanco-Arrué et al., 2021). In addition, it has the advantage that it is a noninvasive technique and is sensitive to conductors. The loop source TEM method is widely used for the investigation of groundwater studies and aquifer characterization (Fitterman and Stewart, 1986; Goldman and Neubauer, 1994). Moreover, this method can also provide valuable subsurface information for sedimentary basin studies in arid environments, for example sedimentary geometry as well as bedrock topography (Frischknecht and Raab, 1984; Danielsen et al., 2003; Yogeshwar et al., 2013). The access to sophisticated equipment to cover an extended dynamic range and the high computational resources were part of the challenges at the beginning of applying this method (Christiansen et al., 2006).

This chapter presents a description of the TEM method and theoretical aspects based on Maxwell equations following the comprehensive published work of Ward and Hohmann (1988); Nabighian and Macnae (1991) and Spies and Frischknecht (1991). The active seismic and magnetic method was applied complementary to TEM. The underlying the-

oretical principles of these geophysical methods are not detailed in this work, but can be explored in sources such as Telford et al. (1990), Kearey et al. (2002) and Dentith and Mudge (2014).

2.1 Fundamental electromagnetic quantities and units

Throughout this thesis, vectors and matrices are represented by bold characters. The lowercase characters represent vectors, whereas the uppercase characters represent matrices. An exception are the vector fields $\boldsymbol{E}$, $\boldsymbol{D}$, $\boldsymbol{H}$, and $\boldsymbol{B}$, which are displayed similar to matrices in upper case and bold-italic characters. The list of variables and constants shown throughout this thesis is summarized in Table 2.1. The time derivative of the magnetic field $\partial_t \dot{\boldsymbol{B}}$ is termed induced voltage U_{ind} or simply voltage U. Electrical resistivity ρ is simply termed resistivity.

Table 2.1: List of variables and constants given in the International System of Units (SI).

Variable	Symbol	Units
Electric field intensity	$\boldsymbol{E}$	V/m
Electric displacement	$\boldsymbol{D}$	As/m^2
Magnetic field	$\boldsymbol{B}$	T = Vs/m^2
Magnetic field intensity	$\boldsymbol{H}$	A/m
Electric charge density	ϱ	As/m^3
Current density	$\mathbf{j}$	A/m^2
Transmitter current	I	A
Electrical permittivity	$\varepsilon = \varepsilon_0 \varepsilon_r$	As/Vm
Relative dielectric permittivity	ε_r	adimensional
Electrical permittivity of free space	$\varepsilon_0 = 8.845 \cdot 10^{-12}$	As/Vm
Magnetic permeability	$\mu = \mu_0 \mu_r$	Vs/Am
Relative magnetic permeability	μ_r	adimensional
Permeability of the free space	μ_0	Vs/Am
Electrical conductivity	σ	S/m = 1/Ωm
Electrical resistivity	ρ	Ωm
Angular frequency	ω	1/s
Frequency	f	Hz
Wavenumber	k	1/m
Noise level	η_v	V/m^2

2.2 Electrical conduction mechanisms

Electromagnetic methods use the electrical conductivity σ or its inverse, the electrical resistivity ρ as the physical property analyzed. The range of resistivity for common minerals, rock types, and near-surface material varies from 10^{-8} to 10^{14} Ωm (Palacky, 1988; Telford et al., 1990; Auken et al., 2006; Dentith and Mudge, 2014). Electrical conductivity is the capability of materials to sustain long-term current flow via the charge migration mechanism exchange. The propagation of the electric current can occur in different ways: electronic (ohmic), electrolytic, and dielectric conduction (Telford et al., 1990). The **dielectric conduction** occurs in poor conductors or insulators, which have very few or no free carriers. In EM induction techniques at low frequencies and moderate resistivities, this conduction may be insignificant. Therefore, the relative dielectric permittivity is not taken into account in any further way. When materials control charge transport with free electrons, we refer to **electronic conduction**. However, this conduction can be negligible in most rock matrices, with only a few exceptions when high-conductive minerals are present. The primary process is **electrolytic conduction**, a result of the substandard quality of the electronic conductors in most rocks. The resistivity is influenced by the movement and density of the dissolved ions, and the current is carried by ionic conduction (Telford et al., 1990). Elements like the type of electrolyte, temperature, the movement of its ions, or the volume of the fluid play a role in its conduction.

Every material on earth has a specific resistivity value, which is used to display subsurface rock layers, and several ranges of these values are usually produced by different compositions of rocks. The resistivity values of materials on the earth are presented in Fig. 2.1. An appropriate model for the description of the resistivity of a clean porous medium (free of clay and shale) defines the formation resistivity factor f, given by the empirical law of Archie (1942):

$$f = \frac{\rho_{saturated-rock}}{\rho_{pore-fluid}} = \frac{a}{\phi^m}, \tag{2.1}$$

where $\rho_{saturated-rock}$ is the resistivity of the fully saturated rock and $\rho_{pore-fluid}$ that of the saturating pore fluid, fractional porosity ϕ, constant a and the cementation exponent m. Archie's law applies only to rocks without clay or metallic minerals and depends on its porosity, saturation level, and resistivity of the pore fluid. Typical values for these parameters can be found in, e.g. Keller (1988). Note that Archie's equation assumes that all conduction occurs through the pore fluid in which the rock matrix plays a passive role in conduction processes (Dentith and Mudge, 2014). Clay minerals have a high ion exchange capacity. This leads to an interaction between ions in the pore fluid, and negative surface charges of the rock matrix cause an electric double layer at the interface. Hence, wet clay can exhibit extremely low resistivity values. Nevertheless, in pore fluid with high conductivity, electrolytic conduction is expected to dominate (Ward, 1990). Consequently, the existence of clay minerals in sedimentary layers is influenced by their voids, particle size, bulk, and dispersion throughout the rock body and the surface area of the pores. It should be noted that a small content of clay minerals can significantly increase the bulk conductivity, mainly when their grain size is small (Dentith and Mudge, 2014).

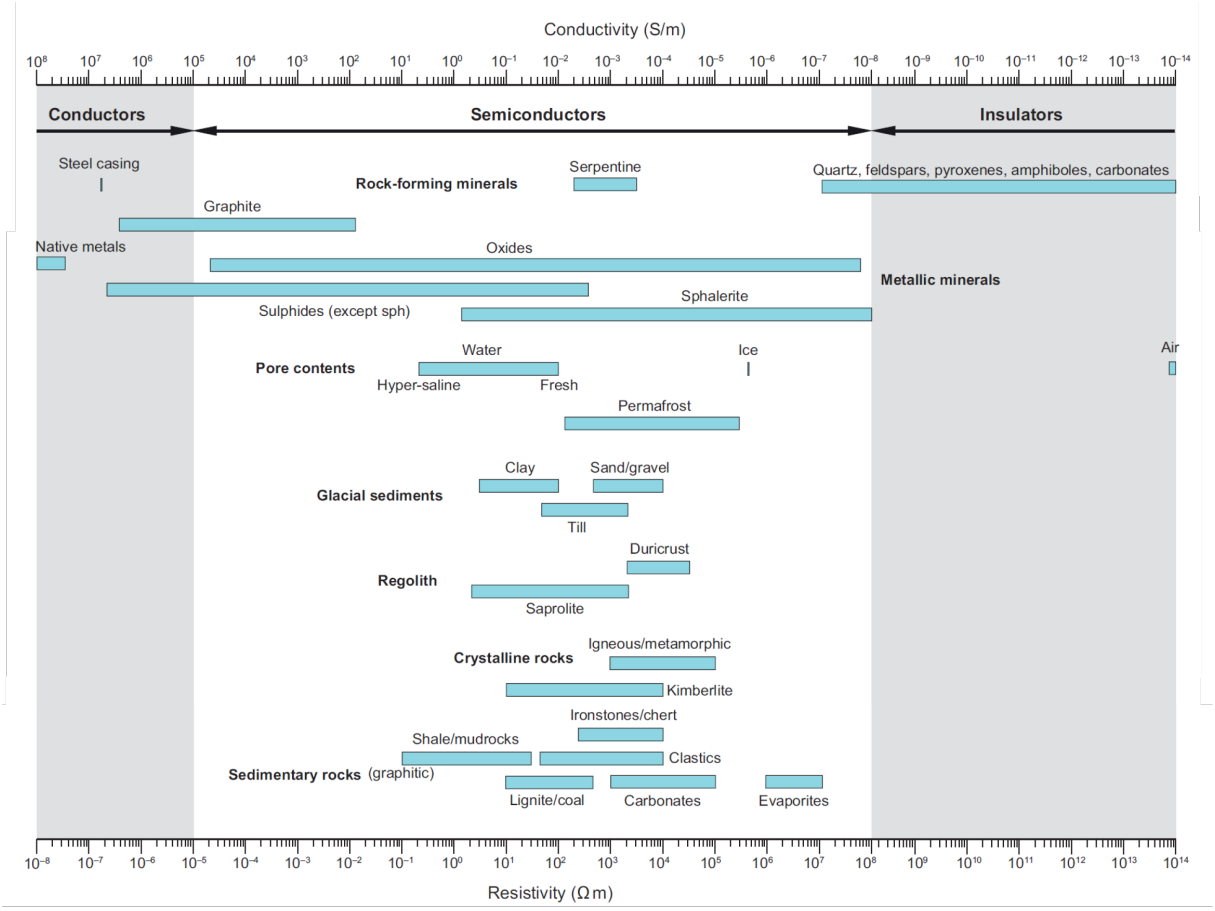

Figure 2.1: The resistivity and conductivity range of common minerals, rock types and near-surface materials, taken from Dentith and Mudge (2014).

2.3 Maxwell's equations

The principle of electromagnetic induction is explained by Maxwell's equations. The interaction of electric and magnetic fields and their basic foundations are summarized in the following expressions and their constitutive relationships. In differential form, they are given by:

$$\nabla \cdot \boldsymbol{D} = \varrho \tag{2.2}$$

$$\nabla \cdot \boldsymbol{B} = 0 \tag{2.3}$$

$$\nabla \times \boldsymbol{E} = -\frac{\partial \boldsymbol{B}}{\partial t} \tag{2.4}$$

$$\nabla \times \boldsymbol{H} = \frac{\partial \boldsymbol{D}}{\partial t} + \boldsymbol{j} \tag{2.5}$$

Equation 2.2 defines the **Gauss's Law** in which the sources of the electric displacement field $\boldsymbol{D}$ can be identified as the electric charge density ϱ. Equation 2.3 states the **Gauss's law for magnetic fields**, in which the magnetic field $\boldsymbol{B}$ is source-free. Equation 2.4 corresponds to **Faraday's law of induction**, which states a time-varying magnetic field $\boldsymbol{B}$ as the cause for a circulating electric field intensity $\boldsymbol{E}$ of opposite sign. Finally, **Amperè's law** is given in Equation 2.5, a total electric current density $\boldsymbol{j}$ causes a circulation

magnetic field intensity $\boldsymbol{H}$. In addition, these variables can be coupled by the constitutive relationships for a linear isotropic medium:

$$\mathbf{B} = \mu_o \mu_r \mathbf{H} = \mu \mathbf{H} \tag{2.6}$$

$$\mathbf{D} = \varepsilon_o \varepsilon_r \mathbf{E} = \varepsilon \mathbf{E} \tag{2.7}$$

$$\mathbf{j} = \sigma \mathbf{E}, \tag{2.8}$$

where ε_r the relative permittivity, μ_r the relative permeability, ε_0 and μ_0 are the permittivity and the permeability of the free space, respectively. In general, the variables ε, σ and μ are described by tensors, but in isotropic media simplify to scalars ($\mu = \mu_0$ and $\varepsilon = \varepsilon_0$).

The Ohm's law in Equation 2.8 describes the relationship between the total electric current density and the electrical conductivity σ for an isotropic conductor. In addition, the current density is source-free in homogeneous regions, and this follows the expression 2.9:

$$\nabla \cdot \boldsymbol{j} = 0. \tag{2.9}$$

2.3.1 Telegraph and Helmholtz equation

Telegraph or wave equations are derived following the assumptions that no free charges exist outside of any external sources ($\nabla \cdot \boldsymbol{E} = 0$) and the current density is source free in regions of homogeneous conductivity 2.9. Under these assumptions and considering the simplifications Ohm's law 2.8 as well as the constitutional relation 2.6 and 2.7, the Maxwell's equations are used to derived Telegrapher's equations by taking the curl of Faraday's law 2.4, replacing with the Amperè's law 2.5 and subsequently 2.6 we obtain a second order differential equation for the electric field intensity $\boldsymbol{E}$. An equation for the magnetic field intensity $\boldsymbol{H}$ is derived in the same manner. This leads to the following equation:

$$\nabla \times (\nabla \times \boldsymbol{E}) = -\mu\sigma \frac{\partial \boldsymbol{E}}{\partial t} - \mu\epsilon \frac{\partial^2 \boldsymbol{E}}{\partial t^2}. \tag{2.10}$$

Using the vector identity $\nabla \times (\nabla \times \boldsymbol{\mathcal{F}}) = \nabla(\nabla \cdot \boldsymbol{\mathcal{F}}) - \Delta \boldsymbol{\mathcal{F}}$ and $\nabla \cdot \boldsymbol{\mathcal{F}} = 0$, implies $\nabla \times (\nabla \times \boldsymbol{\mathcal{F}}) = -\Delta \boldsymbol{\mathcal{F}}$, and considering that $\boldsymbol{\mathcal{F}}$ can either be $\boldsymbol{E}$ or $\boldsymbol{H}$, the Telegraph or wave equation takes the form:

$$\Delta \boldsymbol{\mathcal{F}} - \mu\sigma \frac{\partial \boldsymbol{\mathcal{F}}}{\partial t} - \mu\epsilon \frac{\partial^2 \boldsymbol{\mathcal{F}}}{\partial t^2} = 0 \qquad \boldsymbol{\mathcal{F}} \in \{\boldsymbol{E}, \boldsymbol{H}\}. \tag{2.11}$$

By applying a Fourier transformation to the Telegraph equation 2.11 in the frequency domain, through the time derivative as $\partial \boldsymbol{\mathcal{F}}/\partial t \rightarrow i\omega \boldsymbol{\mathcal{F}}$, the Helmholtz equation is obtained:

$$\Delta \boldsymbol{\mathcal{F}} - i\omega\mu\sigma \boldsymbol{\mathcal{F}} + \mu\epsilon\omega^2 \boldsymbol{\mathcal{F}} = 0 \qquad \boldsymbol{\mathcal{F}} \in \{\boldsymbol{E}, \boldsymbol{H}\}. \tag{2.12}$$

The first derivative term of $\boldsymbol{\mathcal{F}}$ in Equation 2.12 describes the conduction processes while the second derivative term represents the displacement currents. The Helmholtz equation 2.12 can also be expressed with the wavenumber k which includes the physical properties of the medium, where $k^2 = \mu\epsilon\omega^2 - i\omega\mu\sigma$.

In non-conducting media ($\sigma = 0$) no conduction processes occur. This results in pure wave equations, which is not true within the Earth's subsurface. However, the displacement current can be neglected for the frequencies utilized and the moderate resistivities, as they are much smaller than the conduction currents ($\omega\mu\sigma \gg \omega^2\mu\epsilon$). Therefore, this statement leads to the quasi-stationary model of electromagnetic field propagation. Thus, in the quasi-static approximation the Telegraph 2.11 and Helmholtz 2.12 expressions are simplify to:

$$\Delta\boldsymbol{\mathcal{F}} = \mu\sigma\frac{\partial\boldsymbol{\mathcal{F}}}{\partial t}, \tag{2.13}$$

$$\Delta\boldsymbol{\mathcal{F}} = i\omega\mu\sigma\boldsymbol{\mathcal{F}}, \tag{2.14}$$

which are known as diffusion equations 2.13 and 2.14 expressed in time and frequency domain.

2.3.2 Solution of the diffusion equation in time domain

The diffusion equation in the time domain leads to the **Step excitation** solution. According to Ward and Hohmann (1988), considering an uniform conductor with conductivity σ, for an impulse EM field at time $t = 0$ in the plane $z = 0$, the solution has the following form:

$$\boldsymbol{\mathcal{F}} = \boldsymbol{\mathcal{F}}_0\frac{\sqrt{\mu\sigma}z}{2\pi^{\frac{1}{2}}t^{\frac{3}{2}}}e^{-\frac{\mu\sigma z^2}{4t}}. \tag{2.15}$$

The maximum depth z_{max} of the EM fields is obtained taking the z-derivative for a fixed time $t > 0$ of the Equation 2.15. Then, equating to zero results in the diffusion depth δ_{TD} for time domain soundings where the EM fields obtain their maximum for $t > 0$:

$$\delta_{TD} = \sqrt{\frac{2t}{\mu\sigma}}. \tag{2.16}$$

The velocity v_{TD} of the maximum EM-fields can be obtained forming the time derivative of the diffusion depth in the time domain, as follows:

$$v_{TD} = \frac{1}{\sqrt{2\mu\sigma t}}. \tag{2.17}$$

In this manner, for a fixed time t the diffusion depth and the velocity increase in poor conductors. In a good conductor, both variables decrease.

Another solution is based on Ward and Hohmann (1988), the **Plane wave** solution for a uniform conductor, which leads to the solution of the diffusion equation in the frequency domain. Here, the diffusion depth for the frequency domain refers to the skin depth, in which the amplitude of the EM wave is reduced by the factor $1/e$, and is proportional to $\sqrt{1/\omega}$, whereas the diffusion depth in the time domain is proportional to $\sqrt{t}$.

2.4 Loop source transient electromagnetics

The transient electromagnetic (TEM) method is an active EM method and is evaluated in the time domain. TEM measurements can be applied to detect deep and shallow explorations. In the first case, a common approach is the long offset transient electromagnetic (LOTEM) method, where a grounded bipole transmitter is typically used, and components of the electrical and magnetic fields are recorded at a certain distance along the broadside or inline of the transmitter position. Typically, the LOTEM method measures the responses of the earth in distances of about 1-10 km (Strack, 1992). Secondly, also called near-surface exploration, the standard setup is to use a loop source as a transmitter, which usually is ungrounded and acts as an inductive source. As receivers, a magnetometer, an induction coil, or a wire loop are usually used to record the magnetic field's vertical component (or its time derivative). Some devices are capable of measuring all three components of the magnetic field simultaneously. Sometimes, this approach is also referred to as the short offset transient electromagnetic method. In general, this type of approach is useful for detecting layers in the order of tens to hundreds of meters. In this thesis, it refers to the loop source transient electromagnetic, or simply TEM.

In the loop source TEM method, the current flowing through the ungrounded transmitter loop establishes a primary magnetic field. The primary magnetic field change is produced by abruptly turning off or turning on a steady current. When the current is switched off, eddy currents are induced that flow in a closed trajectory which go outward and downward decreasing their intensity over time. Fig. 2.2a illustrates the result of the current flow below the transmitter loop, commonly also referred to as a *smoke ring*. Considering a uniform half-space, as shown in Fig. 2.2b, after a very short period of time, the actual induced current diffuses downward at an angle of approximately 30 degrees (Nabighian and Macnae, 1991; Dentith and Mudge, 2014). Then, taking into account the velocity (see Equation 2.17), and as the system continues to diffuse into the subsurface, the equivalent current filament takes place at an angle of approximately 47 degrees. The system of eddy currents produces a secondary transitory magnetic field, which decreases from the surface down and can be detected by a receiver as a time-dependent decaying voltage.

There are several transmitter-receiver configurations to conduct TEM. The most common are shown in Fig. 2.3. One is called a single loop setup, using the same wire as the transmitter-receiver (Fig. 2.3a). Alternatively, another setup, known as a central or in-loop setup, in which the receiver is placed in the center or somewhere inside the transmitter loop (Fig. 2.3b). In addition, if the transmitter and receiver have the same geometry and are placed as separate loops, it is referred to as a coincidence loop. Another setup is the separated loop, in which the transmitter and receiver loops are placed separately at a certain distance, similar to the Slingram configuration (Fig. 2.3c). Other types of array are also possible and are well described in Nabighian and Macnae (1991).

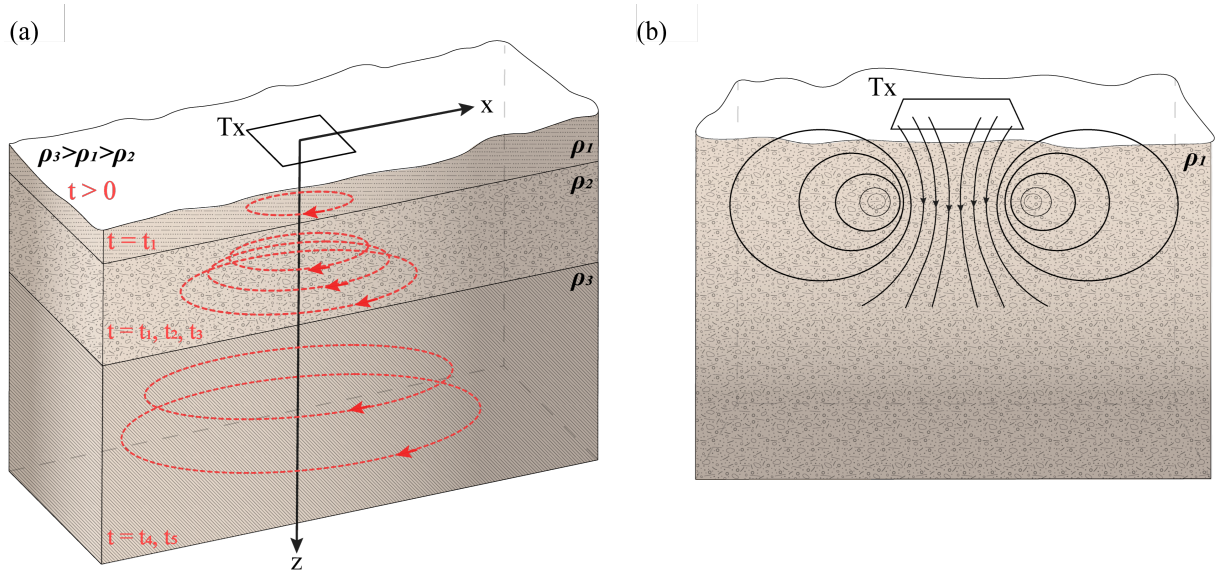

Figure 2.2: (a) System of equivalent current filaments at various times after current switch-off in the transmitter loop. (b) Magnetic field lines and equivalent current filament for one particular time over a conducting half-space after current switch-off. Modified from Nabighian and Macnae (1991).

As mentioned above, when the current switches off at time t_0, the induction process occurs due to the abrupt change of the primary magnetic field. Due to the ohmic loss process, the induced surface currents dissipate into the conductive subsurface with increasing time. Fig. 2.2a shows the propagation of exemplary eddy currents at five different times. The diffusion current propagates outward and downward after switching off the transmitter current. In addition, Nabighian and Macnae (1991) described the complete current system using a single current filament model.

It should be pointed out that due to the nonexistence of the vertical component of the electric field **E** (no current density j), the induced current flows in horizontal planes whose propagation depends on the conductivity distribution in the subsurface for a uniform or layered half-space. Hence, the horizontal electric field is represented by a pure toroidal shape with a tangential electric mode (TE mode). The magnetic field lines induced by the current filament system at a specific time are described as a pure poloidal shape and are sketched in Fig. 2.2b.

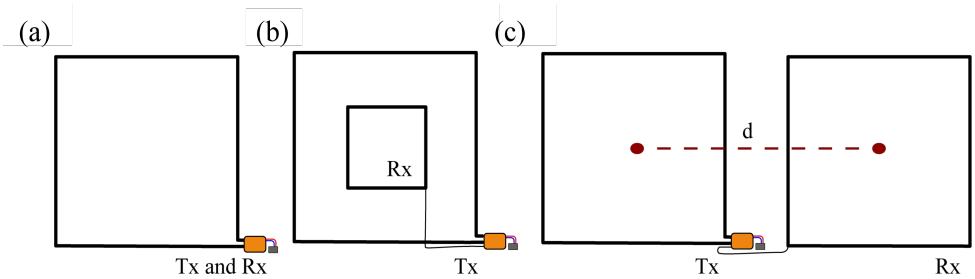

Figure 2.3: Common configurations for transmitter-receiver setups: (a) Single Loop (b) Central Loop and (c) Separate or Fixed Loop. Modified after Nabighian and Macnae (1991).

There are many types of transmitter current waveforms. In several TEM devices, the standard is the 50% duty cycle which is illustrated in Fig. 2.4. This indicates that one

current switch-off and one switch-on pulse cover half of the T period cycle. The depicted waveform is often referred to as a square waveform. The y label in Fig. 2.4a illustrates the direct current (Turn-on ramp and On-time), which can be positive $+I_0$ or negative $-I_0$ due to the different polarity. After switching off the current at t_0, the time it takes the current to decrease to zero is often called the turn-off ramp time or simply the ramp time. Then, after the primary magnetic field from the transmitter loop has dissipated, the change in the secondary magnetic field induced by the eddy currents is possible to measure during the off-time and is recorded at distinct time gates t_i. In this example, the receiver is assumed to be in the center. The gates are arranged with a logarithmic increase in time length to improve the signal/noise ratio (S/N) at late times.

Fig. 2.4d represents two possible transient behaviors recorded in the data collection stage. The late times of the transients are usually important when the target is to detect the basement. Often, this indicates strong resistive layers. If the TEM measure detects a high resistive environment, the decay is much steeper than in a low resistive environment.

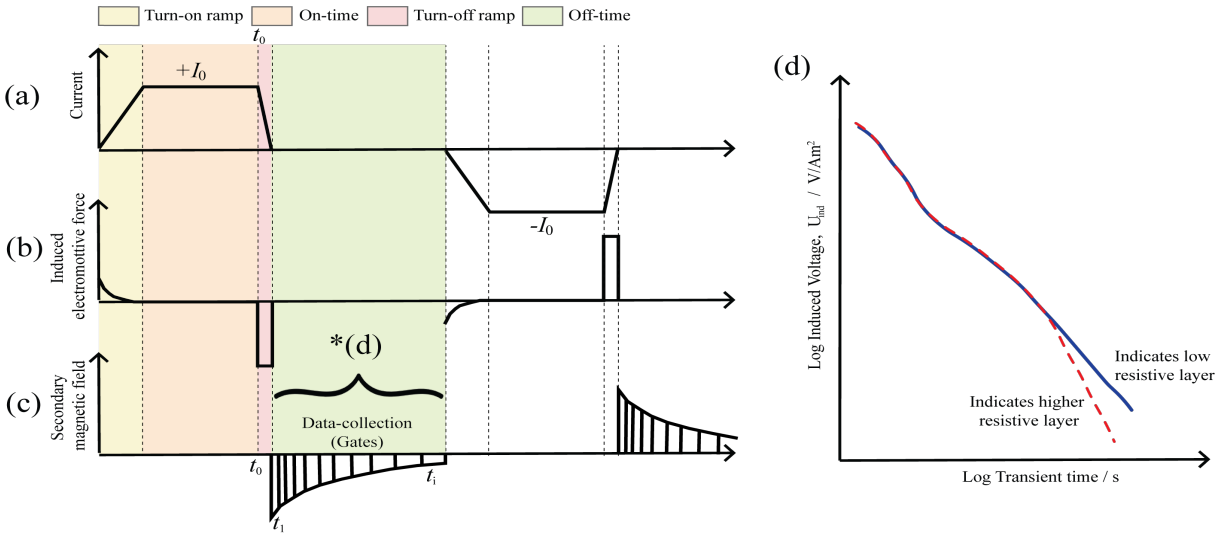

Figure 2.4: Scheme of a typical transmission pulse for a central loop TEM configuration. (a) shows the current in the transmitter current waveform for a 50% duty cycle. (b) is the induced electromotive force in the subsurface. (c) is the secondary magnetic field collected trough so-called gates by the receiver coil with t_i the distinct acquisition times. (d) Induced voltage in a receiver loop over a low and high resistive subsurface. Modified from Nabighian and Macnae (1991), Christiansen et al. (2006), Kirsch (2006) and Yogeshwar (2014).

Several authors have summarized the advantages and disadvantages of the TEM method (Frischknecht and Raab, 1984; Goldman and Neubauer, 1994; Dentith and Mudge, 2014). Some of the features to highlight are the following:

- Strong sensitivity for conductive targets.
- Relatively large depths of investigation are achieved with small transmitter loop sizes.
- Suitable for working in hard conditions, ensuring fast and non-invasive data acquisition.
- Low sensitivity for resistive targets.

2.4.1 Solution for a uniform conducting half-space

The analytical solution for a homogeneous half-space and simplified sources can be derived assuming a horizontal loop with radius a and current I located at $z = 0$, the vertical component of the magnetic field $\dot{H}_z$ at the center of the loop due to a step excitation is given by Ward and Hohmann (1988):

$$\dot{H}_z = \frac{-I}{\sigma\mu_0 a^3}\left[3erf(\Theta a) - \frac{2}{\sqrt{\pi}}\Theta a(3 + 2\Theta^2 a^2)e^{-(\Theta^2 a^2)}\right], \tag{2.18}$$

with $\Theta = \frac{1}{\sqrt{2}\delta_{TD}} = \sqrt{\frac{\mu\sigma}{4t}}$ The Gaussian error function $erf(x)$ is often used to describe diffusion processes.

$$erf(x) = \frac{2}{\sqrt{\pi}}\int_0^x e^{-\tau^2}dt. \tag{2.19}$$

It should be pointed out that for a rectangular transmitter loop with area A_{rx} an equivalent radius $\tilde{a} = \sqrt{\frac{A_{rx}}{\pi}}$ may be used. Other transmitter-receiver configurations and theoretical approximations are found in Ward and Hohmann (1988) and Spies and Frischknecht (1991).

Equation 2.18 can be reduced to two different approximations which relate $\dot{H}_z$ and the subsurface resistivity $\rho = 1/\sigma$. According to Spies and Frischknecht (1991), the induction number $\beta = a/\delta_{TD}$ can be used to refer to the zone sounding. In the case where $\beta < 1$, the near zone soundings is valid, this leads to the first approximation for late time stages $t \to \infty$ (and $\Theta \to 0$), the Equation 2.18 reduces to

$$\dot{H}_{z,lt} = \frac{-Ia^2}{20\sqrt{\pi}}(\mu\sigma)^{\frac{3}{2}}t^{-\frac{5}{2}}, \tag{2.20}$$

On the other hand, if the induction number is $\beta >> \sqrt{10}$, it refers to the far-zone sounding. This case leads to the second approximation for early times after switching off $t \to 0$ (and $\Theta \to \infty$), the Equation 2.18 simplifies to

$$\dot{H}_{z,et} = \frac{-3I}{\sigma\mu a^3}, \tag{2.21}$$

If the subsurface is homogeneous and isotropic, this yields true resistivity via the early-late time approximate equations. However, using the same equation for a heterogeneous subsurface yields the apparent resistivity ρ_a. This concept gives us a first impression of the resistivity structure and an initial input for the further inversion techniques. Rearranging the terms of Equations 2.20 and 2.21, the late time apparent resistivity is given by:

$$\rho_{a,lt} = \left[\frac{-Ia^3}{20\sqrt{\pi}}\right]^{\frac{2}{3}} t^{\frac{-2}{3}}\mu\dot{H}_{z,lt}, \tag{2.22}$$

In a similar manner, the early-time apparent resistivity is:

$$\rho_{a,et} = \frac{-a^3}{3I}\dot{H}_{z,et}. \tag{2.23}$$

It should be pointed out that the apparent resistivity should be treated carefully to avoid misinterpretation (Goldman and Neubauer, 1994). The late apparent resistivities $\rho_{a,lt}$ are useful for qualitative interpretation. However, they cannot reflect the resolution of the utilized TEM receiver system and noise measurements cannot be transformed (Spies and Frischknecht, 1991; Yogeshwar, 2014).

Throughout this thesis, the apparent late-time resistivity is derived as a qualitative measure and only for visualization of the TEM data. In contrast, the induced voltage is used as a quantitative measure because it corresponds to the measured data and is the input for all the inversion techniques.

2.4.2 Solution for a 1D layered half-space

The derivations for a 1D layered half-space have been well described and discussed by several authors (e.g. Weidelt, 1986; Ward and Hohmann, 1988). Here, a brief description is given based on the approach used in the EMUPLUS inversion algorithm, which is used to derive the 1D inversion of the TEM data.

The induced voltage U_{ind} measured by a receiver loop is generated by a horizontal electric dipole (HED) source at $z = 0$, follows the expression:

$$U_{z,ind}(t,r) = \frac{1}{2\pi}\int_{-\infty}^{\infty} \mu A_{rx} e^{i\omega t}\frac{D_0 sin\phi}{4\pi}\int_0^{\infty}\frac{B_E(k)-k}{B_E(k)+k}kJ_1(kr)dkd\omega, \tag{2.24}$$

where A_{rx} is the receiver area and $D_0 = Idl$ the dipole moment. The variables r and ϕ are the distance and angle, respectively. $B_E(k)$ is the reciprocal impedance obtained at the surface, k is the wavenumber, and J_1 is the first-order Bessel function.

For a rectangular transmitter loop, the solution is obtained by superposition of the response of numerous elementary dipoles with moment $m = Idl$. In order to achieve an accurate approximate solution, the length of the elementary dipole dl is determined by the induction number, which in the time domain depends on the source-receiver separation.

In order to obtain an accurate solution, more dipoles are needed in the near than in the far zone. Equation 2.24 is used to derive one dipole and cannot be solved analytically since it involves the calculation of a Bessel integral following the expression:

$$g(r) = \int_0^{\infty} f(k)J_v(kv)dk,\ v = 1. \tag{2.25}$$

These kinds of integrals can be numerically evaluated with the fast Hankel transform due to the oscillating nature of Bessel functions. Further explanations of the fast Hankel transformation and solutions for different dipole sources, and the derivation of components like H_x and H_y, are given in Weidelt (1986); Ward and Hohmann (1988); Martin (2009).

2.4.3 Depth of investigation

The depth of investigation (DOI) for the central loop TEM configuration using the late time approximation (near zone) is often estimated by the expression suggested by Spies (1989) and is given by:

$$\delta_{doi} = 0.55 \left(\frac{I A_{Tx} \bar{\rho}}{\eta_v} \right)^{\frac{1}{5}}, \tag{2.26}$$

where A_{Tx} is the size of the transmitter loop in m^2, I is the transmitter current in A units and η_v is the voltage noise level measured in nV/m^2. The δ_{doi} depends directly on the average resistivity $\bar{\rho}$ with $z \leq \delta_{doi}$:

$$\bar{\rho} = \frac{1}{\delta_{doi}} \int_{z=0}^{\delta_{0doi}} \rho(z) dz. \tag{2.27}$$

The δ_{doi} is used to estimate the lower depth bound of the 1D inversion models. The noise level η_v was measured at each source location and mostly corresponds to the last time point used at each sounding. However, δ_{doi} is considered a rough estimate due to the easily overestimations regarding resistive 1D models. Therefore, in this thesis, the same procedure as in Yogeshwar (2014) is used, only 70% of δ_{doi} is considered as the depth of exploration. Moreover, the depth of diffusion in the time domain, as articulated in Equation 2.13, is also used to determine the depth at which a layer can be detected at a given time point and the conductivity of the overburden. Both δ_{doi} and δ_{TD} are used as a preliminary estimate for the validation of all 1D inversions, and a qualitative interpretation is given based on the depth of investigation derived from the subsurface resistivity distribution.

CHAPTER 3

1D Inversion theory

Inverse modeling techniques are often used to search for an optimal subsurface distribution of physical properties based on geophysical data. In this manner, inversion of a geophysical data set aims to find model parameters that can explain the measured data. In this chapter, the inversion problem in geophysics used throughout this thesis is briefly introduced. In more detail, the Marquardt and Occam inversion schemes, which are implemented in the utilized 1D inversion algorithm EMUPLUS are explained (Scholl, 2005). In addition, the model parameter Importances used to estimate the model uncertainties are also described. The inversion techniques presented in the following sections are fundamental for 1D inversion algorithms. For additional information on inversion theoretical principles, see Meju (1994) and Menke (2018).

3.1 Problem formulation

For a given TEM data set, the induced voltages at a certain location can be stored in a data vector $\boldsymbol{d} \in \mathbb{R}^N$ containing N elements with their corresponding data errors $\delta\boldsymbol{d} \in \mathbb{R}^N$ as follows

$$\boldsymbol{d} = (\boldsymbol{d}_1, \boldsymbol{d}_2, \boldsymbol{d}_3, ..., \boldsymbol{d}_N)^T \tag{3.1}$$

$$\delta\boldsymbol{d} = (\delta\boldsymbol{d}_1, \delta\boldsymbol{d}_2, \delta\boldsymbol{d}_3, ..., \delta\boldsymbol{d}_N)^T, \tag{3.2}$$

where T denotes the transpose operator. Assume a model vector $\boldsymbol{m} \in \mathbb{R}^M$ that contains M elements in the same way as

$$\boldsymbol{m} = (\boldsymbol{m}_1, \boldsymbol{m}_2, \boldsymbol{m}_3, ..., \boldsymbol{m}_N)^T, \tag{3.3}$$

the inversion problem seeks to find a model $\boldsymbol{m} \in \mathbb{R}^M$, which explains the observed data $\boldsymbol{d}$ within their errors $\delta\boldsymbol{d}$. Therefore, the calculation of the model response $\boldsymbol{d}'$ of the observed data is the forward problem as a function of $\boldsymbol{m}$:

$$\mathbf{d}' = \boldsymbol{F}(\mathbf{m}), \tag{3.4}$$

where $\boldsymbol{F}$ is the forward modeling operator that indicates the transformation from the model to the data space. In general, the forward operator comprises the solution of the impulse-response of U_{ind} given in Chapter 2.

If sufficient information is available, the data and the model parameters follow $N = M$, the solution can be uniquely determined, and the problem is *even determined*. This leads to a simple inverse formulation $\boldsymbol{m} = \boldsymbol{F}^{-1}(\boldsymbol{d})$ with one exact solution. However, if more data information than unknown parameters are available, the problem is *over-determined* ($M < N$) and usually no unique solutions exist, therefore, a model that best explains the data is chosen. In contrast, if there are more unknowns in the model parameters than in the data, the inverse problem becomes *under-determined* ($M > N$) and infinite solutions can be determined that explain the data. However, it might be the case that some model parameters are better resolved than others. Consequently, the inversion problem is often considered to be *mixed-determined*. Even with a larger data set than model parameters, the data information may lead to a poor structure since the data and model parameters are not independent information. The latter refers to mixed-determined inverse problems. These types of inverse problem are usually referred to as ill-posed, and in order to be solved, a constraint is required to stabilize the solution.

One common inversion approach to minimize the misfit between the measured data vector $\boldsymbol{d}$ and model response $\mathbf{d}'$ is using the weighted least squares criterion

$$\Phi_d = (\boldsymbol{d} - \boldsymbol{d}')^T \boldsymbol{W}_d^2 (\boldsymbol{d} - \boldsymbol{d}') = \epsilon^T \boldsymbol{W}_d^2 \epsilon, \tag{3.5}$$

where Φ_d is the data cost function, also called misfit function. $\epsilon = (\boldsymbol{d} - \boldsymbol{d}')$ denotes the residual vector. $\boldsymbol{W}_d^2$ is the squared weighting matrix with reciprocal standard deviations (data errors) on the main diagonal $\boldsymbol{W}_d$:

$$\boldsymbol{W}_d = \begin{pmatrix} \frac{1}{\delta d_1} & & 0 \\ & \ddots & \\ 0 & & \frac{1}{\delta d_N} \end{pmatrix}. \tag{3.6}$$

Most geophysical data sets, as well as the algorithms utilized in this thesis, follow Gaussian statistics. Therefore, the least squares method is used. Consequently, the data fit χ can be obtained as follows

$$\chi = \sqrt{\frac{\Phi_d}{N}} = \sqrt{\frac{1}{N} \sum_{i=1}^{N} \frac{(d_i - d_i')^2}{\delta d_i^2}}; \quad i = 1, ..., N, \tag{3.7}$$

where $\chi = 1$ indicates a well-fitted data error, χ <1 correspond to overfitted data, and χ >1 means not sufficiently fitted. Additionally, the relative root mean square (RMS) in percent is given by

$$RMS = \sqrt{\frac{1}{N}\sum_{i=1}^{N}\frac{(d_i - d_i')^2}{d_i^2}} \times 100\ [\%];\ i = 1, ..., N. \tag{3.8}$$

It should be noted that both χ and RMS are used to estimate the data fit. However, the least squares method (also called the norm L_2) follows the Gaussian distribution in most data sets. Therefore, these variables can lead to an inaccurate quantitative measure of data fit if significant outliers are present.

The least squares method is usually used to solve over-determined problems where too much data is present to obtain an exact solution. Then, the cost function $\Phi_d(\boldsymbol{m})$ can be minimized by taking the derivative with respect to the model parameters $\boldsymbol{m}$ and setting it equal to zero: $\frac{\partial \Phi_d(\boldsymbol{m})}{\partial \boldsymbol{m}} = 0$. Therefore, in a linear case, the least squares solution of Equation 3.5 has the following form:

$$\boldsymbol{m} = (\boldsymbol{F}^T \boldsymbol{W}_d^2 \boldsymbol{F})^{-1} \boldsymbol{F}^T \boldsymbol{W}_d^T \boldsymbol{W}_d \boldsymbol{d}. \tag{3.9}$$

In addition, in most applied geophysical problems, the data are associated with a forward operator that depends on a nonlinear system equations (Meju, 1994) on which the cost function is defined as follows:

$$\Phi_d = (\boldsymbol{d} - \boldsymbol{F}(\boldsymbol{m}))^T \boldsymbol{W}_d^2 (\boldsymbol{d} - \boldsymbol{F}(\boldsymbol{m})), \tag{3.10}$$

Then, one approach to resolve the nonlinear inversion problem is to linearize the forward operator by a first-order Taylor expansion for small model perturbations $\Delta \boldsymbol{m}_k = \boldsymbol{m} - \boldsymbol{m}_k$ and a given model $\boldsymbol{m}_k$.

The forward operator follows the expression:

$$\boldsymbol{F}(\boldsymbol{m})\Big|_{\boldsymbol{m}_k} \approx \boldsymbol{F}(\boldsymbol{m}_k) + \frac{\partial \boldsymbol{F}}{\partial \boldsymbol{m}}\Big|_{m_k} \Delta \boldsymbol{m}_k = \boldsymbol{F}(\boldsymbol{m}_k) + \boldsymbol{J}\Big|_{\boldsymbol{m}_k} \Delta \boldsymbol{m}_k, \tag{3.11}$$

where $\boldsymbol{J}$ is the Jacobian, or also called the sensitivity matrix $N \times M$. The higher-order terms in Taylor's expansion are neglected. The entries of the matrix contain the partial derivatives of the forward operator with respect to the model parameters in the following form:

$$\boldsymbol{J}_{ij} = \frac{\partial \boldsymbol{F}_i}{\partial \boldsymbol{m}_j}\Big|_{m=m_k};\ i = 1, ..., N;\ j = 1, ..., M. \tag{3.12}$$

The Jacobian matrix can be utilized as a measure of resolution. The absolute values of the matrix are shown if the data are sensitive to the perturbation of the model. Well-resolved

parameters have high-valued entries in the Jacobian matrix, meaning that the Forward operator is sensitive to small perturbations. For poorly resolved parameters, the entries of the Jacobian matrix tend to be small or close to zero, which means that the variation of the model weakly affects the data.

Changing the forward operator in Equation 3.10, the new cost function follows:

$$\Phi_d(\Delta \boldsymbol{m}_k) = (\boldsymbol{d} - \boldsymbol{F}(\boldsymbol{m}_k) - \boldsymbol{J}\Delta \boldsymbol{m}_k)^T \boldsymbol{W}_d^2 (\boldsymbol{d} - \boldsymbol{F}(\boldsymbol{m}_k) - \boldsymbol{J}\Delta \boldsymbol{m}_k). \tag{3.13}$$

Similarly to the linear problem, the derivative of Equation 3.13 with respect to the model update $\Delta \boldsymbol{m}_k$ is calculated and equated to zero. Thereby, the least squares solution for the model update takes the following form:

$$\Delta \boldsymbol{m}_k = (\boldsymbol{J}^T \boldsymbol{W}_d^2 \boldsymbol{J})^{-1} \boldsymbol{J}^T \boldsymbol{W}_d^2 (\boldsymbol{d} - \boldsymbol{F}(\boldsymbol{m}_k)). \tag{3.14}$$

3.1.1 Nonlinear optimization approaches

Gradient based approach

One way to find the model update is the Gradient descent method, also called the Steepest descent method. This approach is a straightforward optimization algorithm where the model update $\Delta \boldsymbol{m}_k$ is searched in the direction of the negative gradient of the nonlinear cost function Φ_d in Equation 3.13 as follows:

$$\Delta \boldsymbol{m}_k = -\gamma \frac{\partial \Phi_d}{\partial \boldsymbol{m}_k}. \tag{3.15}$$

The minus indicates a negative gradient search direction and γ is a constant that denotes the step size of the model correction. The derivative of a nonlinear cost function with respect to the model parameters takes the form:

$$\frac{\partial \Phi_d}{\partial \boldsymbol{m}_k} = -2 \left[\frac{\partial \boldsymbol{F}(\boldsymbol{m}_k)}{\partial \boldsymbol{m}_k} \right]^T \boldsymbol{W}_d^2 (\boldsymbol{d} - \boldsymbol{F}(\boldsymbol{m}_k)) = -2\boldsymbol{J}^T \boldsymbol{W}_d^2 (\boldsymbol{d} - \boldsymbol{F}(\boldsymbol{m}_k)). \tag{3.16}$$

Then, equating to zero, the gradient descent solution for the model update $\Delta \boldsymbol{m}_k$ is:

$$\Delta \boldsymbol{m}_k = -2\gamma \boldsymbol{J}^T \boldsymbol{W}_d^2 (\boldsymbol{d} - \boldsymbol{F}(\boldsymbol{m}_k)). \tag{3.17}$$

In order to find the optimal value for the constant γ, a line search procedure is selected in order to minimize $\Phi_d(\boldsymbol{m}_k + \Delta \boldsymbol{m}_k)$ in each k-th iteration. A general description of several line-search techniques is given in Martin (2009). It should be pointed out that the gradient descent method does not require the calculation of the inverse matrix. Another feature is that the approach cannot diverge, however, the rate of convergence decreases for later stages in the inversion.

In order to have better convergence, conjugate gradient techniques are often used in place of simple gradient methods (Rodi and Mackie, 2001; Commer and Newman, 2008).

In many cases, to solve large-scale optimization problems, nonlinear conjugate gradient techniques are used to avoid explicit computations of the Jacobian matrix.

Gauss-Newton approach

In order to achieve the updated model $\boldsymbol{m}_{k+1}$, the model perturbation is added to the model from the previous step k, and with the starting model $\boldsymbol{m}_0(k = 0)$. Then, on each iteration k, the model update $\Delta\boldsymbol{m}_k$ is determined and the current iteration model is updated:

$$\boldsymbol{m}_{k+1} = \boldsymbol{m}_k + \Delta\boldsymbol{m}_k. \tag{3.18}$$

This process is repeated until a model is found that adequately fits the data or a number of desired iterations is reached. This iterative inversion process is typically referred to as the unconstrained iterative least squares fitting or the Gauss-Newton method. In this manner, the cost function fulfills $\Phi_d(\boldsymbol{m}_{k+1}) < \Phi_d(\boldsymbol{m}_k)$. However, the convergence of this technique may be slow due to the strong dependence of a suitable initial model, and if the eigenvalues of the Jacobian are close to zero, the matrix $\boldsymbol{J}^T\boldsymbol{J}$ may be singular or close to singular, which means that the matrix is ill-conditioned and Equation 3.14 would not have a solution. To avoid solution instability or ill-posed problems, the GN method is adapted by imposing additional constraints to the solution which minimizes the cost function in Equation 3.14.

3.2 Marquardt-Levenberg inversion

This algorithm was performed in a way to reduce instability and non-convergence of the ill-posed problem. Levenberg (1944) proposed a damped / constrained least squares approach, which was improved to nonlinear least squares algorithms by Marquardt (1963). In order to stabilize the cost function, a tradeoff parameter (also called the damping parameter) is added to the length of the model update $\Delta\boldsymbol{m}_k$. The total cost function takes the following form:

$$\Phi_d(\Delta\boldsymbol{m}_k) = (\boldsymbol{d} - \boldsymbol{F}(\boldsymbol{m}_k) - \boldsymbol{J}\Delta\boldsymbol{m}_k)^T \boldsymbol{W}_d^2(\boldsymbol{d} - \boldsymbol{F}(\boldsymbol{m}_k) - \boldsymbol{J}\Delta\boldsymbol{m}_k) + \beta^2(\Delta\boldsymbol{m}_k^T\Delta\boldsymbol{m}_k). \tag{3.19}$$

Here, β^2 is also known as the Lagrange multiplier and weights between the data misfit term and the model update term. This type of constraint on the model update is denoted as local regularization. By taking the derivative of the cost function with respect to the model update, equated to zero, the damped square solution is:

$$\Delta\boldsymbol{m}_k = (\boldsymbol{J}^T\boldsymbol{W}_d^2\boldsymbol{J} + \beta^2\boldsymbol{I})^{-1}\boldsymbol{J}^T\boldsymbol{W}_d^2(\boldsymbol{d} - \boldsymbol{F}(\boldsymbol{m}_k)), \tag{3.20}$$

where $\boldsymbol{I} \in \mathbb{N}^{(M\times M)}$ is the identity matrix. This scheme is used for inversion problems with very few model parameters. The damped least squares inversion approach is also called ridge regression (Inman, 1975). The Marquardt-Levenberg scheme deals with singularities

that add β to the main diagonal of $\boldsymbol{J}^T \boldsymbol{W}_d^2 \boldsymbol{J}$. For small values of β, the solution approximates to the Gauss Newton approach. In contrast, for large values of β, the solution is similar to the gradient scheme (Meju, 1994).

3.2.1 Singular value decomposition

Singular value decomposition (SVD) is often utilized in geophysical data analysis to derive the inverse of the weighted Jacobian matrix $\boldsymbol{J}_w$. The procedure states that any $N \times M$ matrix with N data entries and M model parameters can be factorized in the product of three other matrices (Menke, 2018):

$$\boldsymbol{J}_w = \boldsymbol{U}\boldsymbol{S}\boldsymbol{V}^T. \tag{3.21}$$

Here, the $N \times N$ matrix $\boldsymbol{U}$ spans the data space and contains the N eigenvectors of $\boldsymbol{J}_w \boldsymbol{J}_w^T$. In the same manner, the $M \times M$ matrix $\boldsymbol{V}$ contains the M eigenvectors of $\boldsymbol{J}_w^T \boldsymbol{J}_w$. Both matrices are orthogonal and satisfy the property $\boldsymbol{U}^T\boldsymbol{U} = \boldsymbol{V}^T\boldsymbol{V} = \boldsymbol{V}\boldsymbol{V}^T = \boldsymbol{I}$.

The $N \times M$ matrix $\boldsymbol{S}$ is a diagonal eigenvalue matrix. The diagonal elements $(\lambda_1, ..., \lambda_N)$ are non-negative roots of the eigenvalues of $\boldsymbol{J}_w^T \boldsymbol{J}_w$ and refer to as singular values. These singular values are arranged in decreasing order, weighting the influence of the linear combinations on the model result (Hördt et al., 1992; Menke, 2018).

The matrix $\boldsymbol{J}_w$ in Equation 3.20 is substituted by the decomposition in Equation 3.21. Then, the damped least square solution is given by the following expression:

$$\Delta \boldsymbol{m}_k = \boldsymbol{V} \underbrace{(\boldsymbol{S}^2 + \beta^2 \boldsymbol{I})^{-1} \boldsymbol{S}^T \boldsymbol{S}}_{:=\boldsymbol{T}} \boldsymbol{S}^{-1} \boldsymbol{U}^T \boldsymbol{W}_d (\boldsymbol{d} - \boldsymbol{F}(\boldsymbol{m}_k)), \tag{3.22}$$

where the damping matrix $\boldsymbol{T}$ is a diagonal matrix and contains the damping terms in the following form:

$$T_{ii} = \frac{S_{ii}^2}{S_{ii}^2 + \beta^2}. \tag{3.23}$$

Considering the maximum singular value S_{11} and normalizing the damping matrix, Equation 3.23 takes the form:

$$T_{ii} = \frac{\lambda_i^2}{\lambda_i^2 + \upsilon^2}. \tag{3.24}$$

Therefore, υ is the threshold for relative singular values. In general, and for the 1D inversion algorithm EMUPLUS used in this thesis, a default 1% normalized singular value threshold is defined during inversion. Therefore, singular values with a factor of 0.01 less than S_{11} will be damped by a factor of 0.5.

3.2.2 Importances

The measure of whether the model parameters are well resolved can be done through a resolution study called importances $\boldsymbol{L}$ of the model parameter. For this, the $\boldsymbol{V}$ matrix and the damping term $\boldsymbol{T}$ are used in the form:

$$\boldsymbol{L} = \boldsymbol{V}\,\boldsymbol{T}. \tag{3.25}$$

The importance of each parameter is given by

$$Imp_i = L_{ii},\ with\ 0 \leq Imp_i \geq 1. \tag{3.26}$$

Here, the importances indicates how well-resolved the model parameters are, and the range lies between 0 and 1 (from poor to well-resolved). For high values, the influence of the model parameter on the data fit is high. However, a disadvantage of the importances is the significant dependency on the damping matrix and the starting model.

3.2.3 Equivalent models

Equivalent models are considered when the responses of two models are identical within their data errors. A large equivalence occurs when poor or non-resolved model parameters are not supported by data. The Hybrid Marquardt Monte Carlo scheme is implemented in EMUPLUS to derive 1D equivalent models (Scholl, 2005). They are calculated by perturbing each model parameter of a preliminary best-fit model by a predefined percentage value. Models that result in a calculated response with sufficiently low misfit are stored and compared. Equivalent models are also used to evaluate the resolution of the model parameters. High variability means that the model parameters are not well resolved, whereas low variability corresponds to well-resolved model parameters.

3.3 Constrained Occam inversion

In EM methods, the inversion problems are usually nonlinear and ill-posed. In order to find a solution, a stabilizing term is added to the linearized least squares approach in the inverse problem that leads to the damped least squares solution after Tikhonov and Arsenin (1977). Therefore, the objective function $\Phi(\boldsymbol{m})$ to minimize has the following form

$$\Phi(\boldsymbol{m}) = \Phi_d(\boldsymbol{m}) + \lambda\Phi_m(\boldsymbol{m}), \tag{3.27}$$

where λ is the Tikhonov regularization parameter, $\Phi_{\boldsymbol{d}}(\boldsymbol{m})$ is the data misfit term, and $\Phi_{\boldsymbol{m}}(\boldsymbol{m})$ is the model regularization term.

The Occam inversion scheme was introduced by Constable et al. (1987). This approach imposes a smoothness constraint that measures the roughness R of the model $\boldsymbol{m}$. Therefore, the objective function is given as

$$\Phi(\boldsymbol{m}) = (\boldsymbol{d} - \boldsymbol{F}(\boldsymbol{m}) - \boldsymbol{J}\Delta\boldsymbol{m})^T \boldsymbol{W}^2 (\boldsymbol{d} - \boldsymbol{F}(\boldsymbol{m}) - \boldsymbol{J}\Delta\boldsymbol{m}) + \lambda \boldsymbol{m}^T \boldsymbol{R}_{1,2}^T \boldsymbol{R}_{1,2} \boldsymbol{m}. \tag{3.28}$$

Considering a 1D model composed of M free resistivity values (ρ_i) and M layer with predefined thickness. Constraints in the form of roughness are defined as the derivative of the first R_1 and second R_2 order of $\rho(z)$ with respect to depth:

$$R_1 = \int \left(\frac{\partial \rho(z)}{\partial z} \right)^2 dz \quad and \quad R_2 = \int \left(\frac{\partial^2 \rho(z)}{\partial z^2} \right)^2 dz. \tag{3.29}$$

From here, if minimization is achieved, R_1 exhibits the gradient of $\rho(z)$ and becomes very small. In a similar manner, R_2 displays the least curvature of $\rho(z)$. However, in the 1D case, $\rho(z)$ is not continuous, and therefore the discrete form is given:

$$R_1 = \sum_{i=2}^{M} (\rho_i - \rho_{i-1})^2 \quad and \quad R_2 = \sum_{i=2}^{M-1} (\rho_{i+1} - 2\rho_i + \rho_{i-1})^2 . \tag{3.30}$$

For a 1D case, the roughness formulations can be rewritten in matrix notation as $\boldsymbol{R}_1$, $\boldsymbol{R}_2 \in \mathbb{Z}^{M \times M}$ and is expressed as:

$$\boldsymbol{R}_1 = \begin{pmatrix} 0 & 0 & 0 & \dots & 0 \\ -1 & 1 & 0 & \ddots & \vdots \\ 0 & \ddots & \ddots & \ddots & 0 \\ \vdots & \ddots & -1 & 1 & 0 \\ 0 & \dots & 0 & -1 & 1 \end{pmatrix} \quad and \quad \boldsymbol{R}_2 = \boldsymbol{R}_1^T \boldsymbol{R}_1 \tag{3.31}$$

Considering the forward operator given in Equation 3.11, the model update ($\Delta \boldsymbol{m}_k$) after the derivation of Equation 3.28 with respect to the model parameters one gets for the linearized problem:

$$\Delta \boldsymbol{m}_k = (\boldsymbol{J}^T \boldsymbol{W}_d^2 \boldsymbol{J} + \lambda \boldsymbol{R}_{1,2}^T \boldsymbol{R}_{1,2})^{-1} \left[\boldsymbol{J}^T \boldsymbol{W}_d^2 \big(\boldsymbol{d} - \boldsymbol{F}(\boldsymbol{m}_k) \big) - \lambda \boldsymbol{R}_{1,2}^T \boldsymbol{R}_{1,2} \boldsymbol{m}_k \right] \tag{3.32}$$

Occam inversion is widely used to obtain smooth models because it is well known that Marquardt inversions lead to a strong dependency on the initial guess and usually reveal a sharp contrast in resistivity variation in order to obtain a layered model. In the 1D inversion algorithm EMUPLUS, both roughness R_1 and R_2 are implemented (Scholl, 2005). The 1D models calculated by these two roughnesses could also be used as an evaluation for the resolution of model parameters. The Occam R_1 and R_2 models usually differ in zones where inversion is driven solely by regularization and is not supported by data (Yogeshwar et al., 2020). The R_1/R_2 criteria can therefore be used as a rough measure of the depth of the exploration by clipping the models at a depth at which they diverge. On the other side, the regularization term λ weights the mismatch in the data and the roughness of the model. If a large λ is chosen, it improves the weighting of the

roughness of the model, which means that the inversion prefers a smoother model than a smaller data fit. In contrast, if a small λ is used, the roughness is less constrained and resistivity jumps can occur. In general, the Occam inversion is performed with a large initial λ, which decreases successively throughout the iterations. In subsequent iterations, the inversion searches for a λ, which minimizes the misfit (Constable et al., 1987). Practically, a proper λ could be found by multiplying a cooling factor to decrease its value during the inversion, like the strategy described by the L-curve criterion (Hansen and O'Leary, 1993).

CHAPTER 4

Field surveys in the Atacama Desert

One crucial aim of the CRC 1211 project is the reconstruction of the chronology, weathering, and erosion of the basins formed in the Atacama Desert during the Quaternary-Miocene period. Applied geophysical methods are relevant tools for interdisciplinary research. Within CRC 1211, the application of EM methods is a prerequisite to select optimal coring locations, excavation, and sampling sites. Therefore, subsurface models derived from geophysical surveys significantly contribute to the definition of the spatial context for a better understanding of such archives and enrich paleoclimatic research. Sedimentary deposits, such as clay pans, are widespread along the Coastal Cordillera and are sensitive archives of the Atacama paleoclimate, because they contain valuable information on the precipitation history (Ritter et al., 2018a; Diederich-Leicher, 2020). Two extensive geophysical surveys were carried out in October 2018 and November 2019 in the clay pans called PAG and Paranal. Here, the TEM method was utilized, covering the soundings as a 3D grid on each clay pan. The subsurface models resulting from this survey provide key inputs to derive suitable drilling locations for paleoclimate research, avoiding elaborate and costly drilling.

In the first part of this chapter, the objectives of the field campaigns are given, followed by the geological context of the region and a brief geological description of each clay pan. In order to collect the optimal data, the TEM measurements were carried out in a 3D grid covering the whole area of the clay pans. A total of 48 and 133 soundings were performed at the PAG and Paranal sites, respectively. The project also carried out active seismics and magnetics as complementary geophysical methods in both sites. Furthermore, the TEM equipment utilized, the survey setup, and the data processing are described. Then, the TEM field data for both clay pans are shown and briefly discussed. The TEM data processing methods described in detail in this section are also partly published in (Blanco-Arrué et al., 2021, 2022).

4.1 Objectives of the geophysical surveys

The CRC 1211 collects essential information about the climatic and environmental history of the hyperarid core. In this thesis, the TEM method was conducted to investigate the sediment layers in terms of the resistivity distribution. With this, the general objective is to detect the sediment sequences of the clay pans PAG and Paranal. In addition, the main objective of geophysical surveys is to provide detailed information about sedimentary architecture and bedrock topography. Moreover, the geophysical survey at the Paranal site also aims to support drilling projects in the area within the subproject A02.

It should be noted that before the geophysical surveys, no information existed on the thickness of the sediment infill or the basement depth of the clay pans PAG and Paranal, making them challenging sites for geophysical investigations. Because of this, other geophysical methods were carried out to imagine and resolve subsurface properties at different spatial scales, such as magnetic and active seismics. Geophysical methods have different resolution capabilities to resolve the physical properties of the subsurface and are often combined to achieve the optimal target resolution (Díaz et al., 2014; Yáñez et al., 2020; Bücker et al., 2021). The geophysical surveys consider collecting information that allows answering questions like:

- How deep is the basement layer on each clay pan?
- How thick are the sediment layers deposited at the selected sites?
- How heterogeneous is the internal geometry of the clay pan?

Our results provide essential information on the resistivity distribution models and can be linked to various subsurface processes, contributing to paleoclimate research and environmental models. The depth and morphology of the sedimentary layers and the basement rocks interpreted in each clay pan may be integrated into fluvial landscape evolution and environmental models.

4.2 Geological context

The Atacama Desert is located along the western border of South America, between the central Andes and the Pacific Ocean, in northern Chile. It is known to be the driest desert on Earth and extends from southern Peru ($\sim 18°S$) to northern Chile ($\sim 27°S$). Fig. 4.1a shows a regional view and the climatological context of the study area. Here, summer and winter rainfall have a strongly heterogeneous precipitation pattern from north to south, caused by pronounced differences in dominant climate patterns (Houston, 2006). On a large scale, the main factors that contribute to the overall hyperaridity of the Atacama Desert are: (1) the rain shadow of the Andes to the east, blocking the moisture coming from the Atlantic Ocean (Houston and Hartley, 2003), (2) the regional position within the subtropical high pressure belt, and (3) the upwelling of cold water to the west, related to the Humboldt current of the Pacific Ocean (Hartley and Chong, 2002; Clarke, 2006).

The region provides unique opportunities to study surface and subsurface processes, which are severely and predominantly driven by the limited water availability (Houston and Hartley, 2003; Hartley et al., 2005). Water-driven processes in extremely water-limited

environments that cover significant areas on Earth, such as the Atacama Desert, are not well understood. Therefore, studying the climate history of the Atacama Desert is crucial to better understand the controlling factors and the desertification processes.

The Coastal Cordillera, located in the forearc of the Central Andes, is a geomorphological unit formed mainly by Jurassic-early Cretaceous dioritic to granodioritic plutons and Jurassic volcanic rocks Fig. 4.1. These types of rocks comprise remnants of a Mesozoic volcanic arc formed along the forearc region of the Central Andes in northern Chile and southern Peru at the early stage of the modern Andes due to the subduction of the oceanic Nazca plate beneath the continental South American plate since the Jurassic to early Cretaceous (Pardo-Casas and Molnar, 1987).

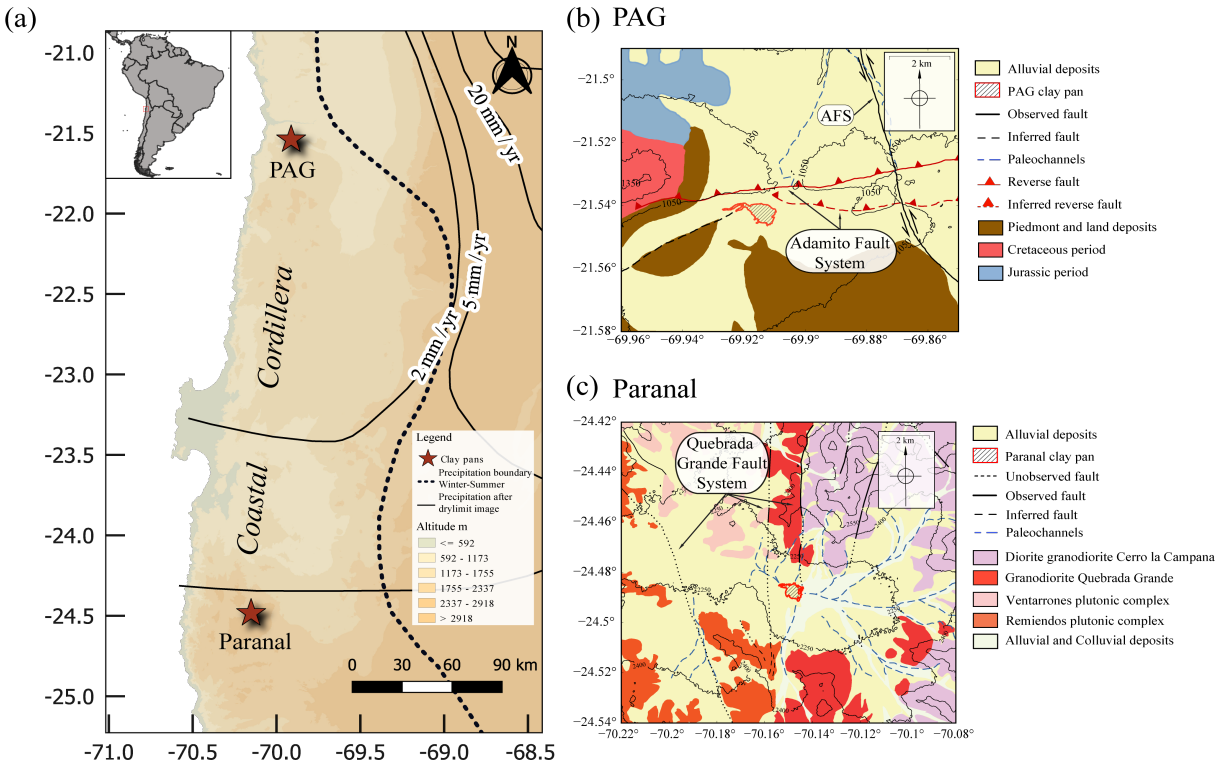

Figure 4.1: (a) Location and climatological context of the survey areas. Climatic setting with the border between winter and summer rainfall zones and mean annual precipitation after (Houston, 2006). The relief map from NASA (2020). (b) Geological context of the PAG clay pan, modified from Quezada et al. (2012) and Vásquez et al. (2018). (c) Geological context of the Paranal clay pan, modified from Domagala et al. (2016). Isolines indicate the elevation in meters above sea level (m.a.s.l.). The lithology with the main intrusives and plutonic complexes is described on the right side.

An essential feature of the Chilean Coastal Cordillera is the Atacama fault system, which conforms to a complex set of faults extending for more than 1000 km between the parallels $21° - 30° S$ (Scheuber and Andriessen, 1990). This has been formed by sinistral movement between the Upper Jurassic and Lower Cretaceous (Scheuber and Andriessen, 1990; Taylor et al., 1998), and as a result of deformation produced by oblique subduction in that period (Scheuber and Gonzalez, 1999; Cembrano et al., 2005). During the Miocene, it would have started its reactivation as a high-angle normal fault system that can be observed today on the surface (Herve, 1987; Scheuber and Andriessen, 1990; Naranjo et al., 1994; Allmendinger and González, 2010). After the Miocene, the Atacama fault

system experienced an extensional deformation, which caused the dominant vertical slip and controlled its present-day morphological expression in the Coastal Cordillera (Herve, 1987; Cembrano et al., 2005; González et al., 2006). Most of the parallel normal faults observed in the trenches along northern Chile are associated with this stage (Niemeyer et al., 1996; Delouis et al., 1998; Von Huene et al., 1999; González et al., 2003). The resulting exposed fault scarps can be observed between $19°S$ and $21.6°S$ in the Coastal Cordillera.

The Cenozoic climate history of arid and hyperarid sites in the Atacama Desert has been studied during the past decades by several authors, covering different aspects, such as chronology, climatic condition, and erosion processes (e.g., Hartley and Chong, 2002; Dunai et al., 2005; Ritter et al., 2019; Diederich-Leicher, 2020; Dunai et al., 2020). The sediment deposition occurred throughout northern Chile during the late Eocene to the early Pliocene. The forearc setting was similar to the present-day environment with sedimentary rocks comprising fluvial, sandflats, evaporite, nitrate and lacustrine deposits, among others (Naranjo et al., 1994; May et al., 1999; Sáez et al., 1999; Hartley et al., 2000). Landscape reconstructions indicate that prominent Miocene and Pliocene alluvial deposits represent large regional erosion/depositional events, whereas Quaternary processes have locally incised into or lap over these regional fluvial deposits (Amundson et al., 2012).

Sedimentary deposits in endorheic basins, such as clay pans, are widespread along the Coastal Cordillera of the Atacama Desert and are mainly formed by drainage blocking due to past tectonic activity, which resulted in perfect sediment traps. Detecting the subsurface geometry of these clay pans provides essential insight into the depositional regimes and sedimentation rates, the uplift history, and is indirectly linked to the period in which the subsurface was exposed to different fluvial or arid periods.

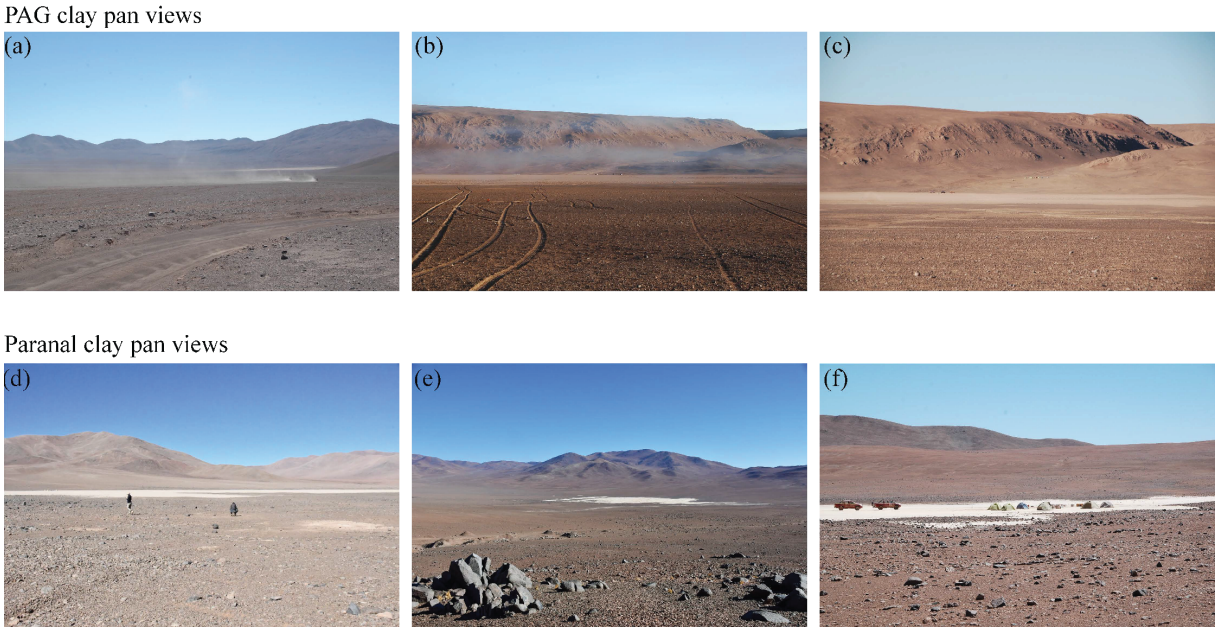

Figure 4.2: PAG views: (a) from east to west (21.55°S/69.87°W, ∼1030 m.a.s.l.), (b) from south to north (21.55°S/69.91°W, ∼957 m.a.s.l.), (c) from south to north (21.54°S/69.91°W, ∼942 m.a.s.l.). Paranal views: (d) from southwest to northeast (24.49°S/70.15°W, ∼2199 m.a.s.l.), (e) from northwest to southeast (24.46°S/70.15°W, ∼2286 m.a.s.l.), (f) from northwest to southeast (24.48°S/70.14°W, ∼2200 m.a.s.l.).

The Coastal Cordillera contains several sedimentary deposits, such as clay pans. These sensitive archives of the Atacama paleoclimate keep information about the climate history and are predominantly visible in the satellite image (Ritter et al., 2018a; Diederich et al., 2020). Particularly, the PAG and Paranal clay pans are located at $20°S$ and $24.5°S$, which were selected sites within the framework of the CRC 1211 project to investigate the precipitation history and variability in the arid and hyperarid core of the Atacama Desert (Dunai et al., 2020).

4.2.1 The Paranal clay pan

The Paranal clay pan is placed in the lowest part of the Pampa Remiendos on which alluvial and colluvial sediments have been mapped (Domagala et al., 2016). However, at the time of the geophysical surveys, no deep-drill core information was available as a beneficial constraint to the geophysical data. In the study zone, the Quebrada Grande fault (QGF) subsystem crossed from north to south (Fig. 4.1a and c). Fig. 4.2d, e, and f exhibits the huge extension of the clay pan location. Concerning the QGF, different studies reveal the existence of mylonites with a sense of sinistral movement, suggesting an age of deformation between 156 - 159 Ma (Scheuber and Andriessen, 1990; Brown et al., 1993). However, studies of minor NNE faults reveal that the QGF subsystem does not have deformation in plutons of the Lower Cretaceous of the Patches Plutonic Complex, so the age of movements would be between the Upper Jurassic and Lower Cretaceous Álvarez et al. (2016). As part of the Atacama fault system, the most important fault in the surrounding area is the Paposo fault, located 18 km to the west of the Paranal clay pan. This huge and prominent geological structure exhibits, on the eastern side, a scarp up to 300 m in height with upward movement of the western block. It is assumed that the Paposo fault forced the deposition, since the scarp interrupts a pre-existing drainage pattern that intersects the Paranal clay pan (Scheuber and Andriessen, 1990).

4.2.2 The PAG clay pan

The PAG clay pan is located in an endorheic basin to the south of the Rio Loa canyon (Fig. 4.1a and b) within the hyperarid core (<2 mm/yr, mean annual precipitation) and nearby the coast of the Pacific Ocean. Due to its location, the site is highly affected by coastal fog (del Río et al., 2018; Walk et al., 2020). The study zone is bounded to the north by the Adamito fault system (Allmendinger and González, 2010; Ritter et al., 2018a). Other authors also call it the Cerro Aguirre fault, and in their recent studies, they proposed that the Cerro Aguirre fault represents a complex upper plate structure forming an active segment boundary of the upper plate (González et al., 2021). For convenience, throughout this thesis this feature is referred to as the Adamito fault system (AFS). The AFS forms a steep scarp, partially modified by gravitational slumping (Fig. 4.2a, b, and c). In addition, to the northeast of the clay pan, the east-west reverse fault structure cut inactive paleochannels, in which vertical offsets of about 130 m are observed (Allmendinger et al., 2005; Carrizo et al., 2008) (Fig. 4.1b). Field observations suggest that the fault cut the surface between 10 and 20 Ma ago, therefore, the AFS is post-early Miocene in age (Carrizo et al., 2008; Allmendinger and González, 2010). Lacustrine

sedimentation in the study zone may have begun at any time after ∼ 9 Ma (Ritter et al., 2018a).

PAG borehole data

An intensive drill campaign was conducted at the PAG site in 2017 within the CRC 1211 project. The recovered well data reveal key lithology summarized in two main sequences: (a) silt and clay stones with gypsum layers below 31 m depth, indicating long-term lacustrine sedimentation, and (b) colluvial sediments up to the base at 52 m depth (Fig. 4.3a). The whole-core non-contact resistance (NCR) data were used to validate and interpret the TEM results. Fig. 4.3c displays the bulk NCR data with a clear contrast at 30 m depth. Moreover, Diederich-Leicher (2020) indicates a strong dependency between the NCR data and the grain size distribution in which the high values of the NCR data exhibit a high clay content. A more detailed description of the PAG clay pan, as well as a detailed core analysis, can be found in Ritter et al. (2019), Diederich-Leicher (2020), and Dunai et al. (2020).

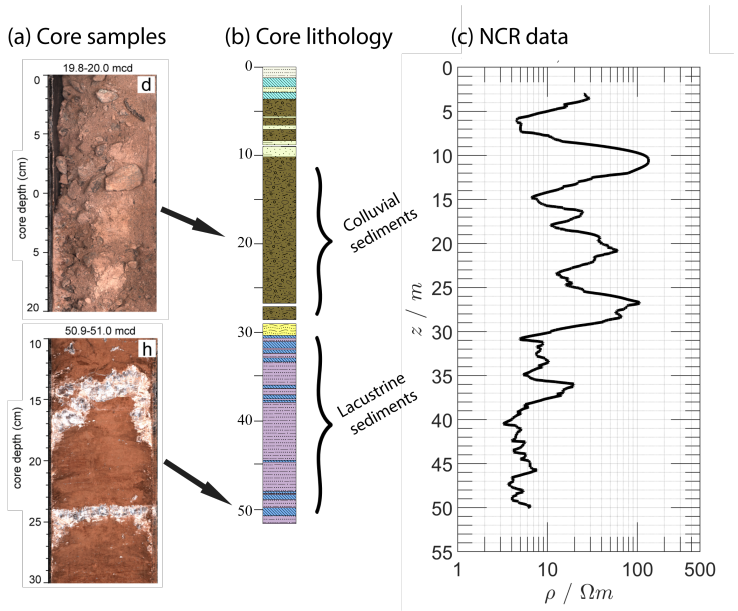

Figure 4.3: (a) Two Line-scan images showing characteristic core sections between 19.8-20.0 m depth referring to the colluvial sediments and between 50.9-51.0 m depth associated to the lacustrine sediments. (b) Lithological description of the PAG core. (c) The non-contact resistivity (NCR; black line). Modified from Diederich-Leicher (2020).

4.3 Field setup

To fulfill the goals outlined in Section 4.1, data collection was carried out through two surveys in October 2018 and December 2019. An extensive first survey was performed using the TEM method and active seismics in both PAG and Paranal clay pans. Then, in the second survey, a more dense spatially dense TEM data set was carried out on a 3D grid for the Paranal site. In addition to this, a magnetic survey was performed to complement the TEM results. The benefit of this additional survey was to reduce the uncertainties of derived subsurface models, to provide suitable drilling locations for subproject A02.

TEM measurements were carried out on a 3D grid that covered the entire surface of the PAG and Paranal clay pans. A total of 48 and 133 soundings were recorded on the surface of the PAG and Paranal clay pans, respectively. Fig. 4.4 shows that the TEM sounding locations for the Tx-40 and Tx-80 are displayed as red and blue squares in each clay pan, respectively. In each clay pan, the soundings were sorted into different profiles. A brief description of the profiles is summarized in Tables 4.1 and 4.2. In addition, the coordinates of each sounding are given in the Appendix A1. In addition to TEM, additional active seismic measurements were performed on both clay pans. The locations of the seismic profiles are summarized in Table 4.3. More details on seismic data acquisition, processing and results refer to Ninnemann (2020).

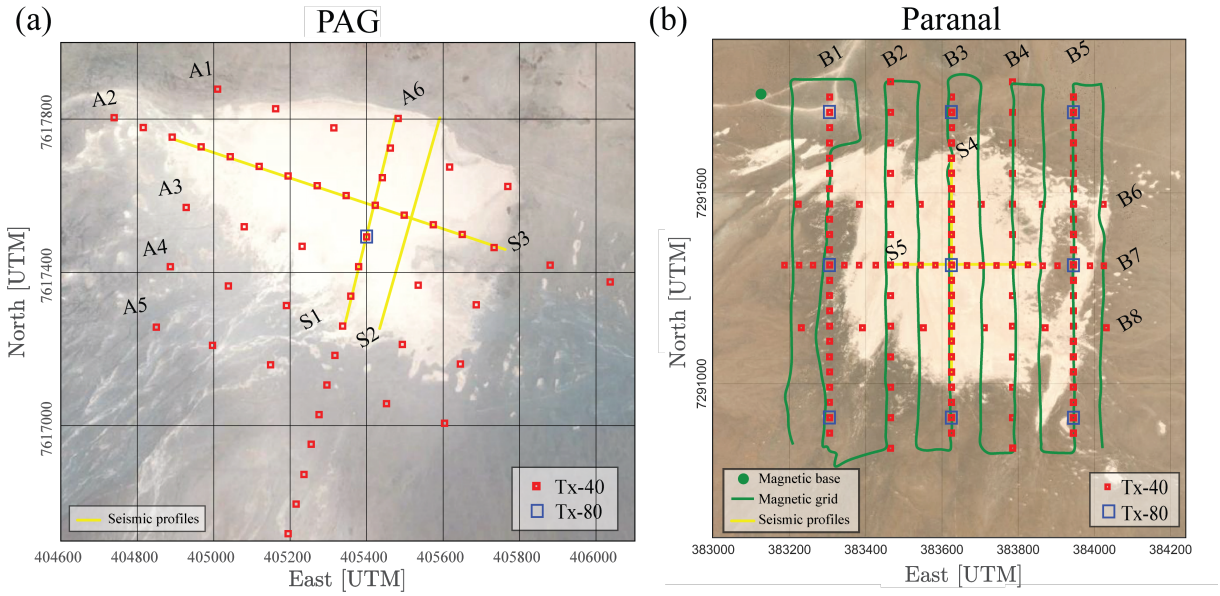

Figure 4.4: Geophysical survey layout for (a) PAG and (b) Paranal clay pans. The TEM soundings in red and blue squares correspond to Tx-40 and Tx-80 setup, respectively. Seismic profiles in yellow and, in the case for the Paranal site, the magnetic base station and measured grid in green. Details of each TEM profile can be seen in Tables 4.1 and 4.2 Maps data: ESRI satellite image (World Imagery, 2021).

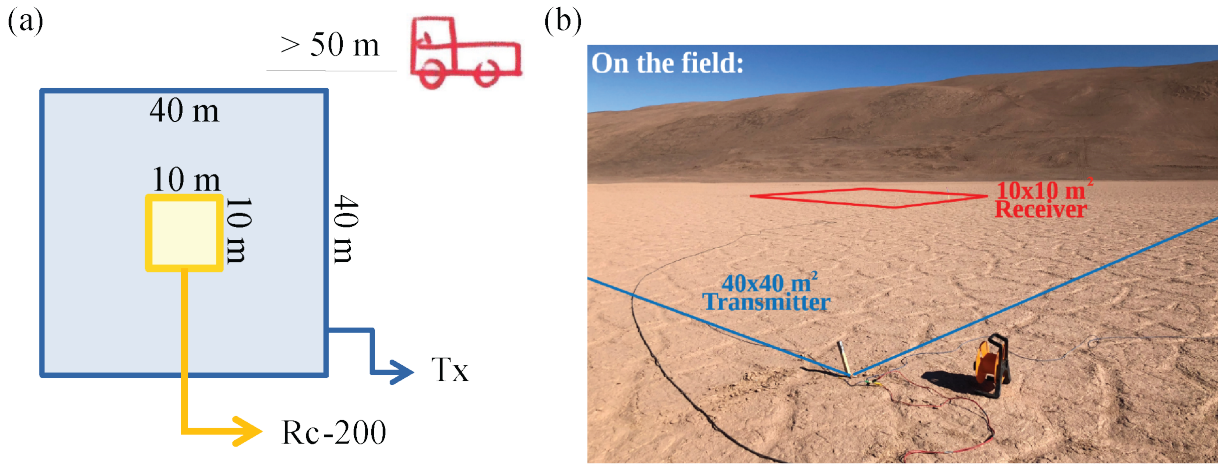

Figure 4.5: (a) Scheme layout using a Central loop configuration, with a $40 \times 40\ m^2$ transmitter and a $10 \times 10\ m^2$ receiver loop. It is suggested to keep a distance larger than 50 m between the car/truck and the measure location to avoid coupling effects. (b) Picture of the transmitter and receiver setup on the field.

TEM soundings were performed using a central loop configuration, which places an outer loop as a transmitter and an inner loop as a receiver in the center (Fig. 4.5a). The WalkTEM device was used to acquire the TEM data set for each of the clay pans.The receivers *Rc-5* and the *Rc-200* have an amplitude gain factor of 7 (ABEM, 2016). In most soundings, the Tx-40 setup was utilized, with a size of $40 \times 40\ m^2$ for the transmitter and $10 \times 10\ m^2$ for the receiver. Fig. 4.5b displays the central loop scheme in the field. In addition, the $80 \times 80\ m^2$ transmitter and a $10 \times 10\ m^2$ receiver size (Tx-80 setup) were utilized in some stations as reference points. Concerning the receivers, the *Rc-200* has a 10 m loop side with two turns to collect high-quality data at late times. Additionally, the device can use another receiver coil, so-called *Rc-5*. This antenna is a $0.5 \times 0.5\ m^2$ loop with 20 turns internally and is usually used to gather high-quality early times data.

Both transmitter loop sizes (Tx-40 and Tx-80 setup), as well as the receivers *Rc-5* and the *Rc-200* were used to evaluate TEM data quality. Their respective comparisons and descriptions are given in the following sections.

Table 4.1: Parameters of the TEM Profiles for the PAG clay pan. The asterisk (*) indicates that the profile includes soundings with Tx-80 setup. The sounding locations are displayed in Fig. 4.4a.

Profile	**Length** (m)	**Orientation**	**Soundings**
A1	800	NW-SE	6
A2	2400	NW-SE	16
A3	800	NW-SE	6
A4	800	NW-SE	6
A5	800	NW-SE	6
A6	1120	NE-SW	16*

Table 4.2: Parameters of the TEM Profiles for the Paranal clay pan. The asterisk (*) indicates that the profile includes soundings with Tx-80 setup. The sounding locations are displayed in Fig. 4.4b.

Profile	**Length** (m)	**Orientation**	**Soundings**
B1	880	N-S	26*
B2	960	N-S	13
B3	880	N-S	26*
B4	960	N-S	13
B5	880	N-S	26*
B6	840	N-S	13
B7	840	W-E	11
B8	840	W-E	28*

Table 4.3: Parameters of the seismic profiles for both clay pans. The seismic locations are displayed in Fig. 4.4.

Profile	**Clay pan**	**Length** (m)	**Orientation**	**Geophones**
S1	PAG	576	N-S	288
S2	PAG	576	N-S	288
S3	PAG	960	W-E	480
S4	Paranal	576	N-S	288
S5	Paranal	384	W-E	192

4.4 TEM data processing

The processing of TEM field data is described in the following sections. The equipment provides two acquisition modes depending on the required depth of exploration. One mode is the Low Moment (LM) with low current (∼2 A) at a high transmitter cycle frequency (∼222 Hz), for acquiring early time data. The second mode, the High Moment (HM) with high current (∼11 A) and low cycle frequency (∼25 Hz), with longer off-times for recording late-time data and deep subsurface imaging. In addition, electromagnetic noise was measured at each station. For further details or more comprehensive descriptions, consult the user manual of the WalkTEM device (ABEM, 2016).

4.4.1 Measurement settings

The WalkTEM device allows for the use of different predefined scripts, which contain the necessary settings to collect the high/low moment and the noise measurements. The scripts vary in the number and length of these time windows. The description of the scripts used is shown in Table 4.4. In order to achieve the proposed objectives, more prolonged transients were needed.

The recorded signal is exponentially decreasing on each sounding, so it is integrated and sampled in terms of gates (see Fig. 2.4). Consequently, scripts with more gates were mostly used to detect the basement. Once the script is chosen, the time duration of the measurement depends on the number of repetitions, the so-called cycles. The total number of transients per script depends on the number of cycles per measurement. Generally, the number used for the soundings varies from 3 to 6 cycles. After the measurement is performed, the device calculates an average (so-called sweep) by stacking all the acquired transients. It should be noted that on each cycle, one noise sweep for each moment is measured, except for the scripts with 32 gates that only measure one HM noise sweep per cycle. The data soundings can be read in a *.usf* format with all sweeps of the LM and HM response.

Table 4.4: General description of the used scripts.

Script	Mode	Frequency (Hz)	Current (A)	# Sweeps per cycles	Stack Size per sweep
$10_{ms} - 32_{gates}$	HM	25	~6.48	5	500
	LM	222.5	~0.96	5	1080
	Noise	25	~0	1	500
$10_{ms} - 40_{gates}$	HM	25	~6.48	10	500
	LM	222.5	~0.96	10	1068
	Noise LM	25	0	1	500
	Noise HM	222.5	0	1	500
$30_{ms} - 40_{gates}$	HM	12.5	~6.48	13	250
	LM	222.5	~0.96	13	712
	Noise LM	12.5	0	1	250
	Noise HM	222.5	0	1	712

4.4.2 Robust stacking and High-Low joint

In the processing stage, a robust stacking scheme with a 95% threshold level was used to account for outliers. Consequently, 5% of the data were discarded. The robust stacking was calculated separately for the LM and HM response, and the individual data points are typically distributed around their mean value. Then, to obtain one long transient, the LM and HM stacked transients were stitched together on an overlapped data point. Fig. 4.6a shows the raw data for LM, HM and noise at station B3T12 to describe the processing stage. Here, the script $10_{ms} - 40_{gates}$ and a Tx-40 setup were used.

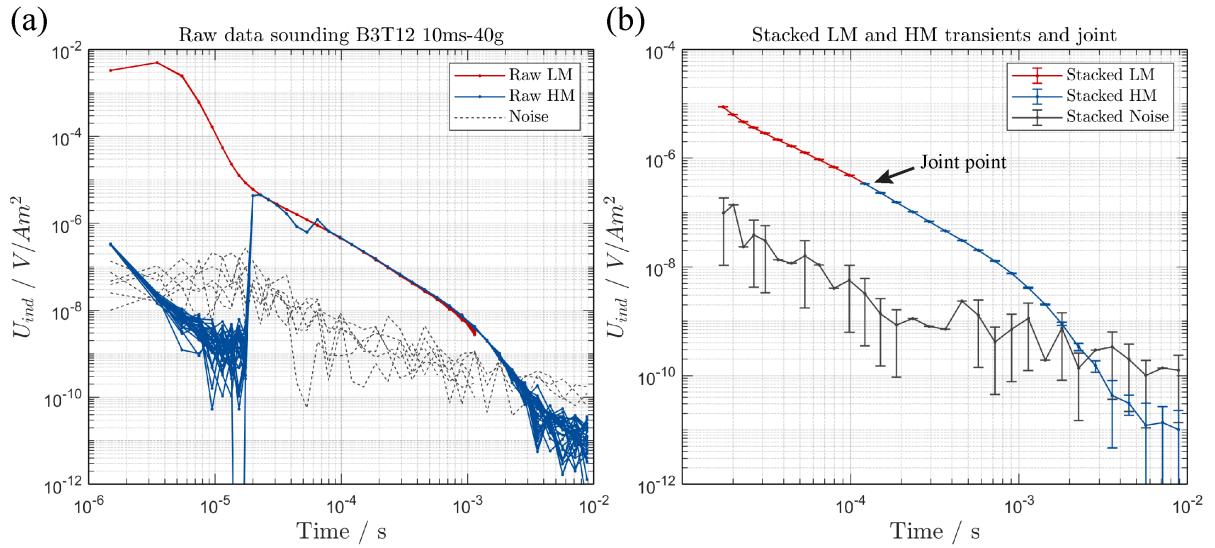

Figure 4.6: (a) LM and HM raw data responses for the sounding B3T12 using the script $10_{ms} - 40_{gates}$. (b) Stacked LM and HM transients. The change in color of the transient from red to blue indicates the junction point between the LM and HM modes. The stacked noise is displayed in gray color.

It is highlighted that all LM transients (red lines) show a similar trend with very little dispersion over the time range. However, a strong jump in the first time decade (between $t = 10^{-6} - 10^{-5}$ s) is observed and should be studied in more detail to rule out possible

instrumental noises. The HM responses (blue lines) cover almost three decades at early times with a slight distortion around $t = 6 \times 10^{-5}$ s. In addition, HM transients exhibit a large variation at late times when crossing the noise trend at $t = 2.5 \times 10^{-2}$ s. Moreover, different noise sweeps can be seen with the same trend over the time decades, on which an average of the noise floor can be observed around $\eta \sim 2 \times 10^{-10}$ V/Am^2.

4.4.3 Testing different receiver coils

In order to evaluate the TEM data in the field and access a better transient quality, the recorded signal using the receiver coils *Rc-5* and *Rc-200* were compared at early/late times. Fig. 4.7 shows the stacked data for station B3T12 using the (a) *Rc-5* and (b) *Rc-200* receiver antennas, respectively.

The comparison shows that both the LM and the HM responses exhibit larger error bars for the *Rc-5* antenna, especially at late times. Similarly, a higher trend of noise level is measured with it, making fewer data points usable at late times. On the contrary, the stacked HM and LM transients show smaller error bars for the *Rc-200* antenna. The error range is reduced to 11% at late times compared to the HM response from the *Rc-5*. In addition, more data points with small error bars can be used, as they are well above the noise level, especially at late times up to 3×10^{-3} s, which allows observing deeper structures.

It should be noted that the bump at early times is still visible using both antennas and no significant differences were observed. Based on these tests, only the *Rc-200* receiver was further used to get better quality data and more prolonged transients. From a logistical point of view, the use of one receiver coil speeds up the acquisition stage by collecting more soundings on each clay pan.

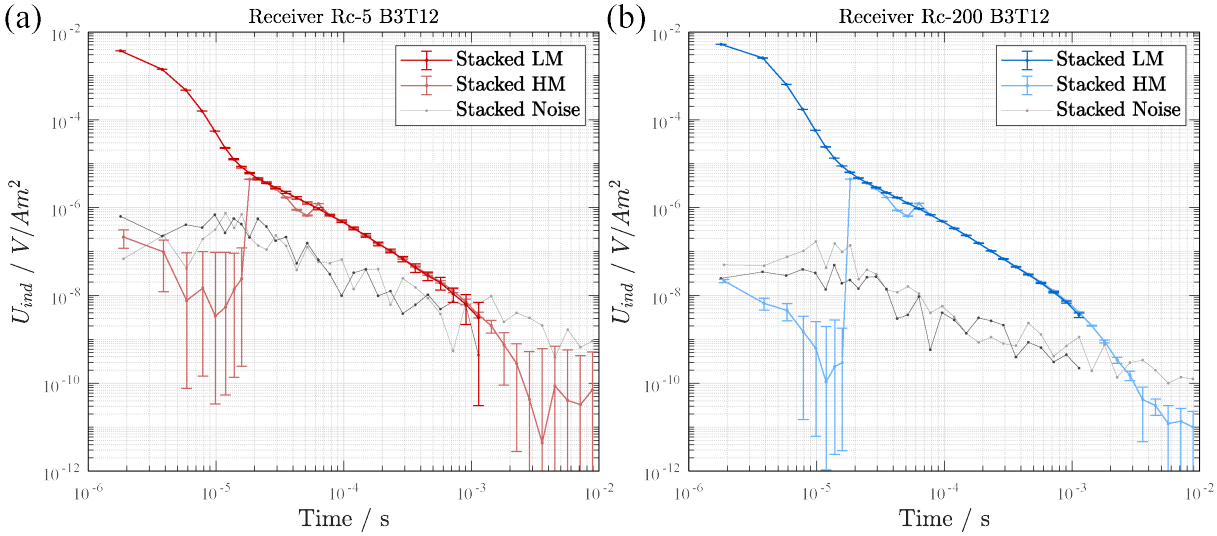

Figure 4.7: Antennas test at sounding B3T12. The TEM response using (a) *Rc-5* and (b) *Rc-200*. The noise level is displayed in gray.

4.4.4 Early time analysis

In order to prevent oscillation in the TEM measurements, parallel resistors are also used to damp the transient decay. Banana plugs are utilized to connect the resistors to the terminals of the WalkTEM device. Consequently, a 200 or 330 Ω is suggested for a Tx-40 setup and a 330 Ω parallel damping for the Tx-80. Moreover, 330 Ω is also recommended for cases where the surface is very resistive (ABEM, 2016). Different damping resistors were experimentally tested to evaluate the early time data points and to achieve a better quality in the LM responses (Fig. 4.6 a). The comparison is shown in Fig. 4.8.

It can be seen that for the damping resistor of 200 Ω, the transient exhibits a less pronounced bump at early times (red color). Now, considering the nature of our sites, the presence of a very resistive layer on the surface might be an issue, and a higher resistor value is recommended. However, the transient decay with 300 Ω exhibits a higher bump. Moreover, even choosing a higher value of 470 Ω, the same effect is visible. Furthermore, collecting a smooth decay early times transient without the strong bump was very challenging. On the basis of these tests, the choice of a higher resistor produces an overdamped turn-off current. Therefore, the turn-off ramp will take longer (cf. 2.4). This might partially explain the observed bump and the altered voltage values at the initial gates (personal communication A. Edsen, Guideline Geo AB). Nevertheless, the possibility that issues with the receiver's instrumentation contributed to this problem cannot be dismissed. This assessment recommends employing a 200 Ω damping resistor and taking into account time data points beyond $t = 1.5 \times 10^{-5}$ s for additional analysis and inversion of the TEM field data.

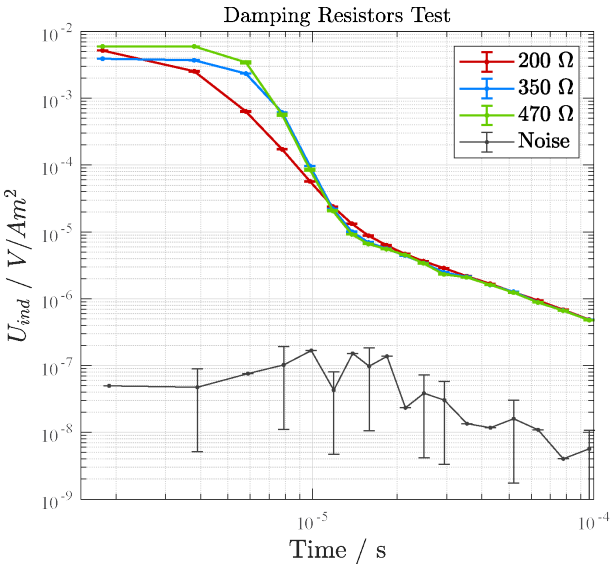

Figure 4.8: Damping resistors test at sounding B3T12. The TEM response using 200 Ω (red), 350 Ω (blue), and 470 Ω (green). The noise level is displayed in dark gray.

Ramp Time

The use of different damping resistors exhibits a change in the behaviors of transients at an early time. However, the observed bump persists in most of the TEM data (Fig. 4.8). Therefore, one task that must be considered is the analysis of the ramp time. As it was described in Section 2.4, the ramp time covers the time on which the current dissipate completely (Fig. 4.5). In order to discard the influence of current at early times, the transmission pulse is measured in the field using an oscilloscope, and the turn-off ramp time is analysed. For each moment, the measured current is compared with the turn-off ramp time values given by the device for default, including the antenna delays. For the applied field configuration, the ramp time for the Tx-40 setup is 3 μs in LM and 5.5 μs in HM.

Fig. 4.9 shows the measured turn-off current for the LM and HM oscilloscope records for stations B3T12 and B1T08, respectively. In both cases, a 200 Ω damping resistor was used. On the one hand, the LM record exhibits strong oscillations while the current dissipates, especially before the ramp time given by the device (∼3 μs). After this time, slight variations of less than 0.01 A are visible until the current reaches 0 A (Fig. 4.9a). On the other hand, the HM record generally exhibits a smooth dissipation, except for one hard oscillation around ∼1 μs, the measured current reaches 0 A around ∼ 6.6 μs in agreement with the default values of the device.

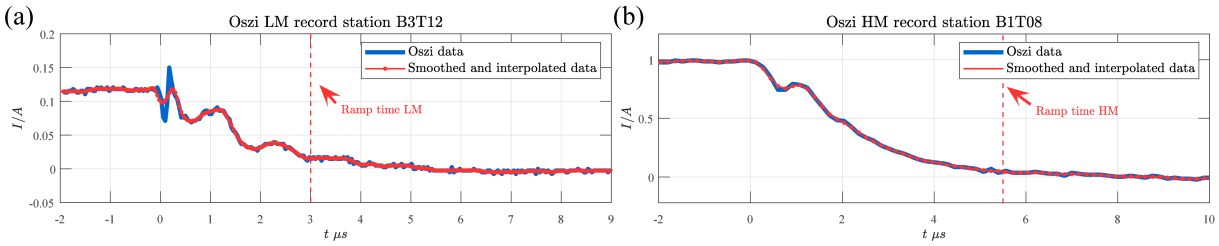

Figure 4.9: Oscilloscope record with the turn-off measured current. (a) LM for station B1T08. (b) HM for station B3T12.

Despite this, it can occur that the current does not completely dissipate during the turn-off ramp, reproducing an oscillating signal at the early times. Some authors refer to the *ringing effect*, and it is suggested that it can be reduced by using a damping resistor with lower resistance (Mårdh, 2017). Subsequently, the early times oscillations in the ramp time for the LM mode do not explain the bump in the PAG/Paranal data. However, the effect of the damping resistors cannot be ruled out. After all these analysis, it was suggested to remove the early time data up to $1.5 \times^{-5} s$ as they are most likely related to technical receiver issues working in a very high resistive environment (personal communication A.Edsen, Guideline Geo AB).

4.4.5 Late times analysis

The TEM field data were analyzed at late times, focusing on two aspects: the quality of the data using different transmitter loop sizes and the measured noise level of each site to be considered as a threshold for the data that will be used for the inversion stage. Here, it was possible to compare two transients measured in separate surveys but at the same location in the Paranal clay pan. An interesting feature to mention is that due to logistical issues, during the first survey, the truck position was <50 m away from the receiver position. This was no longer needed in the second survey in which the position of the truck was kept >100 m. Fig. 4.10 shows a comparison between the two transients: B3T12-Old (Oct. 18') and B3T12-New (Dec. 19'). In both cases, the transients exhibit a similar decay, indicating a conductive response. However, a different trend is observed between the old and new transients after the noise level at $2 \times 10^{-3} s$.

It can be seen that the noise level observed for the Paranal site is around $\eta = 3 \times 10^{-10} V/Am^2$. Therefore, the TEM data on this site can be used for further processing and inversion up to the mentioned threshold. This confirms that the truck could potentially impact the measured transients beyond the noise threshold. Since only a single survey was performed at the PAG site, this behavior is still not assessed. However, the noise level at this site is observed at approximately $\eta = 5 \times 10^{-9} V/Am^2$, which confirms the high quality of the data. Further analysis and a detailed examination of the transients for each site are discussed in subsequent subsections.

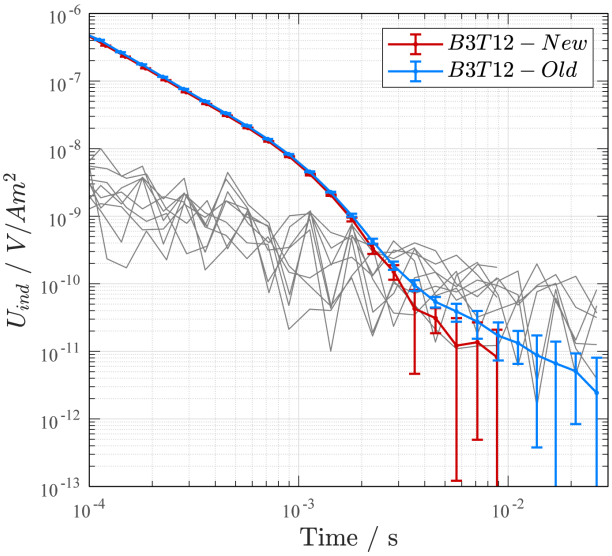

Figure 4.10: Evaluation of induction effects at sounding B3T12. The TEM response measure during the first (Old) and second (New) fieldwork. The noise level is displayed in gray.

Testing different transmitter sizes

In order to evaluate the data at late times, the transmitter loop sizes of about $40 \times 40\ m^2$ (Tx-40) and $80 \times 80\ m^2$ (Tx-80) were compared and are shown in Fig. 4.11. Both transients display a consistent induced voltage response. In addition, a strong decay at late times is observed in both transients, indicating the presence of a resistive layer at depth. However, at late times, larger error bars are observed for the Tx-80 response, suggesting that the increase in transmitter size implies a bigger area affected by a heterogeneous subsurface.

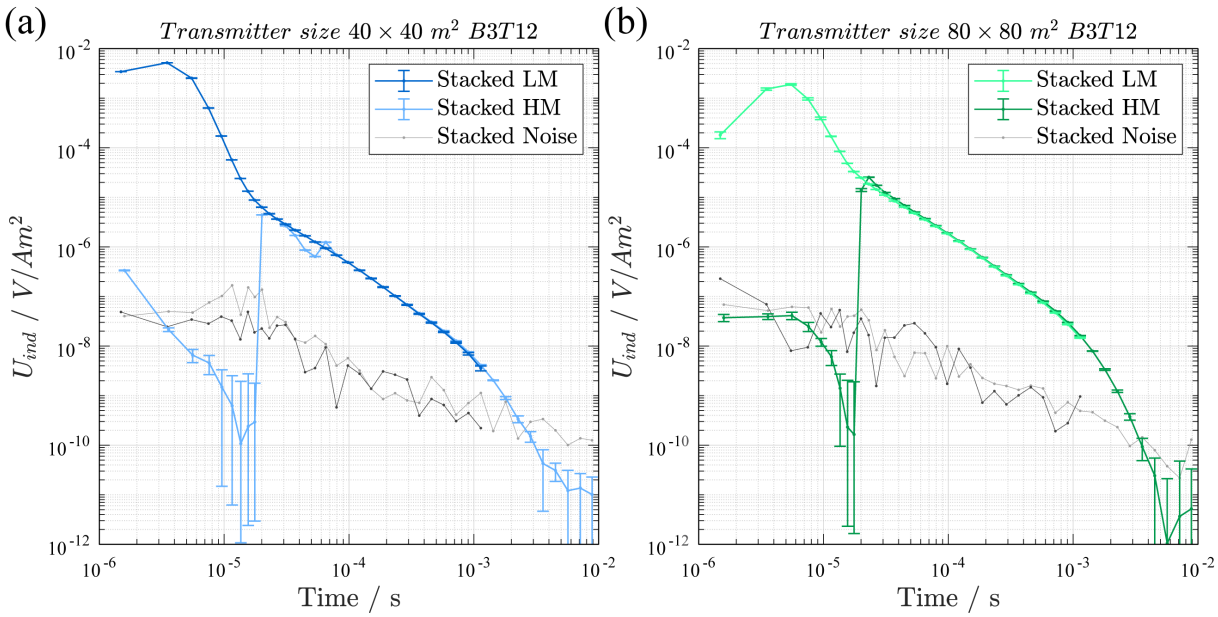

Figure 4.11: Stacked transients for the sounding B3T12 using (a) $40 \times 40\ m^2$ and (b) $80 \times 80\ m^2$ transmitter loop size. The stacked noise level of each moment is displayed in grays colors.

Based on the analyzed transients, the Tx-40 setup is sufficient to collect information on a resistive layer beneath the presence of a conductor. However, more than the analysis of the induced voltage, modeling, and inversion techniques must be applied to confirm that the basement is properly resolved. Moreover, in order to speed up the survey measurements, the Tx-40 was mainly used, and the Tx-80 setup was kept as a reference point and used to contrast the 1D inversion results. The further comparisons are described and analyzed in Chapter 5.

4.5 TEM field data

Examining TEM data involves assessing the induced voltage U_{ind}, which can be evaluated based on the signal-to-noise ratio. After selection, these high-quality data are typically utilized for forward modeling and inversion. The U_{ind} curves contain general information on the subsurface and its conductivity pattern. However, U_{ind} varies over several decades in magnitude and is difficult to visualize on a logarithmic scale. Instead, a standard transformation to apparent resistivity in late times $\rho_{a,lt}$ (see Equation 2.22) is used as a complement, which reduces the dynamic range and gives a first idea of the subsurface structure (Spies and Frischknecht, 1991). Nevertheless, this approximation does not reflect the real subsurface and has to be interpreted carefully. It should be pointed out that the data visualization is only for a qualitative view in order to get a first idea of the shallow subsurface resistivity and to derive preliminary interpretations.

The following subsections describe the field data on each clay pan in terms of U_{ind} and $\rho_{a,lt}$. First, a sounding at the center and another at the edge is selected to compare the transient decay over each clay pan. Secondly, a plan view of the entire TEM data set is displayed at three different times to analyze the behavior of the transients along each clay pan. For a detailed inspection, the U_{ind} and $\rho_{a,lt}$ for each TEM sounding are attached in Appendices A2 and A3, respectively.

4.5.1 The PAG TEM data

The PAG clay pan exhibits transients with high data quality in a time range of two to three decades. Fig. 4.12 shows the induced voltage and the late apparent resistivity of soundings A6T5 and A6T11 before neglecting late data points. A fairly low noise level is visible, which is expected due to the scarcity of anthropogenic noise sources at the study site. The noise level was stacked and shows an average of $\eta = 5 \times 10^{-9}\ V/Am^2$ at $t = 1 \times 10^{-3}$ s at all stations. The A6T5 sounding shows a slow transient decay, while the A6T11 sounding exhibits a fast decay that reaches the noise level at earlier times (Fig. 4.12a). Note that the transient length for A6T5 and A6T11 differs due to the use of different scripts (see Table 4.4). By comparing the apparent resistivity, station A6T5 shows the presence of a conductor body followed by an increase in the apparent resistivity at late times (Fig. 4.12b). This latter feature could be an indicator of a resistivity increase at depth. In contrast, station A6T11 shows the presence of a conductor at late times, following the trend of the noise level. Based on the observed induced voltage curves, the faster decay in transient A6T11 could be related to coupling effects or the influence of the truck mentioned above (Fig. 4.10). Besides, the presence of a deep conductor can not

be ruled out at this stage. Further modeling tests should be performed and interpreted in the respective geological context. Despite this, and as mentioned in the processing stage, only the TEM data until they reach the range of the noise level is considered for further modeling and inversion. Therefore, as for the A6T11 station, data points with larger error bars between $t = 6 \times 10^{-4}s$ and $t = 3 \times 10^{-3}s$ in the noise level range were excluded for further modeling and inversion process. Subsequently, the same procedure was applied to all the soundings with the same trend over the range of the noise level. Refer to Appendix A2 for observed the processed induced voltage and apparent resistivity for each PAG sounding.

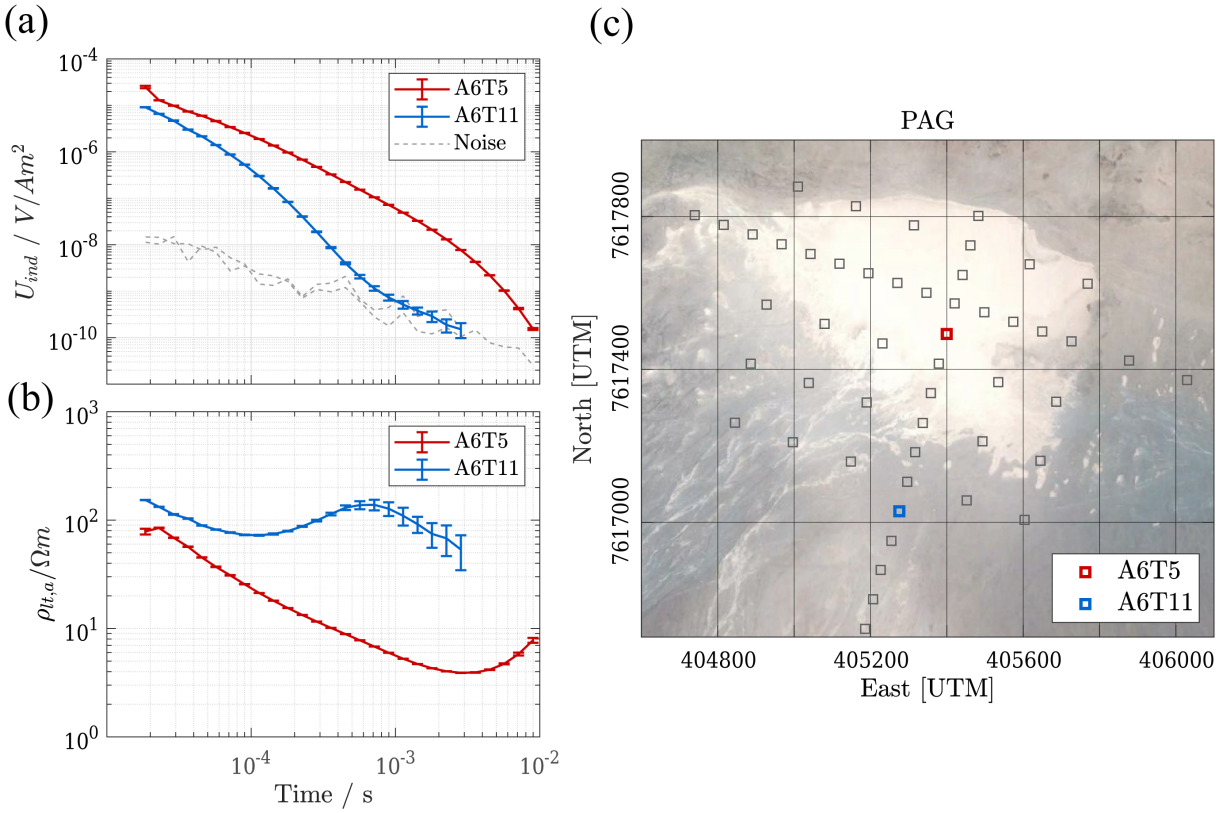

Figure 4.12: Soundings at A6T5 and A6T11. (a) The induced voltage (U_{ind}) and (b) late-time apparent resistivity ($\rho_{a,lt}$). The stacked noise level of each sounding is plotted as dashed gray line. (c) Plan view of PAG clay pan with the location of the TEM soundings. Google Earth map image.

A spatial overview of the PAG TEM data set is illustrated in Fig. 4.13 as color-coded maps of the induced voltage U_{ind} for three selected times: $t_1 = 2 \times 10^{-5}$ s, $t_2 = 2 \times 10^{-4}$ s, and $t_3 = 2 \times 10^{-3}$ s. The observed U_{ind} at t_1 display larger values in the center and some southern soundings but without a visible pattern. But this is not the case for the distribution of U_{ind} in t_2 in which the soundings exhibit higher values at the center while lower values at the edges of the clay pan. The same pattern can be observed at t_3.

The observed transients at the PAG site illustrate a good quality of TEM data (Fig. 4.12). Based on the observed U_{ind} distributions, it can be seen that the transients show a slow transient decay in the center of the clay pan, especially for intermediate late times t_2 and t_3 (Fig. 4.13 b and c). Therefore, as a preliminary outcome, based on the observed induced voltages, the TEM field data confirm the presence of a conductor body at the center of the PAG clay pan.

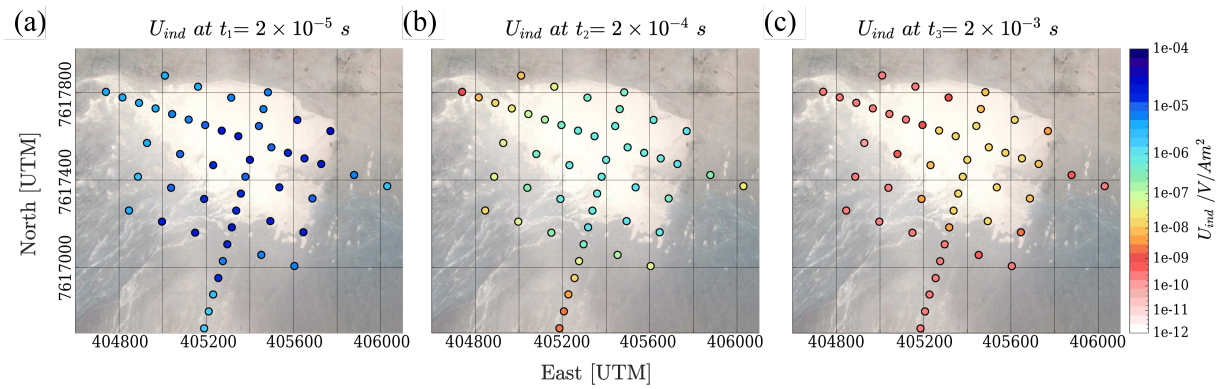

Figure 4.13: Spatial distribution of induced voltage U_{ind} for three transient times: (a) $t_1 = 2 \times 10^{-5}$ s, (b) $t_2 = 2 \times 10^{-4}$ s, and (c) $t_3 = 2 \times 10^{-3}$ s for all soundings at the PAG clay pan. Google Earth map image.

4.5.2 The Paranal TEM data

Similarly, high data quality is also observed in the transients at the Paranal site, covering a time range of two to three decades. Fig. 4.14 shows the induced voltage and the late apparent resistivity of soundings B3T12 and B3T23. The noise level in most stations shows an average of $\eta = 3 \times 10^{-10}$ V/Am^2 at $t = 2 \times 10^{-3}$ s. The soundings exhibit the same transient length, indicating the same script for the data acquisition. The B3T12 transients exhibit a slightly slower decay than B3T23 (Fig. 4.14a).

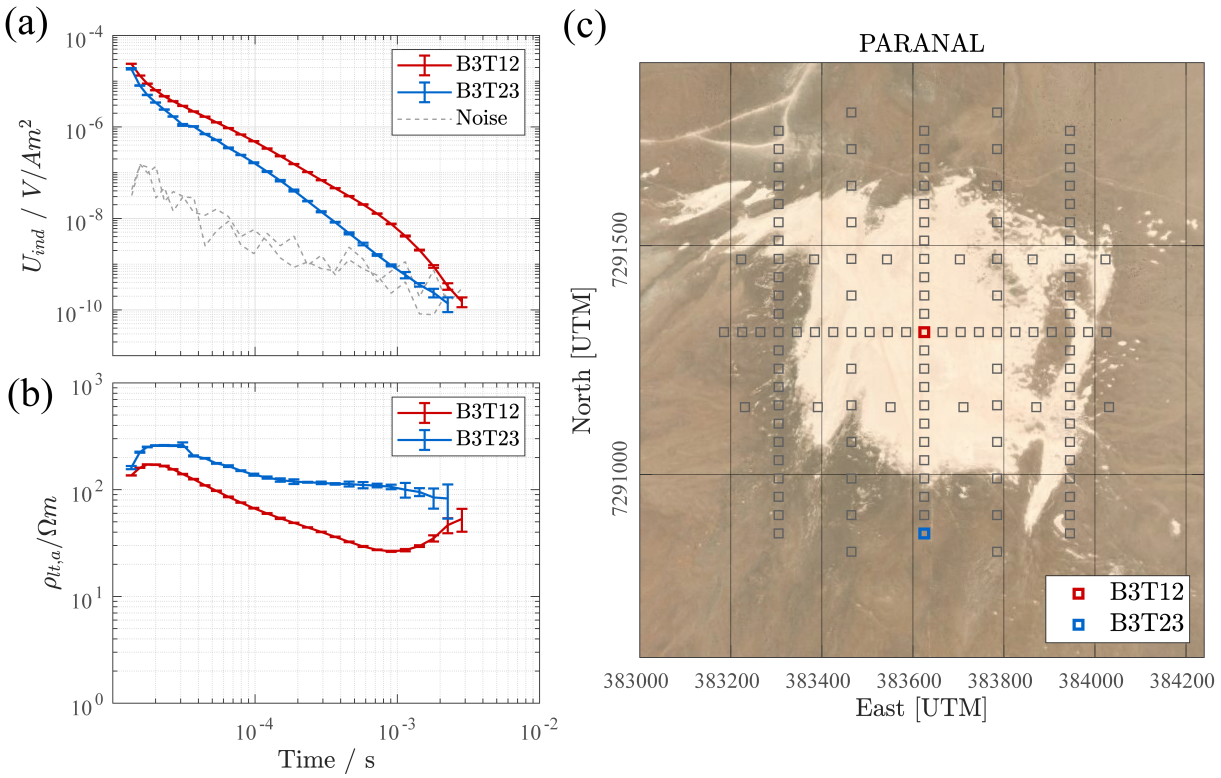

Figure 4.14: Soundings B3T12 and B3T23. (a) The induced voltage (U_{ind}) and (b) late-time apparent resistivity ($\rho_{a,lt}$). The stacked noise level of each sounding is plotted as dashed gray line. (c) Plan view of Paranal clay pan with the location of the TEM soundings. Google Earth map image.

By comparing the apparent resistivity, station B3T12 indicates the presence of a conductor of about 30 Ωm followed by an increase at later times (Fig. 4.14 b). However, station B3T23 barely indicates a change in apparent resistivity over time with values around 100-200 Ωm. The spatial distribution of U_{ind} of the Paranal TEM data set is illustrated at three selected times: $t_1 = 2 \times 10^{-5}$ s, $t_2 = 2 \times 10^{-4}$ s, and $t_3 = 2 \times 10^{-3}$ s in Fig. 4.15. At early times (t_1), higher induce voltage values are observed at the western edge of the clay pan. However, some isolated soundings also show these values. At intermediate-late times (t_2), the distribution of U_{ind} follows a west-east pattern with small values to the north and south of the clay pan, indicating that the transient decays faster at those locations. This pattern also is observed at late times (t_3). The illustrated data at the Paranal clay pan exhibit high-quality data with a visible conductor in most soundings. The observation of this exposed a clear west-east pattern from the observed plan view U_{ind} distributions at different times, on which a preliminary impression of the extension of this conductor is derived.

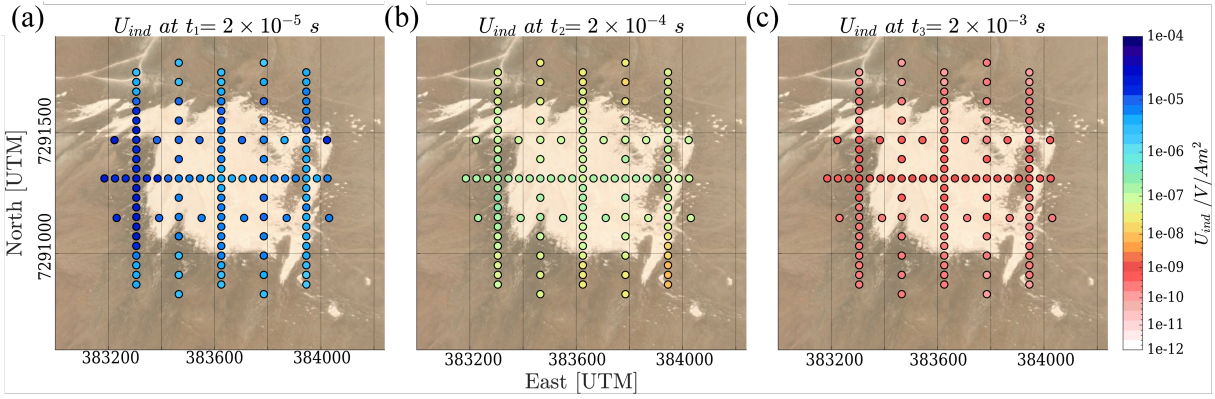

Figure 4.15: Spatial distribution of induced voltage U_{ind} for three transient times: (a) $t_1 = 2 \times 10^{-5}$ s, (b) $t_2 = 2 \times 10^{-4}$ s, and (c) $t_3 = 2 \times 10^{-3}$ s for all soundings at the Paranal clay pan. Google Earth map image.

4.6 TEM error estimates

Active electromagnetic methods, such as the TEM method, are commonly exposed to be significantly affected by different types of noise. Using a logarithmic gate technique, the signal-to-noise ratio (S/N) is often expressed as (Kirsch, 2006):

$$\frac{S}{N} = \sqrt{n}\frac{S_o}{N_o}. \tag{4.1}$$

Where $\frac{S_o}{N_o}$ is the signal-to-noise ratio of a single TEM sounding and n is the number of stacks.

One systematic approach that helps reduce the noise is to increase the number of measurements n because S/N is proportional to $\sqrt{n}$. According to Kirsch (2006), a double amount of n is needed to improve S/N by a factor of 1.41. In the presented thesis, the number of stacks per sweep is more than double and is well described in Table 4.4. However, other types of error can not be ruled out. For example, errors related to instrumental

issues, geometric deviations, geological uncertainties, and electromagnetic noise must be considered (Spies and Frischknecht, 1991).

The processed TEM data for the PAG and Paranal clay pans are represented as histograms and shown in Fig. 4.16. For each site, the distribution of the stacked observed data and their respective error data overlapped. The observed data on each clay pan are distributed depending on the occurrence of U_{ind} acquired and processed transients.

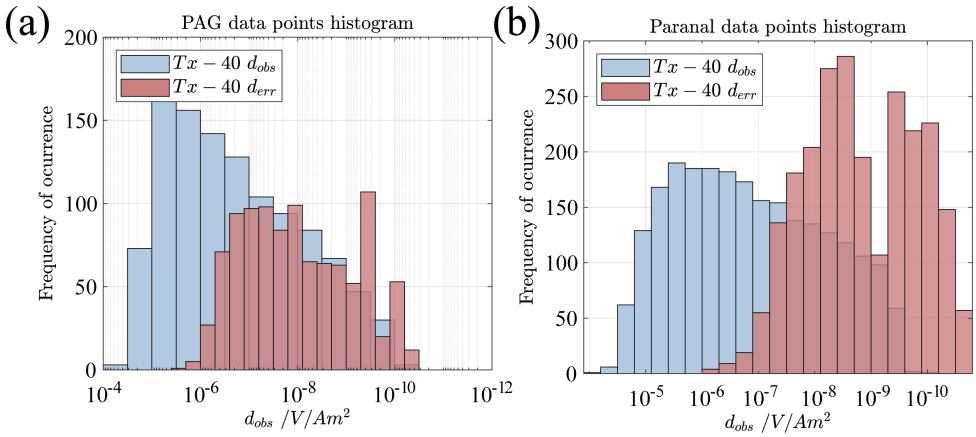

Figure 4.16: Distribution of processed TEM data and errors of the clay pans (a) PAG and (b) Paranal.

The PAG site exhibits a higher occurrence at early times than late times due to the transient decay of the acquired data, on which less late time points are usable due to the noise level threshold (Fig. 4.16a). The Paranal site illustrates less pronounced bias, indicating that most processed transients cover a similar time range (Fig. 4.16b). Similarly, these patterns on each clay pan are visible in Figs. 4.13 and 4.15. In addition, both sites illustrate a data error following a Gaussian distribution.

4.7 Summary of the field surveys and processing stage

A successful campaign was conducted in the PAG and Paranal clay pans. On each survey, active seismics and magnetics were performed simultaneously as TEM, exhibiting a well-coordinated data set and ensuring valuable data. The TEM method has the advantage of being a noninvasive EM approach, and as mentioned in this chapter, the use of Tx-40 accelerates the measures. Besides, the flat surface of the clay pans helped even more to keep a fast acquisition.

The analysis of the raw observations exhibits high-quality TEM data for both sites. A careful inspection was performed for the raw TEM data sets, on which different distortions were evaluated and analyzed. A uniform criterion was applied for the TEM data sets with a standard processing approach performed in order to maintain the quality and select as much TEM data as possible. A robust stacking and joint procedure between the LM and HM modes was performed for all soundings for the PAG and Paranal clay pans. At this stage, most of the observed distortions observed at the early times of the LM mode were neglected due to the joint procedures, which select the best quality part of each transient mode.

On the one hand, from the analysis of the early times, the TEM data was selected from $t = 1.5 \times 10^{-5} s$. It is suggested to consider further modeling studies to properly understand the early-times behavior and to exclude possible technical receiver issues. However, from the late-time analysis, the TEM data was selected until it reached the noise level range of their respective clay pan. The noise level threshold observed on each clay pan differs. After processing, the PAG and Paranal site have an average noise level of about $\eta_{noi,PAG} = 1 \cdot 10^{-9}\ V/Am^2$ and $\eta_{noi,Paranal} = 3 \cdot 10^{-10}\ V/Am^2$, respectively. These observations are crucial in derive the error-weighted relative differences analyzed and described in the following modeling and inversion sections. Furthermore, the possibility of a deep conductor in the PAG is evaluated through 2D forward modeling studies and is described and analyzed in Chapter 6.

The final stacked transients of the PAG and Paranal data sets exhibit a transient decay over two to three-time decades. Inspection of U_{ind} and $\rho_{a,lt}$ at each site provides a preliminary impression of the conductivity distribution. The evaluated soundings at the PAG site illustrate a slow decay of transients in the center of the clay pan. For the Paranal site, the transients with a slow decay are observed in a west-east orientation at the center of the clay pan. On the basis of this, both TEM data sets are promising. Further modeling and inversion schemes need to be applied to resolve the subsurface in terms of model parameters such as the electrical resistivity and thicknesses. These results are described and analyzed in detail in the following chapters 5 and 6.

CHAPTER 5

TEM 1D Inversion results

This chapter presents the 1D inversion results of the TEM data for the PAG and Paranal clay pans in terms of resistivity depth models. Two conventional one-dimensional techniques were used to invert the processed data: the damped Marquardt-Levenberg (Scholl, 2005) and a multilayered Occam smooth model, which uses a first- and second-order (R_1, R_2) smoothness constraint functional for the objective function (Constable et al., 1987). The uncertainties of the models are derived using equivalent models (Menke, 2018). Moreover, the quality of the inversion results is evaluated by the model parameter importances and forward modeling studies. It is important to note that the 1D interpretation needs to be done carefully because, in some cases, the field data are affected by multidimensional subsurface effects that cannot be explained by 1D models (Sudha et al., 2011; Yogeshwar and Tezkan, 2018). Therefore, it is suggested to perform a 2D forward modeling study to investigate different 2D/3D effects, which is described in more detail in Chapter 6.

First, two 1D models for each clay pan are analyzed, one in the center and another from the edge. The resistivity distribution, uncertainties, and fit are discussed for a comprehensive interpretation. In the same context, a comparison between the Tx-40 and Tx-80 soundings is also shown, in order to validate the quality of the TEM data. Secondly, a quasi-2D resistivity depth profile, the A6 in the PAG site and the B3 in the Paranal site are shown and discussed in terms of the available geological information. The rest of the profiles of each clay pan are compiled in the Appendices A7 and A8. Furthermore, the TEM 1D models were integrated with magnetics and active seismic surveys, in order to provide an integrated geophysical interpretation. The 1D inversion results obtained in the Paranal clay pan are partly published in Blanco-Arrué et al. (2022).

5.1 TEM 1D models

The 1D inversion of the TEM data consisted mainly of two parts. Firstly, the 1D Occam inversion is performed with a predefined number of 30 layers with logarithmically equidistant layer thicknesses. In addition, a maximum of 800 m as base layer depth was used in all stations. The thickness of the first layer ranges between 10 m at the edges and 5 m at the center of each clay pan due to the observed apparent resistivity changes. In terms of the model parameterization, these limits are suitable and sufficient. Secondly, the Marquardt inversion is performed and, as was mentioned in Chapter 3, this approach strongly depends on the starting model. In order to obtain a meaningful model, the 1D Occam results were used to define a proper one for each station. Generally, for the 1D Marquardt inversion, three layers were sufficient for most of the soundings in both clay pans. The equivalent models and the model parameter importances are also illustrated to discuss the model uncertainty.

5.1.1 The PAG clay pan

For better visualization and explanation, the A6T5 and A6T11 stations, located in the center and edge of the clay pan, are shown in Fig. 5.1. The 1D models of these sites are represented by a three-layer case in which the second layer exhibits a higher conductivity. Initially, the A6T5 1D model (5.1a) presents a first layer approximately 30 m deep with a resistivity of around 200 Ωm, succeeded by a second layer approximately 80 m thick that is highly conductive, having a resistivity of 5 Ωm. Beneath the conductive layer, a resistive base layer of around 500 Ωm is observed at about 100± 10 m depth. The equivalent models indicate high resolution for the bottom depth and resistivity of the first and second layers. However, for the resistive base layer, larger uncertainties are observed (Fig. 5.1a). Secondly, the A6T11 1D model (Fig. 5.1b) displays a first layer of $\sim$ 40 m depth with a higher resistivity of $\sim$ 600 Ωm, and is followed by a thin conductive second layer of $\sim$ 10 m thick with $\sim$ 20 Ωm. Beneath the conductive layer, a resistive base layer is observed higher than 1000 Ωm at about 60 m depth. The equivalent models of A6T11 indicate high resolution for the bottom depth of both shallow layers. However, large resistivity uncertainties, given by the equivalent models, are observed for the resistive first and base layers (Fig. 5.1b).

The model parameter importances in both 1D models exhibit values of around 0.9 for all layer depth, which means a well-resolved depths of the layer interfaces. When the resistivity distribution of both models is compared, the first and third layers exhibit a similar range of resistivities. However, the second layer at the edges of the PAG clay pan (A6T11) presents high conductivity ($\sim$ 20 Ωm) with low resolution derived from the equivalent models and the importances (Fig. 5.1b). In terms of misfit values, the 1D models are well resolved with $\chi \sim 1$ except for the 1D Marquardt model of sounding A6T11 that is not sufficiently fitted with $\chi \sim 1.3$ (Fig. 5.1a and b). The DOIs derived from the TEM 1D models suggest reliable models above 270 and 210 m depth for A6T5 and A6T11, respectively (Fig. 5.1a and b). As mentioned in Chapter 3, another approach to estimate the depth of exploration is to look closely at the divergence between the R1 and R2 models. In the A6T11 station, the R1 and R2 1D models diverge at around $\sim$ 100 m depth, indicating poor resolution at larger depths. In general, the data and the fitting

for both stations, shown in Fig. 5.1 c, indicate a good fitting in the error range of the observed data. Based on the 1D models presented for the PAG clay pan, the thickness of the conductor varies from ∼ 80 m in the center to ∼ 20 m at the edge, suggesting a first glimpse of the shape of the second conductive layer. For completeness, all 1D models of the PAG clay pan are presented in the Appendix A4.

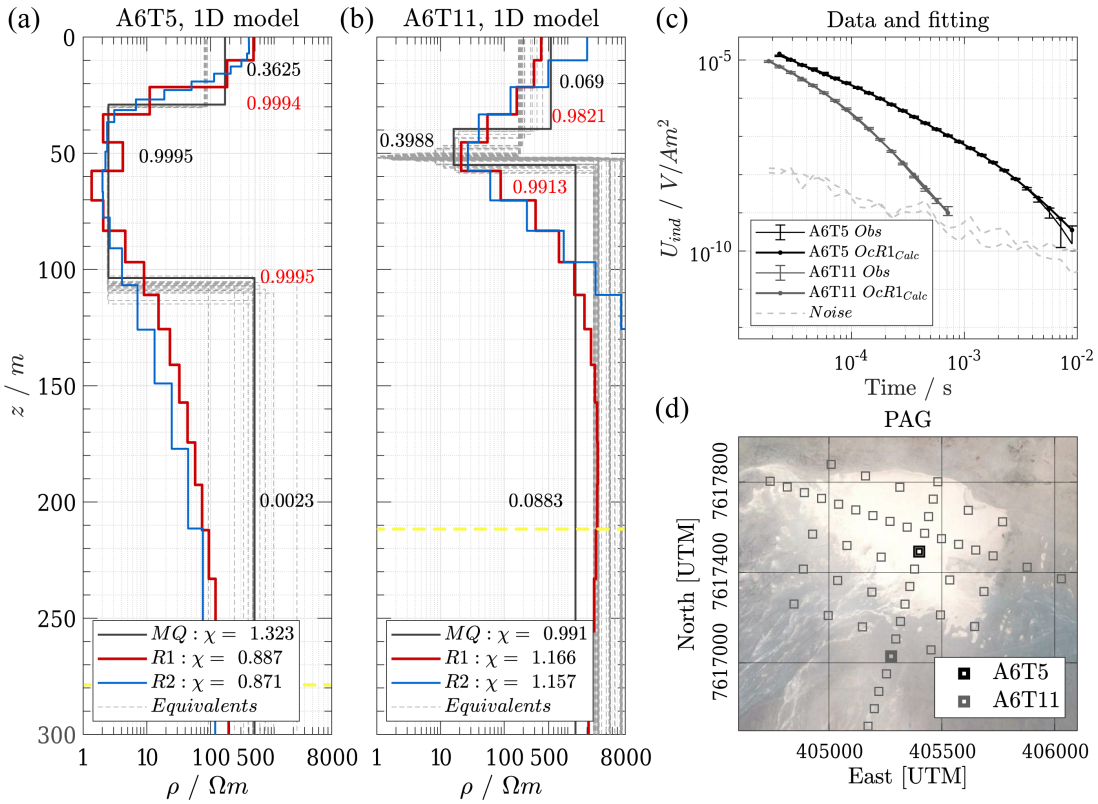

Figure 5.1: Marquardt, Occam R1/R2 and the equivalent 1D models for stations (a) A6T5 and (b) A6T11 at PAG site. The importances are displayed in red (layer depth) and black (resistivity). The DOI after Spies (1989) is marked as a yellow dashed line. The χ value is given in the legend of each model. (c) Observed and calculated TEM data for each inversion approach and both stations. The stacked noise level of each sounding is plotted as dashed grey line. (d) Map location of the stations in the clay pan.

5.1.2 The Paranal clay pan

Similarly, the TEM 1D models B3T12 and B3T23 illustrate a three-layer case for the Paranal clay pan, as shown in Fig. 5.2. In the center, station B3T12 displays a first layer of depth ∼ 50 m with a resistive layer of ∼ 200 Ωm, and is followed by a conductive layer of approximately ∼ 110 m thick with 20 Ωm. Below the conductive layer, a resistive base layer of around 500 Ωm at 160±11 m depth. The equivalent models indicate high resolution for the first and second layers, whereas high uncertainties are observed only for the resistivity of the base layer (Fig. 5.2a). A slightly different scenario is visible at the southern edge of the clay pan: a thick first layer of ∼ 80 m is derived with a resistive layer of ∼ 200 Ω m and is followed by a thin conductive layer of ∼ 10 m thick and ∼ 30 Ωm. Below the conductive layer, a resistive base layer of about 100 Ωm is observed at 90 m depth 5.2 b).

The high importances in both 1D models ($\sim$ 1) show that the layer depths are well resolved. However, low importances values arise for the resistivity of the base layer, particularly for the second layer of the B3T23 1D model (Fig. 5.2b). This observation is also confirmed by the large dispersion of equivalent models. In terms of misfit values, the B3T23 1D model is well resolved and exhibits good data misfits of χ <0.9 for the Marquardt, Occam R1 and R2 approaches, while B3T12 is not sufficiently good with $\chi \approx 1.3, 2.1$, and 1.7 (Fig. 5.2a). The DOIs obtained at both stations suggest reliable 1D models above 275 and 420 m depth, respectively (Fig. 5.2a and b). Here, the 1D B3T12 model also presents a divergence in the R1 and R2 models at a depth of roughly 170 m, implying low resolution below that depth. This information allows a proper interpretation of the complete three-layer subsurface structure observed by the 1D models. The data and the fitting in Fig. 5.2c show long high-quality transients with strong decay at late times, for which a good fitting of the data, within the error ranges of the observations, is obtained for both stations. The thickness of the conductive layer on these 1D models varies from $\sim$110 m in the center to $\sim$ 20 m at the edge (Fig. 5.2a and b). For completeness, all 1D models of the Paranal clay pan are presented in the Appendix A5.

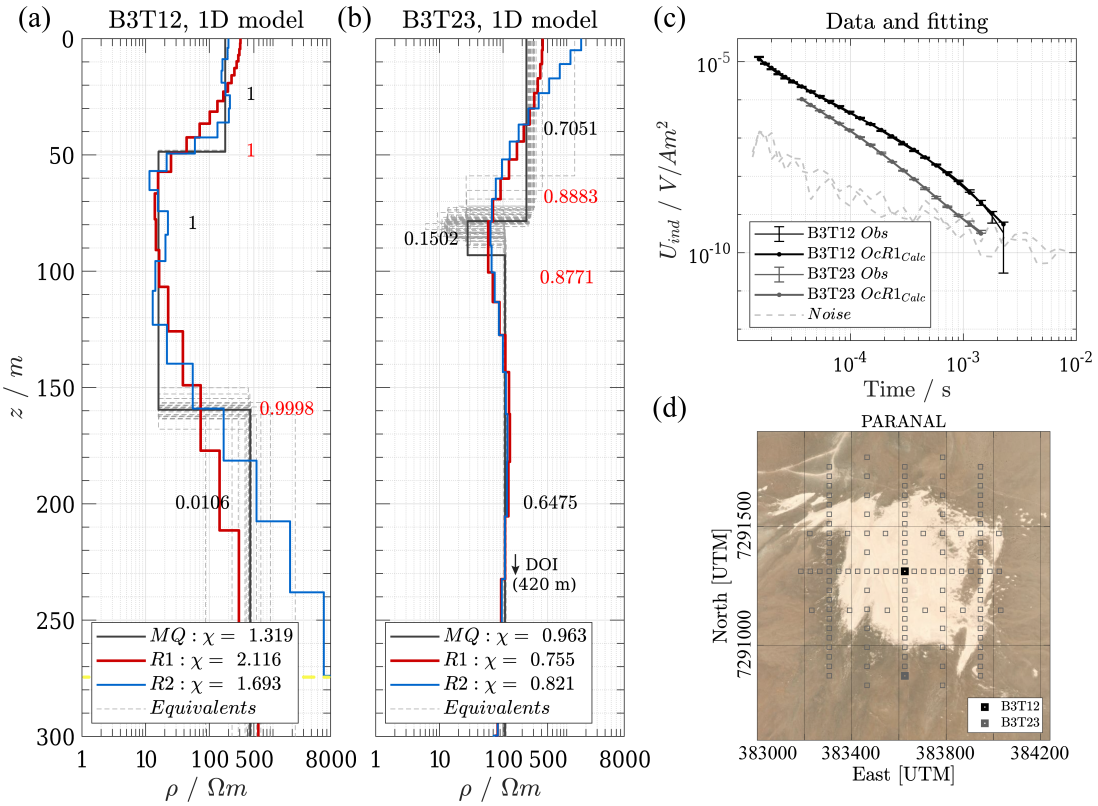

Figure 5.2: Marquardt, Occam R1/R2 and the equivalent 1D models for stations (a) B3T12 and (b) B3T23 at Paranal site. The importances are displayed in red (layer depth) and black (resistivity). The DOI after Spies (1989) is marked as a yellow dashed line. The χ value is given in the legend of each model. (c) Observed and calculated TEM data for each inversion approach and both stations. The stacked noise level of each sounding is plotted as dashed grey line. (d) Map location of the stations in the clay pan.

5.1.3 1D forward modeling study

In general, based on the TEM 1D models obtained for each clay pan, large resistivity uncertainties are derived from the base layer. A good approach to analyze transients

and to confirm the presence of the resistive basement layer is to perform a standard 1D modeling study. A representative sounding of each clay pan was chosen for qualitative data visualization and initial assessment of resistivity changes. The study examined the synthetic output of three distinct 1D models: (1) the 1D synthetic output based on the Marquardt 1D inversion; (2) the 1D synthetic output of the identical model, excluding a resistive base layer; and (3) the 1D synthetic output of the same model, however, incorporating a base layer with enhanced resistivity approximately 1×10^6 Ωm.

In Fig. 5.3a and d, the induced voltage obtained in A2T10 (PAG) and B3T12 (Paranal) is shown. The transients are then transformed to apparent resistivities (see equation 2.22) and shown in Fig. 5.3b and e, followed by the relative differences between each synthetic 1D response and the observed data (Fig. 5.3c and f). In both stations, the observed data show a strong decay at late times, which is related to high apparent resistivities (see Fig. 5.3b and c).

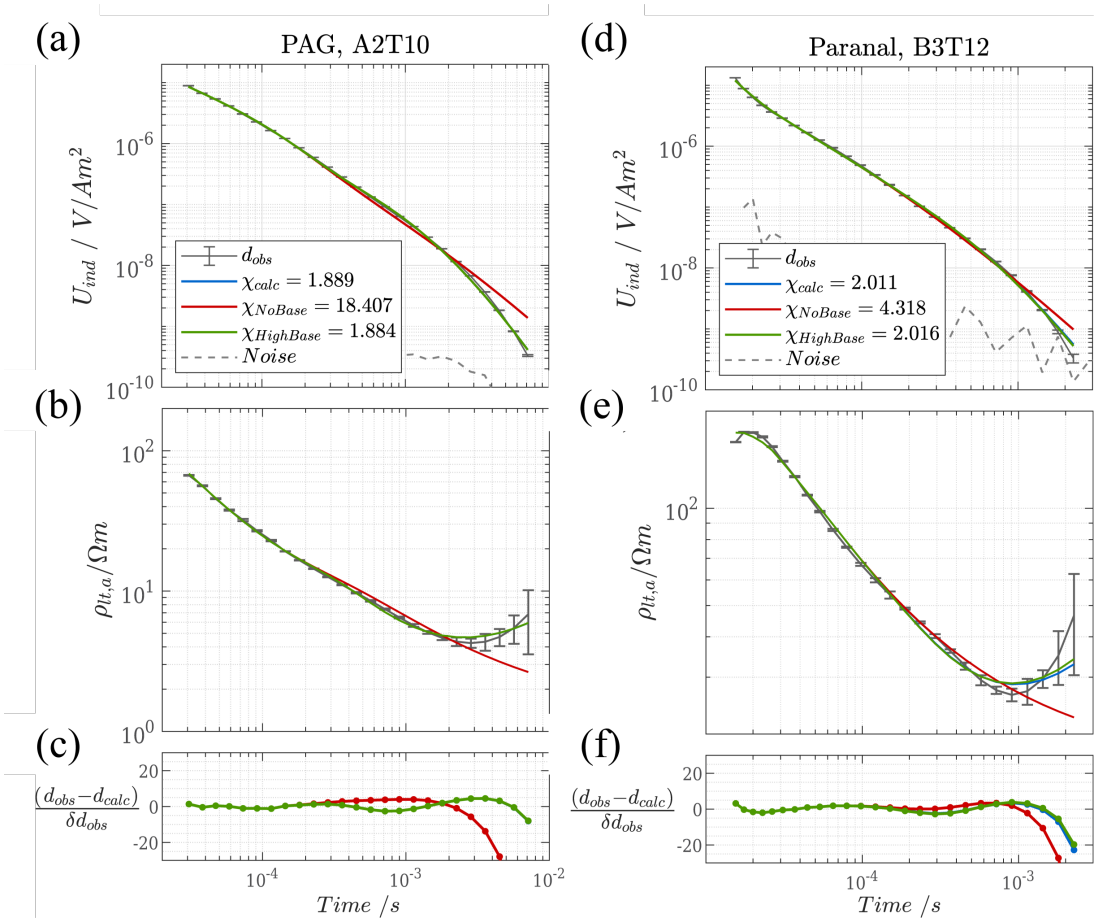

Figure 5.3: Basement evaluation by a 1D forward modeling. The induced voltage (U_{ind}) is displayed for sounding (a) A2T10 and (b) B3T12. The χ value is given in the legend of each model. (b) and (d) late-time apparent resistivity ($\rho_{a,lt}$). The stacked noise level of each sounding is plotted as dashed grey line. (c) and (f) displayed the relative difference between each 1D synthetic response and the observed data.

Based on our synthetic studies, the model without a resistive basement has high values χ and therefore has a poor fit to the observed data (transient red, PAG $\chi \approx 18$ and Paranal $\chi \approx 4$). This is also observed in the relative differences, which are larger at later times. However, assuming a resistive basement with different values (blue and green transients),

a similar fit is observed for the PAG clay pan ($\sim \chi = 1.8$) and the Paranal ($\sim \chi = 2$) clay pan. Although the fitting is within the observed error bars, this feature confirms the uncertainties about the resistivity of the base layer, which is not well resolved for the 1D models. Hence, 1D synthetic studies indicate that our data accurately determine the depth of the basement beneath the conductive layer, yet they do so with limited resolution regarding resistivity. It should be noted that the TEM technique is an active electromagnetic method that is highly responsive to conductive materials, but less so to insulating materials (Goldman et al., 2011). Moreover, lateral heterogeneities can be present in the subsurface, leading to distortion effects on the data that can often not be explained by 1D models (Newman et al., 1987). Thus, it is suggested to perform a 2D forward modeling to analyze the validity of the derived 1D models, which is explained in the next chapter.

5.1.4 Tx-40 and Tx-80 comparison

In order to validate the TEM data and confirm the presence of a resistive base layer below the conductor, the soundings Tx-40 and Tx-80 were analyzed and compared as a complementary approach. Here, the Tx-40 and Tx-80 soundings conducted at station B3T12 in the Paranal site are described throughout this section. Due to similarity, the station A6T5 in the clay pan of PAG is attached in the Appendix A6.

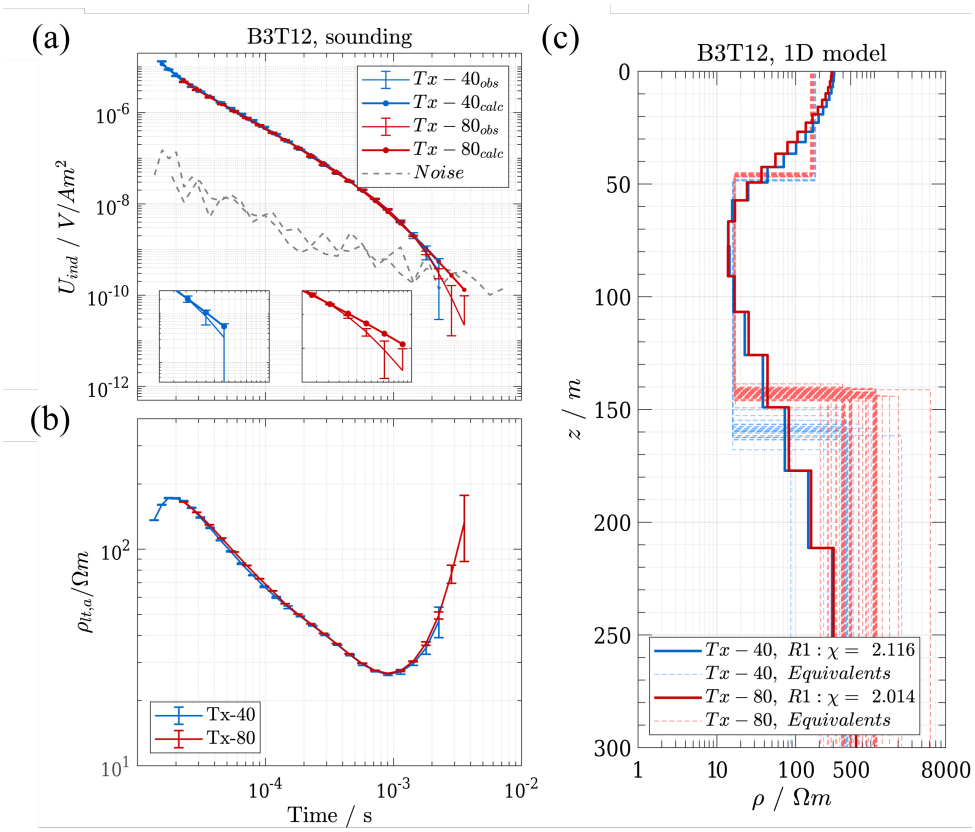

Figure 5.4: Tx-40 and Tx-80 soundings at station B3T12. (a) Observed and calculated induced voltage (U_{ind}). The stacked noise level is in dashed grey. (b) Late time apparent resistivity ($\rho_{a,lt}$). (c) Occam R1 inversion and equivalent models derived from the Marquardt approach at B3T12 using Tx-40 and Tx-80. The χ value is given in the legend of each model.

In Fig. 5.4a, the observed and calculated data for Tx-40 and Tx-80 at station B3T12 are displayed. Here, the stacked noise level is plotted as a reference, and the induced voltage decay of both transients is consistent with each other. The Tx-80 exhibits a long and good-quality transient in which a few extra data points at late times can be used for further inversion due to low error bars. After the proper transformation, the apparent resistivity is displayed in Fig. 5.4b. The late-time data for both transmitter setups clearly indicate an increase of resistivity at depth around $t = 1 \times 10^{-3}$ s. The TEM 1D models are in good agreement, the resistivity distribution of the three layers is consistent between both setups, but slight differences on the top depth of the base layer are observed. It should be pointed out that the Tx-80 set-up provides a larger DOI due to the increased transmitter moment and higher signal-to-noise ratio (Fig. 5.4c).

The equivalent models exhibit a large variation in resistivity in the base layer (>500 Ωm). As mentioned above, higher uncertainties indicate a low resolution in terms of the resistivity for the base layer. In addition, the base layer depth of the Tx-80 1D model is located at shallower depths than the Tx-40 1D model, around 145 m depth. This can be an effect due to different distortion effects. Since a larger transmitter loop size is used, a higher transmitter moment is expected, leading to more influence by 2D or 3D effects. This shall be discussed in more detail in the 2D forward modeling study in Chapter 6.

Overall, based on analysis and comparison between the Tx-40 and Tx-80 soundings and 1D models, a clear resistive base layer is detected and can be interpreted as bedrock. Further confirmation of this feature is discussed through the integration of geological information in the following subsections.

5.2 Profile A2 in the PAG clay pan

In order to observe the geometry of the conductive layer across the clay pan, the 1D models are stitched together in one profile. The profile A2 is composed of 16 soundings and is one of the main transects of the PAG site oriented west-east (see Fig. 4.4a). The 1D stitched Marquardt results are illustrated in Fig. 5.5a. Here, an extended first layer of $\sim$ 30 m thick with resistivities between 80-200 Ωm is observed, followed by a conductive layer of around $\sim$ 5 Ωm. This latter conductive layer is observed along the entire profile A2, from west to east, but with variations on its thickness. In the west side (stations T1-T6), the thickness is around 20 m and increases toward the center (stations T10-T12), where it reaches a maximum of around 80 m thick (Fig. 5.5a. Beneath the conductive layer, a resistive base layer is observed all along the profile A2 (>300 Ωm). In addition, the upper and lower depth ranges of the conductive layer, obtained by the equivalent models, show a low variation, indicating a well-resolved conductive boundary along the profile (Fig. 5.5).

The 1D inversion results derived by the Occam R1, R2, and Marquardt approaches are in good agreement, on which a clear geometry of the conductive layer is observed. In addition, the DOI is derived above $\sim$ 700 m.a.s.l., suggesting high-reliability models down to $\sim$ 250 m depth. The global data misfit for profile A2 exhibits values of $\chi = 1.7$ for Marquardt and $\chi = 1.4$ for Occam R1/R2. Observations along the profiles indicate that the conductive layer has gentle slope angles below 10°, suggesting a relatively flat clay

pan configuration. It should be noted that in the Occam R2 1D inversion result of T16, located at the eastern edge, a second conductive layer can be seen at deeper depths. The same behavior is observed in the profile A6, between stations T12 and T15 south of the clay pan (see Fig. A7.5). Further interpretation is difficult because the deeper layer is below the achieved DOI, which signifies low resolution. Nevertheless, potential distortion influences such as multidimensional subsurfaces should not be dismissed and need careful consideration.

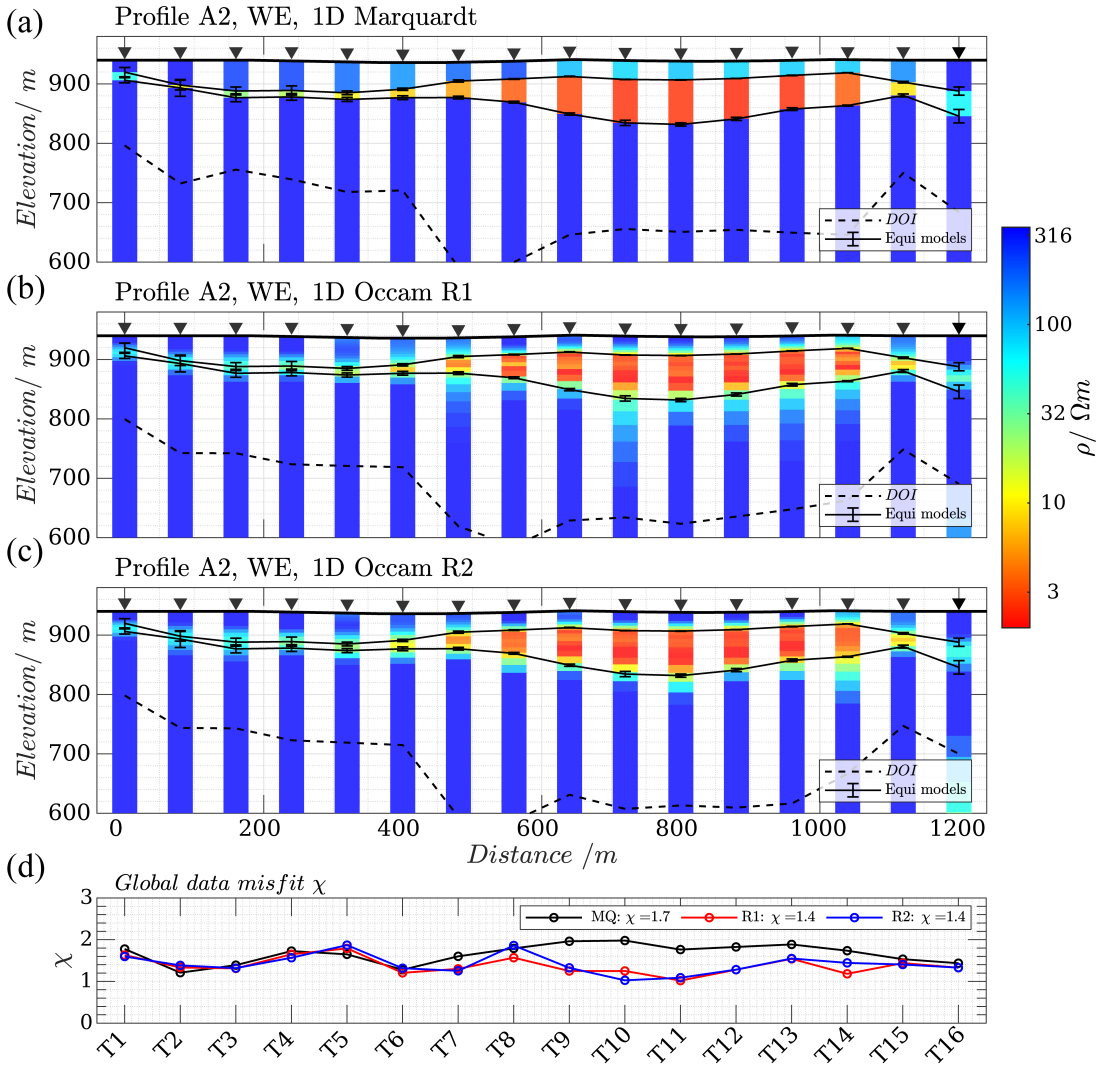

Figure 5.5: 1D stitched inversion results using (a) Marquardt, (b) Occam R1 and (c) Occam R2 models for profile A6 in the PAG clay pan. Stations are illustrated by black triangles. The DOI is plotted as a dashed line. The top and bottom depth of the second layer, including their error ranges, are displayed as error bars in black. (d) Global data misfit χ of each approach along the profile.

5.3 Profile B3 in the Paranal clay pan

For the Paranal site, profile B3 is composed of 23 soundings and is the central transect oriented north to south (see Fig. 4.4b). Figure 5.6 displays the 1D stitched results for the corresponding profile. The resistivity distribution of the clay pan can be interpreted as a three-layered structure and is confirmed in all the inversion approaches. As a general

description, a first layer with a high resistivity greater than 100 Ωm is observed with a thickness of about 50 m. The resistive layer is followed by a second layer of approximately 20 Ωm, whose thickness varied from ∼20 m at the edges to ∼110 m in the center of the clay pan. Then a more resistive base layer with ∼200 Ωm is derived. In addition, a pant-leg-shaped conductivity increase within the base layer towards both sides of the profile is observed. This can also be seen by the different stitched 1D profiles within the inversion approaches by the Marquardt, Occam R1 and R2 models (Fig. 5.6 a, b, and c). The DOI can be seen below 2000 m.a.s.l., suggesting reliable models up to ∼ 250 m depth. The global data misfit is good with $\chi \approx 1.2$ for Marquardt and Occam R2 and $\chi \approx 1.1$ for Occam R1 models. Models with high χ values are not fitted sufficiently, such as those placed at the center of the clay pan (e.g., between stations T10-T15).

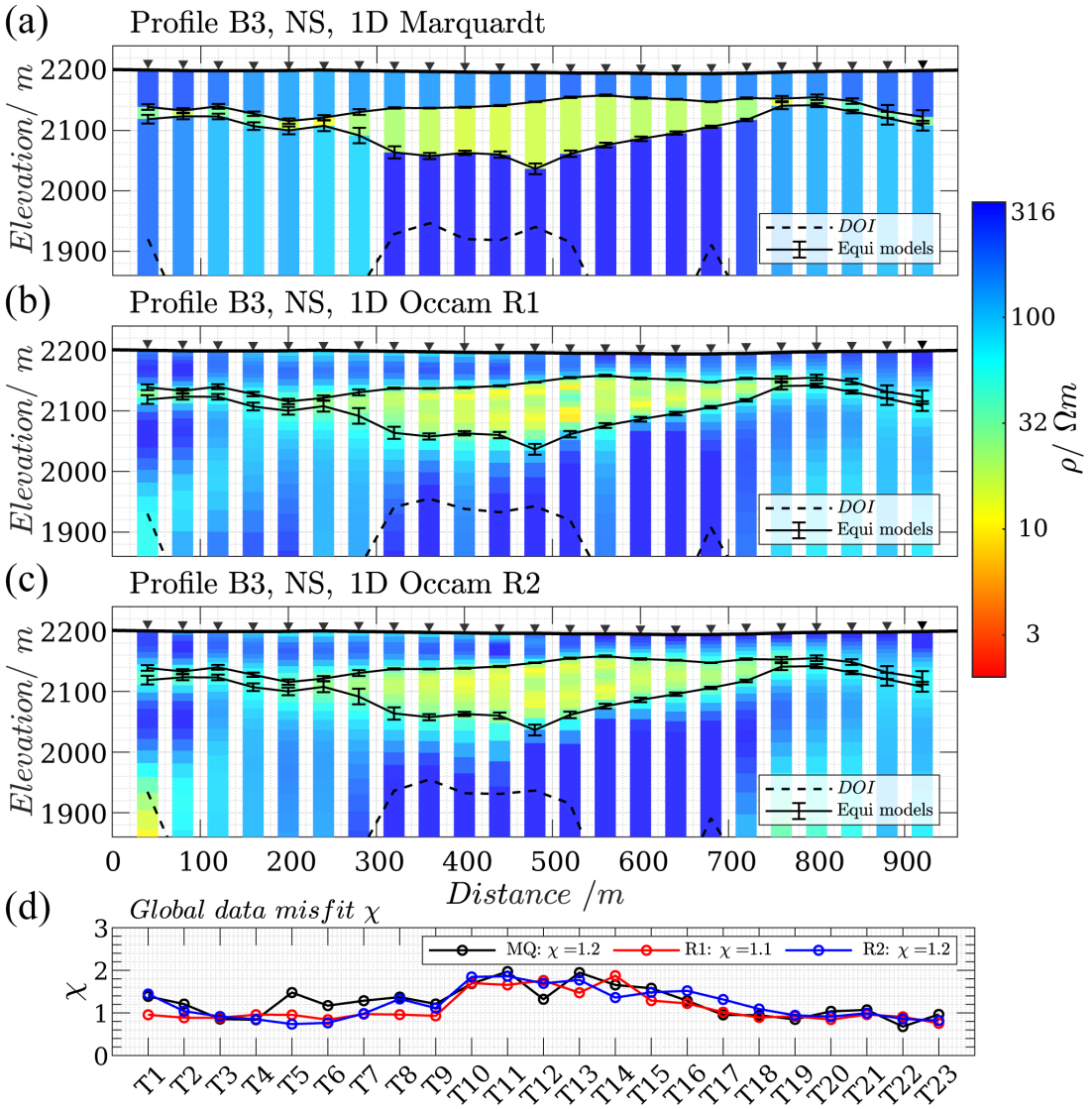

Figure 5.6: 1D stitched inversion results using (a) Marquardt, (b) Occam R1 and (c) Occam R2 models for profile B3 in the Paranal clay pan. Stations are illustrated by black triangles. The DOI is plotted as a dashed line. The top and bottom depth of the second layer, including their error ranges, are displayed as error bars in black. (d) Global data misfit χ of each approach along the profile.

To summarize, when viewed from a north-south perspective, profile B3 clearly displays a channel-like formation at its center, where the base's slope angles vary slightly, showing a range between 13° and 20° on either side. The equivalent models suggest depth uncertainties of a maximum range of 11 m in the basement depth layer. As noted previously, the slope angles and configurations of these clay pans could result in multiple multidimensional effects, which are further explored and elaborated in Chapter 6.

5.4 Validation with borehole data

The remote location of the clay pans and the scarce information about the sediment layer formations transform the validations of our 1D models into a complex task. As mentioned in Section 4.2, the NCR data obtained by the PAG drill core campaign in 2017 was the only key data set used to compare and validate TEM 1D models up to 52 m. In contrast, the Paranal clay pan lacked borehole data during the acquisition, processing, and analysis phases of the 1D model results. However, a thorough drilling campaign was carried out at the Paranal site as part of the CRC 1211 project, with drilling activities conducted in January 2022. On this occasion, Dual Induction Logging (also referred to as DIL) was used to measure the reciprocal resistivity using an Induction Log Medium (ILM) with a two-coils dual focused array. The preliminary results of the drill core campaign were used to confirm the TEM 1D results in the Paranal clay pan (personal communication Dr. V. Wennrich).

In this section, two comparative analyzes are given: (1) in the PAG clay pan, where the A6T5 1D model is compared with the NCR borehole data up to 52 m, and (2) in the Paranal clay pan, where the B3T12 1D model is contrasted with the DIL borehole data up to 120 m. In both cases, the 1D models are interpreted in terms of the geological information retrieved from these data sets and are shown in Figs. 5.7 and 5.9.

The PAG borehole data

The 1D model A6T5 derived by different inversion approaches is represented up to 52 m depth by two resistive layers. Figure 5.7 displays the NCR data, on which a clear transition is observed at a depth of 30 m.

The lithology given by Diederich-Leicher (2020) describes the first layer as colluvial sediments, followed by lacustrine sediments. Therefore, based on the 1D models, the first and second layers can be interpreted as colluvial and lacustrine sediments explained by changes in the grain size distribution of the different lithologies (sand and gravel in colluvial strata versus clay and silt in lacustrine). Moreover, this layer contrast is also observed in the NCR resistivity data as a sharp change below 30 m depth, consistent with the top boundary of the conductive layer from the 1D models. However, some large NCR resistivity fluctuations are visible above 30 m, indicating a heterogeneous composition. Hence, the TEM method exhibits high performance in detecting the contrast between both types of sediments and provides valuable constraints for further geological models.

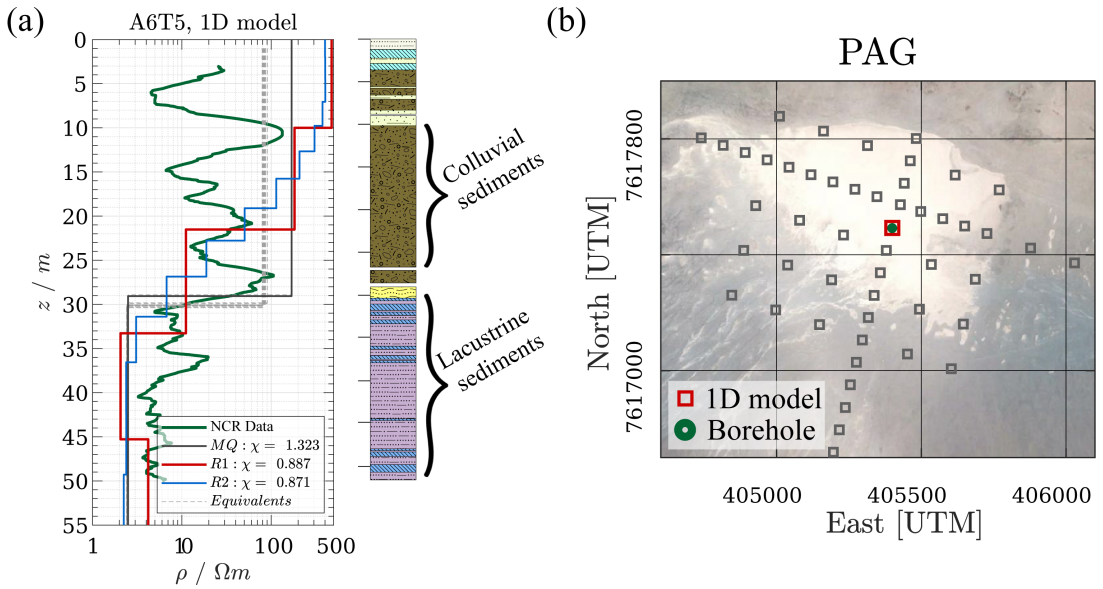

Figure 5.7: Comparison with borehole data: (a) A6T5 1D model with Marquardt, Occam R1 and R2 and equivalent models. The NCR data is illustrate in green. The lithology of the drill core is display next to the 1D model. (b) Sounding and borehole at PAG location.

The Paranal borehole data

In Fig. 5.8, the preliminary results of the recovered borehole data are shown. It reveals key lithology summarized in three main sedimentary sequences: (a) sediments with a maximum of 52 m of fine grain size, followed by (b) fluvial conglomerate with large boulders (>1 m) between 52 and 171 m depth, and (c) granodioritic bedrock weathered below (Fig. 5.8 a).

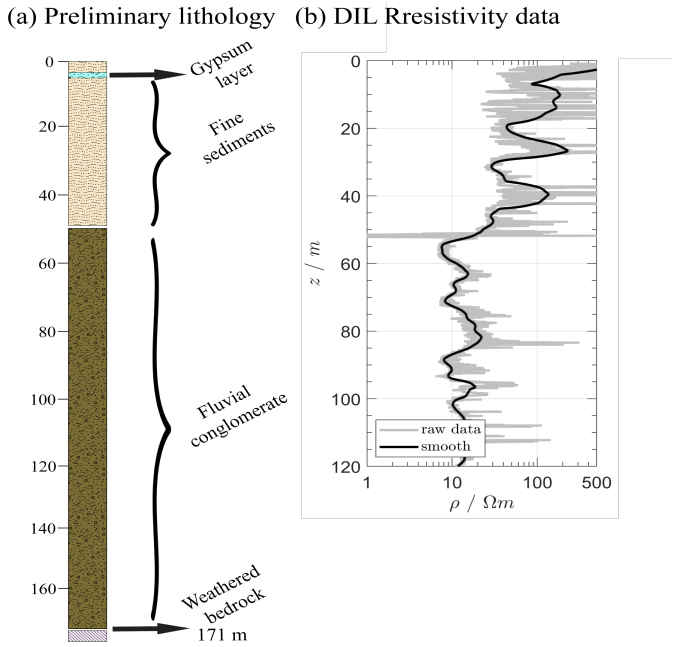

Figure 5.8: (a) Preliminary lithological description of the Paranal core in meter below the surface. (b) The resistivity logging data up to 120 m depth (personal communication with Dr. V. Wennrich).

Furthermore, DIL data were acquired using a system that operates at a frequency of 39.0625 kHz and the effective spacing between the coils was 510 and 810 mm (Comprobe Ltda.). Due to logistical constraints, the DIL resistivity data collection was limited to a depth of 120 meters. Figure 5.8b displays the raw and bulk resistivity data with a clear contrast at a depth of 50 m. Furthermore, the 1D B3T12 model, located at the same site as the core drilling campaign, was used to confirm the inversion results using the DIL borehole data and preliminary lithological data (see Fig. 5.9). The DIL data exhibit low resistivity fluctuations along the well, indicating a good resolution in all depths. High resistivity values (>20 Ωm) are observed above ∼ 50 m, while low resistivity values (<20 Ωm) are derived below this depth. There is a high correlation between the DIL resistivity data and the TEM 1D model, especially because a clear contrast at ∼ 50 m is derived from both techniques. The discussion of the preliminary lithological data up to 174 m depth is given in the next section about the integrated interpretation for the Paranal clay pan.

The successful validation of the TEM data compared to the lithology and DIL/NCR data verifies the overall reliability of the 1D models for both clay pans. Different sediment sequences are detected at the PAG and Paranal sites using the TEM method. The current section is the key input utilized in the geological interpretation discussed in the following sections.

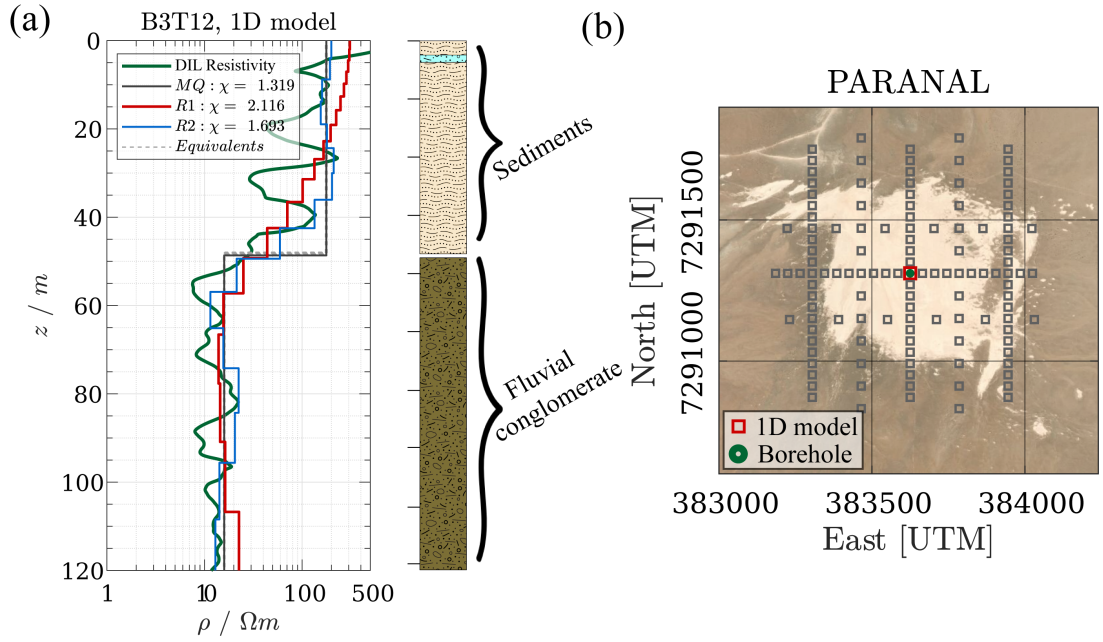

Figure 5.9: Comparison with borehole data: (a) B3T12 1D model with Marquardt, Occam R1 and R2 and equivalent models. The DIL data is illustrate in green. The preliminary lithology of the drill core is display next to the 1D model. (b) Sounding and borehole at Paranal location.

5.5 Integrated interpretation

The 1D inversion results presented in the previous sections were integrated into a conclusive interpretation of the subsurface structure of the Paranal and PAG sites. As specified in Chapter 4.3, active seismic and magnetic surveys were carried out as complementary

geophysical methods within the project. Throughout this section, the geophysical results were divided into two parts: (1) in the PAG clay pan, the integration with active seismic is given and incorporated with the geological information, and (2) in the Paranal clay pan, the results of the active seismic and magnetic surveys are interpreted and combined with the TEM 1D results, thus providing a comprehensive geoscientific interpretation.

5.5.1 The PAG site

Integration with active seismics

The seismic tomography, also called P wave velocity models, has been derived from the seismic data using first-arrival travel-time tomography. The software used by TomoPlus (GeoTomCG) employs a nonlinear refraction travel time tomography implementation which minimizes the misfits of average slowness (travel times divided by ray lengths) and apparent slowness (travel time derivatives with respect to distance), constrained with a Tikhonov regularization (Zhang and Toksöz, 1998). For more details on the processing and inversion of seismic data, refer to (Ninnemann, 2020). Here, the seismic profiles S1 and S3 in the clay pan of PAG are shown in Fig. 5.10. Profile S2 was excluded from the interpretations as no TEM soundings were measured at the location of the seismic profile (Fig. 4a).

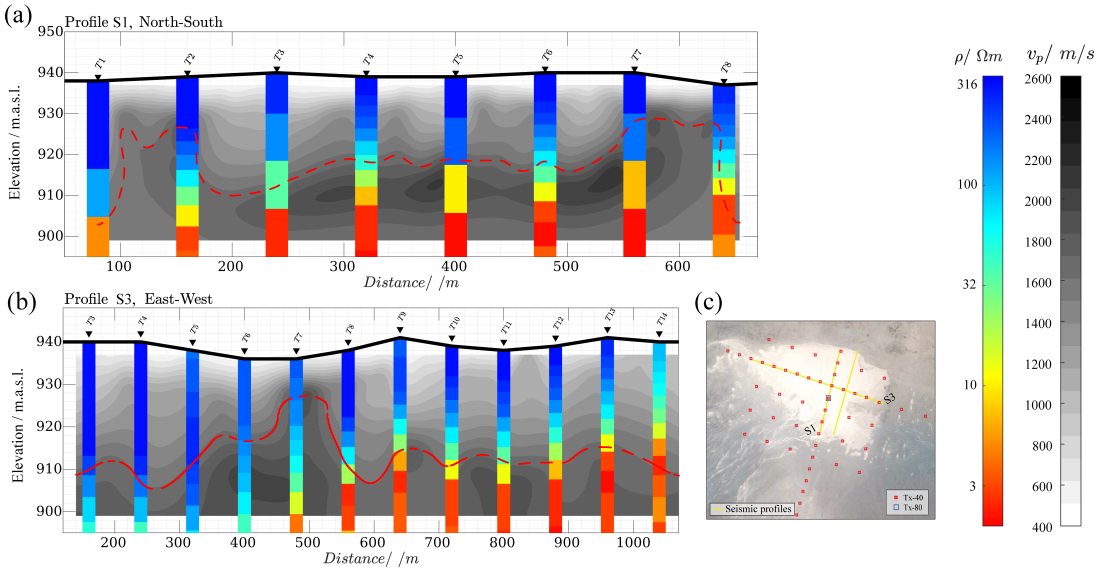

Figure 5.10: P wave velocity model for profiles S1 (a) and S3 (b). The TEM 1D models using Occam R1 for profiles PA6 (a) and PA2 (b) are overlapped. The color bars for velocity and resistivity are displayed on the left side. Seismic isoline at 1600 m/s is shown in yellow line for each profile. (c) Map location of profiles S1 and S3 at PAG site.

The seismic data quality is good enough to pick all visible first arrivals that were tracked over the entire profile length for most of the seismic source locations. With respect to seismic noise, it is preferred to conduct the measurements during the morning, avoiding strong winds, especially in the afternoon. In addition, anthropogenic noise was naturally low due to the remoteness of the site. However, some local earthquakes were detected, causing interference in the data. Therefore, high-pass filtering was used to attenuate low-frequency events. The inverted models were blended using ray coverage to show only those

parts with finite ray coverage in the subsurface. For further details on the ray-coverage patterns observed in profiles S1, S2 and S3, as well as the processing methodologies, see Ninnemann (2020).

It should be noted that all P wave velocity models were derived using the same elevation. Figure 5.10 displays the P wave velocity model for profiles S1 and S3 (see the black / white color bar). For simplicity, the seismic profiles were fixed to the average altitude of the TEM 1D models. In addition, the TEM 1D models derived at the same x-y position are overlapped for comparison. In the active seismic method, the maximum depth of investigation z_{max} can be estimated to be about a quarter of the spread length (Frei and Keller, 2000). However, this approximation is just a rough estimate. The depth of investigation for these profiles is considered between 40 and 50 m. Figure 5.13c shows the location of profiles S1 and S3 on a map as a reference.

The results from the active seismic survey can be interpreted as a two-layer structure on which some high P wave velocity values are concentrated between 30-40 m depth. The greater visible contrast is illustrated as a red dashed line at 1600 m/s, which indicates a heterogeneous stratigraphic boundary. Profile S1 exhibits large uncertainties that can be seen at the edges of the tomography results (Fig. 5.1 a) and that could be associated with low ray coverage. However, the contrast in velocity of the P wave is clearly observed in the center of the clay pan. Moreover, the same contrast is observed in profile S2, with high-velocity values reaching shallow depths (around 920 m.a.s.l.) at around 500 m profile distance (Fig. 5.1b).

Compared with the TEM 1D models, along both profiles, the velocity contrast is in good agreement with the upper boundary of the conductive layer, except for the locations mentioned above. These discrepancies between the two geophysical models may result from the measurement and investigation of distinct physical parameters. In addition, the exclusion of topography changes in the velocity model can also affect the seismic results, especially between 300 - 600 m distances in the profile S3. However, this characteristic can be neglected in profile S1 due to the minimal change in topography (less than 1 m). The resistivity and seismic P wave velocity models are consistent with each other and give a clear transition between the two sedimentary layers.

Sedimentary lithology and basin geometry

A well-constrained resistivity and seismic velocity contrast is visible at $\sim$ 30 m depth within the sediment sequences (Figs. 5.10 and 5.5). As discussed above, the general structure is well validated. The lower resistivity of lacustrine sediments can then likely be traced back to a higher clay content, porosity, and/or compaction. The porosity differences of the sediment units might also explain the seismic velocity change in the colluvial / lake transition derived from the tomography results. Furthermore, the PAG site is located within the hyperarid core (<2 mm/yr MAP) but nearby the coast of the Pacific Ocean. Hence, the clay pan is currently more affected by coastal fog (del Río et al., 2018; Walk et al., 2020), leading to a higher availability of dissolved ions (Dunai et al., 2005; Diederich-Leicher, 2020). Higher ion concentrations in the former lake periods, which are well documented in the gypsum layers in the lacustrine strata (Diederich-Leicher, 2020), could explain the lower electrical resistivity of the lacustrine sediments ($\sim$ 5 Ωm).

The PAG drill core reveals that the first resistivity contrast at ∼ 30 m depth is interpreted as a lithological change from colluvial to lacustrine sediments. Subsequently, the total sedimentary thickness at each station is calculated by adding together the depths of the first and second layers from the 1D models. This means that the sedimentary thickness obtained in this study is equivalent to the depth at the base of the second layer. Figure 5.11 displays the sedimentary thickness interpreted of all TEM soundings based on the Marquardt inversion approach. Changes in the geometry of the clay pan are clearly observed, especially the large thicknesses in the center. The derived sedimentary thickness suggests the boundaries of a former paleolake which is in good agreement with the geological and geomorphological evolution models proposed by Ritter et al. (2018b).

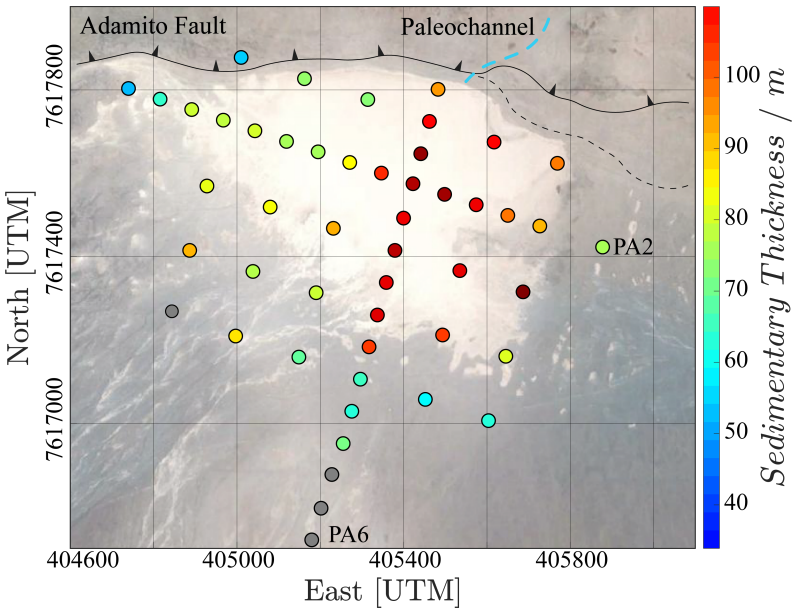

Figure 5.11: The sedimentary thickness for the PAG clay pan at each station was derived by 1D inversion results using the Marquardt technique. Grey dots correspond to the stations where no conductive sediment layer was obtained.

Figure 5.12 illustrates different 3D views on which the geometry of the sediment sequences can be observed in terms of resistivity. The extension of the lacustrine sediments can be seen in the northwest-southeast and west-east orientations (Fig. 5.12b and c). From a geophysical point of view, it is challenging to make assumptions about the role of the Adamito fault in the geometry of the PAG clay pan. However, by closely looking at the sedimentary shape, a flat smooth geometry is observed in profile A2, parallel to the Adamito fault with lower slope angles (>5°). However, profile A6, perpendicular to A2 (northeast-southwest), shows a more pronounced slope angle at the southern edge. Moreover, the maximum sedimentary thickness is located where the paleochannel intersects the clay pan. Presumably, uplift along the Adamito fault and the lack of discharge in the fluvial incision caused the current state of the PAG clay pan with a more significant infiltration of fluids, generating a flat conductive body with low slope angles, as observed (Figs. 5.12b and c).

It should be emphasized that the sediment core provides crucial insights to a depth of 52 m, after which direct lithological data are unavailable. Furthermore, results from the TEM 1D model indicate that sedimentary thickness reaches a maximum of approximately 103±10 m. Consequently, based on regional and local geological data, it is deduced that the clay pan comprises two sedimentary sequences that overlie a resistive layer, which is identified as bedrock.

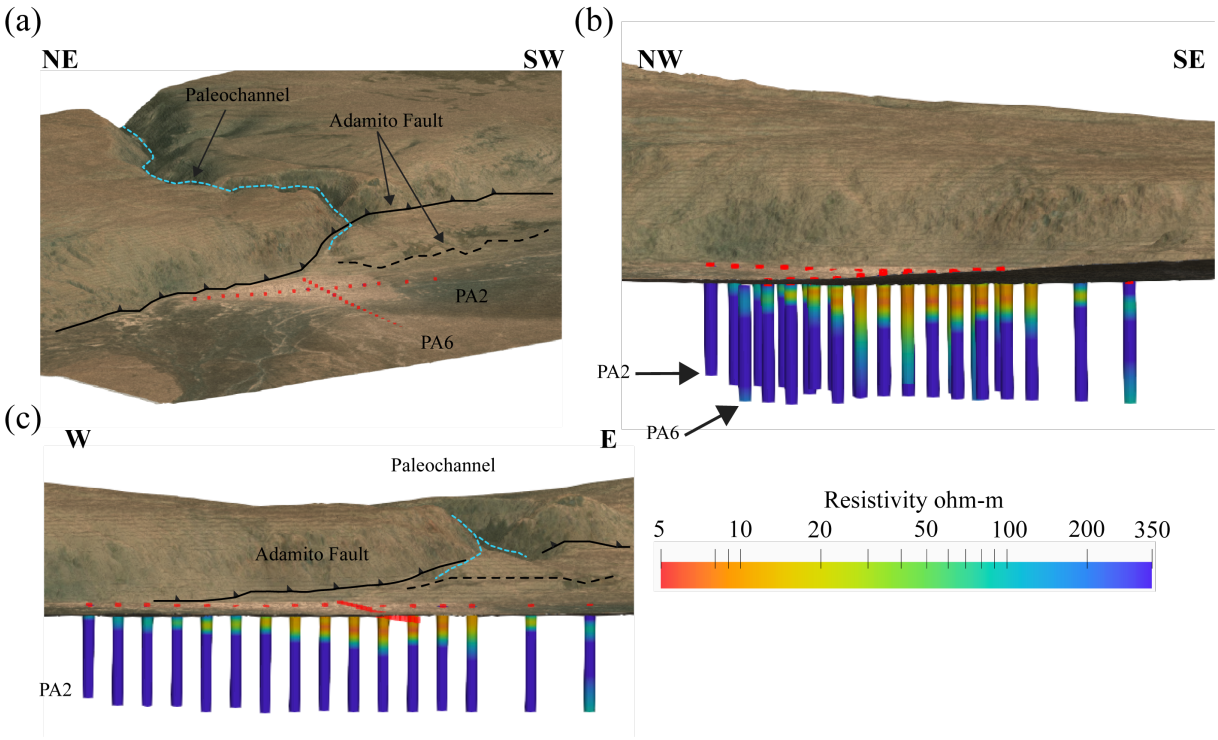

Figure 5.12: 3D view of the PAG clay pan. (a) View of the study site from the top with the TEM sounding locations. (b) NW-SE orientation. (c) W-E orientation, looking to the north. Satellite image obtained from ESRI satellite image (World Imagery, 2021). All TEM 1D models are shown up to the DOI. The elevation is shown with double vertical exaggeration. Created in Paraview (Ahrens et al., 2005).

5.5.2 The Paranal site

Integration with active seismics

For the Paranal seismic results, the same processing and inversion procedure mentioned in the PAG site was followed (Ninnemann, 2020). The seismic tomography of the S4 and S5 profiles at the Paranal site is shown in Fig. 5.13. The Marquardt 1D models derived at the corresponding places along the profile are overlapped for a better interpretation of the velocity models. Here, the maximum depth of investigation z_{max} along profiles S4 and S5 varies between 60 and 70 m. Figure 5.13c shows the location of profiles S4 and S5 on a map as a reference. A strong contrast of velocity values is observed along both profiles between 2140 and 2160 m.a.s.l. The seismic isoline at 1600 m/s is highlighted in Fig. 5.13a and b. Compared with the TEM 1D models of each profile, both physical parameters highlight this contrast in which higher velocities correlate with lower resistivities and vice versa. The first and second layers of the Paranal site derived from the TEM 1D models are interpreted as colluvial sediments and fluvial conglomerate, respectively (Fig. 5.9). The low resistivity of the fluvial conglomerate can be associated with a higher clay content in the matrix support. However, large boulders (>1 m) were also observed, which could explain the unexpected resistivity values of $\sim 20\Omega m$, suggesting a lower water content. Moreover, porosity differences between sediment units could also explain the seismic velocity change in the colluvial / fluvial transition derived from tomography results. When comparing the TEM profiles and the tomography model, a transition

between the sediment layers is observed in both models at similar depths, approximately 50 m (Fig. 5.13).

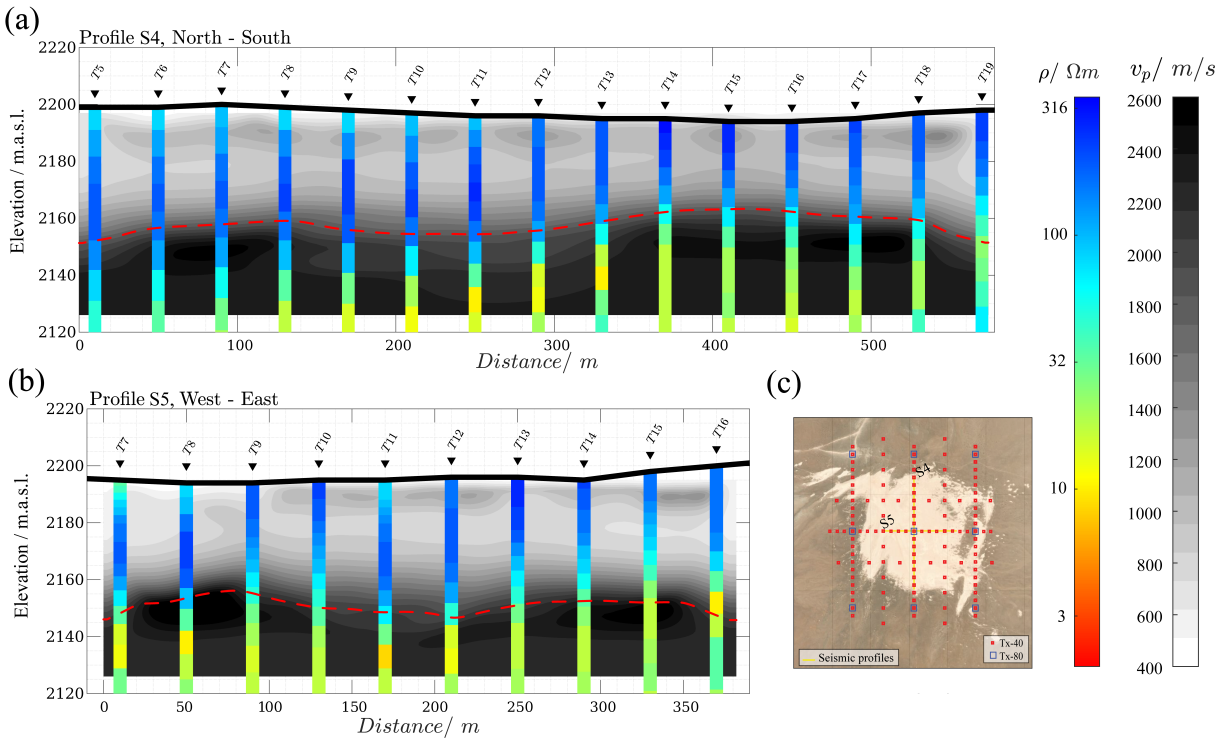

Figure 5.13: P wave velocity model for profiles S4 (a) and S5 (b). The TEM 1D models using Occam R1 for profiles PB3 (a) and PB7 (b) with the P wave velocity model overlapped in the background. The color bars for velocity and resistivity are displayed on the right-hand side. Seismic isoline at 1600 m/s is shown in red line for each profile. (c) Map location of profiles S4 and S5 at Paranal site.

Integration with magnetics

Magnetic surveys were carried out for the Paranal clay pan during the second survey in December 2019. Magnetic data processing was performed with the Oasis Montaj software (Oasis, 2021). For processing, diurnal variations and the international geomagnetic reference field (IGRF) were taken into account. The total magnetic field strength of the area is roughly 22.800 nT. A value of 23.43° and -3.82° was used for the inclination and declination, respectively. The magnetic anomaly of the total field was obtained by subtracting the IGRF from each point, according to its latitude, longitude, altitude, date, and measurement time. Subsequently, to eliminate spikes and outliers, a moving window was applied to obtain an adequate magnetic anomaly of the total field.

To better understand the magnetic data, two conventional filter techniques were used: the Reduction to The Pole (RTP) and the Analytic Signal (AS). The RTP is used to transform the magnetic anomalies resulting from the inclined magnetism of nonpolar regions into their equivalent polar response where the magnetism is vertical (Dentith and Mudge, 2014). In this way, the RTP is used to identify the correct location of magnetic anomalies in the area (Ibraheem et al., 2018). Positive anomalies indicate the position of magnetic sources, assuming that the magnetization occurs in the same direction as the magnetic field of the Earth. However, if the bodies have remanent magnetism, this process may present unsuitable results (Aina, 1986).

On the other hand, the AS filter can be applied to determine the geometry of the magnetic source (Roest et al., 1992). It is calculated as the square root of the sum of squares of the derivatives in the x, y, and z directions (Marson and Klingele, 1993):

$$|AS(x,y)| = \sqrt{\left(\frac{\partial M}{\partial x}\right)^2 + \left(\frac{\partial M}{\partial y}\right)^2 + \left(\frac{\partial M}{\partial z}\right)^2}, \tag{5.1}$$

where $|AS(x,y)|$ is the amplitude of the analytic signal in (x,y), M is the observed magnetic field at (x,y), and $\frac{\partial M}{\partial z}$ are the vertical first-order derivatives of the observed field. The AS enhances short wave length and therefore the resolution of shallow bodies while decreasing the resolution of deeper sources (Rajagopalan, 2003). In addition, the Radially Averaged Power Spectra (RAPS) was calculated to estimate the depth of magnetic sources. The following expression suggested by Spector and Grant (1970) determines the depth of the magnetic sources:

$$h = \frac{S}{4\pi}, \tag{5.2}$$

where h is the depth and S is the slope of the logarithmic energy spectrum.

Magnetics is a well-known geophysical method with a strong sensitivity in detecting magnetic targets. As mentioned in Chapter 4, there were no subsurface data or direct geological information available to constrain our TEM results, and interpretations regarding the basement could need to be revised. Based on regional geology, some assumptions can be made based on the location of the clay pan and the type of intrusives in the surroundings (see Fig. 4.1c). Therefore, taking advantage of the magnetic data set, a 2D forward modeling was performed to investigate the presence of the bedrock. For this, the GM-SYS package is available in Geosoft Oasis Montaj software (Oasis, 2021). The techniques used are well described by few authors (Talwani, 1964; Won and Bevis, 1987). The magnetic susceptibility ranges used are consistent with those of the published values (Ishihara and Ulriksen, 1980; Clark and Emerson, 1991).

Figure 5.14 summarizes the results of the magnetic survey with the (a) magnetic anomaly field, (b) RTP response, and (c) AS response derived from the magnetic data, as well as (d) the RAPS result of the magnetic data and (e) the estimated depth of the main magnetic sources. From these results, it is possible to derive the following qualitative interpretations:

- A positive magnetic anomaly is observed at the western side of the study area, whereas a negative anomaly can be seen to the southeast of the clay pan (Fig. 5.14a). The boundary between both anomalies coincides with the inferred position of a trace of QGFS (Fig. 4.1 c).
- A similar signature is derived from the RTP response (Fig. 5.14b). Due to the RTP procedure, which locates the magnetic anomalies above the causative bodies, assuming a remanent magnetization smaller than the induced magnetism, a positive anomaly towards the northwest of the clay pan is observed.

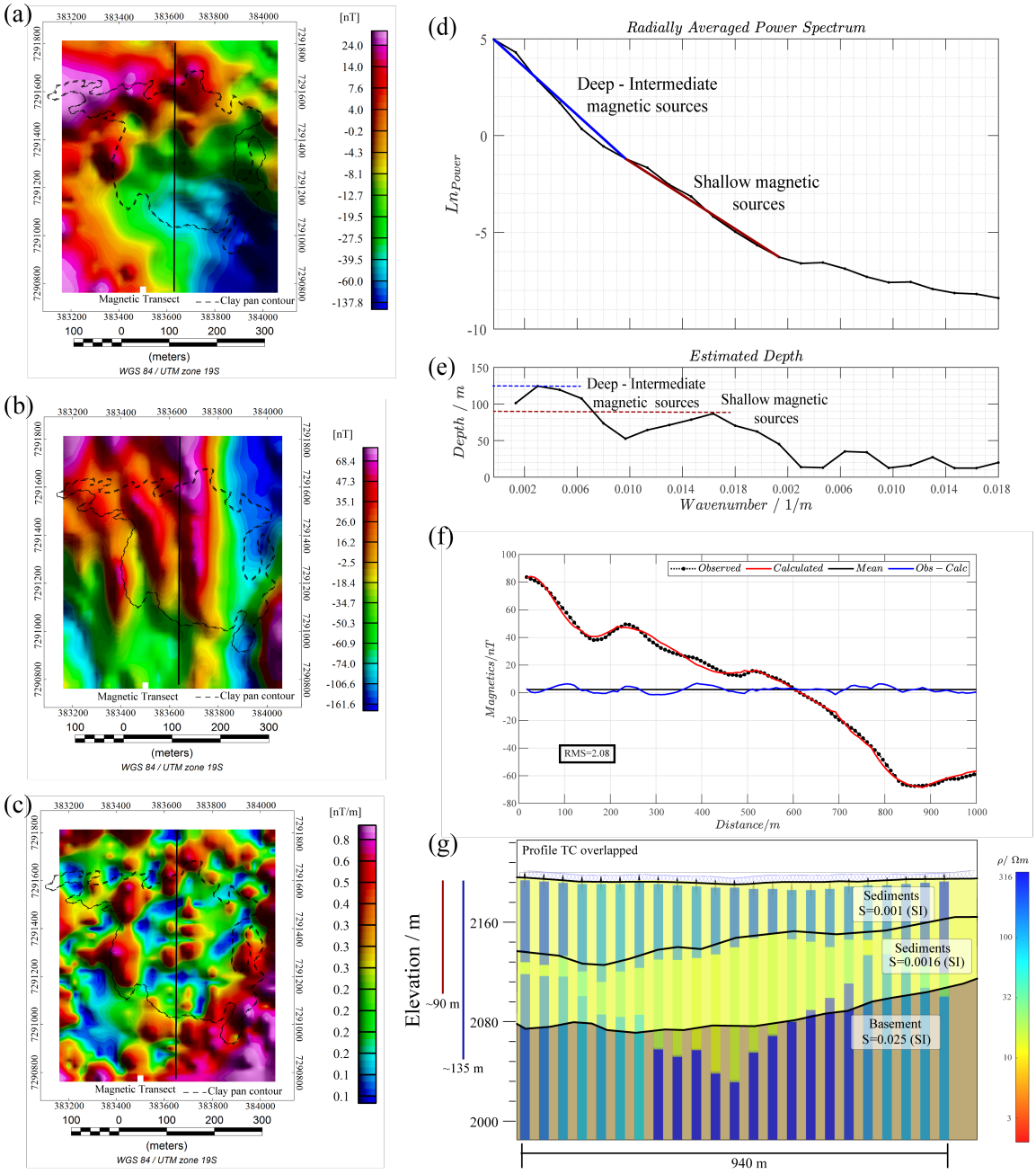

Figure 5.14: Maps of (a) the Magnetic Anomaly, (b) the RTP, and (c) AS response of the Paranal site. The black line corresponds to the transect on which the 2D forward modeling was derived. The clay pan boundary is shown as a dashed black line. (d) 2D radially averaged power spectrum curve. The trend of the deep-intermediate and shallow magnetic sources is highlighted in blue and red lines, respectively. (e) Estimated depth of the Deep-Intermediate and Shallow magnetic sources. (f) Forward modeling of the magnetic data, observed and calculated magnetic transect at the same location of profile PB3 (Fig. 4.4b). (g) 2D model of the RTP response in the magnetic transect. The TEM 1D models of the profile PB3 using the Marquardt technique are overlapped. A more detailed description can be found in Fig. 5.6b. Published in Blanco-Arrué et al. (2022).

- From the AS response, some shallow magnetic sources are visible within the clay pan. However, higher AS values match the clay pan border well (Fig. 5.14 c).
- The RAPS technique (Fig. 5.14d) yields two clear regions in which the curve follows roughly a power law. The depth estimates for deep to intermediate depths and for

shallow depths are approximately $\sim$ 135 and $\sim$ 90 m, respectively (Fig. 5.14 e). These values are in good agreement with the averaged depth of the sedimentary units derived from the TEM 1D models.

Figures 5.14f and g show the 2D forward modeling results of the RTP magnetic transect using the RTP response overlapped with the TEM 1D inversion results of the profile PB3. On the left side, the depths estimated by the RAPS techniques are shown (Fig. 5.14e). Similarly to the TEM 1D models of the profile PB3, the 2D magnetic model indicates a three-layer 2D model of the subsurface. The sediments are modeled with a very low magnetic susceptibility value ($\sim$ 0.001 SI) followed by a base layer with high magnetic susceptibility values ($\sim 0.25 \pm 0.02$ SI), typically observed for gabbros, diorites, monzogranites, and granodiorites rocks. Differences can be seen at the edges, where the 2D magnetic model does not follow the clay pan geometry derived by the TEM 1D models (Fig. 5.14g). This feature can be caused by a few circumstances: (1) Magnetics is known to be highly nonunique and the estimated magnetic susceptibility values may differ at depth and also along the profile; (2) the techniques are sensitive to different physical properties and have different resolution capabilities. The TEM method is sensitive to detect conductive layers, but it loses resolution with depth, especially when resistors are present in the subsurface. Despite the slight differences, the magnetic data can be well fitted, and the 2D magnetic model is consistent and meaningful. The RMS between the observed and calculated magnetic data is 2.08 which is acceptable (Fig. 5.14f).

Sedimentary lithology and basin geometry

As mentioned in the previous section, the resistivity models derived from TEM of the Paranal site can be interpreted as two sediment sequences of fine sediments and fluvial conglomerate (Fig. 5.9). The sediment succession of the clay pan is 160$\pm$10 m thick, above the contrast of the basement. The preliminary lithology obtained by the drill core campaign gives us valuable information to confirm our TEM 1D inversion results.

Figure 5.15 shows the B3T12 1D model in contrast to the completely borehole lithology. In addition, the velocity-depth curves derived from the tomography results of seismic profiles S4 and S5 at the intersection of both profiles (B3T12 location) are shown in Fig. 5.15. At shallow depths, the velocity-depth curves exhibit a high-velocity layer between 2 and 10 m depth, which can be interpreted as a thin gypsum layer, based on the lithology information. However, from the TEM 1D models, this cannot be seen due to the low resolution at shallow depths. The latter is observed by the divergence between the Marquardt and Occam R1 1D models (black and red 1D models), at least above 20 m depth. Furthermore, the comparison between the 1D models and the lithology shows that the base layer of the 1D models corresponds to weathered granodiorite bedrock below 171 m, thus confirming the TEM results. It should be noted that the drill location and planification were determined in part on the basis of the TEM results, which shows the successful application of this technique.

The shape of the sediment sequences is also evident from the three-dimensional spatial representation of the derived TEM 1D models. The configuration of the fluvial conductive conglomerate shows a clear west-east alignment, as shown in Fig. 5.16.

Complementary, Fig. 5.17a displays the sedimentary thickness of all TEM soundings, based on the Marquardt inversion approach. Here, changes in the geometry of the clay pan are clearly observed, particularly the thicker sediment sequence is detected. In addition, for a better visualization of the conductive sediments, the 20 Ωm and 25 Ωm resistivity isolines at 90 m depth are displayed, showing the west-east paleochannel shape. The drainage catchment can be interpreted by the sedimentary thickness, whose thickness varies between 100 and 170 m, and reaches a maximum depth in profile B7 and in the center of profile B3 (Fig. 5.17b). The Paranal clay pan is placed outside the hyperarid core of the Atacama Desert (<5 mm / year MAP, see Fig. 4.1 a) and is thus influenced by more frequent rain events and even snow episodes due to its geographical location (higher in altitude and more distant from the coast). Therefore, the sedimentation thickness observed at Paranal is likely the result of more fluvial and surface runoff due to higher precipitation rates as well as the less evolved gypsum cover in the catchment (Fernández-Martínez et al., 2019; Pfeiffer et al., 2021). Therefore, it is suggested that the initial lake formation took place in the former west-east oriented paleochannel as part of an old drainage system (Fig. 4.1c).

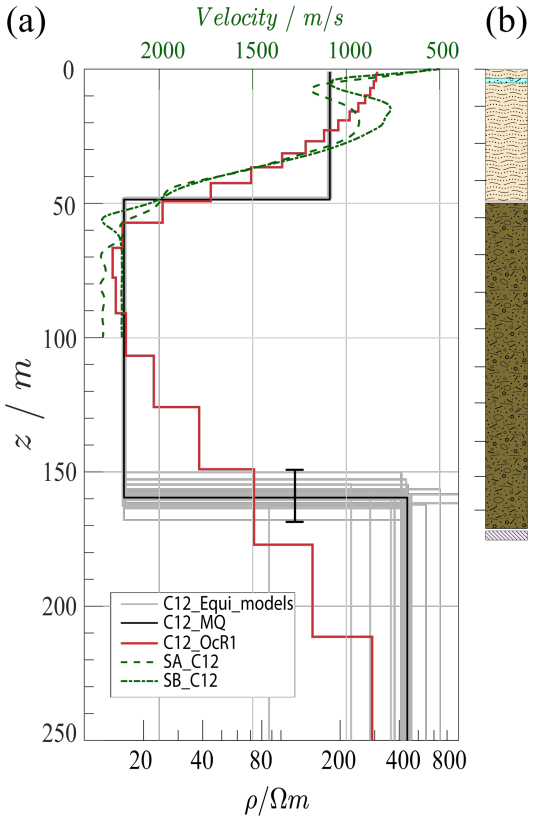

Figure 5.15: (a) Marquardt, Occam R1 and the equivalent 1D models for station B3T12 at Paranal site. The error bar shows the uncertainty of the variation of the interface depths of the equivalent models. SA_C12 and SB_C12 are the velocity-depth curves derived from the tomography results of the seismic profiles S4 and S5 at the same location of station B3T12 and (b) Preliminary lithological description of the Paranal core.

Basement and fault system

The resistivity values obtained for the third layer of the 1D models clearly indicate the presence of a resistive basement (>300 Ωm) that was confirmed by the borehole core (Fig. 5.15). The Paranal clay pan covers plutonic complexes of different ages, but they are assumed to have similar magnetic properties based on the geological composition. Our 2D magnetic modeling results indicate a third layer at approximately 135 m depth with high magnetic susceptibility that agrees with typical values for intrusive rocks as documented for the Paranal catchment (Fig. 4.1c and 5.14). The latter relates to the magnetic deposits beneath the sediments. The analysis of the magnetic anomaly and the RTP response (Fig. 5.14b) visualize the spatial distribution of magnetic anomalies beneath the sediments. A significant change from the northwest to the southeast is observed. This change from a positive to negative RTP response suggests a strong dependency on existing basement units. The large positive magnetic anomaly is associated with the Ventarrones plutonic complex and the Granodiorite Quebrada Grande to the northwest, whereas the negative

anomaly corresponds to the Diorite-granodiorite Cerro La Campana towards the east (Fig. 5.14a). The position of the magnetic anomaly change is consistent with the inferred eastern trace of the QGFS, as visible on the geological map that cuts directly through the clay pan (Fig. 4.1c and 5.17b). The general structural geology of the strike-slip Atacama fault systems is well studied, with a fault core and a damaged zone leading to possible high porosity and metamorphosis/deterioration (Mitchell and Faulkner, 2009). The basement below the Paranal clay pan can thus be partly interpreted as a damaged zone of the strike-slip QGFS. The inferred eastern trace of the QGFS separates the Diorite-granodiorite Cerro La Campana to the east and the Granodiorite Quebrada Grande to the west (see Fig. 4.1 c).

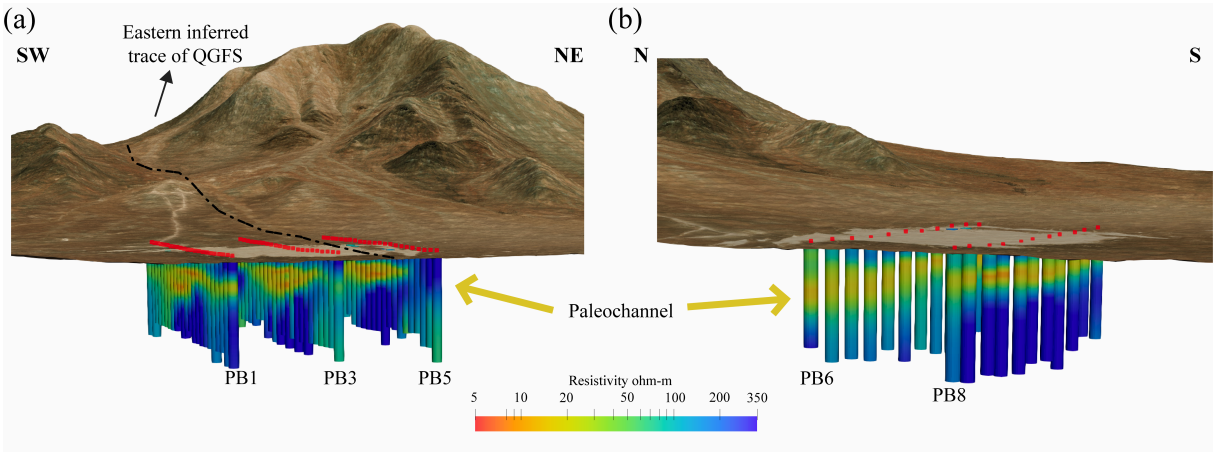

Figure 5.16: 3D view of the Paranal clay pan. (a) SW-NE orientation view with the north-south profiles B1, B3 and B5. (b) N-S orientation view with the west-east profiles B6 and B8. Satellite image obtained from ESRI satellite image (World Imagery, 2021). All TEM 1D models are shown up to 1900 m.a.s.l. The elevation is shown with double vertical exaggeration. Created in Paraview (Ahrens et al., 2005).

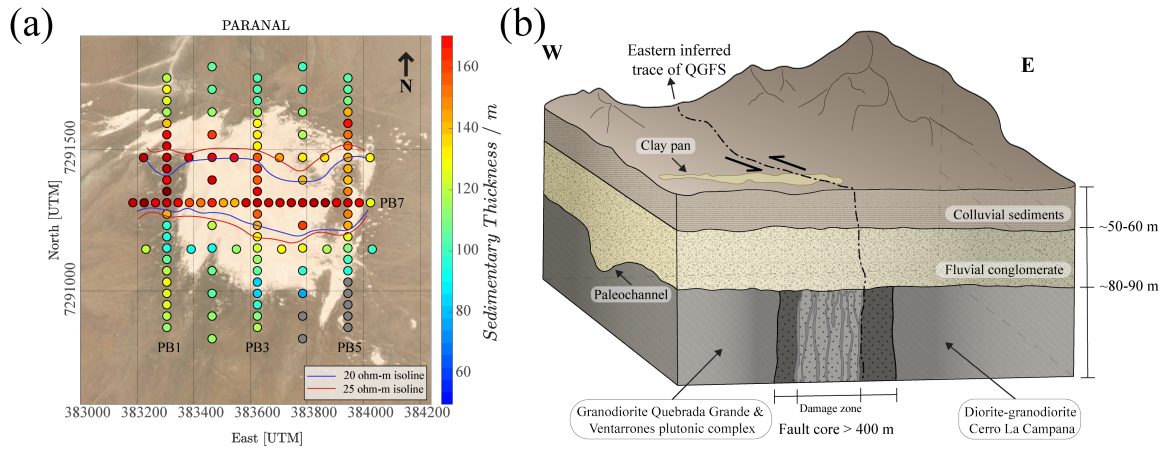

Figure 5.17: (a)The sedimentary thickness of each station based on the Marquard 1D model. Grey dots correspond to the stations where no conductive sediment layer was derived. Isolines of 20 and 25 Ωm in blue and red color at 90 m depth. (b) Graphical illustration of the Paranal clay pan based on the integrated interpretation. Based on Blanco-Arrué et al. (2022).

5.6 Summary of 1D inversion

The derived 1D inversion results presented in this chapter are consistent among each other and, in both clay pans, a three-layered resistivity structure is well resolved. A conductive layer is detected between two resistive layers, for which a resistivity characterization down to depth of $\sim$ 300 m is reliable. At the PAG site, the resistivity subsurface structure can be interpreted as a paleolake with a succession of colluvial and lacustrine sediments followed by the basement. The latter is in good agreement with the revised geological information. Based on the derived 2D resistivity depth sections, the geometry of the lacustrine sediments is well resolved with apparent low slope angles ($<10°$) at the edges. The maximum sedimentary thickness is derived at 100$\pm$ 10 m and is located right where the intersection with the respective paleochannel is placed on the surface, which is assumed to be one of the main fluvial incisions before the uplift of the Adamito fault. The PAG TEM 1D models are generally well resolved. However, the presence of a second deep conductor at the edges is questionable and might lead to misinterpretations. In the case of the Paranal site, the resistivity subsurface structure is interpreted as an old paleochannel where a sedimentary succession of fine sediments and fluvial conglomerate is detected. The maximum sedimentary thickness is derived at 160 $\pm$ 10 m and is located in the center of the clay pan, in a west-east direction. The geometry of the fluvial conglomerate exhibits slope angles of approximately 20° at the northern and southern edges, which might be part of the main old drainage system of the Paranal site. In addition, the magnetic results at the Paranal clay pan are consistent with the geological outcrop map, where the eastern inferred trace of the QGFS cuts directly the clay pan. The analysis of magnetic survey data reveals a positive magnetic anomaly where the Ventarrones plutonic complex and the Granodiorite Quebrada Grande are located. Therefore, the basement below the Paranal clay pan can be partly interpreted as a damaged zone of the strike-slip QGFS. The top depth of the base layer at the Paranal clay pan is generally well resolved, but slight underestimations arise for the resistivity of the base layer. The comparison between the TEM 1D profiles and the tomography results in both clay pans is consistent with the depth between the respective sediment layers. In both clay pans, the TEM 1D profiles and the tomography results show changes in the P wave velocity and resistivity that are consistent with a sedimentary interface. In particular, a negative linear correlation is visible, where high P wave velocities correlate with low resistivities and vice versa. Considering that both sites are affected by different climatic conditions, the drainage catchment of the Paranal site is significantly smaller than that of the PAG clay pan, and higher slope angles with a significantly thicker sedimentary infill are derived, suggesting strong fluvial transport and presumably a site more exposed to pluvial periods. The results presented improve our understanding of sediment transport in this hilly and arid environment. The application of different geophysical methods provides a better understanding of the sites studied, which benefits an integrated geoscientific investigation. In our case, the preliminary lithology of the drill-core campaign in Paranal gives us very valuable information to confirm the TEM results. The presented results achieved the primary objectives of the geophysical surveys. In order to validate the quasi-2D resistivity depth sections derived, and in particular to answer and evaluate the questions that arose from the TEM 1D inversion results on each clay pan, the field data is interpreted by means of a 2D forward modeling in Chapter 6 and a 3D inversion is performed to resolve the complex geometry of the clay pan for an independent and independent interpretation in Chapter 7.

CHAPTER 6

2D Forward modeling study

The PAG and Paranal TEM field data sets were used to derive 1D layered subsurface models, as illustrated and well described in Chapter 5. For each station, the obtained 1D model was analyzed and interpreted with available geological information and complemented with active seismic and magnetic results. However, multidimensional effects can misinterpret the TEM field data if the conductivity structure is highly heterogeneous and cannot be represented by a 1D subsurface (Newman et al., 1987; Goldman and Neubauer, 1994). Based on the 1D inversion results, the resistivity of the base layer varies laterally, especially at the edges of the profiles in both clay pans. Therefore, whether a 1D interpretation is adequate or not is questionable and might not be sufficient in certain subsurface scenarios. In order to evaluate possible distortions more carefully, a 2D forward modeling study is suggested (Yogeshwar and Tezkan, 2018). For the purpose of avoiding any misinterpretations and to validate the derived 1D models, the resulting quasi-2D resistivity depth sections are investigated through a 2D forward modeling study. As a general scope, this study aims to find a proper 2D model that fits the TEM data, including the possible 2D effects, and represents a more realistic subsurface structure. Throughout this chapter, 2D effects are investigated based on several 2D subsurface scenarios. The 2D models were evaluated considering two main aspects: (1) the slope angle variation of the clay pan and (2) the different bottom width of the conductive body.

The Spectral Lanczos Decomposition Method (SLDMem3t) code is used to perform these analyzes. This code is based on the finite difference (FD) algorithm that allows the computation of transient EM fields in the time domain in three dimensions and for arbitrary model parameterization (Druskin and Knizhnerman, 1988, 1994; Druskin et al., 1999). Comprehensive 2D / 3D modeling studies have been applied involving time-domain methods for various source configurations using SLDMem3t (Hördt et al., 1992; Hördt and Müller, 2000; Martin, 2009; Goldman et al., 2011; Sudha et al., 2011; Rödder and Tezkan, 2013; Yogeshwar, 2014). The first section briefly describes the SLDMem3t algorithm and is followed by the search for a suitable FD grid to calculate the synthetic transient data.

The numerical solutions are compared and validated with the semi-analytical responses. Once the grid was validated, 2D models were generated based on a selected profile of each clay pan. The synthetic responses obtained are interpreted and discussed in terms of misfit and error-weighted relative differences. In the end, possible 2D effects are discussed by comparing the 1D inversion of the 2D forward responses and the field-data results.

6.1 The finite difference algorithm SLDMem3t

This section highlights the key characteristics that make the SLDMem3t suitable for measured data sets. For more details on the theory description of the SLDMem3t code, refer to the comprehensive publications (e.g. Hördt et al., 1992; Druskin and Knizhnerman, 1994; Druskin et al., 1999; Martin, 2009; Yogeshwar, 2014). The following theoretical description is based on the non-stationary Maxwell equations in a quasi-static approach. The differential form of Faraday's and Ampere's laws is written as follows:

$$\nabla \times \boldsymbol{E} = -\partial_t \boldsymbol{B}, \tag{6.1}$$

$$\nabla \times \boldsymbol{B} = \mu(\sigma \boldsymbol{E} + \boldsymbol{j}_e), \tag{6.2}$$

where $\boldsymbol{j}_e$ denotes the external current density of an external source before switch-off ($t = 0$), and assume that for most earth materials, the magnetic permeability μ equals the vacuum permeability μ_0. By applying the curl operator on Equation 6.1 and substituting the Ampere law, the diffusion equation takes the form:

$$\nabla \times \nabla \times \boldsymbol{E} + \mu\sigma\partial_t \boldsymbol{E} = -\mu\partial_t \boldsymbol{j}_e, \tag{6.3}$$

In order to solve the 3D forward problem, Equation 6.3 is solved using an FD discretization scheme. The FD approach is widely used in EM methods due to the apparent simplicity of its numerical implementation (Martin, 2009). Note that complex geometries are challenging to produce in the FD method. In those cases, other unstructured grids, such as finite element (FE) schemes, are recommendable. Within the SLDMem3t approach, the electric and magnetic fields are sampled in three dimensions on a Yee-Lebedev staggered grid (Yee, 1966). Fig. 6.1a illustrates the Yee cell where the electrical field components are calculated along the edges of each cell (averaged on the edge), and the magnetic field components are on the cell (averaged on the face). The SLDMem3t algorithm uses a material averaging scheme that allows the calculated model to be independent of the discretized grid (Druskin and Knizhnerman, 1994). In general, the conductivity is assigned directly to each cell in the FD or FE schemes. Here, the physical parameters of the model are assembled within the edge- and face-averaged field positions. Therefore, the field components are calculated at different locations in the grid cell. For an arbitrary 2D resistivity model, an exemplary description of the material averaging is displayed in Fig. 6.1b. In this way, the discretization of the conductivity becomes independent of the FD grid.

The conductive medium is spatially discretized and the operator $\nabla \times \nabla \times$ in Equation 6.3 is approximated by finite differences into a system matrix $\mathbf{A}$. The discretization leads to the following set of differential equations for a current switch-off:

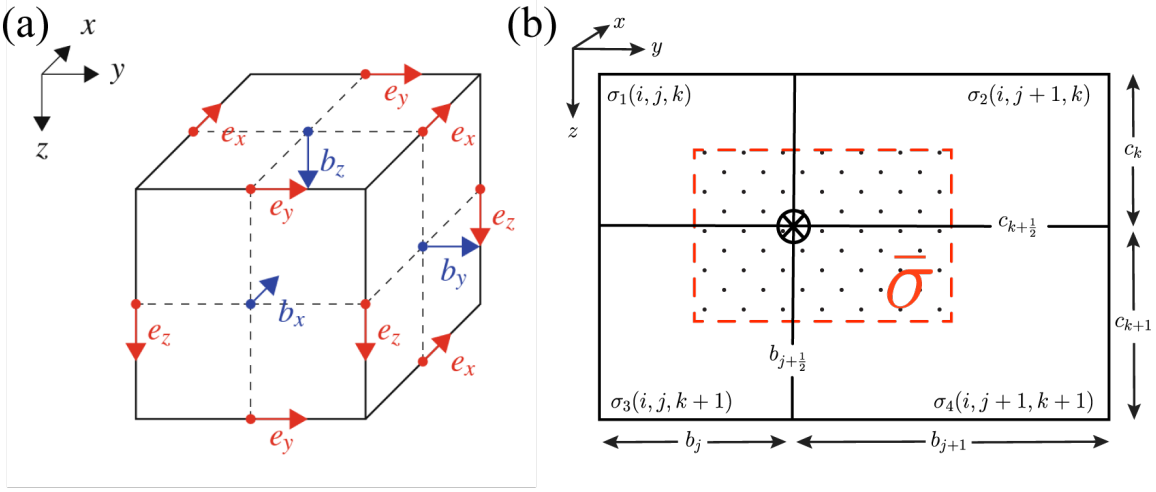

Figure 6.1: (a) Illustration of a Yee-grid cell forming elementary loops where electric and magnetic field components are assumed to be edge-averaged and face-averaged, respectively. Taken from Börner (2010). (b) Geometry for averaging conductivities, where the current flow is in the x-direction. The averaging area $\bar{\sigma}$ is denoted as a red box, and the field component is obtained at $\otimes$. Based on (Weidelt, 1986; Yogeshwar, 2014).

$$\mathbf{A}\hat{\mathbf{E}}(t) + \mu\hat{\sigma}\partial_t\hat{\mathbf{E}}(t) = 0; \quad for \;\; t > 0, \;\; \hat{\mathbf{E}}(t)|_{t=0} = \phi \tag{6.4}$$

where $\mathbf{A}$ is a symmetric, positive definite with sparse $n \times n$ operator matrix, whereas the hat symbol (^) indicates the spatial discretization and ϕ denotes the switch-off field. The value of n is approximately three times the number of points in the grid in the directions x, y, and z. Following Hördt et al. (1992), equation 6.4 is transformed to normalized form and solved by applying the Spectral Lanczos decomposition method (SLMD). An approximate solution can be obtained through the Krylov subspace (Druskin and Knizhnerman, 1994; Druskin et al., 1999). More detailed numerical explanations of the Lanczos method can be found in Hördt et al. (1992), Yogeshwar (2014), and Haroon (2016).

6.2 Grid analysis

A good performance of SLDMem3t involves a proper design and calculation of the grid, which becomes the main aspect of this section. Here, the electrical field values $\boldsymbol{E}$ and the magnetic field values $\dot{\boldsymbol{B}}$ are obtained. The presented analysis followed the grid discretization approach from comprehensive publications such as Hördt et al. (1992), Martin (2009), and Yogeshwar (2014).

Before the forward calculation, the following list of considerations was taken into account to ensure an accurate solution.

- A time range within three decades is recommendable to ensure an accurate transient decay. However, when longer TEM data are collected, a multigrid approach is suggested.
- The automatic grid generator *make_sldm_grid* was used with a logarithmically spaced grid in the three spatial directions (Martin, 2009).

- The resistivity distribution needs to be carefully defined due to the grid dependency. The boundaries of the resistivity contrast must be sufficiently fine to prevent the generation of over-averaged resistivity structures due to the material averaging scheme. Based on the latter, a very fine discretized grid does not guarantee the most accurate synthetic response. Moreover, computational resources might be significantly higher.

- The resistivity contrast ratio was kept to 1/100 as suggested in Hördt et al. (1992). However, inversion schemes cannot guarantee this because larger contrasts can be modeled due to field data.

Firstly, the grid design is verified throughout a one-dimensional resistivity model, for which the synthetic resitivity responses are compared with the 2D model calculations. Based on the 1D inversion results shown in Chapter 5, a model from each clay pan is used for the verification. Consequently, two different three-layer models were selected to check the stability of the grid. In addition, homogeneous half-space 1D models were tested with representative resistivity values observed in each clay pan. The mentioned considerations were taken into account to maintain high data quality. The selected time range for the forward calculations was chosen within three decades, described and illustrated in the processing stage (see Chapter 4). The transients were fixed to 32 logarithmically equidistant data points. The synthetic subsurface scenarios assumed a 40×40 m^2 transmitter loop size. The receiver position was fixed to the center following the central loop configuration.

In this section, a grid line set was chosen to be evaluated for each site. In both cases, the grid spreads logarithmically inward, outward, and downward from the transmitter, according to the minimum and maximum diffusion depths. An exemplary section xy and xz of the grid lines for $n_{x,y} = 70$ and $n_z = 71$ is shown in Fig. 6.2. The transmitter is set up by superpositioning several dipoles that form a loop source, located at the edges between adjacent grid lines (Fig. 6.2). The setting parameters designed for each synthetic case are given in Table 6.1.

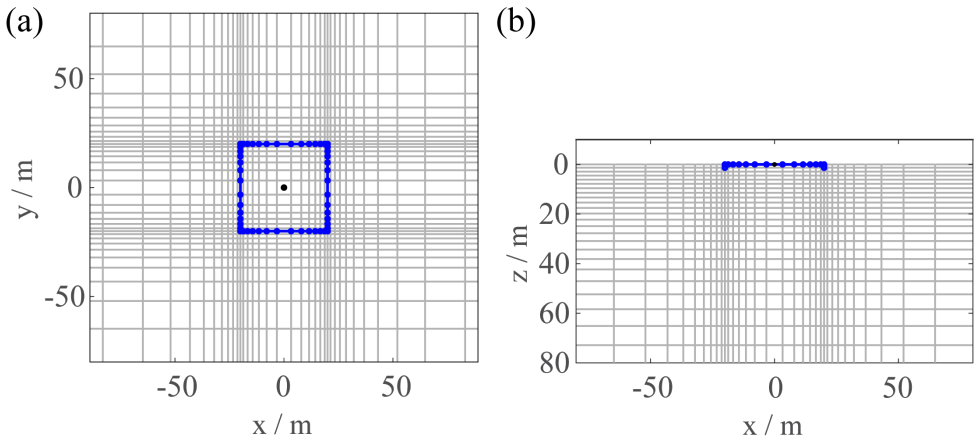

Figure 6.2: (a) xy-plane view and (b) xz-plane view of the grid for the Tx-40 setup. The transmitter is denoted as a blue line and the receiver is located at the center with a black dot. The grid is displayed as gray lines.

Table 6.1: Setting parameters for the grid analysis of a characteristic model of PAG and Paranal clay pans.

Clay pan	**Time range** s	ρ_{1-3} Ωm	z_{1-3} m	**Grid lines** $n_{x,y}, n_z$
PAG	$t = 1.85^{-5} - 2.10^{-2}$	(130, 5, 400)	(30, 110, ∞)	66, 67
Paranal	$t = 1.54^{-5} - 8.85^{-3}$	(180, 16, 440)	(50, 160, ∞)	70, 71

The error-weighted relative differences χ_d, considering the noise level η of each clay pan, and the relative differences (un-weighted) δ_{rd} were calculated between the 1D (Emu+) and 2D (SLDMem3t) synthetic responses. These parameters are given by the following equations:

$$\chi_d = \frac{F(m)_{2D} - F(m)_{1D}}{\delta F(m)_{2D}} \quad , \quad \delta_{rd} = \frac{F(m)_{2D} - F(m)_{1D}}{F(m)_{2D}} \times 100\%, \tag{6.5}$$

where $F(m)_{2D}$ and $F(m)_{1D}$ correspond to the synthetic response of SLDMem3t and EMU +, respectively. The noise level used for each subsurface scenario is based on the observed data mentioned in the processing stage ($\eta_{pag} = 5 \times 10^{-9} V/Am^2$ and $\eta_{paranal} = 3 \times 10^{-10} V/Am^2$). In addition, an error floor of about 3% was considered based on the analysis of the TEM field data (see Section 4.6). In Fig. 6.3, the comparisons for the three-layer case imaging the 1D resistivity substructure at the center of (a) Paranal and (b) PAG sites are shown.

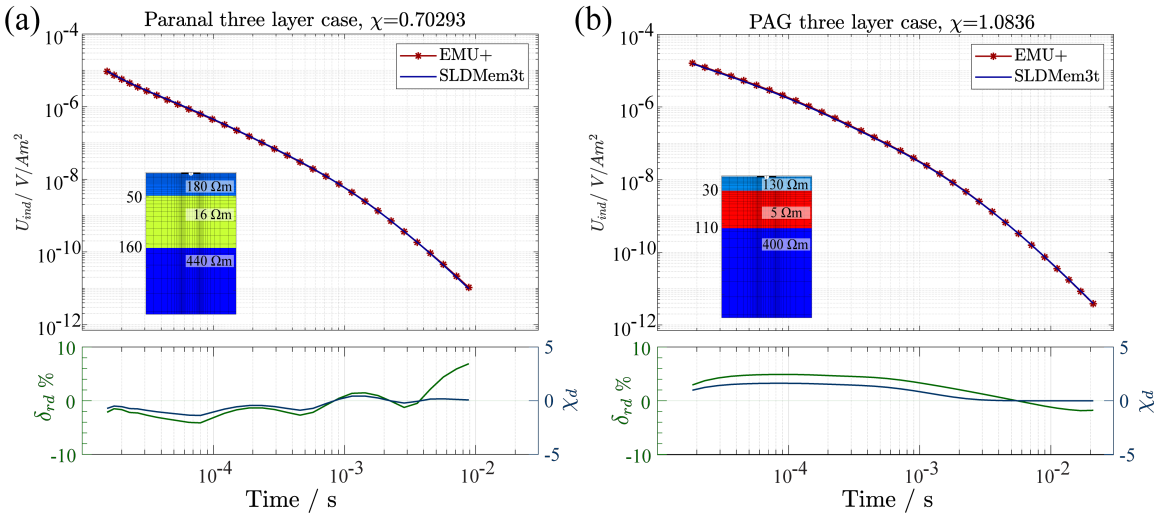

Figure 6.3: Three-layer case comparison of the SLDMem3t and 1D EMUPLUS solutions for (a) Paranal with $n_{xy} = 70$ and $n_z = 71$ and (b) PAG with $n_{xy} = 66$ and $n_z = 67$. Below each comparison, the relative differences (left y-axis, in green) and the error-weighted misfit (right y-axis, in blue) between the synthetic responses are displayed.

In the Paranal case, the relative differences show values less than 2% for most data points, except for times $t > 4 \times 10^{-3}$ s, for which slightly higher relative differences are displayed. In addition, the error-weighted fit between the 2D and the 1D synthetic response is below 2.0, with a global χ slightly overfitted with 0.7. In the PAG site, the relative differences exhibit values lower than 6%, for which deterioration is observed from

early to intermediate times. Despite this, the error-weighted fit is below 2.0 with an optimal global χ around 1. The stability of these two grid line sets and the three-layer cases is generally verified and exhibits good performance.

Comparisons considering a homogeneous half-space with two different resistivities (a) 250 Ωm and (b) 400 Ω m are shown in Fig. 6.4. In both cases, highly deteriorated relative differences are displayed at late times with values >10%, especially for the PAG case observed below $U_{ind} = 1 \times 10^{-12} V/Am^2$ (Fig. 6.4b). However, the global χ is overfitted (< 0.5). The performance observed in homogeneous half-space models is poor when a high resistive body of about 400 Ωm is considered. Further studies with homogeneous half-space models with a value >400 Ωm exhibited a higher mismatch between the semi-analytical and the 2D synthetic response.

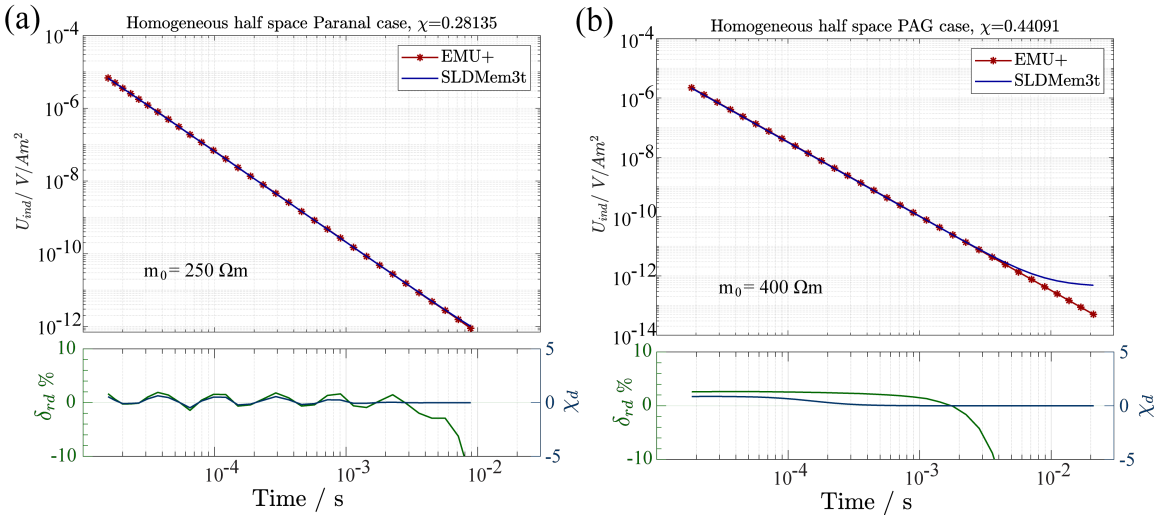

Figure 6.4: Homogeneous halfspace case comparison of the SLDMem3t and 1D EMUPLUS solutions for (a) Paranal with $n_{xy} = 70$ and $n_z = 71$ and (b) PAG with $n_{xy} = 66$ and $n_z = 67$. Below each comparison, the relative differences (left y-axis, in green) and the error-weighted misfit (right y-axis, in blue) between the synthetic responses are displayed.

It can be seen that both grid line sets are sufficiently accurate for both three-layer 1D models. For homogeneous half-space cases, highly deteriorated solutions arise at late times. It should be noted that inaccurate solutions are observed below the noise level measured at each survey site. Therefore, most parts of each clay pan can be represented by a three-model structure, which can be modeled by SLDMem3t in order to provide accurate solutions. Moreover, a small number and size of modeling cells can lead to further distortions, especially at late times. Note that other numbers of modeling cells for n_z and n_{xy} were also tested. However, the results had a comparable performance. Therefore, in order to maintain the proper calculation times without losing quality in the next 2D forward modeling studies, the number of grid lines used was set to a value of n_z = 71 and n_{xy} = 68.

6.3 2D forward modeling scenarios

It is well-known that 2D forward modeling can not outmatch a 2D or 3D inversion. However, this approach may give us insight into the size and extension of possible 2D distortions of the collected TEM dataset. In total, five different scenarios are studied in the following sections and are sketched in Fig. 6.5.

Here, different scenarios are illustrated to investigate: (**a**) the effect of the bottom width of the clay pan; (**b**) the effect of the slope angle on the TEM data; (**c**) the presence of a deep conductive anomaly towards the edge of the PAG clay pan; (**d**) the reliability of the basement resistivity at edges of the Paranal clay pan, and (**e**) the effect of different basement depths in the Paranal clay pan.

Once the grid line set has been validated, the scenarios mentioned above are created based on the resistivity distribution observed on each clay pan. To provide an overview of how the bottom width and slope angle impact the system, a 2D synthetic response was produced by using several 2D models (Fig. 6.5a and b). Then, the other 2D models are generated based on the MQ 1D inversion results described and discussed by the quasi-2D resistivity depth profiles presented in Chapter 5.

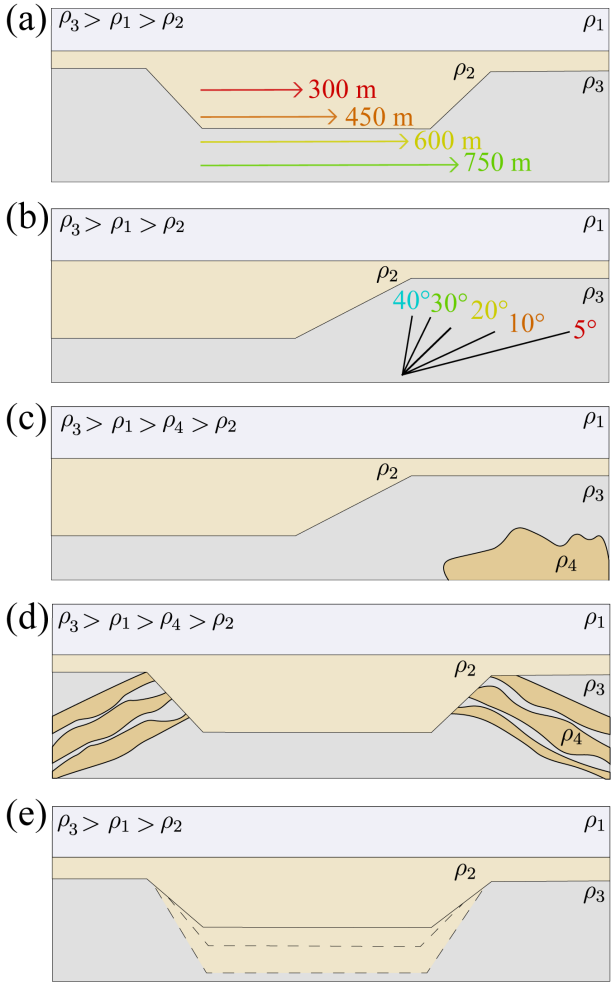

Figure 6.5: Sketch of different 2D forward modeling scenarios. (a) Models to evaluate the effect of the bottom width of the clay pan, considering a slope angle fixed to 20°. (b) Models to evaluate the effect of the slope angles of one side of the clay pan. (c) A model with a deep conductor in one side. The slope angle of the clay pan is kept at 10°. (d) A model with a pant-leg-shaped conductivity anomaly at edges of the clay pan, and (e) Models with different basement depths.

6.4 Slope angle and clay pan resistivity

According to the scope mentioned, two simplified 2D model scenarios were generated following the sketches in Fig. 6.5a and b to analyze the effect of the slope angle and the bottom width of the clay pan. Firstly, Model A was generated with a slope on the right side of the clay pan. Other 2D models were generated varying the slope for values of 5°, 10°, 20°, 30° and 40°. Model A assumes a resistivity distribution as observed at the PAG site and a slope angle of 5° (Fig. 6.6a). Secondly, Model B has been generated with both

lateral sides of the clay pan. Based on this, other 2D models were created by increasing the bottom width of the clay pan, in a positive profile direction for a value of 300 m, 450 m, 600 m, and 750 m. Model B assumes a resistivity distribution observed at the Paranal site with a bottom width of 300 m (Fig. 6.6c). The maximum thickness of the conductive layer is about 150 m, and 29 stations are considered with a total distance of 1760 m in all the 2D models. The grid is discretized with $n_{x,y} = 68$ and $n_z = 71$ with a dimension of the order of 72 cells with an assigned conductivity. Synthetic responses for a central loop configuration are calculated within a time range between $t = 1.14 \times 10^{-5}$ s and $t = 4.5 \times 10^{-3}$ s. In total, 13 stations were located loop-by-loop at the center profile, and then the rest of the soundings were placed along the edges of the profile with a spacing of about 40 m.

As a result, several 2D synthetic responses were calculated using the different configurations of Model A and B (Fig. 6.6a and c). The corresponding values RMS for each slope angle and bottom width are shown for all stations along the profile in Fig. 6.6b and d.

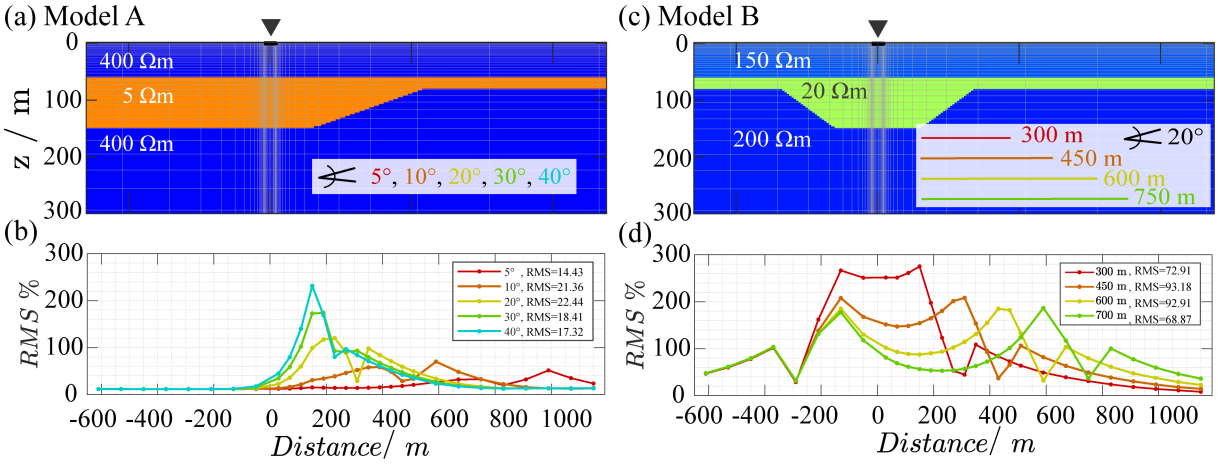

Figure 6.6: Simplified 2D models, for which the grid is displayed as gray lines. The triangle denotes the central loop TEM location (transmitter and receiver), which is located at x = 0 m. The grid is discretized with $n_{x,y} = 68$ and $n_z = 71$. For better visualization, the vertical scale is exaggerated. (a) Model A represents the PAG site and is used to evaluate the effect of different slope angles: 5°, 10°, 20°, 30°, and 40°. Here, a 10° slope angle is used as an example. (c) Model B represents the Paranal site, and it is used to evaluate the bottom width of the conductive body. In this case, the slope angle is fixed to 20°, and a bottom width of 300 m is displayed as a reference. (b) and (d) show the derived values RMS % between the 2D and 1D synthetic responses of each 2D model scenario. The global RMS percentage for each variation is shown in the legend. In both cases, the vertical exaggeration is 2:1.

The obtained RMS for different slope angles shows that high RMS values are observed for the stations located at the top of each slope. In this zone, all cases show that RMS increases with increasing slope steepness. For example, a closer examination of the slope of 40°, the obtained RMS exhibit values $> 150\%$ at those stations. However, the slope of 10° exhibits low RMS values $< 80\%$, for which more stations show high RMS values due to the extension of the slope (Fig. 6.6b). However, a better RMS is present for stations located far from the slope, which can be seen in all variations of Model A. The global RMS show a better fit for the slope of 5° with 14.43% leading to less influence of the slope in the synthetic response. On the basis of these results, the slope angle can strongly influence distortions in the TEM data. Specifically, there is a trade-off between the affected area and the RMS obtained for each station. The affected area is smaller

for larger slope angle values but with a higher data distortion. In contrast, smaller slope angle values affect a larger area but with a lower distortion of the data.

Furthermore, the calculated RMS considering different bottom widths exhibits a huge distortion of the data on both sides of the conductive body (Fig. 6.6d). In fact, the highest RMS values can be seen in stations located just above the base tip of the slope. The comparison between the RMS obtained for the different bottom widths (Fig. 6.6d) suggests that a stronger effect can be seen for the stations right above the bottom of the clay pan when the sides of the slope are closer, as is the case for 300 m ($RMS > 200$). In contrast, for larger bottom widths, such as the 700-m case, stations located in the middle of the clay pan show a smaller data distortion ($\sim 50\%$) than those close to the lower tip of the slope ($\sim 190\%$). The 700 m case also presents the lowest RMS value (68.87%) among the cases explored. Therefore, the obtained RMS for different 2D synthetic observations confirms that the slope angle of the clay pan can produce distortions in the TEM data. Furthermore, a subsurface with a shorter bottom width of the clay pan could also increase the effect of the distortions on the transient responses.

For a more detailed evaluation, the two synthetic models that best represent each survey site, based on the 1D inversion results, are shown in Fig. 6.7, where the calculated transient response is shown for each station.

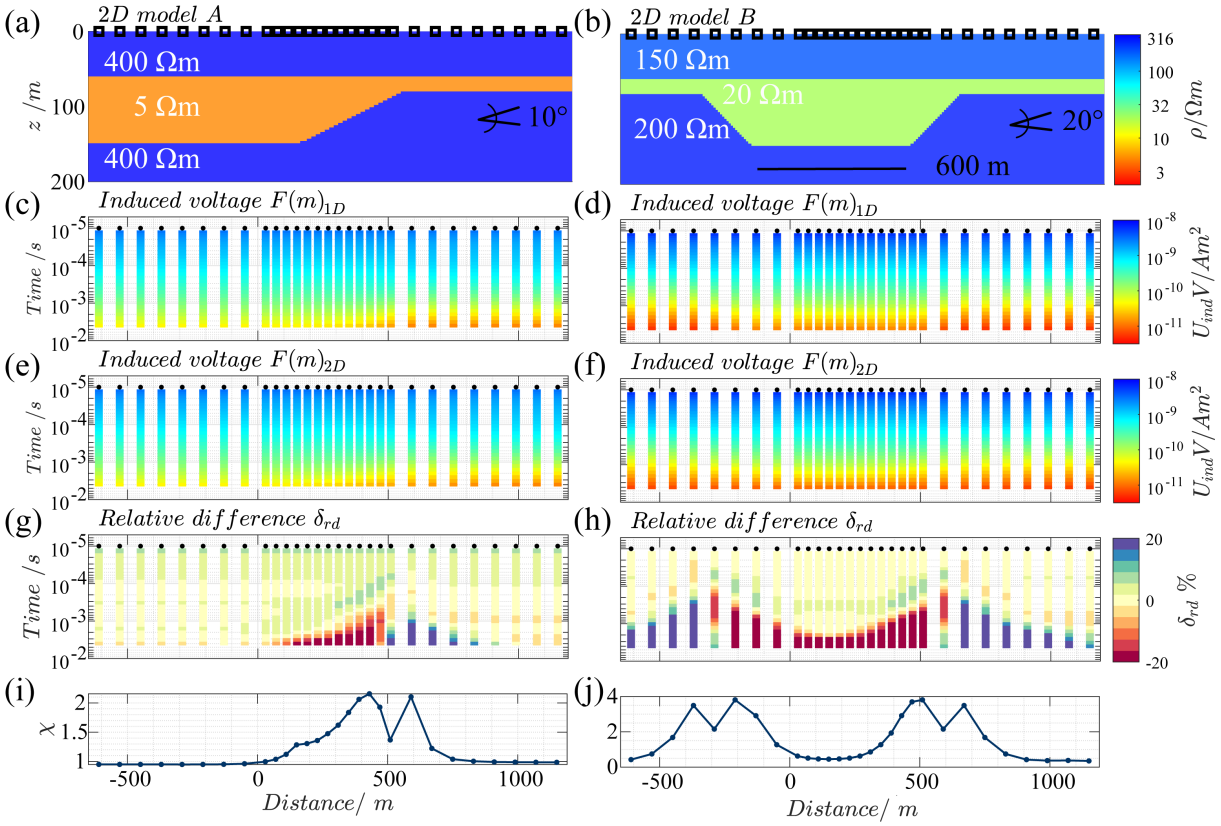

Figure 6.7: Synthetic model response for (a) Model A with a slope angle of 10° and (b) Model B with a slope angle of 20° and an extension of 600 m. In both cases, the vertical exaggeration is 3:1. (c) and (d) show the corresponding induced voltage U_{ind} of the 1D semi-analytical response. (e) and (f) show the induced voltage U_{ind} of the 2D synthetic response. (g) and (h) display the error weighted relative differences δ_{rd} between $F(m)_{2D}$ and $F(m)_{1D}$. (i) and (j) illustrate the global χ values of each sounding.

After evaluating the induced voltages from the 1D and 2D synthetic responses, slight differences can be observed in the stations located right above the slopes for both models. As is the case for Model A at 500 m profile distance of around $t \sim 3 \times 10^{-2}$ s and $t = 1 \times 10^{-3}$ s, for which the 1D semi-analytical responses are more accentuated (Fig. 6.7c and e). In the same case, the same result is observed in Model B on both sides of the slope at the profile distance -100 m and 500 m and in the same time range (Fig. 6.7d and f). Complementary to this, having a closer look at the relative differences, the most distorted synthetic data is observed at late times with values $\delta_{rd} = \pm 20\%$. For example, Model A concentrates the most distorted data along the slope with some minor distortions that are also visible at intermediate times and that follow the trend of the slope of around $t \sim 2 \times 10^{-4}$ s (Fig. 6.7g). In addition, Model B exhibits highly distorted data at late times, but this pattern is observed in all the stations along the profile due to the influence of both slopes (Fig. 6.7h). In addition, the global χ is calculated for each station. Here, Model A exhibits χ values >1.5 around the slope (Fig. 6.7i), whereas Model B displays χ values of about 4 around both slopes (Fig. 6.7j). This follows the same trend observed in terms of the RMS values for Model A with a slope angle of about 10°, where the RMS is about 50 % in the slope surroundings (Fig. 6.6b). In addition, Model B, with a width of about 600 m, exhibits higher RMS values of about 200 % for the stations right above the bottom of each slope (Fig. 6.6d).

The simplified 2D models confirmed the presence of strong 2D effects, especially with the increase of the slope angle of a clay pan side. Moreover, stronger 2D effects are observed for shorter bottom widths of the clay pan, influencing the TEM synthetic data. Therefore, given the slope angle and bottom width of the clay pan, it is expected that 2D effects are present in the TEM field data.

6.5 2D forward modeling for the field data model

The simplified 2D models have demonstrated that subsurfaces with a conductive layer and a certain slope angle or even closer to a clay pan shape with two slopes at the edges lead to non-neglectable 2D effects, which need to be accounted for when interpreting the data in 1D. As already mentioned in Chapter 5, the 1D inversion results exhibit some features that require a more detailed 2D synthetic evaluation.

Taking this into account, more realistic 2D synthetic evaluations were considered to achieve the scopes mentioned in Fig. 6.5c, d, and e. The selected TEM 1D profiles A6 and B3, one from each clay pan, were used to generate proper 2D models (see Figs. A7.5 and 5.6). Then, the 2D synthetic responses obtained were inverted using the 1D Marquardt approach (Scholl, 2005). The time length for each station was fixed based on the time length of observed field data. The analysis and description of the 2D effects in each case was performed using the error-weighted relative difference based on the noise level observed in each clay pan ($\eta_{pag} = 5 \times 10^{-9} V/Am^2$ and $\eta_{paranal} = 3 \times 10^{-10} V/Am^2$).

6.5.1 1D inversion of synthetic profile A6

As mentioned above, one of the main scopes was the analysis of the deep conductor on one side of the PAG clay pan (Fig. 6.5c). Here, profile A6 was used to evaluate the possible distortion in the TEM field data due to 2D effects. The workflow proceeded as follows: a 2D forward modeling was performed for a 2D model with and without the deep conductor, as is shown in Fig. 6.8a and d, respectively. The resistivity of the base layer was fixed at 400 Ωm. The 1D Marquardt inversion results of the 2D synthetic transients of each case are displayed in Fig. 6.8b and e. Furthermore, the 2D effects are described in terms of the error-weighted relative differences (Fig. 6.8c and f).

The 1D inversion of the 2D synthetic data reproduces quite well the resistivity substructure observed by profile A6 (Fig. 6.8b). On the one hand, the shape of the conductive clay pan is adequately resolved (*C1*). On the other hand, the deep conductive anomaly (*C2*) is also well reproduced. In addition, if there were no 2D effects, the error-weighted response between the 2D and 1D forward calculation would be zero. However, this does not occur due to some 2D effects observed, especially with distorted data at intermediate times between T08 and T11 stations (Fig. 6.8c).

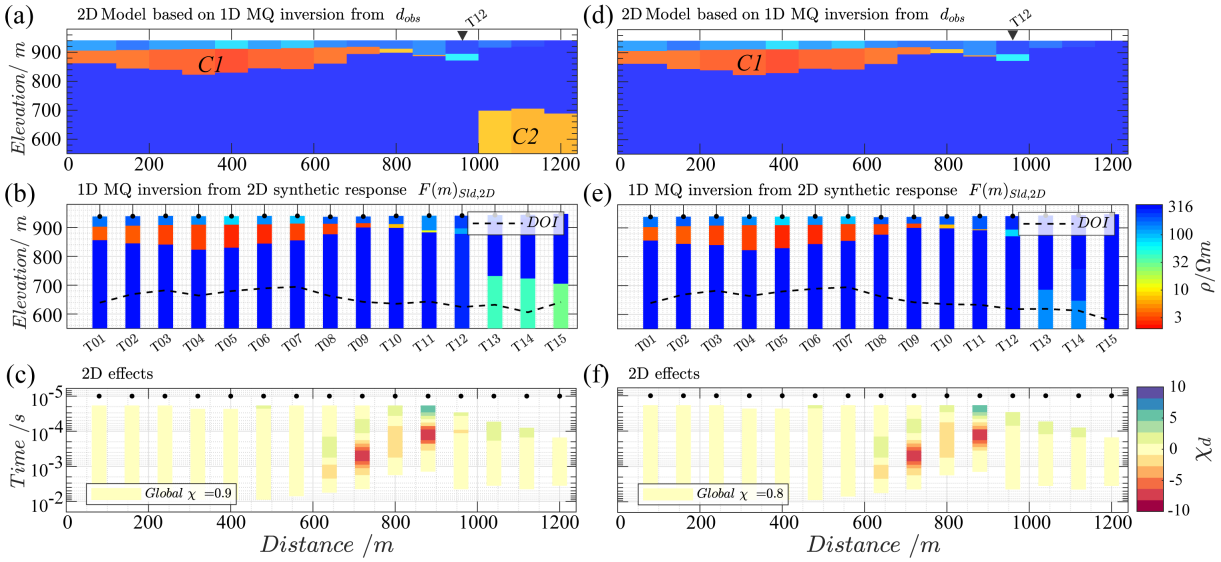

Figure 6.8: 2D Model of profile A6 from the PAG site (a) including a deep conductor *C2*, and (b) without the conductive anomaly *C2*. Station T12 is highlighted with a black inverted triangle. (b) and (e) show the 1D Marquardt inversion from the 2D synthetic response of each 2D model. The DOI is displayed with a black dashed line. (c) and (f) illustrate the error-weighted relative differences χ_d of the respective stations.

To identify where the origin of the observed 2D effects comes from, a second 2D forward modeling was performed excluding the deep conductor *C2* (Fig. 6.8d). From the 1D inversion results displayed in Fig. 6.8e, in the same manner, it can be seen that the geometry of the clay pan is well resolved. However, a deep conductor is slightly visible in stations T13 and T14, representing minor 2D effects. In addition, the latter is also confirmed by the large error-weighted relative differences observed along the slope (stations T08-T11), similar to what is observed for the model with the deep conductor *C2*. In both cases, comparable global $\chi \sim 1$ are obtained (Fig. 6.8f), which suggests an overall good fit of the observed data. Inverted synthetic scenarios, the DOI can be sen between 600 -

700 m.a.s.l., indicating reliable 1D models down to ∼300 m depth. It should be pointed out that the slope angle of the conductor *C1*, even though it distorts the data, does not generate such a strong conductor *C2* at deeper depths.

To verify that the anomaly *C2* is not related to 2D effects, Fig. 6.9 exhibits the observed field data, the 2D synthetic transient of station T12 from both 2D forward modeling scenarios and the 1D synthetic responses using both Emu+ and SLDMem3t algorithms. Regardless of the presence or absence of the deep conductor *C2*, the synthetic responses do not match the field data. Additionally, the 2D responses exhibit slower decay and improved fitting at later times compared to the 1D synthetic solutions. Consequently, distortion effects are evident in both 2D modeling scenarios.

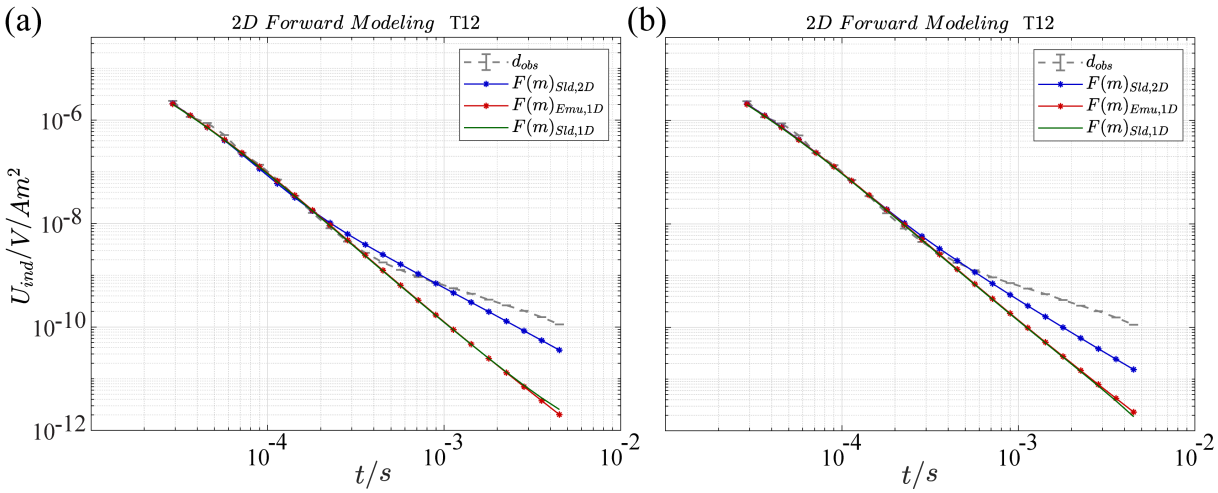

Figure 6.9: 1D and 2D synthetic responses at station T12 derived from (a) the 2D model with the deep conductor, and (b) without the anomaly *C2*. The observed field data A6T12 is also shown for comparison.

It is challenging to find the proper reason for the presence of the anomaly *C2*. The observed decay at late times might suggest that the induction diffusion processes play a role. In addition, the presence of the conductive clay pan *C1* might induce this deep conductor *C2*, leading to artifacts in our 1D models. In general, the 2D forward modeling study gives us certainties that slight 2D effects are present in both 2D model scenarios (with and without *C2*). However, from the derived TEM 1D models, the *C2* is located below the calculated DOI, indicating poor resolution at deeper depths. Hence, for subsequent analysis, it is assumed that the anomaly *C2* lacks geological significance and is likely an artifact.

6.5.2 1D inversion of synthetic profile B3

Following the same procedure as above, 2D forward modeling was performed on profile B3 in the Paranal clay pan to analyze possible distortion effects as sketched in Fig. 6.5d. Here, the resistivity of the basement was evaluated using two different scenarios. First, a 2D model was generated with exactly the same resistivity distribution derived by the Marquardt inversion approach, for which the pant leg-shaped shape is observed (Fig. 6.10a). Secondly, a 2D model was created with a fixed resistivity base layer of about 300 Ωm (Fig. 6.10d). The inverted 2D synthetic transients of each scenario are shown in Fig.

6.10b and e. In addition, the error-weighted relative differences are shown Fig. 6.10c and f.

In the case of the 2D model based on profile B3, the derived 1D models reproduced a three-layer substructure, but the shape of the resolved conductive layer *C1* shows a thinner thickness than the 2D model, especially at the center of the profile, between stations T08 and T16 (Fig. 6.10b). However, the conductive anomaly *C2* is properly resolved at both edges of the profile. Interestingly, high error-weighted values ($\chi_d \sim 10$) are observed following the shape of the conductor *C1* along the profile (Fig. 6.10c). The global χ is about 2.5, indicating the presence of strong distortions. In the same way, the 2D model with a fixed resistivity in the base layer is shown in Fig. 6.10d. Inverted 2D synthetic responses also reproduce a conductive anomaly *C2*, indicating the presence of distortion effects. However, the same behavior is observed for the conductor *C1*, for which a thinner layer is derived (Fig. 6.10e). The error-weighted responses exhibit a strong distortion effect in the surrounding of the conductor *C1* with a global χ of about 3. From the inverted synthetic scenarios, the DOI is observed around 1900 m.a.s.l., suggesting reliable 1D models down to ∼250 m depth.

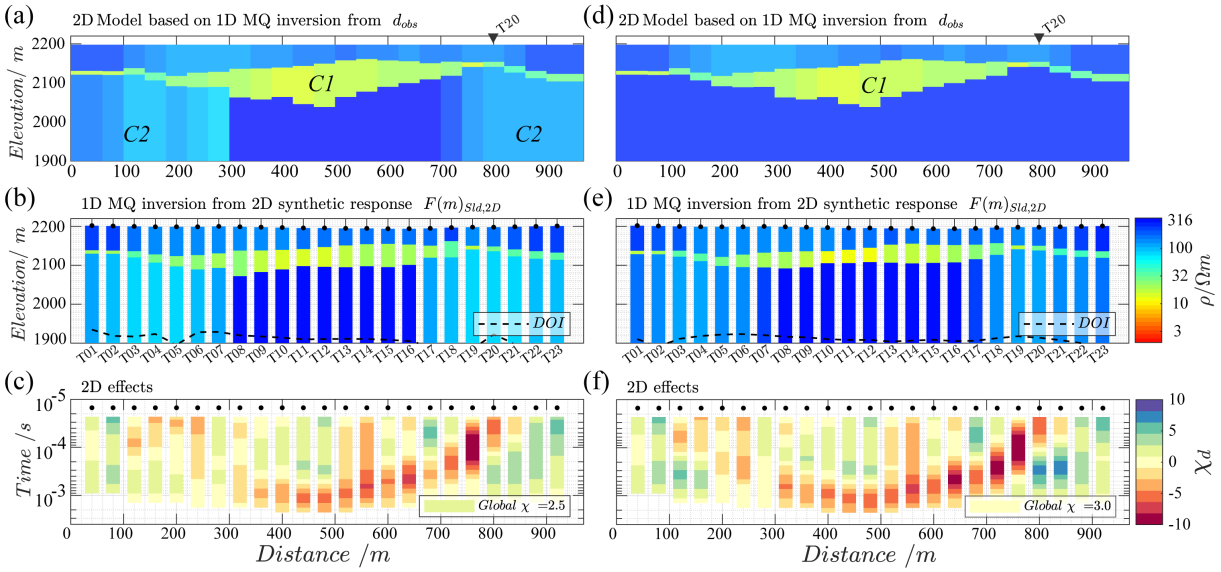

Figure 6.10: 2D Model of profile B3 from the Paranal site (a) including a the pant-leg-shaped conductors *C2*, and (b) with a homogeneous resistivity basement. Station T20 is highlighted as a black inverted triangle. (b) and (e) show the 1D Marquardt inversion from the 2D synthetic response of each 2D model. The DOI is displayed in a black dashed line. (c) and (f) illustrate the error-weighted relative differences χ_d of the respective stations.

For a detailed analysis of the behavior of 2D and 1D synthetic transients, station T20 is plotted for both scenarios in Fig. 6.11. The 2D and 1D responses obtained for the 2D model with the same resistivity distribution exhibit slight variations at late times, but both responses fit well with the observed data (Fig. 6.11a). For the 2D model with a fixed resistivity of the base layer, the 2D synthetic responses fit the observed data well (Fig. 6.11b). However, the 1D synthetic and semi-analytical responses present a higher variation at late times. Therefore, the 2D forward study clearly indicates that 2D effects might be present in the field data set.

The 2D forward modeling for profile B3 shows a clear presence of strong 2D effects in both scenarios. Here, the stations at the edges of the clay pan are influenced by the conductor *C1*, which induces distortions that cause the pant-leg-shaped in the derived 1D inversion. However, it is challenging to argue about the reason for the thin conductive *C1* in both scenarios. To the best of our knowledge, it presumably can be associated with either the observed strong distortion effects or due to an equivalence problem. In order to understand the observed feature in our 2D synthetic responses, an assessment of the thickness layer is performed in the following subsection.

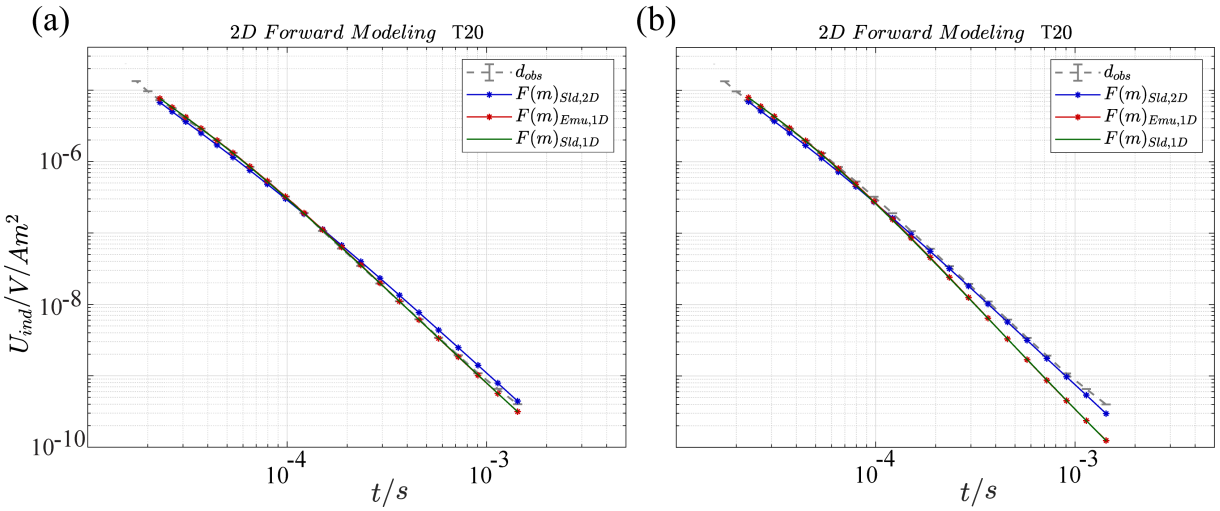

Figure 6.11: 1D and 2D synthetic responses at station B3T20 derived from (a) the 2D model with the pant-leg-shaped conductor, and (b) without the anomaly *C2*. The observed field data B3T20 is also shown for comparison.

6.5.3 Thickness layer evaluation

From the inverted models using the 2D synthetic responses, it is questionable if the layer thickness is underestimated or corresponds to an equivalence problem. To investigate this issue, the 1D model of the 2D synthetic response at station T12 obtained from the exact 2D model is selected to analyze the equivalence range of the second conductive layer (Fig. 6.10a, T12 at the center of the profile). The second layer is perturbed in terms of resistivity and thickness model parameters. The 1D Marquardt inversion results from the B3T12 field data are used as true model values, with $\rho_2 = 10$ Ωm and thickness of about $th_2 = 20$ m (Fig. 5.2a).

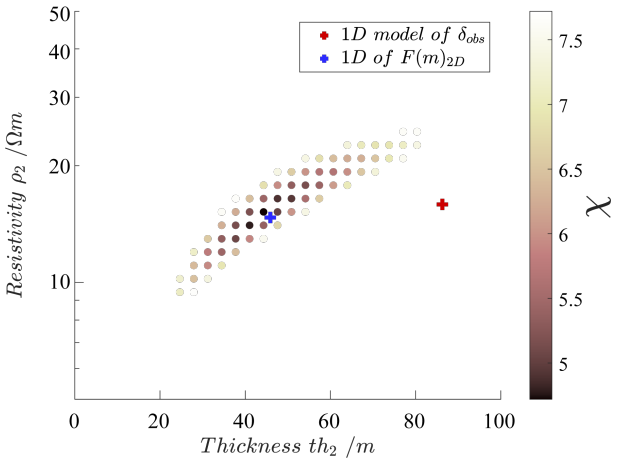

Figure 6.12: Variation of T12 1D model obtained from the 2D synthetic response, in terms of ρ_2 and th_2. The color bar represents the respective χ values of each 1D model. The obtained 1D model from the 2D forward modeling is displayed as a blue cross. The 1D model from the field data is shown as a red cross (station B3T12).

In total, 900 1D models are derived, for which 47 models have a χ between 4.7 and 7 (Fig. 6.12). The model perturbation covers a space of 30 logarithmically equidistant values ranging between 5 Ωm and 50 Ωm for ρ_2, and a thickness th_2 between 5 and 100 meters. In addition, the T12 station shown in Fig. 6.10a is located within this range and has a $\chi = 4.3$ (Fig. 6.12). From this it can be seen that larger values χ are derived when either the resistivity or thickness varies throughout the model parameter space explored. However, the 1D model B3T12, obtained by the TEM field data, is not within the equivalence range. If this were the case, this issue would lead to a thin-layer equivalence, but a large thickness difference is observed between both 1D models (red and blue crosses in Fig. 6.12).

Based on this analysis, the 1D inversion of the 2D synthetic responses might underestimate the thickness of the conductive layer due to the presence of strong 2D effects. Assuming that this phenomenon might be present in the TEM field data, it is suggested to perform a modeling study on which the top depth of the base layer is evaluated to better assess the inversion results of the Paranal TEM data set.

6.5.4 Modeling the top depth of the base layer

In Fig. 6.13, the derived 1D models using the Marquardt inversion technique for the profile B3 (Fig. 5.6) are shown. The variation in basement depth, derived from the equivalence models, is illustrated as an error bar for each model. Based on the 1D inversion results of the field data, a 2D model is generated by interpolating the 1D models of each station (shown in Fig. 6.13b). As stated above, the derived 1D models along profile B3 show a pant-leg-shape conductivity increase within the base layer towards both sides of the conductive anomaly, which might indicate a 2D effect, as was described and discussed before.

The χ_d section shows a deteriorated fit that is partly correlated with the subsurface structure of the clay pan. A highly deteriorated fit is observed at early times, towards the edges of the clay pan, and at late times, in the central part. The global error-weighted fit of the 2D and the 1D synthetic response is about $\chi = 2.0$. A reason for the strong 2D effects observed at the edges might be the large slope angle of the basement towards the edges of the clay pan. As a consequence, the depth of the basement might be slightly underestimated using the 1D inversion approach due to the 2D effects of both clay pan slope angles. To simply test this hypothesis, a new slightly altered 2D model is generated by applying the following changes: (1) a homogeneous resistivity of approximately 200 Ω m was used for the third layer and (2) the depth of the basement was increased by around ∼20 m in the central part (Fig. 6.13d).

The data misfits for each sounding along the profile are shown in Fig. 6.13e. These misfit values are obtained by (1) the original 1D inversions in Fig. 6.13a and (2) the 2D model derived from the 1D models in Fig. 6.13b, and (3) the modified 2D model in Fig. 6.13d. The global data misfit for the 1D models is almost optimal with $\chi = 1.2$. However, a slightly deteriorated fit is observed in the center of the clay pan. The global data misfit for the 2D model is much higher ($\chi = 2.5$) than the other models, for which several stations at the edges are not well fit. When changing the 2D model, the global data misfit improves to $\chi = 1.7$, which is not optimal but is significantly better than the initial 2D model.

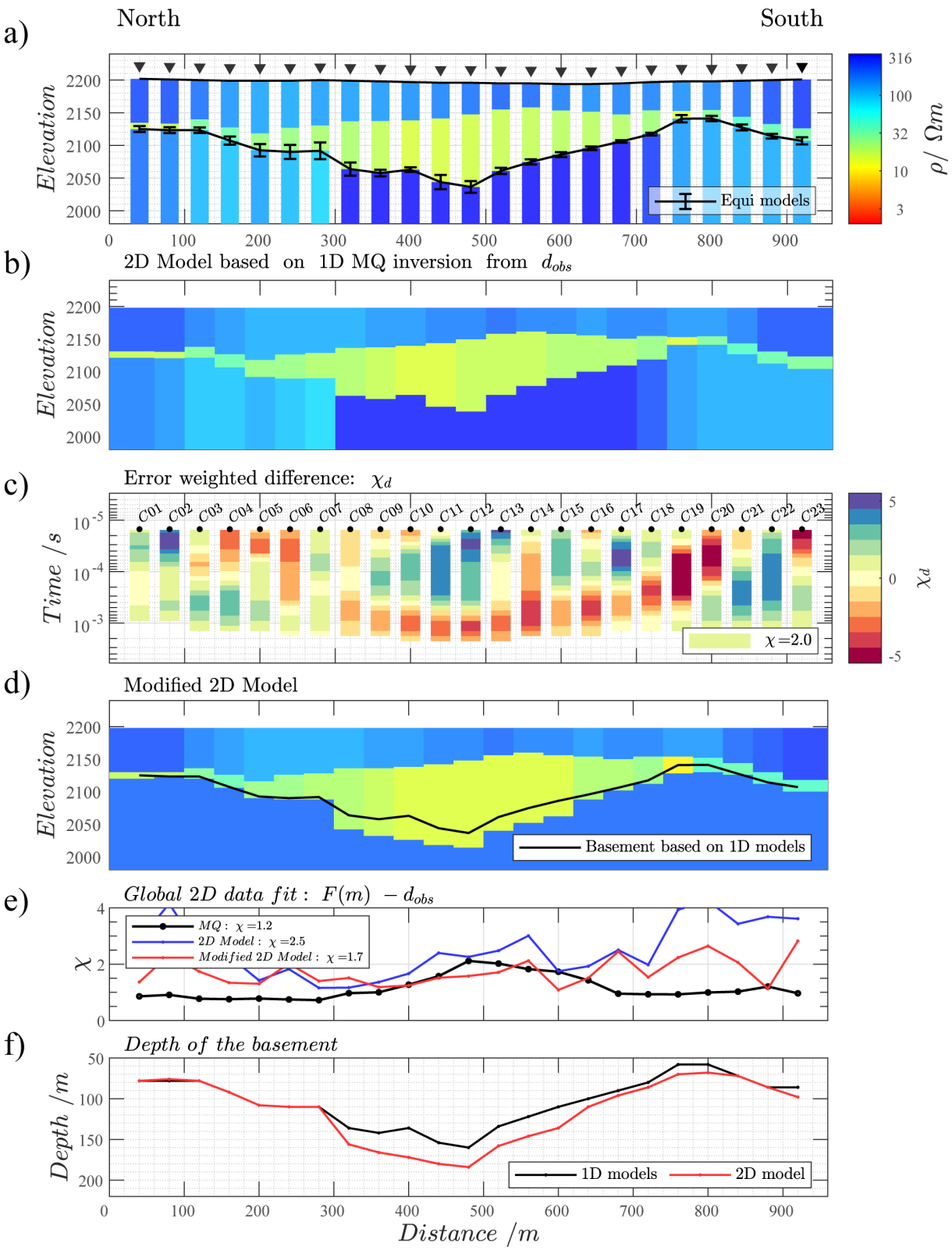

Figure 6.13: (a) Stitched 1D inversion results using Marquardt (MQ) approach for profile B3. The depth range for the basement obtained by the equivalent models is displayed as error bars. The stations are illustrated by inverted black triangles. (b) The 2D model generated by interpolating the resulting profile B3 using the MQ technique. (c) 2D-1D Model fitting: error weighted relative differences χ_d calculated from the 2D model response $F(m)_{2D}$ and the 1D model response $F(m)_{1D}$ (see equation 6.5). (d) Modified 2D model with a thicker conductive layer in the center and the same basement resistivity (∼250 Ωm). The basement depth obtained by the 1D MQ models is displayed as a black line. (e) Global 2D data fit of the derived 1D models (black line), the 2D model (blue line), and the modified 2D model (red line). (f) Basement depth of the 1D MQ models (black line) and the modified 2D model (red line). Published in Blanco-Arrué et al. (2022).

The variation in the basement depth, determined by the 1D models and the adjusted 2D model, is approximately 24 m at the center (Fig. 6.13f), suggesting a more substantial conductive layer. Ultimately, while the TEM 1D models successfully depict the clay pan's structure, they potentially slightly undervalue the basement's depth.

6.6 Summary of the 2D forward modeling study

The SLDMem3t algorithm was used to perform a 2D forward modeling study, following the approaches given by (Hördt et al., 1992; Hördt and Scholl, 2004; Martin, 2009; Yogeshwar, 2014). For this purpose, an initial grid calculation analysis was carried out to check the accuracy of subsurface models with different resistivity contrasts. In this regard, a suitable grid discretization that satisfies the field data behavior for the PAG and Paranal clay pans was calculated. The 2D effects were then evaluated using different 2D model scenarios, which represent the features derived from the 1D inversion results shown in Chapter 5.

Firstly, the simplified 2D model scenarios were created to assess the effects of the slope angle and the bottom width of the clay pan, separately. Based on the modeling, stronger distortion effects are expected in the TEM data for higher slope angles of the clay pan, particularly for the stations right above the slope. In addition, analysis of the bottom width of the clay pan indicates that stronger data distortion would be observed for shorter distances between the sides of the clay pan, due to the double effect of the slopes. These results confirm that possible 2D effects might be present in the TEM field data. Secondly, 2D forward modeling was performed to evaluate the presence of a deep conductor observed in the PAG clay pan. Here, two scenarios were investigated, having profile A6 from the 1D inversion results as a reference. A 2D model with and another without the deep conductor *C2* were evaluated. The outcomes of the modeling clearly show 2D effects in both scenarios, particularly near the location of the clay pan's slope, while the overall form of the clay pan is accurately depicted. Furthermore, in both cases, a deep conductor *C2* is derived and placed below the depth of the investigation, indicating limited resolution and thus reduced dependability.

The synthetic inversion obtained by the different scenarios however exhibits different resistivities for the deep conductor *C2*, indicating that the TEM field data is not only affected by 2D effects but also by artifacts that mainly affect the late times. Then, the same procedure was used to evaluate the features observed in the Paranal clay pan, for which the profile B3 from the 1D inversion results was used. Two 2D models, with and without the pant-leg-shaped conductors at the resistivity base layer, were also assessed for possible 2D effects. These results confirm the presence of strong 2D effects, even higher than what was observed in the 2D forward modeling for the PAG clay pan. Besides, the synthetic inversion results exhibit a thinner layer for the clay pan, which suggests that a detailed evaluation of the top depth of the base layer must be performed. Consequently, the geometry of profile B3 of the Paranal clay pan was modeled for different top depths of the base layer, whose resistivity was fixed to better assess the 2D effects of the clay pan. Overall, a 2D model that better fits the center of the clay pan than the 1D inversion results was found, even though the stations at the edges of the clay pan were challenging to fit better than the 1D inversion results. Therefore, the 2D forward modeling for the presented Paranal case exhibits that the depth of the basement of profile B3 is slightly

underestimated and possibly deeper within a range of 24 m. The 2D forward modeling study was fundamental to better understanding the anomalies observed in the 1D inversion results. Various models were explored to address the anomalies noted, largely verifying the occurrence of 2D effects in the TEM datasets from both PAG and Paranal. Following these studies, it is strongly recommended to apply 2D or possibly 3D inversion to the TEM data to achieve a more precise representation of the clay pans' geometry, as outlined and illustrated in the subsequent chapter.

CHAPTER 7

3D Inversion of the TEM data

The 2D forward modeling study presented in Chapter 6 revealed the presence of distortion effects in the clay pans PAG and Paranal. Generally, a 1D interpretation may still be used to gain preliminary knowledge about the subsurface, as it provides valuable prior information for multidimensional inversion and modeling approaches. Then, the application of 2D and 3D modeling and inversion algorithms can be used to deal with possible multidimensional effects due to highly heterogeneous subsurface structures. However, developing new 3D time-domain algorithms is still an ongoing research area and requires substantial computational resources. Currently, several forward modeling schemes are suitable for TDEM: the Krylov subspace (Druskin and Knizhnerman, 1988, 1994), as briefly mentioned in Chapter 6 and as has been utilized by different authors (e.g., Börner, 2010; Rochlitz et al., 2021). In addition, the Fourier transform approach can be used to convert frequency into time-domain data (Everett, 2012; Heagy et al., 2017). Furthermore, explicit and implicit time-stepping methods are suitable techniques for the mentioned approaches (Um et al., 2010; Liu et al., 2017). Some open source codes exist with approaches for 3D modeling in the time domain. One such code is the Python toolbox CustEM (Rochlitz et al., 2019; Seidel, 2019; Rochlitz et al., 2021), which performs a customizable 3D finite-element modeling of CSEM, TEM, and natural-source electromagnetic data. Furthermore, some improvements in the efficiency of TEM data modeling have been made by Gao et al. (2021), where a multiresolution grid is used to perform a 3D time-domain electromagnetic modeling.

Several comprehensive reviews have published multidimensional time-domain inversion schemes (Haber et al., 2007; Commer and Newman, 2008; Oldenburg et al., 2013). The approaches are mainly divided by the explicit and implicit calculation of the Jacobian matrix. A recent publication by Xiao et al. (2022) used the explicit approach, with an octree-based finite element method, to reduce the mesh cell and optimize the model mesh for 2.5D and 3D modeling and inversion, in a large-scale TEM exploration study. In contrast, the implicit approach can guarantee the efficiency of the Jacobian matrix

calculation, where system matrix decomposition can be done only once and is applied at each time step point. The latter approach is used throughout this chapter, where its performance and accuracy are analyzed.

Consequently, 2D and 3D inversions of the whole TEM data set seek to obtain an independent and most realistic model of the clay pan. This chapter aims to perform a 3D inversion of the Paranal TEM data set (Fig. 4.4b). Here, a recently developed software package 3DTEMInv is applied to multidimensional loop source time-domain electromagnetic data to derive a more accurate geometry of the clay pan (Liu et al., 2024). The 3D loop source inversion algorithm is parallelized using an iterative Gauss-Newton (GN) inversion approach with a finite-volume (FV) forward operator written in the JULIA programming language (Liu et al., 2019b; Peng et al., 2016; Liu et al., 2017; Peng et al., 2021). For the 3D forward modeling, this algorithm uses the implicit time-stepping method, coupled with a Multifrontal Massively Parallel sparse direct Solver (MUMPS) (Amestoy et al., 2006), in order to ensure an accurate solution and stability. The utilized workstations and PCs are linked to the University of Cologne computing center, where the 2D/3D modeling and inversion of the TEM data have been executed in the CHEOPS high-performance computing cluster (Achter et al., 2013).

The 3D forward problem formulation and the inversion schemes are described concisely in the presented chapter. Then, the 3D forward algorithm is validated using 1D semi-analytical (EMU+) and 2D synthetic solutions (SLDMem3t). Here, the synthetic responses are compared and analyzed in terms of error-weighted and unweighted relative differences. In addition, numerical accuracy and computation efficiency are shown and discussed. Afterwards, the 3D inversion scheme is verified by considering 2D and 3D synthetic structures of a basic conductive clay pan scenario. The synthetic responses are inverted considering different smoothing parameters in order to find the proper values to reproduce a 2D structure well. These results are evaluated and analyzed to obtain the most suitable settings for further 3D inversion of TEM field data. Then, the 3D inversion algorithm is applied using realistic conditions, such as the TEM data of the Paranal clay pan. In the first place, the 3D inversion of profile B1 is shown, and the obtained model and the calculated transient responses are analyzed. Subsequently, the 3D inversion of the main profiles B1-B3-B5, including 69 soundings with the Tx-80 reference points, is illustrated. Ultimately, the complete 3D grid TEM field data set for the Paranal clay pan is used to perform a 3D inversion. Furthermore, the normalized coverage and the calculated responses are examined. Then this analysis and the results are contrasted with the 1D inversion results detailed in Chapter 5.

7.1 Theory of the 3D TEM inversion algorithm

The 3D modeling and inversion algorithm used throughout this chapter is based on the finite-volume time-domain method (Liu et al., 2020). The subsequent sections provide a concise overview of the forward modeling and inversion processes. Detailed theoretical insights into TEM forward and inversion modeling are discussed in extensive articles by Haber et al. (2007), Han et al. (2018), and Liu et al. (2024). For more in-depth information, consult the studies by Um et al. (2010), Oldenburg et al. (2013), and Peng et al. (2016).

7.1.1 Forward modeling description

The time-dependent Maxwell equations 2.4 and 2.5 are formulated as diffusion equations. For a given spatial domain Ω and time interval $[0,\ t_f]$, the expressions take the following form:

$$\nabla \times \boldsymbol{E} + \frac{\partial \boldsymbol{B}}{\partial t} = 0, \tag{7.1}$$

$$\nabla \times \mu^{-1}\boldsymbol{B} - \sigma \boldsymbol{E} - \epsilon \frac{\partial \boldsymbol{E}}{\partial t} = \boldsymbol{j}_r(t), \tag{7.2}$$

where $\boldsymbol{E}$ and $\boldsymbol{B}$ are electric and magnetic fields, μ is magnetic permeability, ϵ is permittivity, σ is conductivity (μ, ϵ assumed to be constant values of μ_0 and ϵ_0 in vacuum) and $\boldsymbol{j}_r$ is the current density excited by a loop source. The backward Euler method is used to solve the coupled equations numerically, leading to discrete Maxwell equations 7.1 and 7.2 in time, as follows:

$$\nabla \times \boldsymbol{E}^{i+1} = -\frac{\boldsymbol{B}^{i+1} - \boldsymbol{B}^{i}}{\delta t}, \tag{7.3}$$

$$\nabla \times \mu^{-1}\boldsymbol{B}^{i+1} = \sigma \boldsymbol{E}^{i+1} + \epsilon \frac{\boldsymbol{E}^{i+1} - \boldsymbol{E}^{i}}{\delta t} + \boldsymbol{j}_r^{i+1}, \tag{7.4}$$

where the superscripts i and $i+1$ denote the fields at consecutive time points with a discrete step size δt. According to Liu et al. (2020), the FV method is adopted to discretize equations 7.3 and 7.4 in the spatial domain using the so-called Yee staggered grid (Yee, 1966). Here, the electric and magnetic fields are discretized on edges and faces, respectively (see Fig. 6.1a). The discretized form of the system of equations takes the following form:

$$\mathbf{Curl}\boldsymbol{E}^{i+1} = -\alpha(\boldsymbol{B}^{i+1} - \boldsymbol{B}^{i}), \tag{7.5}$$

$$\mathbf{Curl}^T \boldsymbol{M}_{f\mu}\boldsymbol{B}^{i+1} = \boldsymbol{M}_{e\sigma}\boldsymbol{E}^{i+1} + \alpha \boldsymbol{M}_{e\epsilon}(\boldsymbol{E}^{i+1} - \boldsymbol{E}^{i}) + \boldsymbol{j}_r^{i+1}, \tag{7.6}$$

where $\alpha = 1/\delta t$, $\boldsymbol{E}^i$ and $\boldsymbol{B}^i$ represent the discretized electric and magnetic field sampling points at the edge and the center of the face, respectively, across all grid cells. The **Curl** denotes the discrete operator on the staggered grid for cell edge variables (e.g., $\boldsymbol{E}^i$) $\boldsymbol{j}_r^i$ is defined as the discretized current density vector. $\boldsymbol{M}_{f\mu}$, $\boldsymbol{M}_{e\epsilon}$ and $\boldsymbol{M}_{e\sigma}$ are the averaging matrices for permeability, permittivity, and conductivity, respectively.

A second-order linear partial differential equation system for the electric field $\boldsymbol{E}^{i+1}$ can be obtained by replacing $\boldsymbol{B}^{i+1}$ from Equation 7.5 with Equation 7.6, in the form:

$$\begin{aligned}\mathbf{Curl}^T \boldsymbol{M}_{f\mu}\mathbf{Curl}\boldsymbol{E}^{i+1} + \alpha_{i+1}\boldsymbol{M}_{e\sigma}\boldsymbol{E}^{i+1} + \alpha_{i+1}^2 \boldsymbol{M}_{e\epsilon}\boldsymbol{E}^{i+1} = \\ \alpha_{i+1}(\mathbf{Curl}^T \boldsymbol{M}_{f\mu}\boldsymbol{B}^{i} + \alpha_{i+1}\boldsymbol{M}_{e\epsilon}\boldsymbol{E}^{i} - \boldsymbol{j}_r^{i+1}),\end{aligned} \tag{7.7}$$

The electric field $\boldsymbol{E}^{i+1}$ can be calculated from $\boldsymbol{B}^i$, $\boldsymbol{E}^i$ and $\boldsymbol{j}_r^{i+1}$, by solving equation 7.7. From here, rearranging equation 7.5 leads to the calculation of the magnetic field $\boldsymbol{B}^{i+1}$ following the expression

$$\boldsymbol{B}^{i+1} = \boldsymbol{B}^i - \frac{1}{\alpha}\mathbf{Curl}\mathbf{E}^{i+1}. \tag{7.8}$$

Initial conditions

Equation 7.7 must be solved for an initial field, and in this case, the implicit backward Euler method requires a modification to account for current varying over time. In particular, in applications such as LOTEM or TEM, the source signal can be created by the so-called step-on and step-off current cases. For the TEM method, all the initial fields are zero for the current step-on, and then, for the step-off signal, the magnetic fields need to be calculated within the computational domain that is excited by a constant current loop. This requires that the solution be obtained from equations 7.5 and 7.6, which can be achieved by imposing the electric field $\boldsymbol{E}^{i+1} = 0$ and $\alpha = 0$. In addition, to guarantee the divergence-free nature of the magnetic field in numerical computation, a divergence correction is included for the initial field $\boldsymbol{B}^0$ ($\nabla \cdot \boldsymbol{B} = 0$) (Oldenburg et al., 2013; Liu et al., 2017). Then, the expression for the initial magnetic field is as follows:

$$\mathbf{Curl}\boldsymbol{M}_{e\sigma}^{-1}\mathbf{Curl}^T\boldsymbol{M}_{f\mu}\boldsymbol{B}^0 + \mathbf{Grad}\boldsymbol{M}_{e\sigma}^{-1}\mathbf{Grad}^T\boldsymbol{B}^0 = \mathbf{Curl}\boldsymbol{M}_{e\sigma}^{-1}\boldsymbol{j}_r, \tag{7.9}$$

where **Grad** denotes the gradient for the cell node. It should be noted that an analytic alternative method exists to compute the initial magnetic field throughout the Biot-Savart law (Telford et al., 1990), in which a constant permeability must be assumed for the computational domain (Liu et al., 2017). Both analytic and numerical approaches are implemented in the 3D inversion and modeling algorithms, but only the numerical approach is used in the presented chapter.

Once the initial field at $t = 0$ has been determined using Equation 7.9, the diffusive TEM response can be obtained by solving the system of equations with a recursive method (see Equation 7.7), then the equation needs to be rearranged and forms a large sparse linear system in the form:

$$\boldsymbol{A}(\alpha_i)\boldsymbol{E}^{i+1} + \boldsymbol{D}(\alpha_i)\boldsymbol{E}^i = \boldsymbol{C}(\alpha_i)\boldsymbol{B}^i, \tag{7.10}$$

where $\boldsymbol{A}(\alpha_i) = \mathbf{Curl}^T\boldsymbol{M}_{f\mu}\mathbf{Curl} + \alpha_i\boldsymbol{M}_{e\sigma}$, $\boldsymbol{D}(\alpha_i) = -\alpha_i^2\boldsymbol{M}_{e\epsilon}$, $\boldsymbol{C}(\alpha_i) = \alpha_i\mathbf{Curl}^T\boldsymbol{M}_{f\mu}$. This leads to having a system of equations for all time points and can be defined as follows:

$$\begin{pmatrix} \boldsymbol{A}^1(\alpha_1) & & & & & & \\ \boldsymbol{D}^1(\alpha_1) & \boldsymbol{A}^2(\alpha_2) & & & & & \\ & \ddots & \ddots & & & & \\ & & \boldsymbol{D}^i(\alpha_i) & \boldsymbol{A}^i(\alpha_i) & & & \\ & & & \ddots & \ddots & & \\ & & & & \boldsymbol{D}^n(\alpha_n) & \boldsymbol{A}^n(\alpha_n) \end{pmatrix} \begin{pmatrix} \boldsymbol{E}^1 \\ \boldsymbol{E}^2 \\ \vdots \\ \boldsymbol{E}^i \\ \vdots \\ \boldsymbol{E}^n \end{pmatrix} = \begin{pmatrix} \boldsymbol{C}(\alpha_1)\boldsymbol{B}^0 \\ \boldsymbol{C}(\alpha_2)\boldsymbol{B}^1 \\ \vdots \\ \boldsymbol{C}(\alpha_i)\boldsymbol{B}^{i-1} \\ \vdots \\ \boldsymbol{C}(\alpha_n)\boldsymbol{B}^{n-1} \end{pmatrix} \tag{7.11}$$

Here, the system of equations in the form $\boldsymbol{A}^i\boldsymbol{E}^i = \boldsymbol{S}^i$ needs to be solved at each time-stepping point, where $\boldsymbol{A}$ denotes the matrix system, $\boldsymbol{S}$ corresponds to the right-hand side of Equation 7.11. The 3D modeling algorithm used the adaptive time step doubling method (Um et al., 2010) to ensure accuracy and efficiency, and the Multifrontal Massively Parallel sparse direct Solver (MUMPS) is utilized to solve Equation 7.11 recursively (Amestoy et al., 2006). Comprehensive investigations on the performance of the MUMPS solver can be found in (Streich, 2009; Oldenburg et al., 2013). For multisource problems, as presented in this thesis, the solutions for several source locations can be derived using the same factorization. This is due to the invariance of the matrix system $\boldsymbol{A}$ at every specific time. Normally, minimal additional computational costs are incurred (Peng et al., 2016; Liu et al., 2020). The total modeling time will depend on the number of time points as well as the constant step size δt. Once electric fields have been determined, the diffusive TEM responses can be calculated by applying the **Curl** operator using the expression $\frac{d\boldsymbol{B}^i}{dt} = -\mathbf{Curl}\boldsymbol{E}^i$.

7.1.2 3D TEM inverse problem

The 3D inversion algorithm uses a Gauss-Newton (GN) scheme coupled with a preconditioned conjugate gradient method (PCG) to avoid explicit Jacobian calculation in each iteration (Peng et al., 2016). In addition, the Tikhonov regularization approach is used to stabilize the inversion process (Tikhonov and Arsenin, 1977; Constable et al., 1987), as in the Occam inversion approach described in Section 3.3. Therefore, the same expression given in Equation 3.27 is used to minimize the objective function. Then, the data misfit term Φ_d and the model regularization term Φ_m are defined as follows:

$$\Phi_d(\boldsymbol{m}) = \frac{1}{2}\left[\boldsymbol{F}(\boldsymbol{m}) - \boldsymbol{d}_{obs}\right]^T \boldsymbol{C}_d^{-1}\left[\boldsymbol{F}(\boldsymbol{m}) - \boldsymbol{d}_{obs}\right], \tag{7.12}$$

$$\Phi_m(\boldsymbol{m}) = \frac{1}{2}\left(\boldsymbol{m} - \boldsymbol{m}_{ref}\right)^T \boldsymbol{C}_m^{-1}\left(\boldsymbol{m} - \boldsymbol{m}_{ref}\right), \tag{7.13}$$

where $\boldsymbol{F}(\boldsymbol{m})$ indicates the forward modeling operator, $\boldsymbol{d}_{obs}$ is the observed data, $\boldsymbol{C}_d^{-1}$ and $\boldsymbol{C}_m^{-1}$ are the data weighting matrix and model roughness matrix, respectively. $\boldsymbol{m}$ is the vector of the conductivity model expressed as $m = \ln(\sigma)$ to ensure positive conductivity, and $\boldsymbol{m}_{ref}$ is a reference model containing prior knowledge about the model.

The data misfit Φ_d, expressed in Equation 7.12, measures the difference between the calculated and observed data, whereas Φ_m in Equation 7.13, refers to the model regularization term that stabilizes the ill-posed inverse problem. For a 3D inverse problem, the roughness matrix $\boldsymbol{C}_m^{-1}$ has the following form (Lelièvre and Oldenburg, 2009):

$$\boldsymbol{C}_m^{-1} = \boldsymbol{W}_m^T \boldsymbol{W}_m = \alpha_x \boldsymbol{W}_x^T \boldsymbol{W}_x + \alpha_y \boldsymbol{W}_y^T \boldsymbol{W}_y + \alpha_z \boldsymbol{W}_z^T \boldsymbol{W}_z, \tag{7.14}$$

where α_x, α_y, α_z are constants that control the roughness weighting of the model at different orientations, and $\boldsymbol{W}_x$, $\boldsymbol{W}_y$, $\boldsymbol{W}_z$ are first-order finite difference matrices applied to x, y and z directions.

For 3D nonlinear geophysical electromagnetic induction problems, gradient-based optimization approaches are widely used (Meju, 1994; Rodi and Mackie, 2001; Martin, 2009). An advantage of using the GN method to minimize the objective function is the computational efficiency and fast convergence to a local minimum (Peng et al., 2021). By differentiating the objective function with respect to the model and setting it to zero, a system of normal equations is obtained at each iteration:

$$\hat{\boldsymbol{H}}(\boldsymbol{m})\delta\boldsymbol{m} = -\boldsymbol{g}(\boldsymbol{m}), \tag{7.15}$$

where $\delta\boldsymbol{m}$ is the model perturbation, $\boldsymbol{g}(\boldsymbol{m})$ and $\hat{\boldsymbol{H}}(\boldsymbol{m})$ are the gradient and approximate Hessian of the objective function, respectively, which correspond to:

$$\boldsymbol{g}(\boldsymbol{m}) = \boldsymbol{J}(\boldsymbol{m})^T \boldsymbol{C}_d^{-1}(\boldsymbol{F}(\boldsymbol{m}) - \boldsymbol{d}_{obs}) + \beta \boldsymbol{C}_m^{-1}(\boldsymbol{m} - \boldsymbol{m}_{ref}), \tag{7.16}$$

$$\hat{\boldsymbol{H}}(\boldsymbol{m}) \approx \boldsymbol{J}(\boldsymbol{m})^T \boldsymbol{C}_d^{-1} \boldsymbol{J}(\boldsymbol{m}) + \beta \boldsymbol{C}_m^{-1}, \tag{7.17}$$

here $\boldsymbol{J}(\boldsymbol{m})$ is the sensitivity matrix of the TEM data with respect to the model vector $\boldsymbol{m}$.

7.1.3 Model Update

According to Peng et al. (2016), Equation 7.15 can be solved without the explicit calculation of the Jacobian. Consequently, at each GN iteration, the system of normal equations 7.17 is solved using the preconditioned conjugate gradient (PCG) method to obtain the perturbation of the model $\delta\boldsymbol{m}$. Therefore, it requires the product between the Jacobian matrix and its transpose to be computed for every PCG iteration, thus avoiding explicit computation and storage of the sensitivity matrix. In this case, explicit calculation of the Jacobian matrix of electric fields $\boldsymbol{J}_E$ for all time-stepping points is not needed, but it can be calculated by the first derivative of equations 7.5 and 7.7 and using a backward substitution approach. Then, the Jacobian matrix of the collected fields at receiver locations can be obtained using an interpolation procedure (personal communication Dr. Y. Liu and Dr. R. Peng). However, the methods for explicitly computing the Jacobian matrix fall outside the scope of this thesis and will not be elaborated upon.

As mentioned in 3.1.1, a model perturbation $\Delta\boldsymbol{m}$ is obtained at each GN iteration. Here, a line search procedure is used to generate the updated model defined as:

$$\boldsymbol{m}_{k+1} = \boldsymbol{m}_k + \alpha\delta\boldsymbol{m}_k, \tag{7.18}$$

where the step length α is used to control the magnitude of the model update. Here, an inexact line search strategy is employed to determine a reasonable step length α for the model update by satisfying the sufficient decrease condition. It should be pointed out that the standard line search can also be used, but it is not recommended for 3D inversion problems due to the expensive computational costs (Peng et al., 2016). Here, the 3D algorithm uses the weak Wolfe condition (Nocedal and Wright, 1999) stated as follows:

$$\varphi(\boldsymbol{m}_k + \alpha\delta\boldsymbol{m}_k) \leq \varphi(\boldsymbol{m}_k) + c\alpha\Delta\varphi(\boldsymbol{m}_k)^T\delta\boldsymbol{m}_k, \tag{7.19}$$

where c is a very small constant, usually defined as a value of 10^{-4}. Other authors also referred to this method as the Armijo line search method (Martin, 2009).

Once the direct solver MUMPS is used for forward modeling and the matrix system is factorized, the same factorization can be used repeatedly without calculating it again for all the PCG iterations. As a rough estimate, the Jacobian matrix operations or its transpose with vectors are equivalent to one forward calculation, which means that two additional forward solves are required at every PCG iteration Peng et al. (2016). Thus, the use of computational resources and expenses is minimized. More information on the PCG method is available in numerous detailed sources cited in the literature (Nocedal and Wright, 1999; Haber et al., 2007; Oldenburg et al., 2013; Schwarzbach and Haber, 2013).

7.1.4 Regularization parameter

As mentioned in Chapter 3, the regularization parameter β is introduced to solve the nonlinear ill-posed inverse problem. In the case of the Marquardt approach, the damping parameter β constrains the model update $\Delta\mathbf{m}_k$. In addition, for the Occam approach, an optimal β is usually determined by the discrepancy principle between the data mismatch $\Phi_d(\boldsymbol{m})$ and the model regularization term $\Phi_m(\boldsymbol{m})$. However, applying this to the case of a 3D inversion involves additional computational costs. Therefore, the 3D inversion algorithm uses a cooling scheme to determine the regularization parameter β at each GN iteration, which is also referred to as a relaxation scheme (Rodi and Mackie, 2001). Usually, a large regularization parameter is selected in early iterations to stabilize the inversion process. Subsequently, the regularization parameter β gradually decreases to emphasize data fitting more until a desired data misfit is reached.

In order to solve the optimization problem, the 3D inversion algorithm uses the regularization parameter β_N defined as:

$$\beta_N = \frac{\beta_0}{\gamma^N}, \tag{7.20}$$

where β_N is the regularization parameter in each GN iteration, β_0 is the initial regularization parameter, γ is a scalar constant controlling the damping rate of the regularization parameter, usually defined as a value of 2, and N denotes the current GN iteration.

7.1.5 Normalized coverage

According to Yogeshwar (2014), one suitable way to assess the sensitivity and reliability of the inversion results is to calculate the normalized coverage C_j for all the parameters of the M model, which is calculated by summation of each column of the Jacobian matrix:

$$C_j = \frac{1}{C_{max}} \sum_{i=1}^{N} |\boldsymbol{W}_{d,ii} \boldsymbol{J}_{ij}|, \qquad j = 1, ..., M, \tag{7.21}$$

where the error weighting matrix $\boldsymbol{W}_d = \boldsymbol{C}_d^{-1}$ is used to scale the Jacobian matrix by the data error.

The coverage C_j is an essential procedure for analyzing the resolution of the model parameters of an inverse model. Here, $\boldsymbol{C}$ is normalized by its maximum C_{max} and to each cell to eliminate its influence on the Jacobian matrix and better visualize the relative effect of the model parameters. Typically, the larger the C_j value of a cell, the better resolution. Based on Martin (2009), in order to distinguish between well- and poorly resolved model parameters, a coverage threshold of 10^{-2} is suggested for a central loop configuration. Then, smaller values correspond to nonresolved cells. Note that the coverage threshold might vary if another type of loop configuration is used.

7.2 Validation of the forward calculation

In this section, the accuracy and performance of the 3D algorithm were evaluated by comparing 1D semi-analytical and 2D synthetic responses. Within the modeling stage, two essential steps must be considered. Firstly, a model mesh must be defined to ensure reasonable accuracy of numerical solutions. The second step is to select suitable time-stepping parameters that can derive precise transients with minimum computational effort. Following the same settings as in Chapter 6, a 40×40 m^2 transmitter loop size was assumed with a receiver position fixed to the center (central loop configuration). In addition, the vertical component $\partial_t B_z$ is selected for the forward modeling response as measured for the field data. To evaluate the performance of the 3D modeling algorithm, the error-weighted relative differences χ_d and the relative difference (unweighted) δ_{rd} were calculated between the synthetic responses 1D / 2D (Emu + / SLDMem3t) and 3D (3D modeling algorithm) and are described and analyzed in the following sections. All tasks were run on the High-Performance Computing CHEOPS of the RRZK Cologne (Achter et al., 2013), using a Nehalem EX processor with 32 cores and 500 GB of RAM.

7.2.1 Model mesh design

The FV is discretized in three dimensions with $N_x \times N_y \times N_z$ cells and minimum cell sizes of $d_x \times d_y \times d_z$ in meters. In order to reduce possible boundary effects, nine non-uniform cells are attached to the upper-shallow part of the grid, representing the air layer with a resistivity of 10^8 Ωm. Note that selecting the proper grid mesh can significantly reduce computational costs, especially for 3D inversion. In addition, to guarantee an accurate solution and to find a feasible model mesh for their conductivity distribution, three model meshes were generated based on the Paranal survey design shown in Chapter 4. The model meshes **A**, **B**, and **C** were tested and evaluated to find the most suitable parameterization of the model. Here, most soundings have a 40 m distance along the profile. Based on this, the mesh **A** was created using a cell distance of about 20 m between the sources in x-direction and 10 m in z-direction, keeping a grid line between the sources. Then, the mesh **B** was extended in x-direction to keep the cell distance if multiple sources were used in the mentioned direction. In the same manner, one grid line is kept between the sources along the profile. In addition, in the z-direction, the cell distance was reduced to 5 m for the first five grid lines. Additionally, the configuration of mesh **C** expanded to twice the number of grid lines along the x-distance of the profile, maintaining a separation of two grid lines between sources. Cell spacing remained consistent at 40 m in the y-direction across all model meshes. The total cell count was adjusted based on the computational resources at hand. Note that in the presented work, the sources are allocated on each cell edge of the corresponding mesh for reliable responses (personal communication with Dr. Y. Liu).

The details of each model mesh are given in Table 7.1. All model meshes were evaluated using a station in the center (x-y direction) and on the top surface (z direction).

Table 7.1: Computational domain for different mesh designs utilized for the forward calculation. N_i and d_i correspond to the number of cells and cell size, respectively, along $i = x$, y and z directions

Mesh grid	$N_x \times N_y \times N_z$	$d_x \times d_y \times d_z$ / m
A	$38 \times 26 \times 39$	$20 \times 40 \times 10$
B	$62 \times 38 \times 39$	$20 \times 40 \times 5$
C	$110 \times 34 \times 36$	$10 \times 40 \times 5$

An explanatory sketch of a model mesh is shown in Fig. 7.1. The limits in each direction are truncated for a better visualization of the discretized space. The red triangle indicates the location of the receiver and transmitter position. The meshes were discretized in space with a maximum boundary extension of about 2560 m and 6400 m from the origin in the x, y and z directions.

It is suggested that the meshes are discretized densely within the area where the sources are placed. Here, a minimum distance of 20 and 40 m was set in the x and y directions, respectively (Fig. 7.1 b). Furthermore, in a z direction, a minimum distance of 5 m to 30 m depth and a cell distance of 10 m up to 200 m depth were considered to ensure precision in the TEM response (Fig. 7.1c).

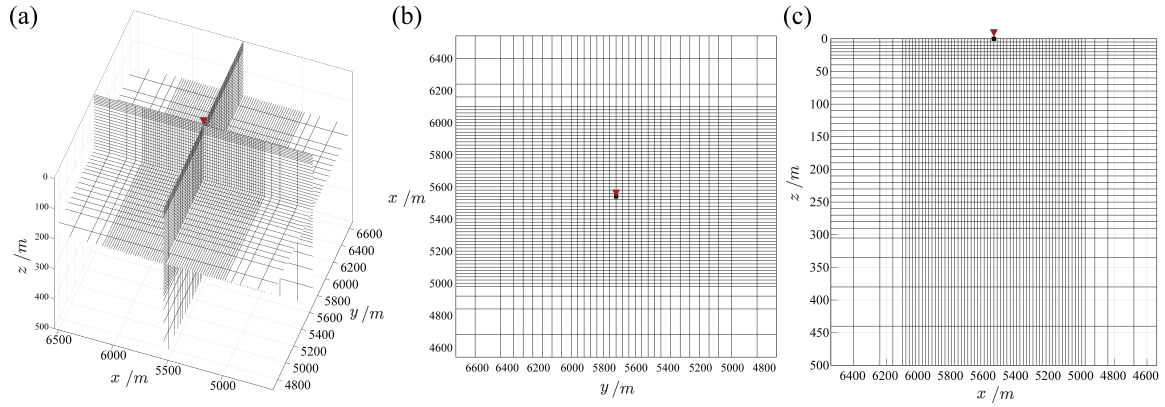

Figure 7.1: Model mesh **B**. The computational domain for a mesh design with $70 \times 37 \times 43$ cells and with a minimum cell size of $20 \times 40 \times 5$ m. The origin of the volume space is at $[x, y, z] = [5540, 5680, 0]$ m. (a) 3D view, (b) $x - y$ view and (c) $z - x$ view. The red triangle indicates the position of one station using a central loop configuration at the center of the model space.

A simple test using one station in a homogeneous halfspace of 200 Ωm reflects the performance of the forward solver. The time-stepping parameters were kept the same for all meshes. Table 7.2 shows the performance in terms of computational time (CT) and resources (RAM) for different meshes considering one station. The results show that the forward calculation uses ∼9 GB of memory resources for the model mesh **A**. Double RAM is needed for the mesh **B** (∼20 GB), and almost triple RAM is taken for the mesh **C** (∼30 GB). In addition, in terms of CT, the mesh grid **A** took ∼2.5 min, the mesh **B** almost ∼9 min, and the mesh **C** more than 13 minutes.

As expected, due to the smaller number of cells, the mesh **A** uses less RAM and takes less run time (see Table 7.2). However, the low run-time cannot ensure an accurate TEM response. To evaluate the accuracy of the TEM solutions, a careful inspection of the transient responses and multidimensional analysis must be carried out. The performance obtained gives us a first approximation of the use of the 3D modeling algorithm. Based on this, it is important to find the proper discretization to use enough computational resources to obtain an accurate TEM response. Since this is a test using one sounding, computational resources may be limited by adding more stations and for further 3D inversion. Note that a different discretization can lead to obtaining other performances.

Table 7.2: Performance of different type of meshes for one station and a single 3D forward calculation.

Mesh grid	$N_x \times N_y \times N_z$	CT / min	RAM / GB
A	$38 \times 26 \times 39$	2.48	8.93
B	$62 \times 38 \times 39$	8.24	20.3
C	$110 \times 34 \times 36$	13.18	29.92

7.2.2 Time iteration settings

As mentioned in the theoretical description, the 3D modeling and inversion algorithm is discretized in the time-domain using the backward Euler method. In this way, selecting the proper time-setting parameters would lead to fewer computational resources but to

TEM responses with good accuracy. In order to set the optimal time iteration points (T_p), four time-stepping settings were tested based on the field data time ranges.

The time iteration points are defined depending on the starting time point t_s, the last time point t_l, the delta time ΔT_0, which is the first time step size, and the number of intervals N_{int} per time-step size. Once the number of intervals is reached throughout the time iteration points, the timestep size ΔT_0 will be multiplied by a factor of R^i. Then, the time iteration point can be recursively calculated using the following expression:

$$\mathbf{Tp}_{j+1} = \mathbf{Tp}_j + R^i \cdot \Delta \mathbf{T}_0, \tag{7.22}$$

where j is the iteration of the vector of time points and i is the interval of time steps.

The chosen time iteration settings are described in Table 7.3. In all tests, the calculated time ranged between $t = 1 \times 10^{-5}$ s and $t = 1 \times 10^{-2}$ s, with a total number of 31 data points.

Table 7.3: Time-stepping parameters for each test. The variables t_s is the start time point, t_l the last time point, $\Delta \mathbf{T}_0$ the delta time, and N_{int} the total number of in intervals.

Test	t_s s	t_l s	$\Delta \mathbf{T}_0$	Ratio	N_{int}	Total step number
T_1	1×10^{-7}	1×10^{-2}	1×10^{-7}	2	50	551
T_2	1×10^{-6}	1×10^{-2}	1×10^{-6}	2	50	401
T_3	5×10^{-6}	6.2×10^{-3}	1×10^{-6}	4	30	151
T_4	5×10^{-7}	1×10^{-2}	5×10^{-7}	3	40	281

The 3D forward modeling was performed for one station located at the center (x-y direction) and top (z-direction) of the model meshes **A**, **B** and **C**. In all tests a three-layer case of 200, 20 and 300 Ωm was considered. In addition, efficiency was evaluated for all the time-stepping parameters mentioned in Table 7.3 (T_1, T_2, T_3 and T_4). Table 7.4 shows the performance for the four tests and all the meshes of the model.

The performance obtained exhibits lower RAM using the time-stepping parameters T_3. Followed by the time-stepping parameters T_4 and T_2 showing an increase in RAM in more than 50% and 75%. Thus, T_1 is the one in which more computational efforts are utilized. The same trend is observed in terms of CT. In this context, it seems that the number of steps plays a key role in the performance of the forward calculation. However, the fewer steps chosen cannot ensure an accurate solution. Similarly, the performance of T_1 consumes higher computational time and resources, possibly limiting the number of stations that could be included in further inversions.

As indicated by Equation 7.22, reducing the gap between the initial time point and the specified delta time enhances accuracy. Similarly, better performance of the modeling response can be obtained by setting a small ratio value with a high number of intervals. However, based on the tests performed, setting up these parameters leads to a higher number of total steps, solving several backward substitutions, and increasing the run time

and computational costs in the modeling process. Therefore, selecting the proper time-stepping settings to keep the accuracy good enough and avoid the use of unnecessary computational resources is essential. The following subsections focus on analyzing the accuracy of the TEM solutions, based on the synthetic tests presented, to select a time-stepping setting that allows the following inversion tasks.

Table 7.4: Performance using different Time-stepping parameters. CT is the computational time and RAM corresponds to the total resources utilized.

Test	**Model Mesh**	CT / min	RAM / GB
T_1	**A**	3.96	15.40
	B	12.95	35.57
	C	20.85	52.60
T_2	**A**	3.02	11.77
	B	9.88	27.00
	C	15.80	39.87
T_3	**A**	1.87	5.84
	B	6.38	13.05
	C	10.34	19.14
T_4	**A**	2.48	8.93
	B	8.19	20.30
	C	13.12	29.92

7.2.3 One-dimensional subsurface

The validation was carried out by comparing the 1D semi-analytical solution with the 3D forward modeling response considering two different 1D subsurface structures: a homogeneous half-space of 200 Ωm and a three-layered model of 200, 20 and 300 Ωm. The 3D algorithm was used for all time-stepping tests and the three model meshes described above (see Tables 7.1 and 7.3). The error model consists of a relative percentage of 3% of the synthetic data and an absolute noise level set to $\eta = 3 \times 10^{-10}\, V/Am^2$, same as it was used for the 2D forward modeling study in Chapter 6. The semi-analytical 1D and 3D responses obtained with the model mesh **B** for both 1D models are shown in Fig. 7.2.

Based on the 3D responses obtained, the synthetic responses T_2 and T_3 exhibit large χ values greater than ∼2.5. In contrast, T_1 and T_4 are accurate with an optimal χ ∼1 (Fig. 7.2a and b). It should be pointed out that 3D responses using the T_3 exhibit a greater mismatch with the 1D solution at early times and a high χ value. Similarly, the relative differences of T_3 and T_2 also exhibit the most deteriorated data greater than 20%, especially at early data points (Fig. 7.2d). Nevertheless, for the T_1 and T_4 responses, slightly deteriorated data is observed at the early-intermediate time points with relative differences of around ∼5% (Fig. 7.2c and d). Moreover, the same trend at early times is observed by the error-weighted relative differences (Fig. 7.2e and f).

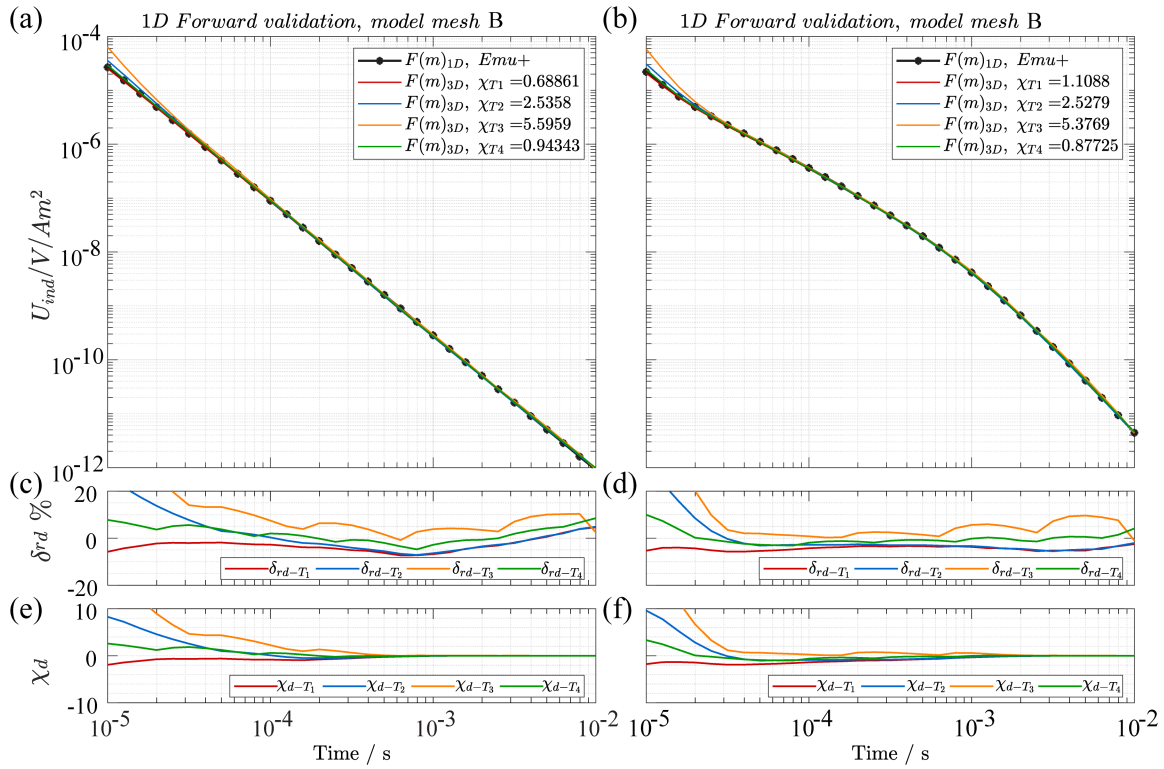

Figure 7.2: Comparison between the 1D semi-analytical and the 3D numerical solutions using the model mesh **B** for (a) a homogeneous half-space of 200 Ωm and (b) a three-layer case model. Different time-stepping setting parameters are tested and are displayed in each case. The corresponding relative differences δ_{rd} in percentage (c, d) and the error-weighted relative difference χ_{rd} (e, f) are displayed below each plot.

For each time-stepping setting, the error-weighted relative differences obtained utilizing the model meshes **A**, **B** and **C** are presented in Table 7.5. Due to the similarity of the transient behavior, the synthetic responses of the model meshes **A** and **C** are included in Appendix A9.

Table 7.5: Validation for a 1D homogeneous halfspace and a three-layer case using different model meshes (**A**, **B** and **C**) and different time-stepping settings (T_i). Error-weighted relative differences (χ) are displayed for each test.

1D model	Homogeneous halfspace				Three-layered subsurface			
Model Mesh	T_1 χ	T_2 χ	T_3 χ	T_4 χ	T_1 χ	T_2 χ	T_3 χ	T_4 χ
A	1.55	1.56	4.57	0.41	2.80	1.93	4.28	1.64
B	0.69	2.54	5.60	0.94	1.11	2.53	5.38	0.88
C	0.74	2.48	5.56	0.89	1.20	2.50	5.34	0.86

In summary, the 3D modeling algorithm was evaluated using different types of model meshes and time-stepping parameters to illustrate the code performance. It should be pointed out that this stage seeks to find suitable inversion parameters to obtain the most accurate 3D responses. The calculated 3D responses were analyzed in terms of the obtained error-weighted relative differences. The better χ, the higher the accuracy. Based

on 3D solutions, both 1D models using T_1 and T_4 exhibit better χ utilizing the meshes **B** and **C**, indicating accurate solutions. In addition, poor χ values are observed using T_3 in all model meshes and in both 1D models. The obtained χ values in the model mesh **B** and **C**, for different time-stepping settings, do not follow a linear trend. The latter can be explained by the different number of cells chosen (N_x, N_y, and N_z) (see Table 7.1). Therefore, the evaluation also shows how sensitive the 3D algorithm is to a slight increase in the number of grid lines. A proper time-stepping setting and a model mesh are found to derive accurate TEM responses at this stage. However, for further modeling studies, a proper evaluation of the effect of different model meshes is suggested, e.g., fixing the number of cells in different directions. Taking into account the computational resources, the T_1 solution takes ∼15 GB more than T_4 due to the total number of steps (see Table 7.3). Hence, from the forward modeling presented for a 1D model, and being conservative in the use of computational resources, the T_4 is chosen for further modeling and inversion studies.

7.2.4 Two-dimensional subsurface

Validation of a 2D subsurface was performed assuming a three-layer case with a simple clay pan shape. A profile of 23 stations was considered that imagined the same setup as PB3 (Fig. 5.6). On the one hand, the finite-difference algorithm in the time domain SLDMem3t (Druskin and Knizhnerman, 1994, 1988) is utilized. As described in Chapter 6, the algorithm uses a material averaging scheme that basically decouples the model from the finite-difference grid. For this case, the same number of grid lines ($n_z = 71$ and $n_{x,y} = 68$) were assumed with grid dimensions typically of the order of 2875 cells. On the other hand, for the 3D modeling algorithm, the discretization of the model needs to be conditioned on the number of sources that will be used, in order to keep the sources on the cell edge.

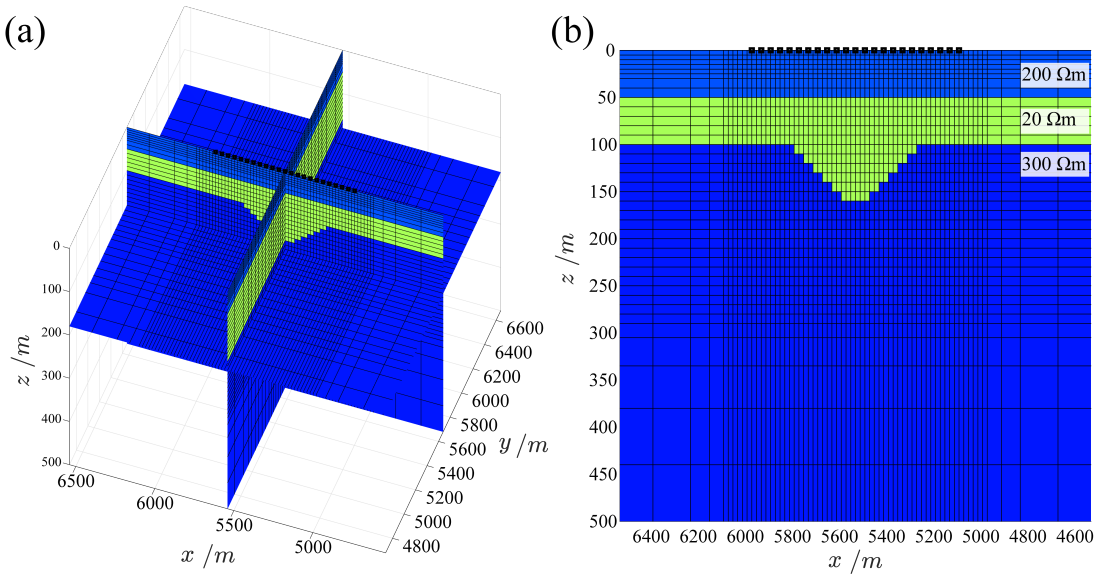

Figure 7.3: Extended version of the model mesh **B** for the 2D forward modeling validation using $N_x \times N_y \times N_z = 70 \times 37 \times 43$ cells. (a) 3D view and (b) 2D cross-section. Stations are displayed in black squares. The model mesh displays a distance of ±1000 m and ±500 m from the origin in the x-y and z-direction.

The model mesh **B** was adapted to multisources along the profile in the y-direction, and the number of grid lines in the z-direction was also increased to ensure an accurate solution at late times. The new model mesh contains a number of 70×37×43 cells and keeps a minimum cell size of about 20×40×5 m (Fig. 7.3). The time-stepping setting used for the forward modeling was T_4 (see Table 7.3). The observation time ranges between $t = [10^{-5} - 10^{-2}]$ s with 31 logarithmically equidistant time data points. The mesh of the medium model imaging a 2D conductivity structure and the location of the 23 sources along the clay pan shape are shown in Fig. 7.3. Note that the conductivity is fixed in the x-direction to ensure a 2D conductivity structure (Fig. 7.3a).

As mentioned in the theory section, the 3D modeling algorithm here utilized enables parallelization across multiple sources to accelerate the whole computation. In this way, a group of transmitters is allocated to one process. In each process, the factorization of Equation 7.11 is performed once and is used for the corresponding group. Note that the large-sparse matrix system is solved using MUMPS with parallel threads. In general, 6 to 8 processes were utilized depending on available computational resources, distributing the 23 stations in groups of 4 or 3 transmitters.

The forward calculation using the SLDMem3t and the 3D modeling algorithm are shown in Fig. 7.4. The 2D cross section of the 3D model displays the 2D subsurface structure and the grid lines along the profile (Fig. 7.4a). A good agreement between 2D and 3D forward responses can be seen at all stations, indicating accurate modeling (Fig. 7.4b and c). Based on the relative differences, slight distortions are visible at early times around $t = 10^{-5}$ s, and also at $t = 10^{-4}$ s with absolute values $\delta_{rd} \sim 10\%$, with a global RMS of 5.95 (Fig. 7.4d). Moreover, minimal distortions of the error-weighted relative differences are shown around $t = 10^{-4}$ s with $\chi_d < 4$ and a global fit of approximately $\chi = 1.81$.

Stations T12 and T22 are selected to compare both forward calculations in terms of transient decay. The results are shown in Fig. 7.5. In the same way, as was described in Fig. 7.4, a similar trend is observed for both synthetic solutions, as they exhibit large values $\delta_{rd} \sim 10\%$ around $t = 5 \times 10^{-5}$ s. In particular, station T12 also exhibits high relative differences at late times compared to T22. Despite this, both stations show an adequate global χ 1.8. Therefore, the 2D forward modeling for a three-layer case shows overall good accuracy and performance.

In general, the comparison between both forward calculations displays accurate responses in the analyzed cases. For completeness, the results using the model mesh **C** are included in Figs. A9.12 and A9.13 (see Appendix A9). The responses obtained exhibit similar RMS and χ values (6.19 and 1.33, respectively), indicating a similar accuracy for the calculated responses. However, it should be noted that the mesh **C** utilized higher computational resources and took double the run time of the results presented in this chapter.

Based on the resulting validation, the inversion settings parameters, such as the model mesh and the time-stepping utilized, exhibit good accuracy and meet the requirement for further verification of the 3D inversion algorithm. Therefore, considering the available computational resources, the same model mesh and time-stepping parameters are selected to verify the 3D inversion algorithm scheme described in the following section.

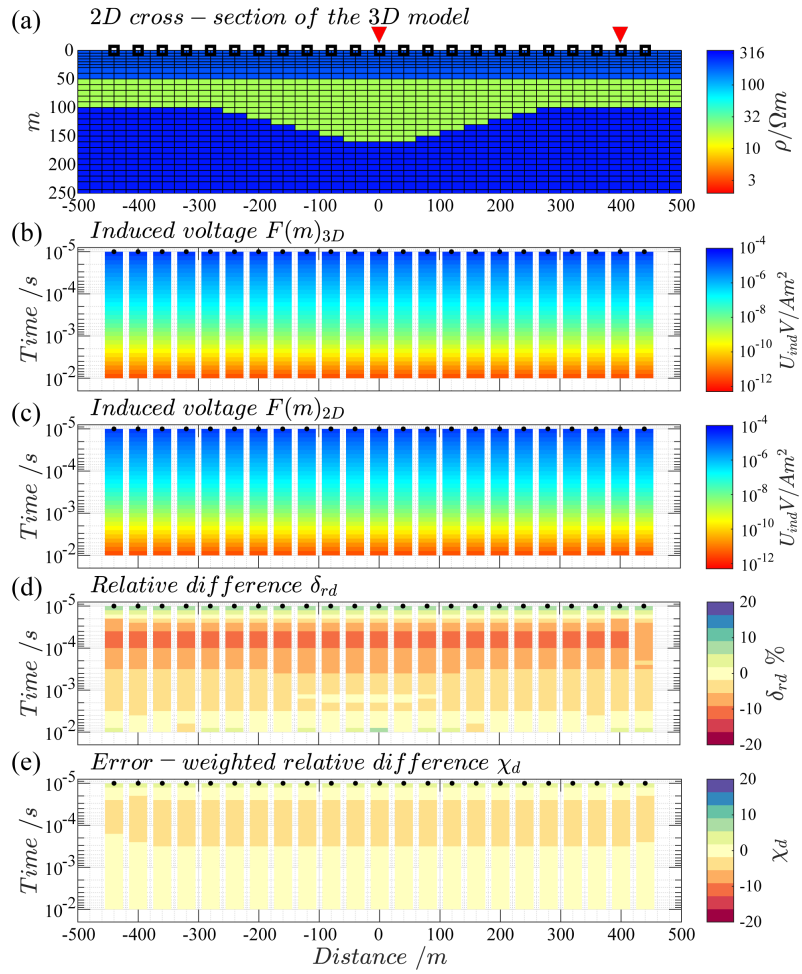

Figure 7.4: Comparison between the 2D and 3D forward responses using the extended model mesh **B**. (a) 2D cross-section of the 3D finite model with $N_x \times N_y \times N_z = 70 \times 37 \times 43$ cells. Red triangles show the position for stations T12 (center) and T22 (edge). (b) Induced voltage U_{ind} of the 3D forward modeling algorithm. (c) Induced voltage U_{ind} of the 2D synthetic response. (d) Relative differences δ_{rd} and (e) Error-weighted relative differences δ_{rd} between $F(m)_{3D}$ and $F(m)_{2D}$ synthetic responses.

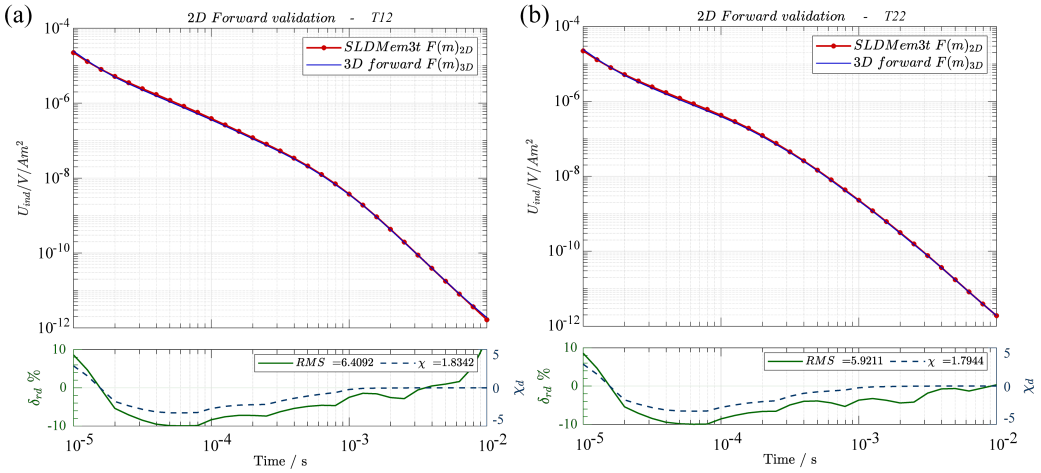

Figure 7.5: Transient comparison between the 2D and 3D forward response for the station (a) T12 at the center and (b) T20 at the edge of the profile. Below each comparison, the relative differences (to the left in green) and the misfit (to the right in blue) between the responses are displayed.

7.3 Verification of the 3D inversion algorithm

As stated in previous sections, the 3D algorithm performs forward and inversion modeling based on a 3D finite volume (Liu et al., 2019a; Peng et al., 2021; Liu et al., 2024). Therefore, a pure 2D parametrization is not possible. Instead, the proper selection of the smoothness weighting parameters (α_x, α_y and α_z in Equation 7.14) enable us to emulate a 2D forward modeling. Thus, this section focuses on analyzing the influence of the smoothness weighting parameters in three directions to mimic a 2D imaging forward and inverse modeling.

Based on the 3D view of the 1D inversion results for the Paranal clay pan (Fig. 5.16), a 2D resistivity structure is observed elongated in a y direction. In this way, the verification of the 3D inversion algorithm consists of performing an inversion of synthetic responses using the same model mesh as before, with 23 sources in the center of the x-direction and a simplified conductivity subsurface structure of the profile PB3 (Fig. 7.3). Taking into account computational resources and the required run time, the time-stepping settings used to obtain the forward and inverted solutions were T_1 and T_4, respectively.

The key aspects evaluated and analyzed throughout this section are the effects of the smoothness in the y-direction (α_y) and the smoothness in the x- and z-directions (α_x, α_z). In order to describe the effect on the parameterization, a fixed error of 3% was considered. In addition, error-weighted relative differences using an absolute noise level of $\eta = 3 \times 10^{-10}\ V/Am^2$ were calculated to compare the down-weighted behavior at late times and its resolution. Finally, the convergence rate for each option is also described. Following the same methodology, the 3D inversion algorithm was evaluated and verified using synthetic responses derived from a 3D subsurface structure, which is briefly described in one of the subsections. It should be noted that this procedure facilitates the selection of proper smoothing parameters for the 3D inversion of the TEM field data shown in the next section.

7.3.1 Effect of the smoothing parameter α_y

The smoothing parameter α_y is set to the following different values: 0.5, 5 and 50. Note that high values of α_y provide a smooth structure in the corresponding direction. In addition, the smoothing weighting parameters were fixed at $\alpha_x = \alpha_z = 0.5$. The inversion results for the mentioned values α_y are shown in Fig. 7.6.

The 2D section of the model mesh, from which the forward solutions were obtained, is displayed in Fig. 7.6a and b. Here, it can be seen that a good value of $\chi \sim 1$ is obtained for all attempts with 5-6 iterations. However, differences in the conductivity structure need to be highlighted. For the same value of α_x-α_y-α_z, the inversion does not resolve the basement, and from the plan view at $z = 170$ m, a 3D structure is clearly seen (Fig. 7.6c, d). Then, for $\alpha_y = 5$, the inversion poorly resolves the resistivity of the basement, and from the plan view, the resolved structure still presents some 3D features (Fig. 7.6e, f). Subsequently, with the setting $\alpha_y = 50$, the conductivity structure and the basement are better resolved. In addition, the plan view at $z = 170$ m exhibits the 2D structure along the y-direction (Fig. 7.6g, h). Complementary to this, higher values of α_y were evaluated, for which more iterations were required to reach an acceptable χ. However,

this implies that the use of a smaller regularization parameter on each iteration results in an overestimated model. These results suggest that the use of $\alpha_y = 50$ is sufficient to smooth the 3D inversion in the y direction.

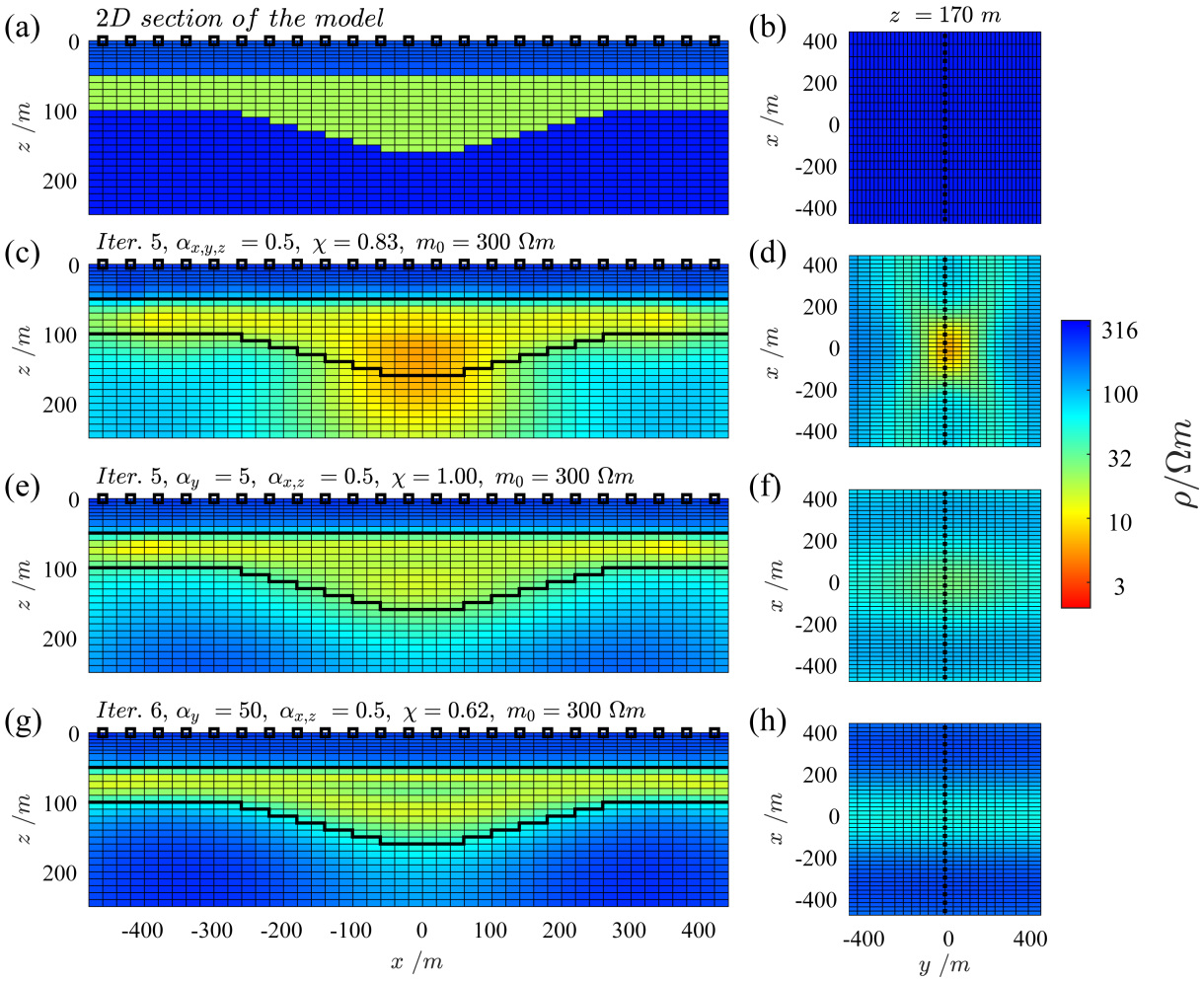

Figure 7.6: Effect of the smoothing parameter in the y-direction (α_y). (a) 2D cross-section and (b) plan view at $z = 170$ m of model mesh used to derive the synthetic responses. In the same order, corresponding inversion results using (c, d) $\alpha_y = 0.5$, (e, f) $\alpha_y = 5$ and (g, h) $\alpha_y = 50$. The shape of the conductor based on the model mesh is highlighted as a black line. Black squares denote the source locations. In all the attempts, the smoothness in x- and z- direction is set up to $\alpha_{x,z} = 0.5$ and a initial model of $m_0 = 300$ Ωm is utilized. The number of iterations used and the χ value are given on each attempt.

In order to have an idea of the resulting transient decay responses, Fig. 7.7 shows the calculated induced voltage of stations T12 (center) and T22 (at the edge) for each α_y value. The comparison between synthetic solutions and calculated responses consistently suggests accurate misfit values in all cases ($\chi < 1$).

For all of the explored α_y, the relative differences in both stations exhibit slight distortions at initial times. In this range, higher distortions are observed for $\alpha_y = 0.5$ and 5 ($\delta_{rd} \sim 8\%$) than for $\alpha_y = 50$, where δ_{rd} is close to 0, indicating a good performance of the calculated synthetic solutions (Fig. 7.7). Furthermore, some distortions are also visible at late times in all the calculated responses, illustrating values around $\delta_{rd} \pm 8\%$. However, it can be seen from the error-weighted relative differences (χ_d) that all these distortions are down-weighted, indicating poor resolution at the data time points $t \sim 10^{-2}$ s. In summary,

based on the calculated transients and the model parametrization, a smoothness weighting parameter of $\alpha_y = 50$ is suggested for an accurate solution.

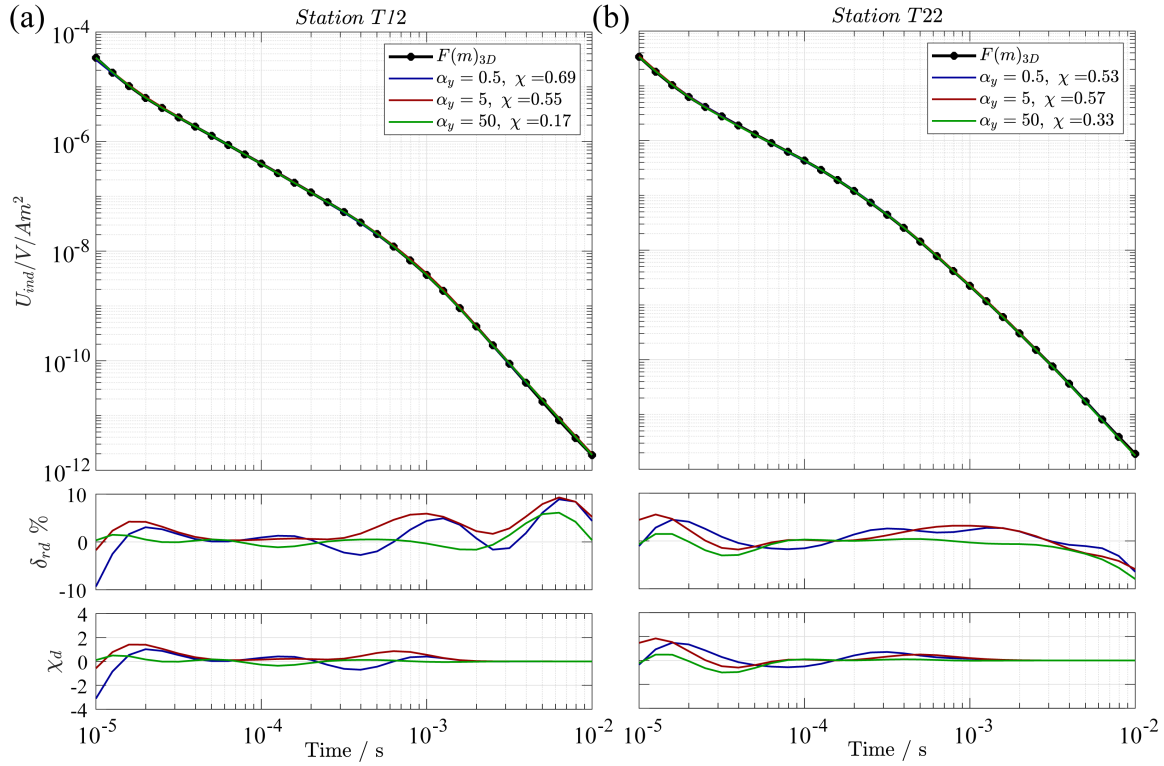

Figure 7.7: Calculated transients of stations (a) T12 and (b) T22 using $\alpha_y = 0.5, 5, 50$. The relative differences δ_{rd} and the misfit (error-weighted χ_d) between the synthetic and calculated responses are displayed below.

7.3.2 Effect of the smoothing parameters α_x and α_z

The evaluation of the smoothing parameter α_y shows how sensitive the performance of the 3D inversion algorithm is. Here, the smoothing parameters α_x and α_z are examined by fixing $\alpha_y = 50$. Then, the synthetic responses were inverted by setting α_x and α_z equally to: 0.01, 1, and 10. The inversion results for the mentioned values α_x and α_z are shown in Fig. 7.8.

The obtained χ values are ~ 1 indicating a good fit for all the cases. However, they require a different number of iterations to reach the desired value, e.g., eight iterations are needed for $\alpha_{x,z} = 0.01$. In contrast, when $\alpha_{x,z} = 1$, only five iterations are required, which speeds up the whole inversion process.

For each case, the resolved conductivity structure exhibits some differences that need to be highlighted. In the case of $\alpha_{x,z} = 0.01$, the inversion partly resolves the basement, and the resistivity subsurface is overstructured. The plan view at $z = 170$ m confirms a 2D structure (Fig. 7.8c, d). Setting the smoothing parameters to $\alpha_{x,z} = 0.01$, inversion resolves the resistivity structure of the subsurface better than in the other cases. In addition, the 2D structure is also validated from the plan view (Fig. 7.8e, f). Subsequently, for the case of $\alpha_{x,z} = 10$, the inversion cannot resolve the basement and the subsurface structure shows a 3D pattern (Fig. 7.8g, h).

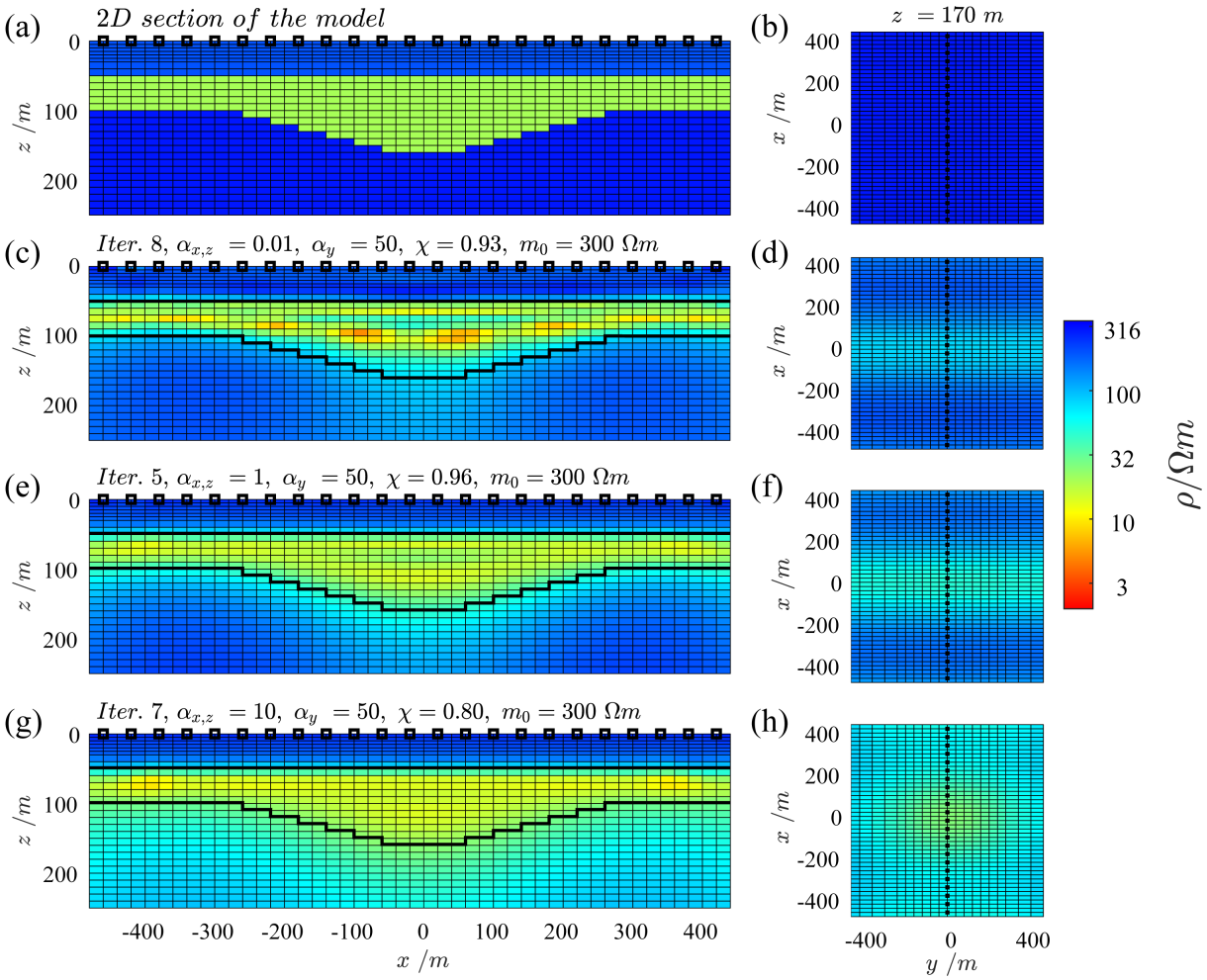

Figure 7.8: Effect of the smoothing parameter in the x- and z-direction (α_x, α_z). (a) 2D cross-section and (b) plan view at $z = 170$ m of model mesh used to derive the synthetic responses. In the same order, corresponding inversion results using (c, d) $\alpha_{x,z} = 0.01$, (e, f) $\alpha_{x,z} = 1$, and (g, h) $\alpha_{x,z} = 10$. The shape of the conductor based on the model mesh is highlighted with a black line. Black squares denote the source locations. In all the attempts, the smoothness in y-direction is set up to $\alpha_y = 50$ and an initial model of $m_0 = 300$ Ωm is utilized. The number of iterations used and the χ value are given on each attempt.

In more detail, the transients for stations T12 and T22 were also analyzed for all cases (Fig. 7.9). The transient decays exhibit relative differences around $\delta_{rd} < 5\%$, except for late times with an increase up to $\delta_{rd} \sim 10\%$. In general, a better fit is obtained for the option $\alpha_{x,z} = 10$.

In summary, a 2D resistivity structure can be obtained for low values of $\alpha_{x,z}$. Besides, from the modeling results, an over-structured resistivity subsurface is obtained for the cases where α_y is orders of magnitude larger than $\alpha_{x,z}$. Therefore, based on the evaluated smooth weighting constraints values and in order to reproduce a 2D structure in the y-direction, a factor of around 100 between α_y and $\alpha_{x,z}$ is suggested to obtain a suitable parameterization model and accurate results. These conditions work for the current setting of stations and resistivity model mesh, but might be different for other cases.

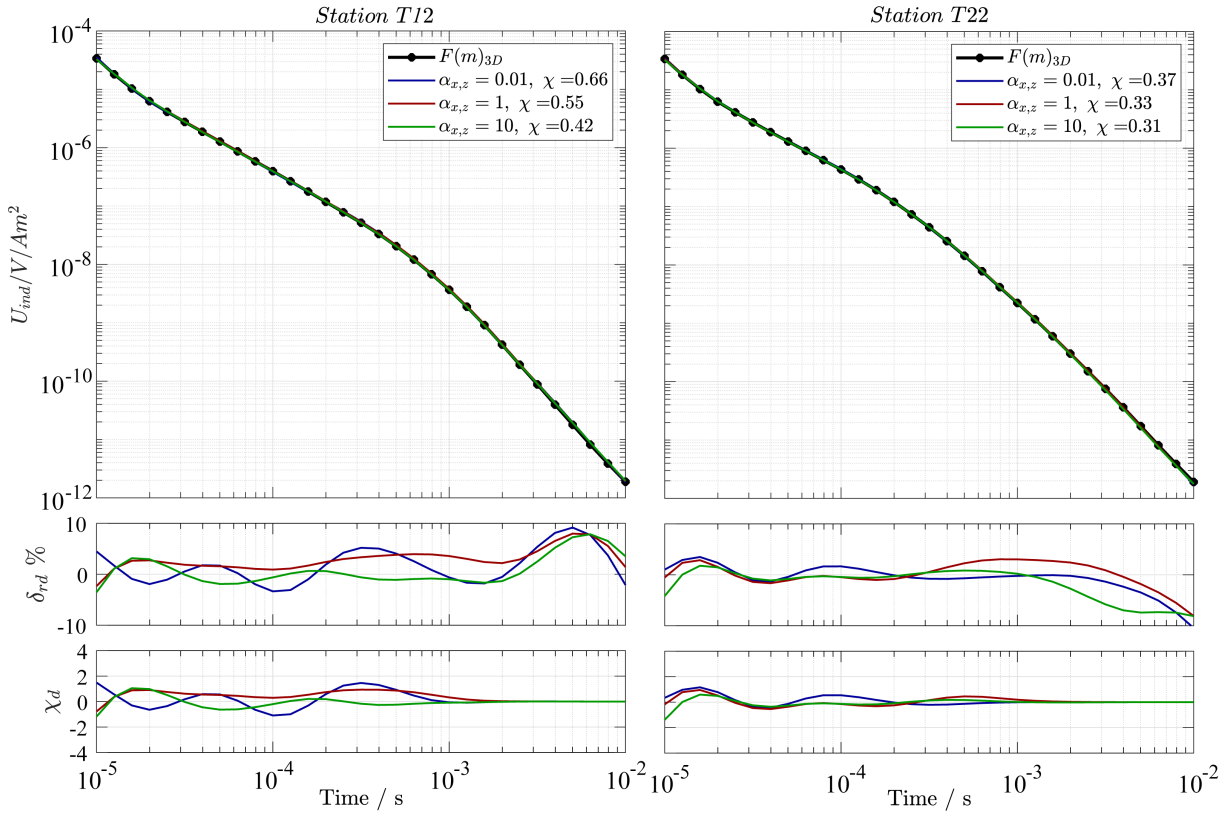

Figure 7.9: Calculated transients of stations (a) T12 and (b) T22 using $\alpha_{x,z} = 0.01, 1, 10$. The relative differences δ_{rd} and the misfit χ_d (error-weighted) between the synthetic and calculated responses are displayed below.

7.3.3 Convergence rate

The 3D inversion algorithm exhibits good performance in the evaluated cases using different smoothing constraint parameters. In all the options, a rather good convergence is obtained and, in some cases, a well-true model is recovered. The Gauss-Netwon approach, linked with the direct solver, is characterized by exhibiting a high convergence rate (Peng et al., 2016; Liu et al., 2024). The convergence rate obtained for the evaluations using different smooth constraint parameters is shown in Fig. 7.10. For all α cases, the convergence of the inversion algorithm is more or less at a similar rate, such that five to eight iterations are needed to minimize the total cost function and fit the synthetic data reasonably well. However, it should be mentioned that different convergence rates might be obtained by using other initial models. Furthermore, in each GN iteration, the regularization parameter β (see Section 7.1.4) dominates the objective function in the early iterations. The regularization parameter β is gradually reduced to put more emphasis on data fitting until a desired data misfit is reached. However, if β becomes smaller, the model regularization term is also reduced, leading to an over-structured resistivity subsurface. Based on these observations and after careful examination of the data fit and the desired model roughness, selecting the model before reaching the fifth-sixth iteration is recommended to avoid scattered and overstructured features in the resulting models.

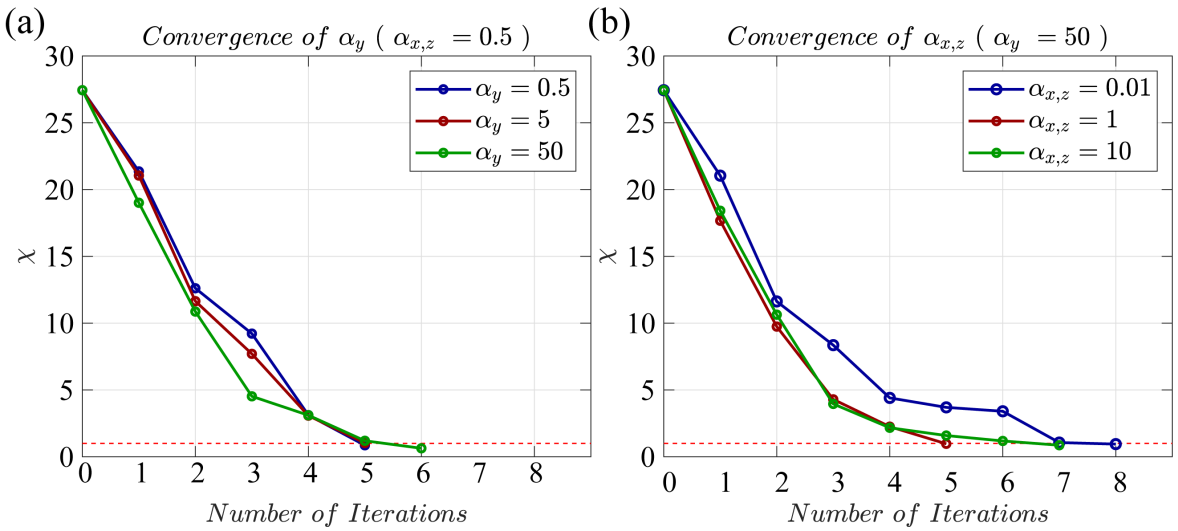

Figure 7.10: The χ value of each iteration using different smoothing constraints of (a) α_y, (b) α_x and α_z. The red dashed line indicates an optimal $\chi = 1$.

7.3.4 Demonstration of a 3D subsurface structure

Previously, based on a 2D subsurface structure, the 3D inversion algorithm has good performance that can properly reproduce a pure 2D model. However, confirmation using a 3D subsurface is essential to visualize the effect of different smooth constraint parameters and evaluate how well the algorithm recovers the subsurface structure. In this manner, the model mesh was readapted to a 3D subsurface structure, for which the same 2D clay pan shape in the y direction was replicated in the x direction, obtaining a 3D clay pan. The 3D model mesh and the plan view are shown in Fig. 7.11.

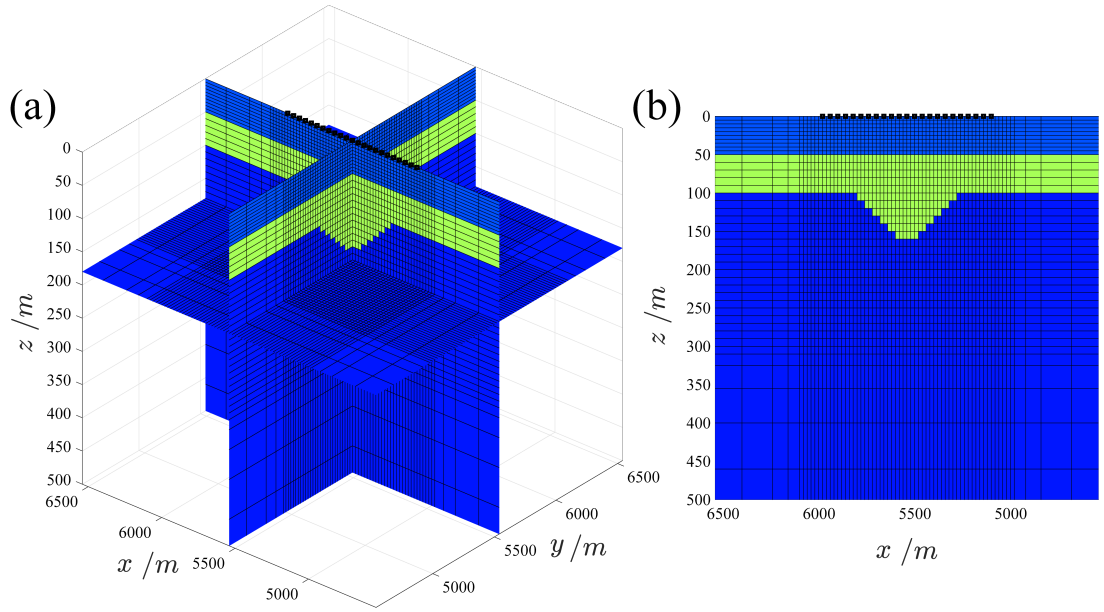

Figure 7.11: Model mesh for a 3D subsurface structure using $N_x \times N_y \times N_z = 70 \times 70 \times 47$ cells. (a) 3D view and (b) 2D cross-section. Stations are displayed in black squares. The model mesh displays a distance of ±1000 m and ±500 m from the origin in the x-y and z-direction, respectively.

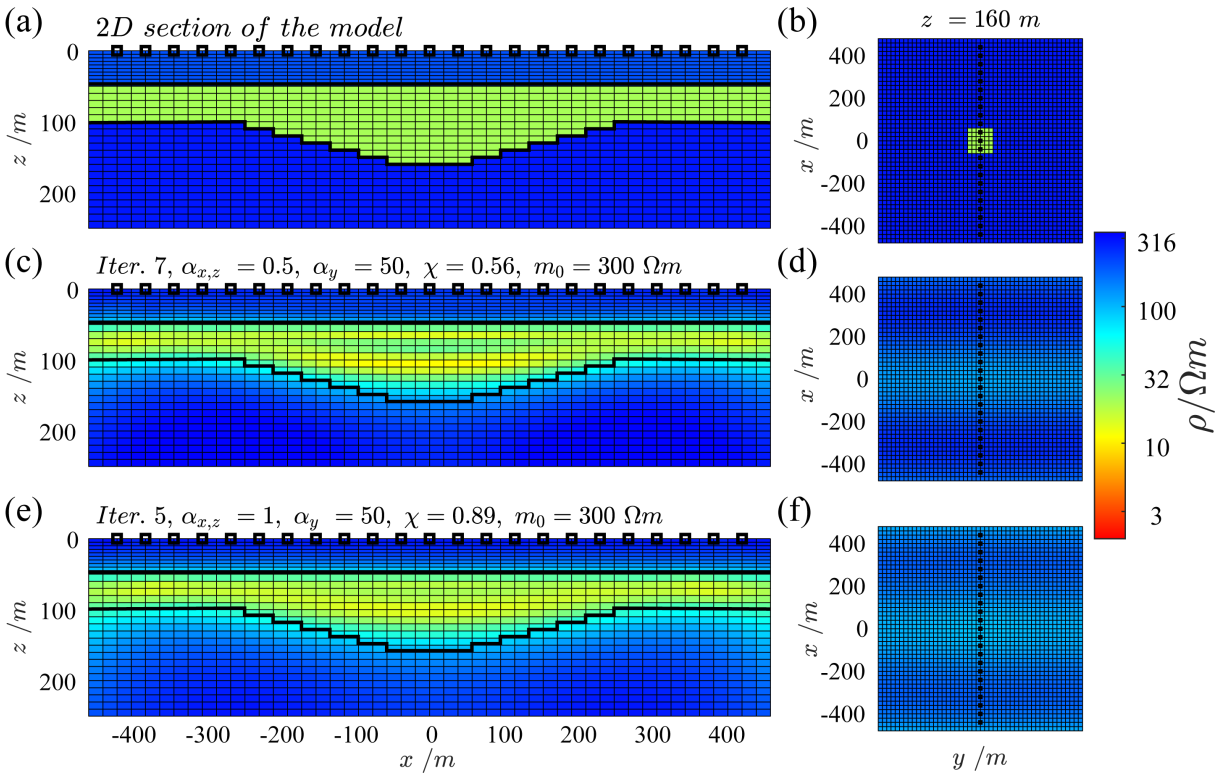

Figure 7.12: Effect of the smoothing parameter $\alpha_{x,y,z}$ for a 3D subsurface structure. (a) 2D cross-section and (b) plan view at $z = 160$ m of the model mesh to derive the synthetic responses. In the same order, corresponding inversion results using (c, d) $\alpha_y = 50$ and $\alpha_x = \alpha_z = 0.5$, and (e, f) $\alpha_y = 50$ and $\alpha_x = \alpha_z = 1$. The shape of the conductor based on the model mesh is highlighted with a black line. Black squares denote the source locations. An initial model of $m_0 = 300$ Ωm is utilized. The number of iterations used and the χ value are given on each attempt.

In Fig. 7.12, the inversion results for two different smooth constraint settings are shown: (1) $\alpha_{x,z} = 0.5$ and $\alpha_y = 50$, and (2) $\alpha_{x,z} = 1$ and $\alpha_y = 50$. In the first case, the inversion requires seven iterations, while the second requires only five to reach an acceptable value of $\chi \sim 1$, highlighting the effect of the different values α_y and $\alpha_{x,z}$ in each inversion. In both cases, the resulting models reproduce the 2D structure along the y direction (Fig. 7.12c and e). Similarly, this can also be observed from the plan view at z=160 m (Fig. 7.12d and f). Based on this, the algorithm is also verified for a 3D subsurface structure, indicating an overall good performance.

7.3.5 General remarks of the synthetic 3D inversion

The 3D inversion algorithm was evaluated using 2D and 3D subsurface structures. Since a pure 2D parameterization is unfeasible, different smooth constraint parameters along the directions x-, y- and z- were tested to find the most suitable setting to reproduce a 2D model. The synthetic results obtained exhibit a very good performance of the 3D inversion algorithm with a high convergence rate. On average, six iterations are needed to reach an acceptable value of χ. Based on these results, α_y>50 might lead to overstructured models. In addition, a low weighting of the smoothing constants along the x and z directions requires more iterations during the inversion process to minimize the total cost function and fit the field data reasonably well. Moreover, different values of α_x/α_z were

tested, for which a 2D structure can also be reproduced if α_y is fixed to a higher value (see Appendix A9). According to the smooth constraint parameters evaluated, a factor of 100 is suggested between α_y and $\alpha_{x,z}$ to obtain a suitable 2D imaging model with accurate results and to avoid larger scattering in the reconstructed model.

7.4 3D inversion of Paranal TEM field data

This section shows the 3D inversion of the Paranal clay pan field data set. The tested and evaluated model mesh generated in the previous Section 7.3.4 for the synthetic studies is used for the mentioned data set. In particular, in the 1D inversion case, only time data points above the stacked noise level were utilized. For 3D inversion, in a search for an independent resistivity model that can better explain the field data, the transient data points were widely selected, considering all data points above $t = 1.5 \times 10^{-5}$ s and thus including more data points within the stacked noise level. Three different inversion results are presented throughout this chapter. First, a 3D inversion using the PB1 profile with 23 stations is shown, whereas the derived models at different iterations are compared together with the calculated responses of selected stations. Subsequently, the results of a multi-profile 3D inversion using the north-south profiles PB1, PB3, and PB5 are presented. Here, a total of 69 stations are used, including the Tx-80 sources. The 2D section of each profile is illustrated, and the calculated responses are analyzed. Finally, the 3D inversion is shown using the whole Paranal data set with 107 stations. These results are compared with the 1D inversion models and the borehole data mentioned in Chapter 5. In all cases a starting model of 10 Ωm was considered.

Given the previous verification of the 3D modeling and inversion algorithm to evaluate the effect of the smoothing parameters $\alpha_{x,y,z}$, it is suggested that α_y be about 100 times larger than $\alpha_{x,z}$, to resolve a 2D structure. Besides, the acquired TEM data in Paranal is denser in the north-south (x) direction than in the west-east (y) direction (see Chapter 4). Because of this, a larger smoothing in the y direction is also needed to compensate for the less dense spacing in the west-east direction. In other words, if the smoothing parameters remain all the same, the parameters of the model can be poorly resolved due to the different inter-source spacing along the different directions. One way to improve the convergence inversion and also ensure well-resolved model parameters is by adjusting the smoothing parameters accordingly. In this case, α_y affects the smoothing along the west-east direction, which corresponds to the preferential orientation of the clay pan. Therefore, considering these two factors, the following default parameters $\alpha_y = 10$ and $\alpha_{x,z} = 0.5$ are chosen to have a feasible run time and a suitable 2D image of the subsurface structure.

In addition, an error floor of about 3% was considered based on the analysis of the TEM field data. The results are analyzed and discussed in terms of the unweighted δ_{rd} and weighted relative differences χ. Additionally, the sensitivity of the obtained results is briefly discussed with respect to the sensitivity/coverage. Inversions were executed on the server of the Institute of Geophysics and Meteorology at the University of Cologne using AMD EPYC 7763 CPUs with 64 cores each and 4TB of RAM.

7.4.1 Single profile inversion

The 2D section of the 3D inversion using the PB1 field data is shown in Fig. 7.13. The sixth, eighth and twelfth iterations are illustrated with their respective χ values. The resulting model in the sixth iteration shows that some structures are partly resolved, such as the presence of a clear conductive body at the center. However, $\chi \sim 11.1$ indicates that more iterations are needed to reach an acceptable χ (Fig. 7.13a). Subsequently, the model obtained in iteration eight has a better $\chi \sim 4.2$, and the geometry of the conductive conductor is much better resolved. However, some blurry zones are visible for the resistivity of the base layer, particularly at the center of the profile (Fig. 7.13b). After the twelfth iteration, the obtained model does not change much and some overstructured zones are observed at the edges of the profile (Fig. 7.13c). Furthermore, a good fit for the resulting model is obtained ($\chi \sim 1.7$). Overall, the 3D inversion resolves a clear 2D conductive structure at the first six iterations, consistent with the synthetic studies performed shown in previous sections.

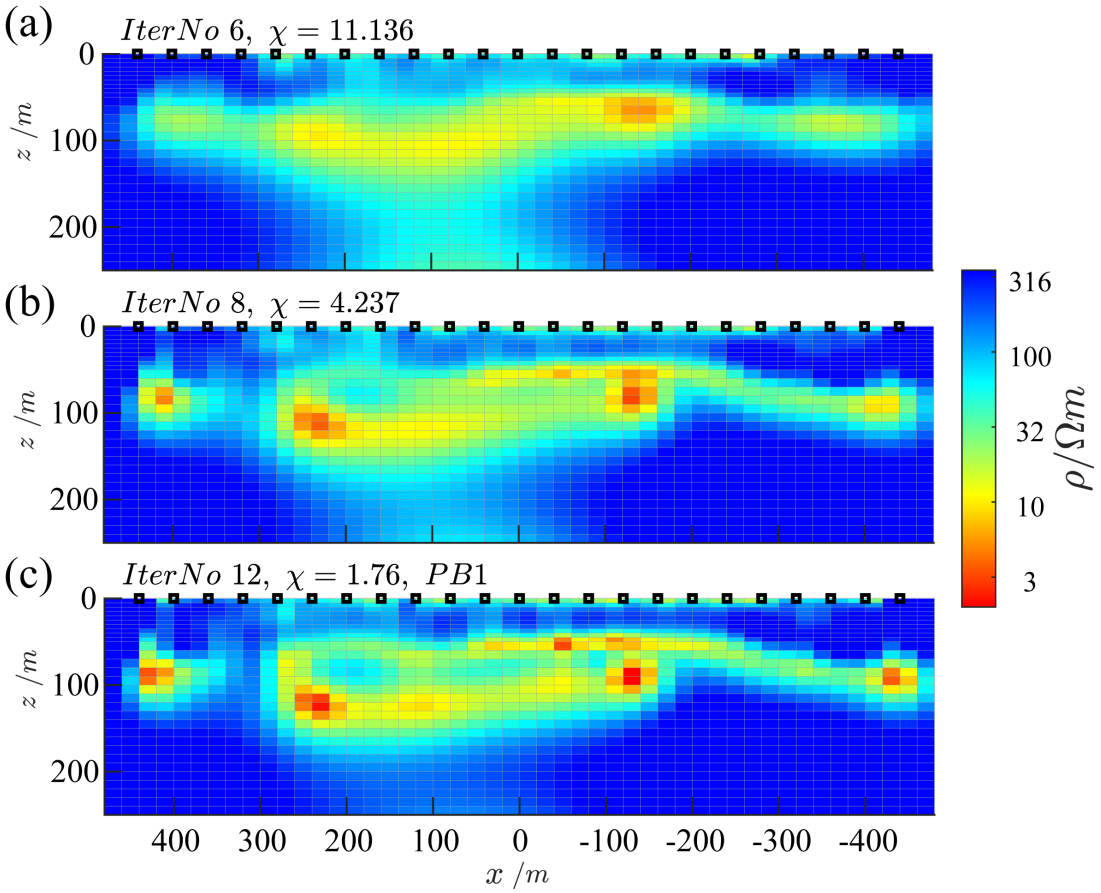

Figure 7.13: The 2D section of the 3D inversion using profile PB1. The (a) 6^{th}, (b) 10^{th}, and (c) 12^{th} model iterations are shown. The χ value is displayed on each iteration. Black squares correspond to the source locations.

In addition, the convergence rate is shown in Fig. 7.14. The first iteration exhibits a value of $\sim$ 750. At the fourth iteration, a high convergence rate is observed but still with a high misfit ($\chi \sim 17$). Then, a lower convergence rate is observed from the eighth iteration, where the misfit is $\chi \sim 2.5$, until the twelfth iteration, with a minimum value of $\chi \sim 1.6$. From the resulting models, and given the low convergence rate, it is suggested to choose an iteration model between the 8^{th} and 12^{th} to avoid overstructured features in the models and keep a good fit. In order to examine the transients derived, the observed and calculated responses in iteration 10^{th} of stations PB1T9 ad PB1T21 are shown in Fig. 7.15. Although the error model was set to 3% during inversion, only for visualization purposes, the field data error is plotted for the observed data where this value is greater than 30%. In the other cases, a 3% data error is illustrated (Fig. 7.15 and the following figures of this chapter). The station PB1T9 exhibits a $\chi \sim 1.9$ and slight mismatches are observed in the relative differences between $t \sim 2 \times 10^{-4}$ s and $t \sim 1.5 \times 10^{-3}$ s. In addition, the error-weighted relative differences show low values $\chi_d < 5$ (Fig. 7.15a). Similarly, a $\chi \sim 1.5$ is derived for station PB1T21, and the relative differences exhibit strong distortions around $t = 1.5 \times 10^{-4}$ s and $\chi_d < 3$. Both calculated transients display a consistent induced voltage response.

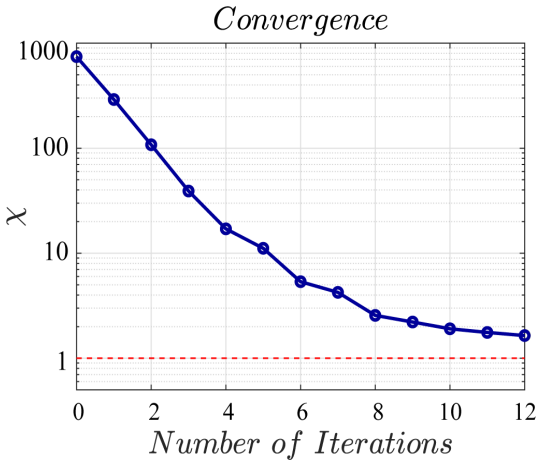

Figure 7.14: The χ value of each iteration.

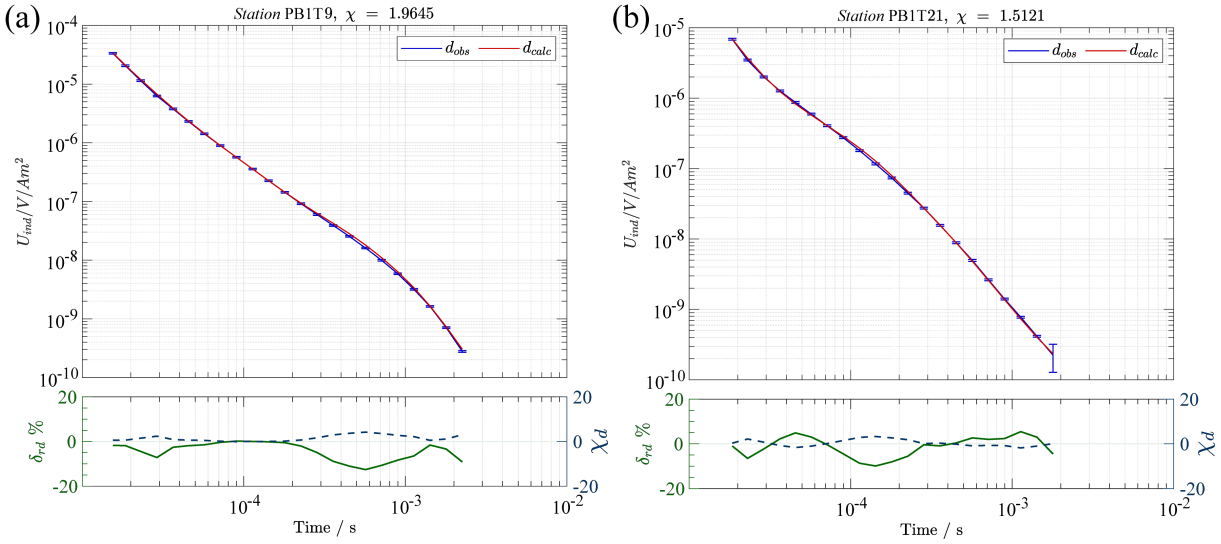

Figure 7.15: Observed and calculated responses for (a) PB1T9 and (b) PB1T21. Below each comparison, the relative differences (left y-axis, solid green line) and the error-weighted misfit (right y-axis, dashed blue line) are displayed.

7.4.2 Multi profile inversion with Tx-80 soundings

The 3D inversion results for the PB1 profile exhibit a well-resolved geometry of the conductive sediments, providing a promising outcome for a 3D inversion, including a greater number of sources. Here, Fig. 7.16 shows the 3D inversion results for the 14^{th} iteration, including 69 stations of the main north-south profiles: PB1, PB3, and PB5. The presented results exhibit a clearly well-resolved 2D conductive structure for all the profiles. The latter can also be observed in the plan view slices on which the structure is elongated due to the given smooth constraints parameters (see Fig. 7.16b, d, and f). The geometry of the conductive body is consistent among the different profiles, for which a deeper part is shown at $x = 300 - 200$ m. However, some isolated conductors are observed at the edges, which do not follow the shape of the clay pan and are present in all profiles, particularly in the northern part of the clay pan (see Fig. 7.16b at $x = 420$ m). For all profiles, a good fit is obtained for the resulting models of the 3D inversion ($\chi \sim 1.6$). It should be noted that adding more sources to the 3D inversion might improve the accuracy of the model and reproduce a more precise geometry of the Paranal clay pan.

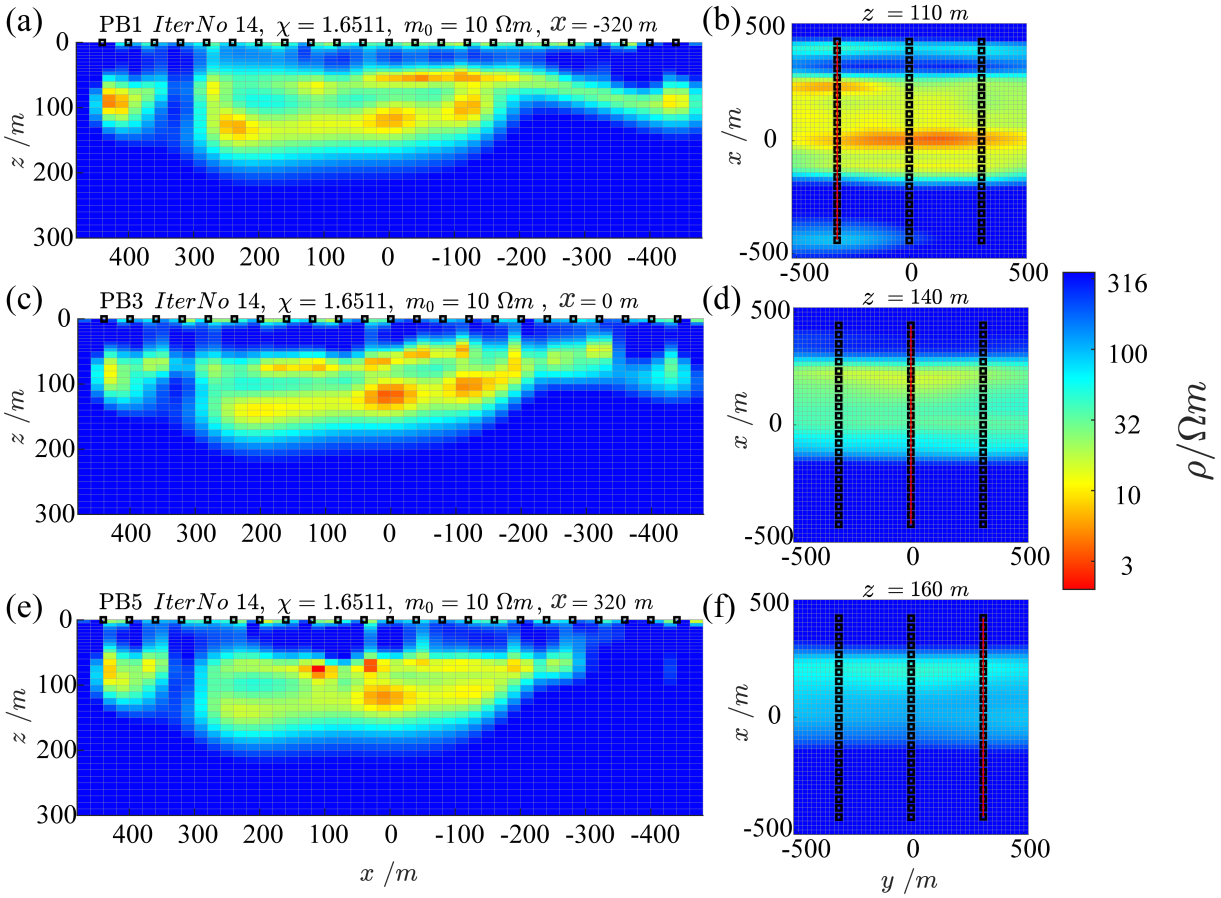

Figure 7.16: 2D sections of the 3D inversion results using profiles (a) PB1, (c) PB3 and (e) PB5 with 69 stations in total (23 for each profile). Black squares denote the source positions. Plan view of the 3D inversion at (b) $z = 110$ m, (d) $z = 140$ m, and (f) (b) $z = 160$ m.

In terms of induced voltage responses, station T12 (located in $x = 0$, the center of each profile) is shown for all profiles in Fig. 7.17. The calculated responses for station PB1T12 exhibit a good fit with $\chi \sim 1.3$. In addition, high relative differences are observed

($\delta_{rd} \sim 10\%$, particularly at late times (Fig.7.17a). In the case of station PB3T12, the observed data is under-fitted ($\chi \sim 2.7$) whereas a high mismatch is observed at late times ($t > 10^{-3}$), based on the relative differences. This is also seen in the error-weighted relative differences with values of around $\chi_d \sim 15$ (Fig. 7.17b). In the case of station PB5T12, an excellent $\chi \sim 1$ is obtained, and both δ_{rd} and χ_d exhibit low values along the time range. The calculated responses are in general consistent with the observed field data. It should be pointed out that in the case of Tx80-PB3T12, the strong transient decay covers a larger time range, including two more data points for the inversion at late times. The latter influences the final calculation of χ, due to the complex task of fitting these late-times data points. Nevertheless, the 3D inversion shows good performance, and most of the transients are correctly fitted, so that a clear 2D structure is well resolved. For more details on the observed Tx-80 TEM data, see Appendix A3.

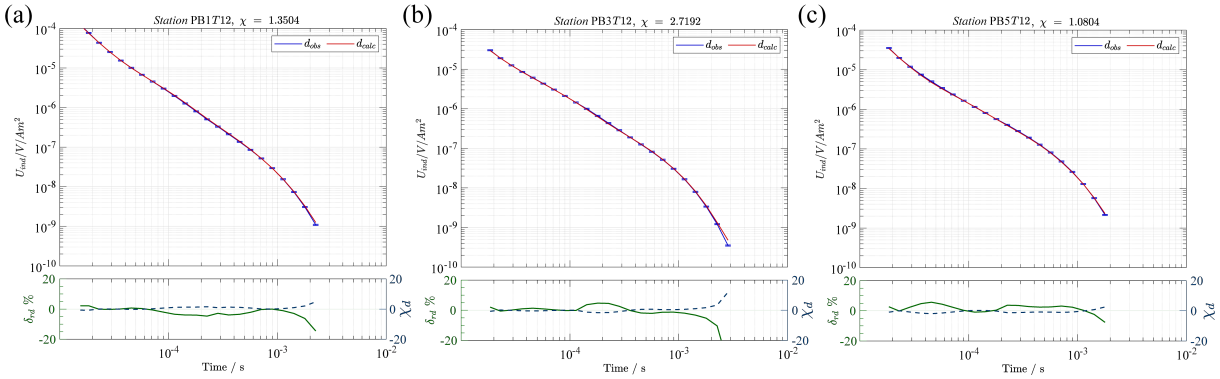

Figure 7.17: Observed Tx-80 soundings and calculated responses for station T12 at profiles (a) PB1, (b) PB3 and (c) PB5. Below each comparison, the relative differences δ_{rd} (left y-axis, solid green line) and the error-weighted misfit χ_d (right y-axis, dashed blue line) are displayed.

7.4.3 3D Inversion of the whole TEM data set

This section shows the 3D inversion of the whole TEM data set of the Paranal clay pan. In the same manner as in the previous section, the 2D sections of the main profiles and the plan views at three different depths are shown in Fig. 7.18. Furthermore, a revised 3D representation of the Paranal clay pan is shown in 7.19, similar to Fig. 5.16, along with the 2D sections PB1, PB3, and PB5 from the 3D inversion result. The derived 3D model is obtained by inverting 107 Tx-40 soundings (sources) well covering the clay pan. The model of the 12^{th} iteration is presented in Fig. 7.18, for which a good misfit is reached ($\chi \sim 1.6$).

Based on the inversion results, the 2D sections are consistent with each other, thus representing a three-layer subsurface structure and a well-resolved geometry of the clay pan. A conductive body, placed roughly between ~ 50 and ~ 200 m depth, is well resolved along all profiles. However, some conductive over-structured features are visible at the edges of PB1 at $x = -100$ m and in PB3 at $x = -300$ m and $x = -200$ m (Fig. 7.18a and c). The comparison between the bottom depth of the conductor obtained by the 1D inversion models and the geometry derived by the 3D inversion exhibits differences, especially at the edges (Fig. 7.18a, c and e).

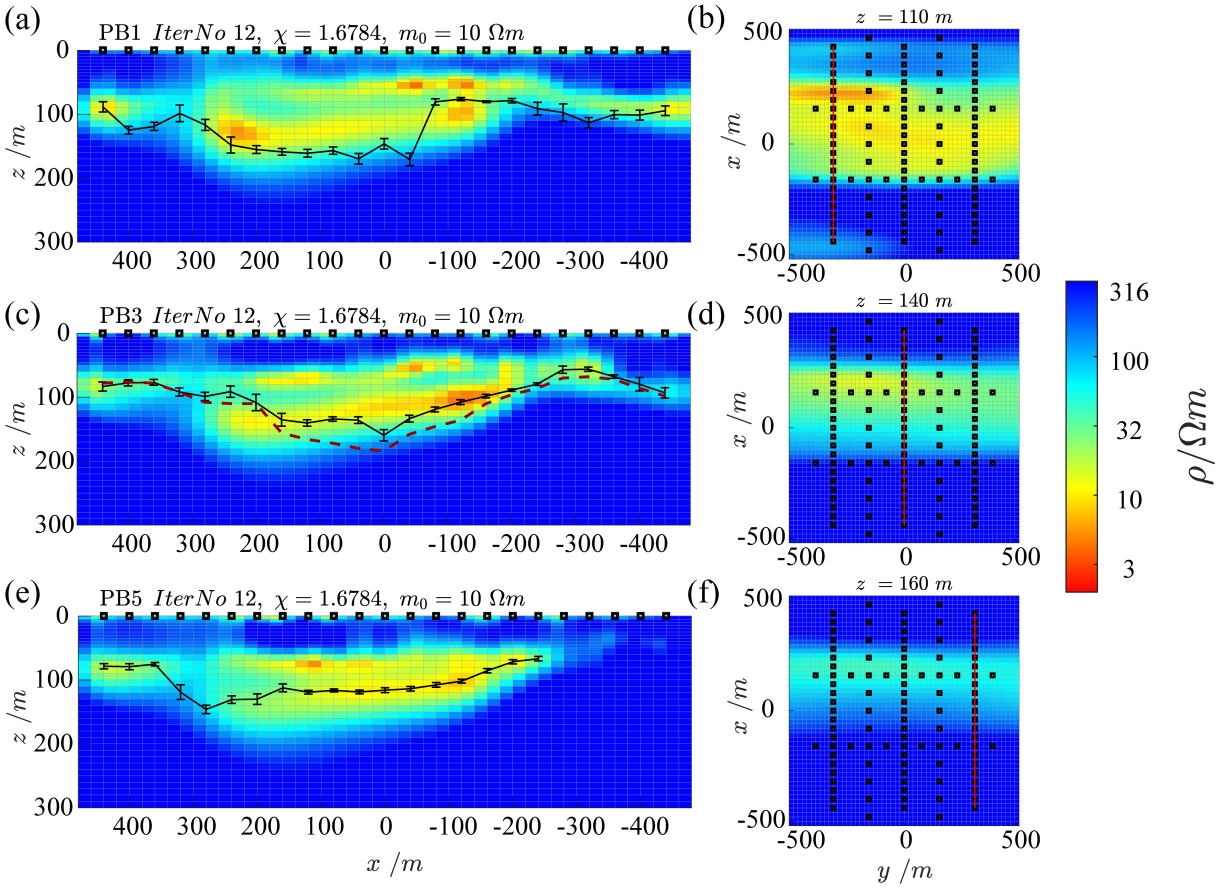

Figure 7.18: 2D sections of the 3D inversion results at profiles (a) PB1, (c) PB3 and (e) PB5 with a total of 107 stations. The bottom depth of the second layer obtained by the 1D equivalent model results shown in Chapter 5, including their error ranges, is displayed as black error bars. Black squares denote the source positions. Red dashed lines indicate the bottom depth of the basement derived by the 2D forward modeling study illustrated in Chapter 6. Plan view of the 3D inversion at (b) $z = 110$ m, (d) $z = 140$ m, and (f) $z = 160$ m.

Upon examining the 2D section of PB1 more closely, it is evident that the 1D models for stations located from $x = -50$ m to $x = -200$ m do not accurately capture the thickness of the conductive body (Fig. 7.18a). Similarly, in the 2D section of PB3, other mismatches are also observed at $x = 100$ m and $x = 300$ m (Fig. 7.18 c). Moreover, in the 2D section of PB5, all stations show this mismatch as differences greater than 50 m are observed for the bottom depth of the conductor (Fig. 7.18e).

In addition, Figure 7.20 displays the coverage distribution from the 3D inversion for profiles PB1, PB3, and PB5. Based on these results, it can be inferred that the model parameters in the first 10 m depth and the conductor at the northern edge at $y = 440$ m are well resolved. In addition, the threshold of about 10^{-2} exhibits good coverage around the conductive layers in all 2D sections, indicating good resolution of the conductive body mentioned. However, the resistivity of the base layer is poorly resolved, which is expected from the TEM method due to its advantage in detecting conductive targets. Therefore, the normalized coverage distribution also exhibits many areas with well-resolved parameters, confirming the high resolution of the conductive layer.

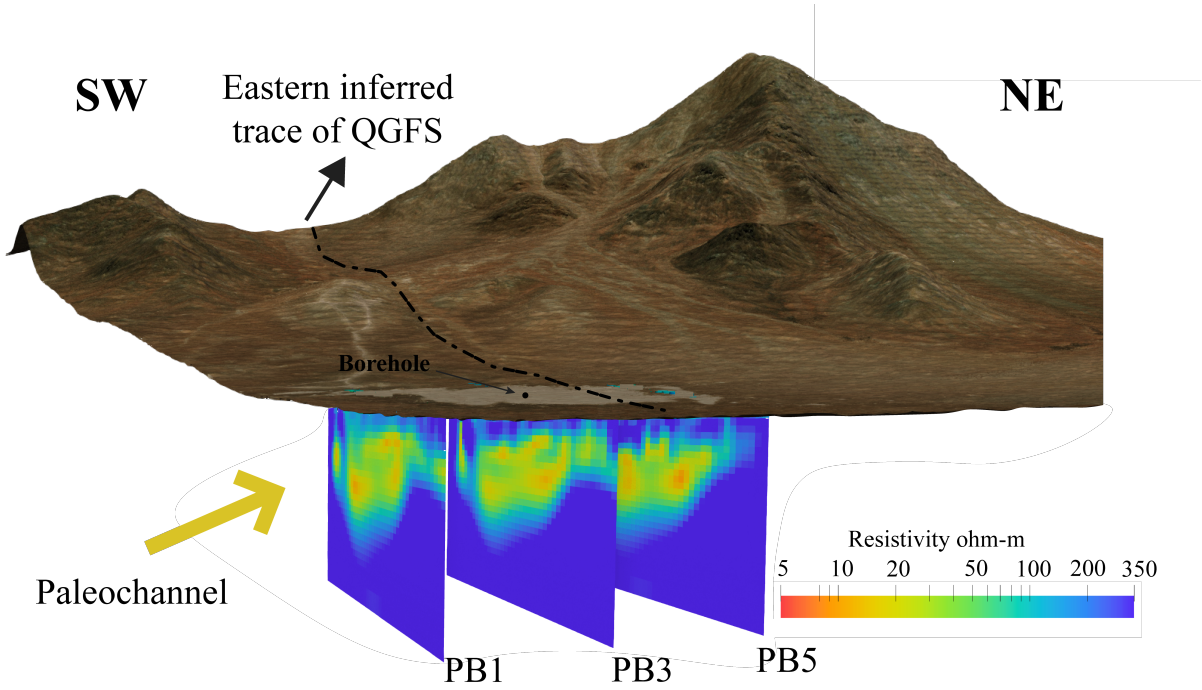

Figure 7.19: 3D view of Paranal clay pan based on the 3D inversion results. SW-NE orientation view with sections at PB1, PB3 and PB5. ESRI satellite image from World Imagery (2021). Average elevation of the 3D models is at 1900 m.a.s.l. The vertical scale is shown with double vertical exaggeration. Created in Paraview (Ahrens et al., 2005).

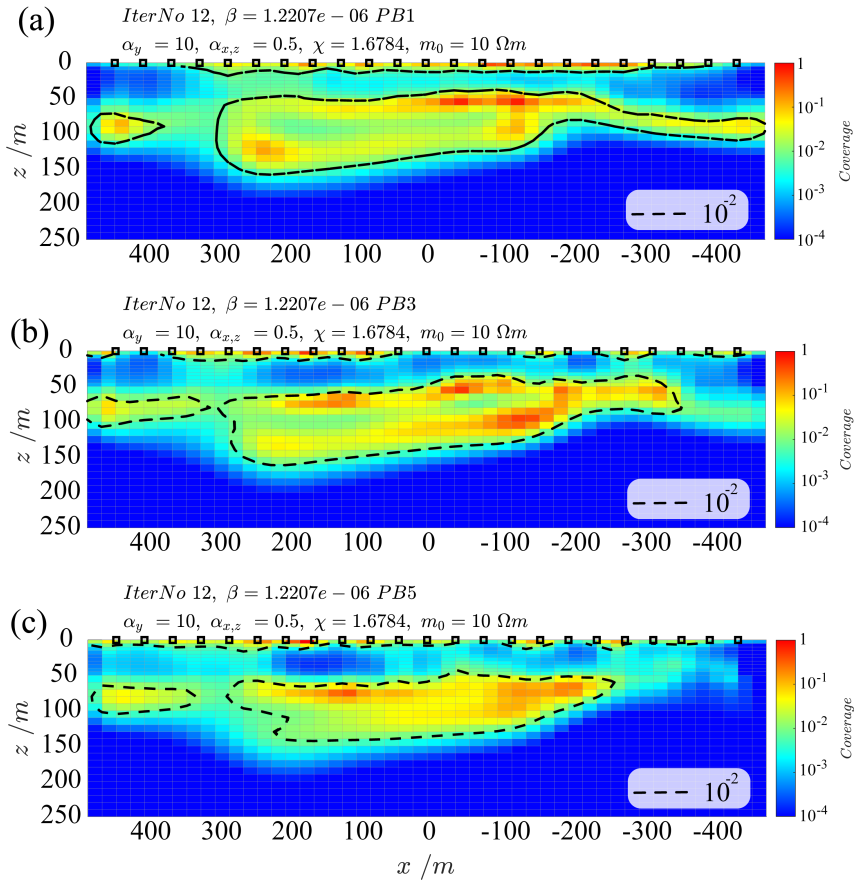

Figure 7.20: Normalized coverage distribution of the model at the same location of (a) PB1, (b) PB3 and (c) PB5. Dashed black lines indicate the threshold coverage at 10^{-2}.

These results validate the presence of a 2D structure and show that the 1D inversion results were affected by distortion effects due to the real geometry of the clay pan. Furthermore, this is also confirmed by the 2D forward modeling study using profile PB3, for which a 2D model with a larger bottom depth of the conductive layer could fit the data better. Hence, given that the 3D inversion accounts for slope effects in its modeling, as outlined in Section 6, the subsurface configuration revealed by the 3D inversion offers a more accurate depiction of the clay pan's geometry compared to that provided by the 1D models, additionally resolving internal structures unattainable with 1D inversions (Fig. 7.19).

Comparison with 1D inversion results

In order to have a comprehensive analysis of the derived 3D model, the 1D inversion results of selected sites are compared with the resistivity distribution of the obtained 3D inversion at the same location. In Fig. 7.21, the comparison is illustrated for stations PB1T12, PB3T12, and PB5T12, which correspond to the sources in the center of each profile. For station PB1T12, all models present similar resistivity values and suggest similar interface depths (Fig. 7.21a). In the same way, this is also observed in the station PB3T12, for which all the resulting 1D and 3D models agree well (Fig. 7.21 c). Furthermore, the resistivity distribution obtained by 3D inversion has a good correlation with the preliminary lithology of the Paranal borehole data, with a perfect match at the top depth of the base layer (Fig. 7.21c). However, this pattern is not seen for station PB5T12, where the 3D resistivity distribution at that location shows a thicker conductive body (Fig. 7.21e).

An interesting observation is the fitting of the induced voltage responses for each station and each approach. For the T12 stations, the 3D inversion does not have the best fit among the different approaches, which does not mean that the 1D models are more reliable or realistic solutions. Instead, the larger χ values are due to the 3D inversion trying to fit longer transients, including data points within the stacked noise level of the respective station (Fig. 7.21b, d, and f). Thus, the misfit might be worse than the 1D approaches in some cases but, in any case, more information can be retrieved (due to more data points being used). This is evident by having a closer look at the induced voltage responses of each station, where the calculated 3D responses have a better fit of the observed data at late times than the calculated responses using the Marquardt or Occam R1 approaches. The same is observed in other stations such as T8, located at $x = 160$ m in profiles B1, B3, and B5 (see Appendix A9.16). In particular, similar induced voltages are observed for T12 using 61 Tx-40 and 9 Tx-80 sources (Fig. 7.17). In this regard, it is worth mentioning that, given the similar length of transients used for the 3D inversion with Tx-40 and Tx-80, similar models representing the geometry of the clay pan are obtained from the 3D inversion (see Figs. 7.17 and 7.18).

Furthermore, the results of the 3D inversion seem to be more realistic than those of the 1D inversion, especially because the former counts better for lateral effects like the clay pan slope or proximity to the edges. Indeed, the notorious differences between the 1D and 3D models for station PB5T12 can be related to the proximity of T12 to the lateral edge of the conductive layer and the resistive surrounding, as can be seen in the southern stations of the mentioned profile ($x = -350$, Fig. 7.21e). As here, in the 1D-inversion case, a

good-fitting model can always be obtained but it might be unrealistic due to possible lateral variations. Instead, the 3D inversion can have worse misfits but a more realistic representation of the subsurface. In any case, it should be noted that better χ might be obtained by careful selection of the data range of each transient or by more iterations through the 3D inversion.

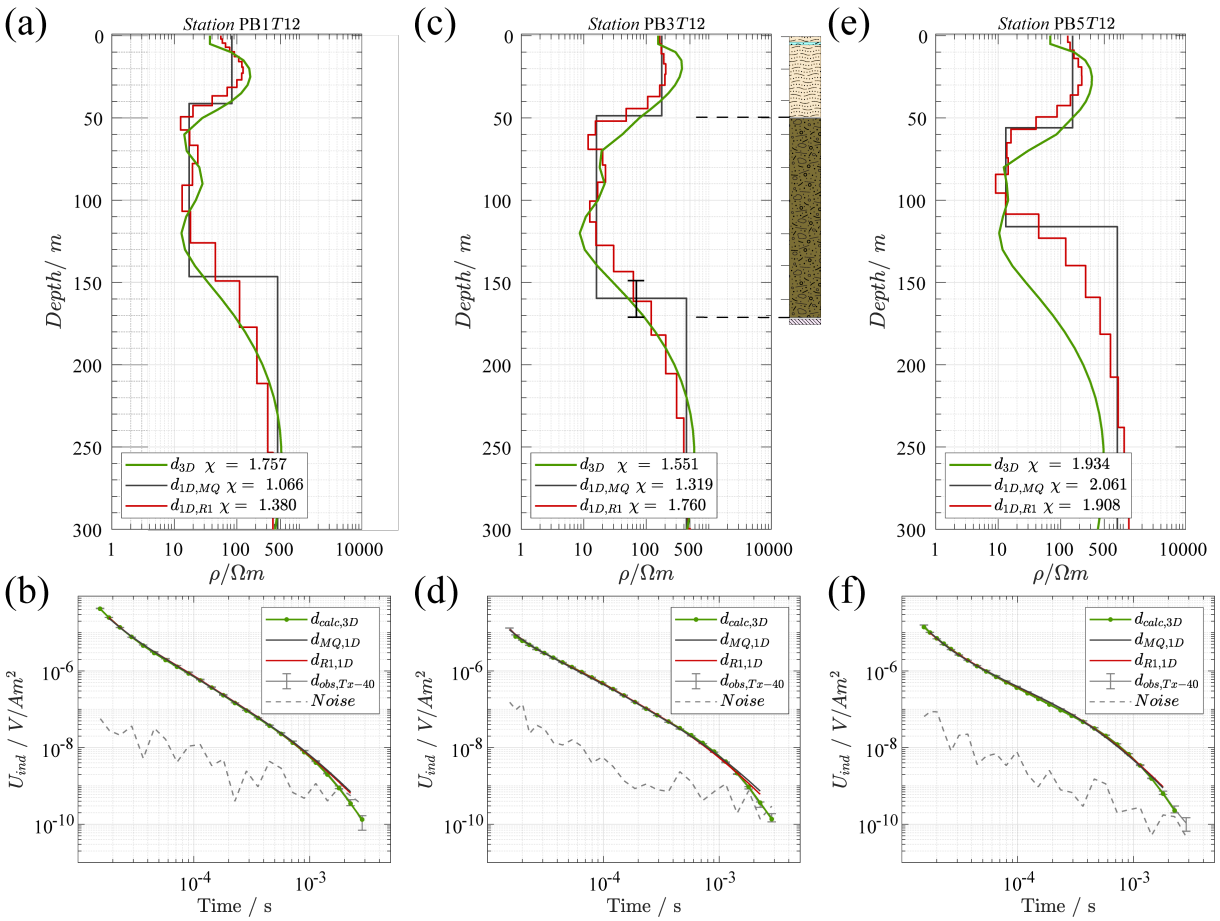

Figure 7.21: Comparison between the 1D models and resistivity distribution of the obtained 3D inversion for the stations (a) PB1T12, (b) PB3T12, (c) PB5T12. The Marquardt and Occam R1 1D inversion is displayed in black and red color. On the right side of the PB3T12 1D model, the Paranal borehole is displayed for comparison. (b, d, f) below each 1D model show the observed and calculated TEM data for each inversion approach. The stacked noise level of each sounding is plotted as a dashed grey line.

Similarly to the single-station analysis, the misfit χ value calculated from the 3D inversion and from the Marquardt and Occam R1 1D approaches are compared for the main profiles PB1, PB3, and PB5. The results are shown in Fig. 7.22. The overall misfit χ of each profile is typically larger for the 3D inversion, which can be explained by the inclusion of more data points at late times. However, the 3D inversion is accepted as a more reliable solution for the reasons mentioned above and also for the coherency of the resulting models. Given the geological context of the clay pan, it is expected the B1, B3 and B5 profiles to be similar to each other, as observed from the results of the 3D inversion. This behavior is not observed for the models derived from the 1D inversion, which show different features among each other. Particularly, profile B1 presents a steep slope around $x = -60$ m that is not observed in the rest of the profiles and which seems to be unrealistic in terms of deposition regimes and geological processes in the area. Thus, even though

the 1D profiles have lower χ than the 3D case (e.g., T15-T18 in Fig. 7.22a), the geometry of the conductive layer from the 3D inversion results is more reliable.

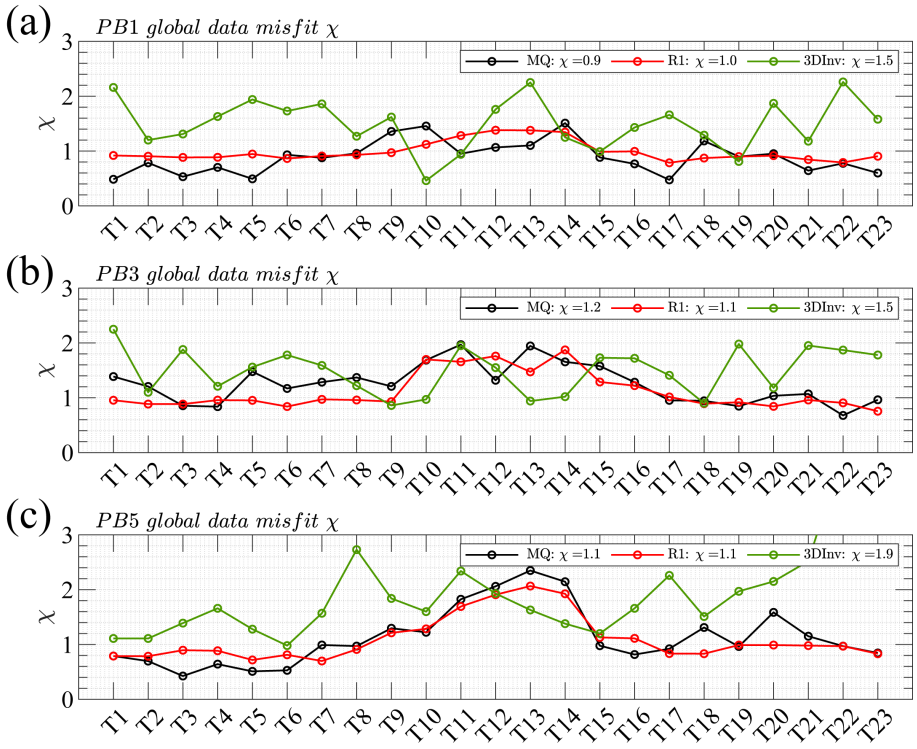

Figure 7.22: Global data misfit χ comparison for (a) PB1, (b) PB3, and (c) PB5. The misfit χ for Marquardt, Occam R1, and the 3D inversion are displayed in blank, red, and green for each station.

7.4.4 Summary of the 3D inversion results

In order to derive an independent resistivity model that deals with the strong 2D effects present in the Paranal clay pan, a 3D modeling and inversion algorithm was used to perform a 3D inversion of the whole TEM field data set. Here, the 3D algorithm, based on the FV time domain method, is used and parallelized using an iterative GN inversion approach (Peng et al., 2016; Liu et al., 2019a, 2024). The 3D forward algorithm was first evaluated using synthetic 1D and 2D solutions. At this stage, the efficiency of the code was tested as well as the estimation of the computational resources required for the proposed objectives. The 3D modeling algorithm was validated and showed good performance in deriving accurate responses. Different model meshes and time-stepping settings were tested to find the most suitable inversion parameters for further inversion of the field data. However, the synthetic studies reflect the high computational cost required for such processes. Suitable time-stepping parameters are found, together with a proper model mesh, for the proposed TEM data set.

Since the 3D algorithm was developed for pure 3D parametrization, a comprehensive verification of the smoothness weighting parameters in the different directions (x, y and z) was performed to find the proper constraints to mimic a 2D forward and inverse modeling. A successful verification of the 3D algorithm was done, finding proper smoothness constraint parameters to reproduce a 2D resistivity structure. The obtained synthetic modeling re-

sults suggest a factor of around 100 between the α_y and $\alpha_{x,z}$ to obtain a suitable 2D model parametrization and accurate results for the proposed subsurface structure.

The 3D inversion of the Paranal TEM data set was performed utilizing proper smoothing constraint parameters based on the 3D synthetic studies and the spacing of the acquired TEM soundings locations. The 3D inversion presents a high convergence rate, such that acceptable solutions can be obtained after the first ten iterations. The 3D model exhibits a well-resolved geometry of the clay pan. This is confirmed by the normalized coverage obtained by the 3D inversion of the whole TEM data set, indicating a high resolution of the derived conductive body. In addition, based on the calculated responses, the use of a longer time range of transients provides more subsurface information for the 3D inversion. However, it should be highlighted that this stage required a huge amount of computational resources on which the possibility of the performance of new inversion attempts was limited. In conclusion, since the effects of the slopes and lateral variations are included in the 3D inversion, the resulting models are a more reliable and realistic representation of the geometry of the clay pan than those derived from the 1D models.

CHAPTER 8

Conclusions and outlook

The presented thesis investigated the selected clay pans PAG and Paranal within the CRC 1211 project primarily using the TEM method. These sedimentary deposits are located in the arid and hyper-arid core of the Atacama Desert, in the coastal Cordillera of northern Chile. These sites are crucial in providing knowledge of surface and subsurface processes in areas limited by water availability. Before this work, no information was available on the detailed internal geometry of the clay pans. In addition, the loop source TEM method was complemented with magnetics and active seismics to resolve different subsurface properties at different spatial scales. Successful geophysical field campaigns were conducted on both clay pans, highlighting the good performance of multimethods working at the same place.

A total of 48 and 133 soundings were performed at the PAG and Paranal sites, respectively. The resistivity distribution of each clay pan was obtained by processing and analyzing the TEM data set and applying conventional 1D inversion approaches such as Marquardt and Occam R1 (Scholl, 2005). Both sites exhibit 1D models with reliable information up to a depth of ∼250 m.

The models obtained from the 1D inversion at the PAG site exhibit a three-layer subsurface structure, where a conductive layer of ~ 5 Ωm is detected between two resistive layers. The 1D models were analyzed in detail by model equivalence and parameter importances, suggesting a good constraint of the layer interfaces. In addition, these results are in good agreement with the revised geological information and were validated with the borehole and NCR resistivity data, which confirms the reliability of the models. The spatial resistivity distribution of the 1D models is interpreted as a paleolake with a succession of colluvial and lacustrine sediments followed by the basement. The maximum sedimentary thickness is derived at 100±10 m.

Similarly, the 1D models obtained in the Paranal clay pan shape a three-layer subsurface structure with a conductive layer of approximately ~ 20 Ωm between two resistive units.

Additionally, as for PAG, the 1D models were analyzed in detail by model equivalence and parameter importances. The resistivities and thicknesses are generally well-resolved and were associated with local and regional geological information, which shape a clay pan with a maximum sedimentary thickness of about 160±10 m. Furthermore, as part of the aims of this thesis, geophysical investigations provided the foundations to derive suitable drilling locations for paleoclimatic research. The results were fruitful, and promising locations were discussed within the CRC 1211 project, providing key information for a successful extensive drill campaign carried out by the CRC 1211 project in January 2022. The initial lithological analysis of one of the locations corroborates the findings suggested by the 1D models in the center of the clay pan. The sequences are interpreted as fine sediments and then as fluvial conglomerate corresponding to the conductive layer and the bedrock. The 3D view of the 1D models of the Paranal clay pan is interpreted as an old paleochannel in a west-east orientation, presumably part of an old drainage network system of Pampa Remiendos. In addition, it is worth mentioning that the bottom depth of the fluvial conglomerate layer was successfully derived from the 1D models and perfectly matches the preliminary lithology obtained ($\sim$ 170 m).

The quasi-2D resistivity depth sections in both clay pans agreed with the seismic tomography results, enriching the geoscientific interpretation based on different physical properties and scales. In particular, the comparison between the TEM 1D profiles and the tomography results at the Paranal clay pan exhibits changes in the P-wave velocity and resistivity that are consistent with the first sedimentary interface. These results are directly linked to the different porosities and composition of the sediment units. In addition, some minor changes were observed in the velocity depth profile below $\sim$ 20 m, which were interpreted as a thin gypsum layer by the drilling data. However, the TEM technique does not identify these variations because of its resolution limitations. Consequently, it is recommended to employ a geophysical multimethod strategy to encompass various resolution levels. Besides, the TEM results were complemented with magnetics data at the Paranal site. The magnetic survey results are consistent with the geological outcrop map, suggesting the presence of the inferred trace of the QGFS below the sediment sequences, which directly crosses the clay pan in a north-south orientation.

Despite the well-resolved depth of the sediment interface, some anomalies were observed in the resistive base layer, especially at the edges of each clay pan. As shown in this thesis work, multidimensional effects can misinterpret the TEM field data if the conductivity structure is highly heterogeneous, and thus a 1D representation might not be valid. Therefore, a 2D forward modeling study was performed that considered the main profiles of each site to investigate and validate the TEM results. The SLDMem3t algorithm was used to perform the 2D forward modeling study (Druskin and Knizhnerman, 1988, 1994; Druskin et al., 1999; Hördt et al., 1992). This step was fundamental to better understand the anomalies observed in the 1D inversion results. Different scenarios representing these observed anomalies were investigated, mainly confirming the presence of 2D effects in the data from both the PAG and Paranal TEM data sets. The 2D synthetic study obtained for profile A6 in the PAG site indicates that the TEM field data is affected by slight 2D effects due to the slope angle ($\sim 10^\circ$) in those stations located directly above or close to the clay pan slopes. The apparent presence of a deep conductor at the edges is presumably due to artifacts that cannot be ruled out, especially at the stations at the edges, which affect the late times within the noise level. Despite these anomalies, the results

obtained are meaningful, and the observed artifacts in the 1D models are below the depth of investigation (DOI). Therefore, the observed artifacts were not part of the geological interpretation. In the Paranal site, the 2D forward modeling study was performed to profile B3, where the presence of strong 2D effects was also confirmed, even higher than what was observed in the clay pan of PAG. In the Paranal clay pan, the 2D forward modeling reveals that the depth of the basement of profile B3 is slightly underestimated and possibly deeper than as derived from the 1D inversion results ($\sim$ 24 m). In addition, the pant-leg-shaped conductors observed in the base layer were also assessed, confirming the 2D effects due to the steeper slope angle and the resistivity distribution observed at the site ($\sim 20°$).

In the last stage of this thesis, since the whole TEM data set was highly affected by multidimensional effects caused, e.g., by the steep slope of the clay pan subsurface structure, a 3D inversion was suggested. For this purpose, the recently published time-domain 3D modeling and inversion algorithm developed by Dr. Yajun Liu and Dr. Ronghua Peng was applied to the Paranal TEM data set (Peng et al., 2016; Liu et al., 2019a, 2020, 2024). Extensive synthetic studies have derived suitable inversion parameters. Different smoothing constraints were evaluated to mimic a 2D model parameterization, considering the prior information obtained by the 1D inversion results and the survey design. The smoothing constraints applied in this inversion are adequate, yet they are not the only possible choices; alternative parameters could similarly approximate the 2D subsurface structure.

The 3D inversion results of the Paranal clay pan deliver a reliable and meaningful geometry of the sediment sequences. Here, a more realistic geometry is derived by dealing with the 2D effects present in the clay pan due to the slope angles and lateral variations. Despite the outstanding performance of the 3D algorithm in the Paranal clay pan TEM data set, other subsurface scenarios might require another type of model parameterization, especially for surfaces with strong changes in their topography. The presented TEM data set was suitable for the evaluated 3D modeling and inverse code due to the flatness of the clay pans. Considering the available computational resources, further inversion and modeling studies, e.g., using other model meshes, initial models or longer running times, are suggested for the Paranal clay pan in order to improve the current 3D models. Despite the low 2D effects observed in the PAG clay pan, a 3D inversion of the TEM data set might be interesting to perform.

In conclusion, the results presented in this thesis are a basis for future investigations of the CRC 1211 project in the Coastal Cordillera of the Atacama Desert, northern Chile. The derived subsurface models provide a detailed image of the resistivity-depth distribution at both clay pans. The geometry of the sedimentary conductive sequences is detected and the thickness is spatially derived at each site. These results agree well with the local and regional geological context, improving the understanding of sediment deposition and transportation in this hilly and arid environment exposed to different aridity, fluvial, and pluvial periods.

Bibliography

ABEM, G. G. Walktem Manual, ArcGIS, 2016. URL `https://www.guidelinegeo.com/product/abem-walktem/`.

Achter, V., Borowski, S., Nieroda, L., Packschies, L., and Winkelmann, V. 2013. Cheops. *Cologne High Efficient Operating Platform for Science, Regional Computing Centre Cologne, University of Cologne*.

Ahrens, J., Geveci, B., and Law, C. 2005. Paraview: An end-user tool for large data visualization. *The visualization handbook*, **717**.

Aina, A. 1986. Reduction to equator, reduction to pole and orthogonal reduction of magnetic profiles. *Exploration geophysics*, **17**(3): 141–145. ISSN 1834-7533.

Allmendinger, R. W. and González, G. 2010. Invited review paper: Neogene to Quaternary tectonics of the coastal Cordillera, northern Chile. *Tectonophysics*, **495**(1-2): 93–110. ISSN 0040-1951.

Allmendinger, R. W., González, G., Yu, J., Hoke, G., and Isacks, B. 2005. Trench-parallel shortening in the Northern Chilean Forearc: Tectonic and climatic implications. *Geological Society of America Bulletin*, **117**(1-2): 89–104. ISSN 1943-2674.

Álvarez, F., Reich, M., Snyder, G., Pérez-Fodich, A., Muramatsu, Y., Daniele, L., and Fehn, U. 2016. Iodine budget in surface waters from Atacama: Natural and anthropogenic iodine sources revealed by halogen geochemistry and iodine-129 isotopes. *Applied Geochemistry*, **68**: 53–63. ISSN 0883-2927.

Amestoy, P. R., Guermouche, A., L'Excellent, J.-Y., and Pralet, S. 2006. Hybrid scheduling for the parallel solution of linear systems. *Parallel computing*, **32**(2): 136–156. ISSN 0167-8191.

Amundson, R., Dietrich, W., Bellugi, D., Ewing, S., Nishiizumi, K., Chong, G., Owen, J., Finkel, R., Heimsath, A., and Stewart, B. 2012. Geomorphologic evidence for the late

Pliocene onset of hyperaridity in the Atacama Desert. *GSA Bulletin*, **124**(7-8): 1048–1070. ISSN 1943-2674.

Archie, G. E. 1942. The electrical resistivity log as an aid in determining some reservoir characteristics. *Transactions of the AIME*, **146**(01): 54–62. ISSN 0081-1696.

Auken, E., Pellerin, L., Christensen, N. B., and Sørensen, K. 2006. A survey of current trends in near-surface electrical and electromagnetic methods. *Geophysics*, **71**(5): G249–G260. ISSN 0016-8033.

Becken, M., Nittinger, C. G., Smirnova, M., Steuer, A., Martin, T., Petersen, H., Meyer, U., Mörbe, W., Yogeshwar, P., and Tezkan, B. 2020. DESMEX: A novel system development for semi-airborne electromagnetic exploration. *Geophysics*, **85**(6): E253–E267. ISSN 0016-8033.

Blanco-Arrué, B., Yogeshwar, P., Tezkan, B., and Díaz, D. 2021. Loop source transient electromagnetics in an urban noise environment: A case study in Santiago de Chile. *Geophysics*, **86**(3): B135–B147. ISSN 0016-8033.

Blanco-Arrué, B., Yogeshwar, P., Tezkan, B., Mörbe, W., Díaz, D., Farah, B., Buske, S., Ninneman, L., Domagala, J., and Diederich-Leicher, J. 2022. Exploration of sedimentary deposits in the Atacama Desert, Chile, using integrated geophysical techniques. *Journal of South American Earth Sciences*, p. 103746. ISSN 0895-9811.

Brown, M., Diaz, F., and Grocott, J. 1993. Displacement history of the Atacama fault system 25° 00 S-27° 00 S, northern Chile. *Geological Society of America Bulletin*, **105**(9): 1165–1174. ISSN 1943-2674.

Bücker, M., Flores Orozco, A., Gallistl, J., Steiner, M., Aigner, L., Hoppenbrock, J., Glebe, R., Morales Barrera, W., Pita de la Paz, C., and García García, C. E. 2021. Integrated land and water-borne geophysical surveys shed light on the sudden drying of large karst lakes in southern Mexico. *Solid Earth*, **12**(2): 439–461. ISSN 1869-9510.

Börner, R.-U. 2010. Numerical modelling in geo-electromagnetics: advances and challenges. *Surveys in Geophysics*, **31**(2): 225–245. ISSN 1573-0956.

Carrizo, D., González, G., and Dunai, T. 2008. Constricción neógena en la Cordillera de la Costa, norte de Chile: neotectónica y datación de superficies con 21Ne cosmogónico. *Revista geológica de Chile*, **35**(1): 01–38. ISSN 0716-0208.

Cembrano, J., González, G., Arancibia, G., Ahumada, I., Olivares, V., and Herrera, V. 2005. Fault zone development and strain partitioning in an extensional strike-slip duplex: A case study from the Mesozoic Atacama fault system, Northern Chile. *Tectonophysics*, **400**(1-4): 105–125. ISSN 0040-1951.

Christiansen, A. V., Auken, E., and Sørensen, K. 2006. *The transient electromagnetic method*, p. 179–225. Springer.

Clark, D. and Emerson, D. 1991. Notes on rock magnetization characteristics in applied geophysical studies. *Exploration Geophysics*, **22**(3): 547–555. ISSN 1834-7533.

Clarke, J. D. 2006. Antiquity of aridity in the Chilean Atacama Desert. *geomorphology*, **73**(1-2): 101–114. ISSN 0169-555X.

Commer, M. and Newman, G. A. 2008. New advances in three-dimensional controlled-source electromagnetic inversion. *Geophysical Journal International*, **172**(2): 513–535. ISSN 1365-246X.

Constable, S. C., Parker, R. L., and Constable, C. G. 1987. Occam's inversion: A practical algorithm for generating smooth models from electromagnetic sounding data. *Geophysics*, **52**(3): 289–300.

Cordell, D., Unsworth, M. J., and Díaz, D. 2018. Imaging the Laguna del Maule Volcanic Field, central Chile using magnetotellurics: Evidence for crustal melt regions laterally-offset from surface vents and lava flows. *Earth and Planetary Science Letters*, **488**: 168–180. ISSN 0012-821X.

Danielsen, J. E., Auken, E., Jørgensen, F., Søndergaard, V., and Sørensen, K. I. 2003. The application of the transient electromagnetic method in hydrogeophysical surveys. *Journal of applied geophysics*, **53**(4): 181–198. ISSN 0926-9851.

del Río, C., García, J.-L., Osses, P., Zanetta, N., Lambert, F., Rivera, D., Siegmund, A., Wolf, N., Cereceda, P., and Larraín, H. 2018. ENSO influence on coastal fog-water yield in the Atacama Desert, Chile. *Aerosol and Air Quality Research*, **18**(1): 127–144. ISSN 2071-1409.

Delouis, B., Philip, H., Dorbath, L., and Cisternas, A. 1998. Recent crustal deformation in the Antofagasta region (northern Chile) and the subduction process. *Geophysical Journal International*, **132**(2): 302–338. ISSN 1365-246X.

Dentith, M. and Mudge, S. T. 2014. *Geophysics for the mineral exploration geoscientist*. Cambridge University Press. ISBN 1139915622.

Díaz, D., Maksymowicz, A., Vargas, G., Vera, E., Contreras-Reyes, E., and Rebolledo, S. 2014. Exploring the shallow structure of the San Ramón thrust fault in Santiago, Chile (33.5 S), using active seismic and electric methods. *Solid Earth*, **5**(2): 837. ISSN 1869-9510.

Diederich, J. L., Wennrich, V., Bao, R., Büttner, C., Bolten, A., Brill, D., Buske, S., Campos, E., Fernández-Galego, E., and Gödickmeier, P. 2020. A 68 ka precipitation record from the hyperarid core of the Atacama Desert in northern Chile. *Global and Planetary Change*, **184**: 103054. ISSN 0921-8181.

Diederich-Leicher, J. L., 2020. *Climate history of the hyperarid core of the Atacama Desert based on clay pan sediments*. Ph.D. Thesis, University of Cologne.

Domagala, J., Escribano, J., De la Cruz, R., Saldías, J., and Jorquera, R. 2016. Nos. 187-188, Cartas Blanco Encalada y Pampa Remiendos, Región de Antofagasta. Escala 1:100.000. Serie Geología Básica. *SERNAGEOMIN*.

Druskin, V. and Knizhnerman, L. 1988. Spectral differential-difference method for numeric solution of three-dimensional nonstationary problems of electric prospecting. *Izvestiya Earth Phys*, **24**: 641–648.

Druskin, V. and Knizhnerman, L. 1994. Spectral approach to solving three-dimensional Maxwell's diffusion equations in the time and frequency domains. *Radio Science*, **29**(4): 937–953. ISSN 1944-799X.

Druskin, V., Knizhnerman, L., and Lee, P. 1999. New spectral Lanczos decomposition method for induction modeling in arbitrary 3-D geometry. *Geophysics*, **64**(3): 701–706. ISSN 0016-8033.

Dunai, T. J., López, G. A. G., and Juez-Larré, J. 2005. Oligocene–Miocene age of aridity in the Atacama Desert revealed by exposure dating of erosion-sensitive landforms. *Geology*, **33**(4): 321–324. ISSN 1943-2682.

Dunai, T. J., Melles, M., Quandt, D., Knief, C., and Amelung, W. 2020. Whitepaper: Earth–Evolution at the dry limit. *Global and Planetary Change*, p. 103275. ISSN 0921-8181.

Everett, M. E. 2012. Theoretical developments in electromagnetic induction geophysics with selected applications in the near surface. *Surveys in geophysics*, **33**(1): 29–63. ISSN 1573-0956.

Fernández-Martínez, M. , Severino, R. d. S., Moreno-Paz, M., Gallardo-Carreño, I., Blanco, Y., Warren-Rhodes, K., García-Villadangos, M., Ruiz-Bermejo, M., Barberán, A., and Wettergreen, D. 2019. Prokaryotic community structure and metabolisms in shallow subsurface of Atacama Desert playas and alluvial fans after heavy rains: repairing and preparing for next dry period. *Frontiers in microbiology*, **10**: 1641. ISSN 1664-302X.

Fitterman, D. V. and Stewart, M. T. 1986. Transient electromagnetic sounding for groundwater. *Geophysics*, **51**(4): 995–1005. ISSN 0016-8033.

Frei, W. and Keller, L. 2000. Hybride Seismik—Eine verbesserte Methode des Aussagepotentials seismischer Daten [Hybrid seismic surveying—A method to better view the information content in seismic data]. *Bulletin für angewandte Geologie*, **5**(2): 229–236.

Frischknecht, F. C. and Raab, P. 1984. Time-domain electromagnetic soundings at the Nevada Test Site, Nevada. *Geophysics*, **49**(7): 981–992. ISSN 0016-8033.

Gao, J., Smirnov, M., Smirnova, M., and Egbert, G. 2021. 3-D time-domain electromagnetic modeling based on multi-resolution grid with application to geomagnetically induced currents. *Physics of the Earth and Planetary Interiors*, **312**: 106651. ISSN 0031-9201.

Goldman, M. and Neubauer, F. 1994. Groundwater exploration using integrated geophysical techniques. *Surveys in geophysics*, **15**(3): 331–361. ISSN 0169-3298.

Goldman, M., Levi, E., Tezkan, B., and Yogeshwar, P. 2011. The 2D coastal effect on marine time domain electromagnetic measurements using broadside dBz/dt of an electrical transmitter dipole. *Geophysics*, **76**(2): F101–F109. ISSN 0016-8033.

González, G., Cembrano, J., Carrizo, D., Macci, A., and Schneider, H. 2003. The link between forearc tectonics and Pliocene–Quaternary deformation of the Coastal Cordillera, northern Chile. *Journal of South American Earth Sciences*, **16**(5): 321–342. ISSN 0895-9811.

González, G., Dunai, T., Carrizo, D., and Allmendinger, R. 2006. Young displacements on the Atacama Fault System, northern Chile from field observations and cosmogenic 21Ne concentrations. *Tectonics*, **25**(3). ISSN 0278-7407.

González, G., Pasten-Araya, F., Victor, P., González, Y., Valenzuela, J., and Shrivastava, M. 2021. The role of interplate locking on the seismic reactivation of upper plate faults on the subduction margin of northern Chile. *Scientific reports*, **11**(1): 1–12. ISSN 2045-2322.

Haber, E., Oldenburg, D. W., and Shekhtman, R. 2007. Inversion of time domain three-dimensional electromagnetic data. *Geophysical Journal International*, **171**(2): 550–564. ISSN 1365-246X.

Han, B., Li, Y., and Li, G. 2018. 3D forward modeling of magnetotelluric fields in general anisotropic media and its numerical implementation in Julia. *Geophysics*, **83**(4): F29–F40. ISSN 0016-8033.

Hansen, P. C. and O'Leary, D. P. 1993. The use of the L-curve in the regularization of discrete ill-posed problems. *SIAM journal on scientific computing*, **14**(6): 1487–1503. ISSN 1064-8275.

Haroon, A., 2016. *Development of novel time-domain electromagnetic methods for offshore groundwater studies: A data application from Bat Yam, Israel*. Ph.D. Thesis, Institute of Geophysics and Meteorology, University of Cologne.

Hartley, A. J. and Chong, G. 2002. Late Pliocene age for the Atacama Desert: implications for the desertification of western South America. *Geology*, **30**(1): 43–46. ISSN 1943-2682.

Hartley, A. J., May, G., Chong, G., Turner, P., Kape, S. J., and Jolley, E. J. 2000. Development of a continental forearc: A Cenozoic example from the Central Andes, northern Chile. *Geology*, **28**(4): 331–334. ISSN 1943-2682.

Hartley, A. J., Chong, G., Houston, J., and Mather, A. E. 2005. 150 million years of climatic stability: evidence from the Atacama Desert, northern Chile. *Journal of the Geological Society*, **162**(3): 421–424. ISSN 0016-7649.

Heagy, L. J., Cockett, R., Kang, S., Rosenkjaer, G. K., and Oldenburg, D. W. 2017. A framework for simulation and inversion in electromagnetics. *Computers Geosciences*, **107**: 1–19. ISSN 0098-3004.

Herve, M. 1987. Movimiento normal de la falla Paposo, Zona de Falla Atacama, en el Mioceno, Chile. *Andean Geology*, (31): 31–36. ISSN 0718-7106.

Hoffmann-Rothe, A., Ritter, O., and Janssen, C. 2004. Correlation of electrical conductivity and structural damage at a major strike-slip fault in northern Chile. *Journal of Geophysical Research: Solid Earth*, **109**(B10). ISSN 0148-0227.

Hördt, A. and Müller, M. 2000. Understanding LOTEM data from mountainous terrain. *Geophysics*, **65**(4): 1113–1123. ISSN 0016-8033.

Hördt, A., Druskin, V. L., Knizhnerman, L. A., and Strack, K.-M. 1992. Interpretation of 3-D effects in long-offset transient electromagnetic (LOTEM) soundings in the Münsterland area/Germany. *Geophysics*, **57**(9): 1127–1137. ISSN 0016-8033.

Houston, J. 2006. Variability of precipitation in the Atacama Desert: its causes and hydrological impact. *International Journal of Climatology: A Journal of the Royal Meteorological Society*, **26**(15): 2181–2198. ISSN 0899-8418.

Houston, J. and Hartley, A. J. 2003. The central Andean west-slope rainshadow and its potential contribution to the origin of hyper-aridity in the Atacama Desert. *International Journal of Climatology: A Journal of the Royal Meteorological Society*, **23**(12): 1453–1464. ISSN 0899-8418.

Hördt, A. and Scholl, C. 2004. The effect of local distortions on time-domain electromagnetic measurements. *Geophysics*, **69**(1): 87–96. ISSN 0016-8033.

Ibraheem, I. M., Gurk, M., Tougiannidis, N., and Tezkan, B. 2018. Subsurface investigation of the Neogene Mygdonian Basin, Greece using magnetic data. *Pure and Applied Geophysics*, **175**(8): 2955–2973. ISSN 1420-9136.

Inman, J. R. 1975. Resistivity inversion with ridge regression. *Geophysics*, **40**(5): 798–817. ISSN 0016-8033.

Ishihara, S. and Ulriksen, C. E. 1980. The magnetite-series and ilmenite-series granitoids in Chile. *Mining geology*, **30**(161): 183–190. ISSN 0026-5209.

Jørgensen, F., Sandersen, P. B., and Auken, E. 2003. Imaging buried Quaternary valleys using the transient electromagnetic method. *Journal of Applied Geophysics*, **53**(4): 199–213. ISSN 0926-9851.

Kearey, P., Brooks, M., and Hill, I. 2002. *An introduction to geophysical exploration*, volume 4. John Wiley Sons. ISBN 0632049294.

Keller, G. V. 1988. Rock and mineral properties. *Electromagnetic methods in applied geophysics*, **1**: 13–52.

Kirsch, R. 2006. Groundwater Geophysics. *Springer*, **493**.

Lelièvre, P. G. and Oldenburg, D. W. 2009. A 3D total magnetization inversion applicable when significant, complicated remanence is present. *Geophysics*, **74**(3): L21–L30. ISSN 0016-8033.

Levenberg, K. 1944. A method for the solution of certain non-linear problems in least squares. *Quarterly of applied mathematics*, **2**(2): 164–168. ISSN 0033-569X.

Liu, Y., Hu, X., and Peng, R. 2017. *3D transient electromagnetic modeling for an arbitrarily anisotropic earth*, p. 1115–1120. Society of Exploration Geophysicists. ISBN 1949-4645.

Liu, Y., Cai, H., Hu, X., and Peng, R. 2019a. 3D forward modeling and analysis for loop-source transient electromagnetic data based on finite-volume method in an arbitrarily anisotropy earth. In *International Workshop on Gravity, Electrical Magnetic Methods and Their Applications, Xi'an, China, May 19–22, 2019*, p. 272–275. Society of Exploration Geophysicists and Chinese Geophysical Society. ISBN 2159-6832.

Liu, Y., Hu, X., Peng, R., and Yogeshwar, P. 2019b. 3D forward modeling and analysis of the loop-source transient electromagnetic method based on the finite-volume method for an arbitrarily anisotropic medium. *Chinese Journal of Geophysics*, **62**(5): 1954–1968. ISSN 0001-5733.

Liu, Y., Yogeshwar, P., Hu, X., Peng, R., Tezkan, B., Mörbe, W., and Li, J. 2020. Effects of electrical anisotropy on long-offset transient electromagnetic data. *Geophysical Journal International*, **222**(2): 1074–1089. ISSN 0956-540X.

Liu, Y., Yogeshwar, P., Peng, R., Hu, X., Han, B., and Blanco-Arrué, B. 2024. Three-Dimensional Inversion of Time-Domain Electromagnetic Data Using Various Loop Source Configurations. *IEEE Transactions on Geoscience and Remote Sensing*, **62**: 1–15. doi: 10.1109/TGRS.2024.3383288.

Mårdh, J. 2017. A geophysical survey (TEM; ERT) of the Punata alluvial fan, Bolivia. *Dissertations in Geology at Lund University.*

Marquardt, D. W. 1963. An algorithm for least-squares estimation of nonlinear parameters. *Journal of the society for Industrial and Applied Mathematics*, p. 11(2), 431–441.

Marson, I. and Klingele, E. 1993. Advantages of using the vertical gradient of gravity for 3-D interpretation. *Geophysics*, **58**(11): 1588–1595. ISSN 0016-8033.

Martin, R., 2009. *Development and application of 2D and 3D transient electromagnetic inverse solutions based on adjoint Green functions: A feasibility study for the spatial reconstruction of conductivity distributions by means of sensitivities.* Thesis, Institute of Geophysics and Meteorology, University of Cologne.

May, G., Hartley, A., Stuart, F., and Chong, G. 1999. Tectonic signatures in arid continental basins: an example from the Upper Miocene–Pleistocene, Calama Basin, Andean forearc, northern Chile. *Palaeogeography, Palaeoclimatology, Palaeoecology*, **151**(1-3): 55–77. ISSN 0031-0182.

Meju, M. A. 1994. *Geophysical data analysis: understanding inverse problem theory and practice.* Society of Exploration Geophysicists. ISBN 1560800275.

Menke, W. 2018. *Geophysical data analysis: Discrete inverse theory.* Academic press.

Mitchell, T. and Faulkner, D. 2009. The nature and origin of off-fault damage surrounding strike-slip fault zones with a wide range of displacements: A field study from the Atacama fault system, northern Chile. *Journal of Structural Geology*, **31**(8): 802–816. ISSN 0191-8141.

Montecinos-Cuadros, D., Díaz, D., Yogeshwar, P., and Munoz-Saez, C. 2021. Characterization of the shallow structure of El Tatio geothermal field in the Central Andes, Chile using transient electromagnetics. *Journal of Volcanology and Geothermal Research*, **412**: 107198. ISSN 0377-0273.

Nabighian, M. N. and Macnae, J. C. 1991. Time domain electromagnetic prospecting methods. *Electromagnetic methods in applied geophysics*, **2**: 427–509.

Naranjo, J. A., Ramirez, C. F., and Pankoff, R. 1994. Morphostratigraphic evolution of the northwestern margin of the Salar de Atacama basin (23° S-68° W). *Andean Geology*, **21**(1): 91–103. ISSN 0718-7106.

NASA. NASA EOSDIS Land Processes DAAC, NASADEM Merged DEM Global 1 arc second V001, 2020. URL `https://doi.org/10.5067/MEaSUREs/NASADEM/NASADEM_HGT.001`.

Newman, G. A., Anderson, W. L., and Hohmann, G. W. 1987. Interpretation of transient electromagnetic soundings over three-dimensional structures for the central-loop configuration. *Geophysical Journal International*, **89**(3): 889–914. ISSN 1365-246X.

Niemeyer, H., Gonzalez, G., and Martinez-De Los Rios, E. 1996. Evolución tectónica cenozoica del margen continental activo de Antofagasta, norte de Chile. *Andean Geology*, **23**(2): 165–186. ISSN 0718-7106.

Ninnemann, L., 2020. *Seismische Abbildung der Struktur dreier Tonpfannen in der Atacama-Wüste mit Hilfe von Ersteinsatz-Laufzeittomographie*. B.sc. thesis, Institute of Geophysics and Geoinformatics, TU Bergakademie Freiberg.

Nocedal, J. and Wright, S. J. 1999. *Numerical optimization*. Springer.

Oasis, M. SEEQUENT, Oasis-Montaj, 2021. URL `https://www.seequent.com/products-solutions/geosoft-oasis-montaj/`.

Oldenburg, D. W., Haber, E., and Shekhtman, R. 2013. Three dimensional inversion of multisource time domain electromagnetic data. *Geophysics*, **78**(1): E47–E57. ISSN 0016-8033.

Palacky, G. 1988. Resistivity characteristics of geologic targets. *Electromagnetic methods in applied geophysics*, **1**: 53–129.

Pardo-Casas, F. and Molnar, P. 1987. Relative motion of the Nazca (Farallon) and South American plates since Late Cretaceous time. *Tectonics*, **6**(3): 233–248.

Pellerin, L. 2002. Applications of electrical and electromagnetic methods for environmental and geotechnical investigations. *Surveys in Geophysics*, **23**(2): 101–132. ISSN 1573-0956.

Peng, R., Han, B., Liu, Y., and Hu, X. 2021. EM3DANI: A Julia package for fully anisotropic 3D forward modeling of electromagnetic data. *Geophysics*, **86**(5): F49–F60. ISSN 0016-8033.

Peng, R., Hu, X., and Han, B. 2016. 3-D Inversion of frequency-domain CSEM data based on Gauss-Newton Optimization. *Chinese Journal of Geophysics*, **59**(5): 560–572. ISSN 0898-9591.

Pfeiffer, M., Morgan, A., Heimsath, A., Jordan, T., Howard, A., and Amundson, R. 2021. Century scale rainfall in the absolute Atacama Desert: Landscape response and implications for past and future rainfall. *Quaternary Science Reviews*, **254**: 106797. ISSN 0277-3791.

Quezada, A., Vasquez, P., Sepúlveda, F., Blanco, N., and Tomlinson, A. 2012. Mapa Compilación Geológica Área Quillagua-Salar Grande 1: 100.000. *Servicio Nacional de Geologica y Mineria Gobierno Regional de Tarapacá.*

Rajagopalan, S. 2003. Analytic signal vs. reduction to pole: solutions for low magnetic latitudes. *Exploration Geophysics*, **34**(4): 257–262. ISSN 1834-7533.

Ritter, B., Binnie, S. A., Stuart, F. M., Wennrich, V., and Dunai, T. J. 2018a. Evidence for multiple Plio-Pleistocene lake episodes in the hyperarid Atacama Desert. *Quaternary Geochronology*, **44**: 1–12. ISSN 1871-1014.

Ritter, B., Stuart, F. M., Binnie, S. A., Gerdes, A., Wennrich, V., and Dunai, T. J. 2018b. Neogene fluvial landscape evolution in the hyperarid core of the Atacama Desert. *Scientific reports*, **8**(1): 1–16. ISSN 2045-2322.

Ritter, B., Wennrich, V., Medialdea, A., Brill, D., King, G., Schneiderwind, S., Niemann, K., Fernández-Galego, E., Diederich, J., and Rolf, C. 2019. Climatic fluctuations in the hyperarid core of the Atacama Desert during the past 215 ka. *Scientific reports*, **9**(1): 1–13. ISSN 2045-2322.

Rochlitz, R., Skibbe, N., and Günther, T. 2019. custEM: Customizable finite-element simulation of complex controlled-source electromagnetic datacustEM: customizable 3D CSEM modeling. *Geophysics*, **84**(2): F17–F33. ISSN 0016-8033.

Rochlitz, R., Seidel, M., and Börner, R.-U. 2021. Evaluation of three approaches for simulating 3-D time-domain electromagnetic data. *Geophysical Journal International*, **227**(3): 1980–1995. ISSN 0956-540X.

Rödder, A. and Tezkan, B. 2013. A 3D resistivity model derived from the transient electromagnetic data observed on the Araba fault, Jordan. *Journal of applied geophysics*, **88**: 42–51. ISSN 0926-9851.

Rodi, W. and Mackie, R. L. 2001. Nonlinear conjugate gradients algorithm for 2-D magnetotelluric inversion. *Geophysics*, **66**(1): 174–187. ISSN 0016-8033.

Roest, W. R., Verhoef, J., and Pilkington, M. 1992. Magnetic interpretation using the 3-D analytic signal. *Geophysics*, **57**(1): 116–125. ISSN 0016-8033.

Sáez, A., Cabrera, L., Jensen, A., and Chong, G. 1999. Late Neogene lacustrine record and palaeogeography in the Quillagua–Llamara basin, Central Andean fore-arc (northern Chile). *Palaeogeography, Palaeoclimatology, Palaeoecology*, **151**(1-3): 5–37. ISSN 0031-0182.

Scheuber, E. and Andriessen, P. A. 1990. The kinematic and geodynamic significance of the Atacama fault zone, northern Chile. *Journal of Structural Geology*, **12**(2): 243–257. ISSN 0191-8141.

Scheuber, E. and Gonzalez, G. 1999. Tectonics of the Jurassic-Early Cretaceous magmatic arc of the north Chilean Coastal Cordillera (22°–26° S): A story of crustal deformation along a convergent plate boundary. *Tectonics*, **18**(5): 895–910. ISSN 0278-7407.

Scholl, C., 2005. *The influence of multidimensional structures on the interpretation of LOTEM data with one-dimensional models and the application to data from Israel*. Ph.D. Thesis, Institute of Geophysics and Meteorology, University of Cologne.

Schwarzbach, C. and Haber, E. 2013. Finite element based inversion for time-harmonic electromagnetic problems. *Geophysical Journal International*, **193**(2): 615–634. ISSN 1365-246X.

Seidel, M., 2019. *A 3D time domain CSEM forward modeling code using custEM and FEniCS*. Ph.D. Thesis, Institute of Geophysics and Meteorology, University of Cologne.

Ślzak, K., Díaz, D., Vargas, J. A., Cordell, D., Reyes-Cordova, F., and Segovia, M. J. 2021. Magnetotelluric image of the Chilean subduction zone in the Salar de Atacama region (23°-24° S): Insights into factors controlling the distribution of volcanic arc magmatism. *Physics of the Earth and Planetary Interiors*, p. 106765. ISSN 0031-9201.

Spector, A. and Grant, F. 1970. Statistical models for interpreting aeromagnetic data. *Geophysics*, **35**(2): 293–302. ISSN 0016-8033.

Spies, B. R. 1989. Depth of investigation in electromagnetic sounding methods. *Geophysics*, **54**(7): 872–888. ISSN 0016-8033.

Spies, B. R. and Frischknecht, F. C. 1991. Electromagnetic sounding. Electromagnetic methods in applied geophysics. **2**: 285–426.

Strack, K.-M. 1992. *Exploration with deep transient electromagnetics*, volume 373. Elsevier Amsterdam.

Streich, R. 2009. 3D finite-difference frequency-domain modeling of controlled-source electromagnetic data: Direct solution and optimization for high accuracy. *Geophysics*, **74**(5): F95–F105. ISSN 0016-8033.

Sudha, K., Tezkan, B., Israil, M., and Rai, J. 2011. Combined electrical and electromagnetic imaging of hot fluids within fractured rock in rugged Himalayan terrain. *Journal of applied geophysics*, **74**(4): 205–214. ISSN 0926-9851.

Talwani, M. 1964. Computation of magnetic anomalies caused by two-dimensional bodies of arbitrary shape. *Computers in the mineral industries*, **1**: 464–480.

Taylor, G., Grocott, J., Pope, A., and Randall, D. 1998. Mesozoic fault systems, deformation and fault block rotation in the Andean forearc: a crustal scale strike-slip duplex in the Coastal Cordillera of northern Chile. *Tectonophysics*, **299**(1-3): 93–109. ISSN 0040-1951.

Telford, W. M., Telford, W., Geldart, L., Sheriff, R. E., and Sheriff, R. E. 1990. *Applied geophysics*. Cambridge university press. ISBN 0521339383.

Tezkan, B. 1999. A review of environmental applications of quasi-stationary electromagnetic techniques. *Surveys in Geophysics*, **20**(3): 279–308. ISSN 1573-0956.

Tikhonov, A. N. and Arsenin, V. I. 1977. *Solutions of Ill-posed Problems: Andrey N. Tikhonov and Vasiliy Y. Arsenin. Translation Editor Fritz John*. Wiley. ISBN 0470991240.

Um, E. S., Harris, J. M., and Alumbaugh, D. L. 2010. 3D time-domain simulation of electromagnetic diffusion phenomena: A finite-element electric-field approach. *Geophysics*, **75**(4): F115–F126. ISSN 0016-8033.

Vásquez, P., Sepúlveda, F., Quezada, A., Aguilef, S., Franco, C., and Blanco, N. 2018. Cartas Guanillos del Norte y Salar de Llamara, Regiones de Tarapacá y Antofagasta, Serie Geología Básica 195-196. 1 mapa escala 1: 100.000.

Viezzoli, A., Christiansen, A. V., Auken, E., and Sørensen, K. 2008. Quasi-3D modeling of airborne TEM data by spatially constrained inversion. *Geophysics*, **73**(3): F105–F113. ISSN 0016-8033.

Von Huene, R., Weinrebe, W., and Heeren, F. 1999. Subduction erosion along the North Chile margin. *Journal of geodynamics*, **27**(3): 345–358. ISSN 0264-3707.

Walk, J., Stauch, G., Reyers, M., Vásquez, P., Sepúlveda, F. A., Bartz, M., Hoffmeister, D., Brückner, H., and Lehmkuhl, F. 2020. Gradients in climate, geology, and topography affecting coastal alluvial fan morphodynamics in hyperarid regions–the Atacama perspective. *Global and Planetary Change*, **185**: 102994. ISSN 0921-8181.

Ward, S. 1990. Resistivity and induced polarization methods geotechnical and environment geophysics. vol. 1, hal. 147. *Tulsa. SEG*.

Ward, S. H. and Hohmann, G. W. 1988. *Electromagnetic theory for geophysical applications*, p. 130–311. Society of Exploration Geophysicists.

Weidelt, P. 1986. Einführung in die elektromagnetische Tiefenforschung. *Lecture Technische Universät Braunschweig*.

Won, I. and Bevis, M. 1987. Computing the gravitational and magnetic anomalies due to a polygon: Algorithms and Fortran subroutines. *Geophysics*, **52**(2): 232–238. ISSN 0016-8033.

World Imagery, E. ESRI Satellite, ArcGIS, 2021. URL `https://server.arcgisonline.com/ArcGIS/rest/services/World_Imagery/MapServer/tile/{z}/{y}/{x}`.

Xiao, L., Fiandaca, G., Zhang, B., Auken, E., and Christiansen, A. V. 2022. Fast 2.5 D and 3D inversion of transient electromagnetic surveys using the octree-based finite-element method. *Geophysics*, **87**(4): E267–E277. ISSN 0016-8033.

Yáñez, G., Perez-Estay, N., Araya-Vargas, J., Sanhueza, J., Figueroa, R., Maringue, J., and Rojas, T. 2020. Shallow anatomy of the San Ramón Fault (Chile) constrained by geophysical methods: implications for its role in the Andean deformation. *Tectonics*, **39**(8): e2020TC006294. ISSN 0278-7407.

Yee, K. 1966. Numerical solution of initial boundary value problems involving Maxwell's equations in isotropic media. *IEEE Transactions on antennas and propagation*, **14**(3): 302–307. ISSN 0018-926X.

Yogeshwar, P. and Tezkan, B. 2018. Analysing two-dimensional effects in central loop transient electromagnetic sounding data using a semi-synthetic tipper approach. *Geophysical Prospecting*, **66**(2): 444–456. ISSN 1365-2478.

Yogeshwar, P., 2014. *A resistivity-depth model of the central Azraq basin area, Jordan: 2D forward and inverse modeling of time domain electromagnetic data*. Ph.D. Thesis, Institute of Geophysics and Meteorology, University of Cologne.

Yogeshwar, P., Tezkan, B., and Haroon, A. 2013. Investigation of the Azraq sedimentary basin, Jordan using integrated geoelectrical and electromagnetic techniques. *Near Surface Geophysics*, **11**(4): 381–390. ISSN 1569-4445.

Yogeshwar, P., Küpper, M., Tezkan, B., Rath, V., Kiyan, D., Byrdina, S., Cruz, J., Andrade, C., and Viveiros, F. 2020. Innovative boat-towed transient electromagnetics — Investigation of the Furnas volcanic lake hydrothermal system, Azores. *Geophysics*, **85**(2): E41–E56. ISSN 0016-8033. doi: 10.1190/geo2019-0292.1. URL `https://doi.org/10.1190/geo2019-0292.1`.

Zhang, J. and Toksöz, M. N. 1998. Nonlinear refraction traveltime tomography. *Geophysics*, **63**(5): 1726–1737. ISSN 0016-8033.

Appendix

A1 TEM sounding locations

Table A1: TEM sounding locations for the PAG clay pan. The sounding name, and UTM coordinates are given.

Sounding	**North** m	**East** m	**Altitude** m	**Sounding**	**North** m	**East** m	**Altitude** m
A1T1	7617879	405010	948	*A3T4*	7617416	405379	940
A1T2	7617828	405162	940	*A3T5*	7617368	405535	939
A1T3	7617778	405314	938	*A3T6*	7617317	405687	940
A1T4	7617725	405462	939	*A4T1*	7617415	404886	939
A1T5	7617676	405617	939	*A4T2*	7617365	405038	940
A1T6	7617625	405769	942	*A4T3*	7617315	405190	938
A2T1	7617855	404588	943	*A4T4*	7617261	405337	937
A2T2	7617830	404664	941	*A4T5*	7617213	405494	939
A2T3	7617805	404740	940	*A4T6*	7617162	405645	937
A2T4	7617779	404815	940	*A5T1*	7617261	404845	942
A2T5	7617754	404891	940	*A5T2*	7617211	404997	941
A2T6	7617728	404967	940	*A5T3*	7617160	405149	940
A2T7	7617703	405043	938	*A5T4*	7617107	405296	940
A2T8	7617678	405119	936	*A5T5*	7617058	405452	940
A2T9	7617652	405195	936	*A5T6*	7617007	405604	939
A2T10	7617627	405271	938	*A6T1*	7617803	405483	938
A2T11	7617601	405347	941	*A6T3*	7617648	405441	940
A2T12	7617576	405422	939	*A6T5*	7617494	405400	939
A2T13	7617551	405498	938	*A6T7*	7617339	405358	940
A2T14	7617525	405574	939	*A6T9*	7617184	405317	938
A2T15	7617500	405650	941	*A6T11*	7617030	405276	941
A2T16	7617475	405726	940	*A6T12*	7616953	405255	941
A3T1	7617571	404928	939	*A6T13*	7616875	405234	943
A3T2	7617520	405080	937	*A6T14*	7616798	405213	944
A3T3	7617469	405232	938	*A6T15*	7616721	405193	947

Table A2: TEM sounding locations for the Paranal clay pan. The sounding name, and UTM coordinates are given.

Sounding	**North** m	**East** m	**Altitude** m	**Sounding**	**North** m	**East** m	**Altitude** m
B1T1	7291751	383305	2201	*B3T1*	7291751	383624	2202
B1T2	7291712	383305	2200	*B3T2*	7291712	383625	2201
B1T3	7291672	383305	2200	*B3T3*	7291672	383625	2200
B1T4	7291631	383305	2199	*B3T4*	7291631	383624	2199
B1T5	7291591	383305	2200	*B3T5*	7291591	383624	2199
B1T6	7291551	383305	2200	*B3T6*	7291551	383625	2199
B1T7	7291511	383304	2199	*B3T7*	7291512	383624	2200
B1T8	7291472	383305	2199	*B3T8*	7291472	383624	2199
B1T9	7291431	383305	2200	*B3T9*	7291432	383625	2198
B1T10	7291391	383305	2199	*B3T10*	7291391	383625	2197
B1T11	7291351	383305	2198	*B3T11*	7291351	383624	2196
B1T12	7291311	383305	2198	*B3T12*	7291312	383624	2196
B1T13	7291272	383305	2198	*B3T13*	7291272	383625	2195
B1T14	7291231	383304	2198	*B3T14*	7291232	383624	2195
B1T15	7291191	383305	2199	*B3T15*	7291191	383624	2194
B1T16	7291151	383305	2198	*B3T16*	7291151	383624	2194
B1T17	7291111	383305	2199	*B3T17*	7291111	383625	2195
B1T18	7291072	383305	2199	*B3T18*	7291072	383624	2197
B1T19	7291032	383305	2199	*B3T19*	7291032	383624	2198
B1T20	7290991	383305	2200	*B3T20*	7290991	383625	2198
B1T21	7290951	383304	2201	*B3T21*	7290951	383624	2199
B1T22	7290911	383305	2202	*B3T22*	7290911	383624	2200
B1T23	7290872	383305	2202	*B3T23*	7290872	383624	2201
B2T1	7291791	383464	2204	*B4T1*	7291791	383784	2202
B2T2	7291712	383464	2201	*B4T2*	7291712	383785	2200
B2T3	7291631	383464	2198	*B4T3*	7291631	383784	2198
B2T4	7291551	383464	2196	*B4T4*	7291551	383785	2196
B2T5	7291472	383464	2194	*B4T5*	7291472	383784	2198
B2T6	7291391	383465	2195	*B4T6*	7291391	383785	2200
B2T7	7291311	383464	2194	*B4T7*	7291312	383785	2200
B2T8	7291231	383464	2192	*B4T8*	7291232	383784	2198
B2T9	7291151	383464	2192	*B4T9*	7291151	383785	2196
B2T10	7291072	383464	2195	*B4T10*	7291072	383784	2195
B2T11	7290991	383464	2199	*B4T11*	7290991	383785	2195
B2T12	7290911	383464	2201	*B4T12*	7290911	383784	2198
B2T13	7290832	383465	2203	*B4T13*	7290832	383785	2200

Table A3: TEM sounding locations for the Paranal clay pan. The sounding name, and UTM coordinates are given.

Sounding	**North** m	**East** m	**Altitude** m	**Sounding**	**North** m	**East** m	**Altitude** m
B5T1	7291751	383945	2200	*B7T1*	7291312	383185	2199
B5T2	7291712	383945	2200	*B7T2*	7291312	383225	2199
B5T3	7291672	383944	2200	*B7T3*	7291312	383265	2199
B5T4	7291631	383945	2200	*B7T4*	7291312	383305	2198
B5T5	7291591	383945	2200	*B7T5*	7291312	383345	2197
B5T6	7291551	383945	2200	*B7T6*	7291312	383385	2196
B5T7	7291512	383944	2202	*B7T7*	7291312	383425	2195
B5T8	7291472	383945	2201	*B7T8*	7291312	383465	2194
B5T9	7291431	383945	2199	*B7T9*	7291312	383505	2194
B5T10	7291391	383945	2199	*B7T10*	7291312	383545	2195
B5T11	7291351	383945	2199	*B7T11*	7291312	383585	2195
B5T12	7291311	383945	2200	*B7T12*	7291312	383625	2196
B5T13	7291272	383945	2201	*B7T13*	7291312	383665	2196
B5T14	7291231	383945	2201	*B7T14*	7291312	383705	2195
B5T15	7291191	383945	2201	*B7T15*	7291312	383745	2198
B5T16	7291151	383945	2199	*B7T16*	7291312	383785	2200
B5T17	7291111	383945	2198	*B7T17*	7291312	383825	2202
B5T18	7291072	383944	2198	*B7T18*	7291312	383865	2202
B5T19	7291031	383945	2197	*B7T19*	7291312	383905	2201
B5T20	7290991	383945	2195	*B7T20*	7291312	383945	2200
B5T21	7290951	383945	2195	*B7T21*	7291312	383985	2199
B5T22	7290911	383945	2196	*B7T22*	7291312	384025	2199
B5T23	7290872	383945	2197	*B8T1*	7291148	383231	2200
B6T1	7291471	383223	2199	*B8T3*	7291148	383391	2194
B6T3	7291471	383382	2197	*B8T5*	7291148	383551	2193
B6T5	7291471	383542	2196	*B8T7*	7291148	383710	2196
B6T7	7291471	383703	2196	*B8T9*	7291148	383870	2197
B6T9	7291471	383863	2202	*B8T11*	7291148	384031	2201
B6T11	7291471	384022	2198				

A2 TEM field data of PAG clay pan

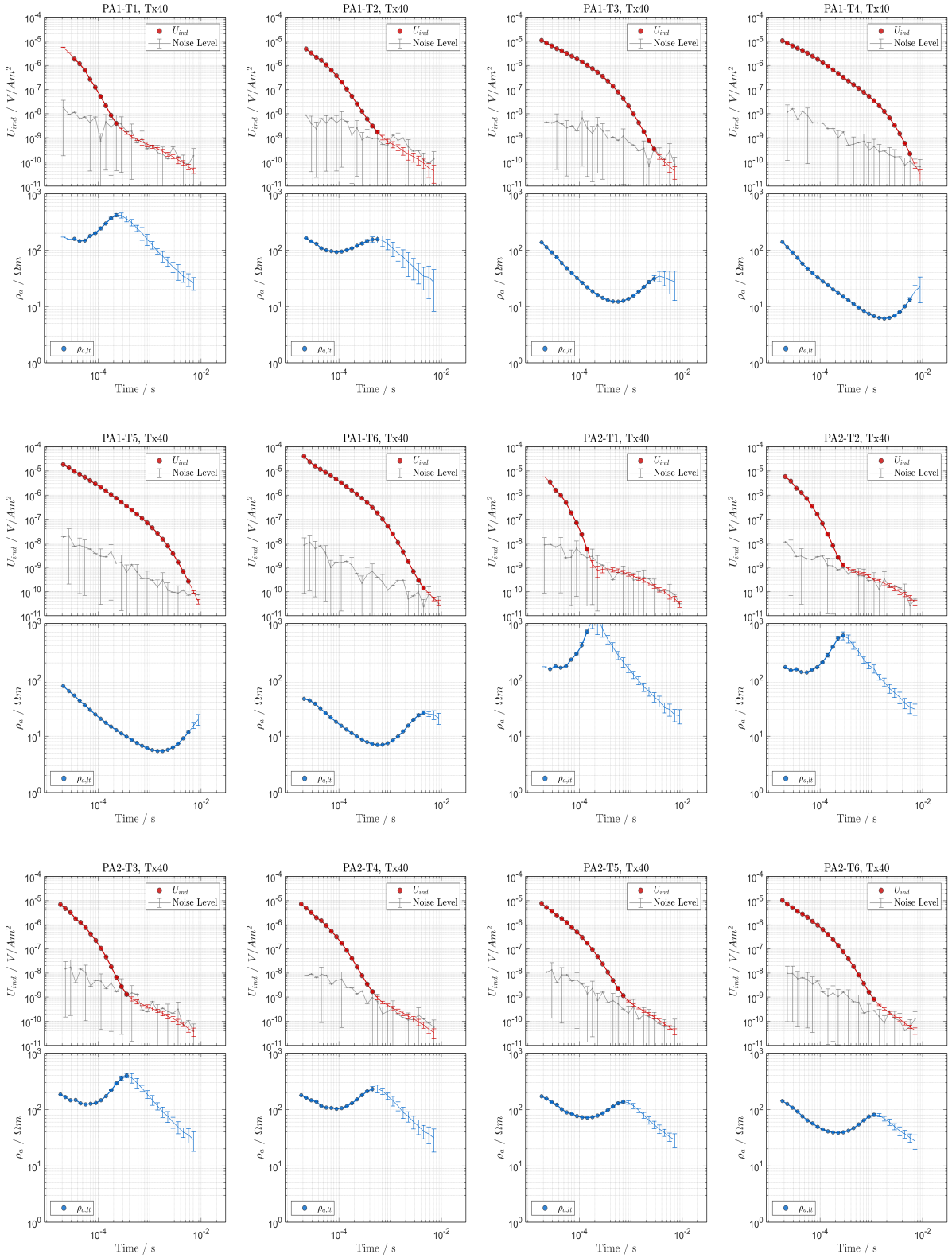

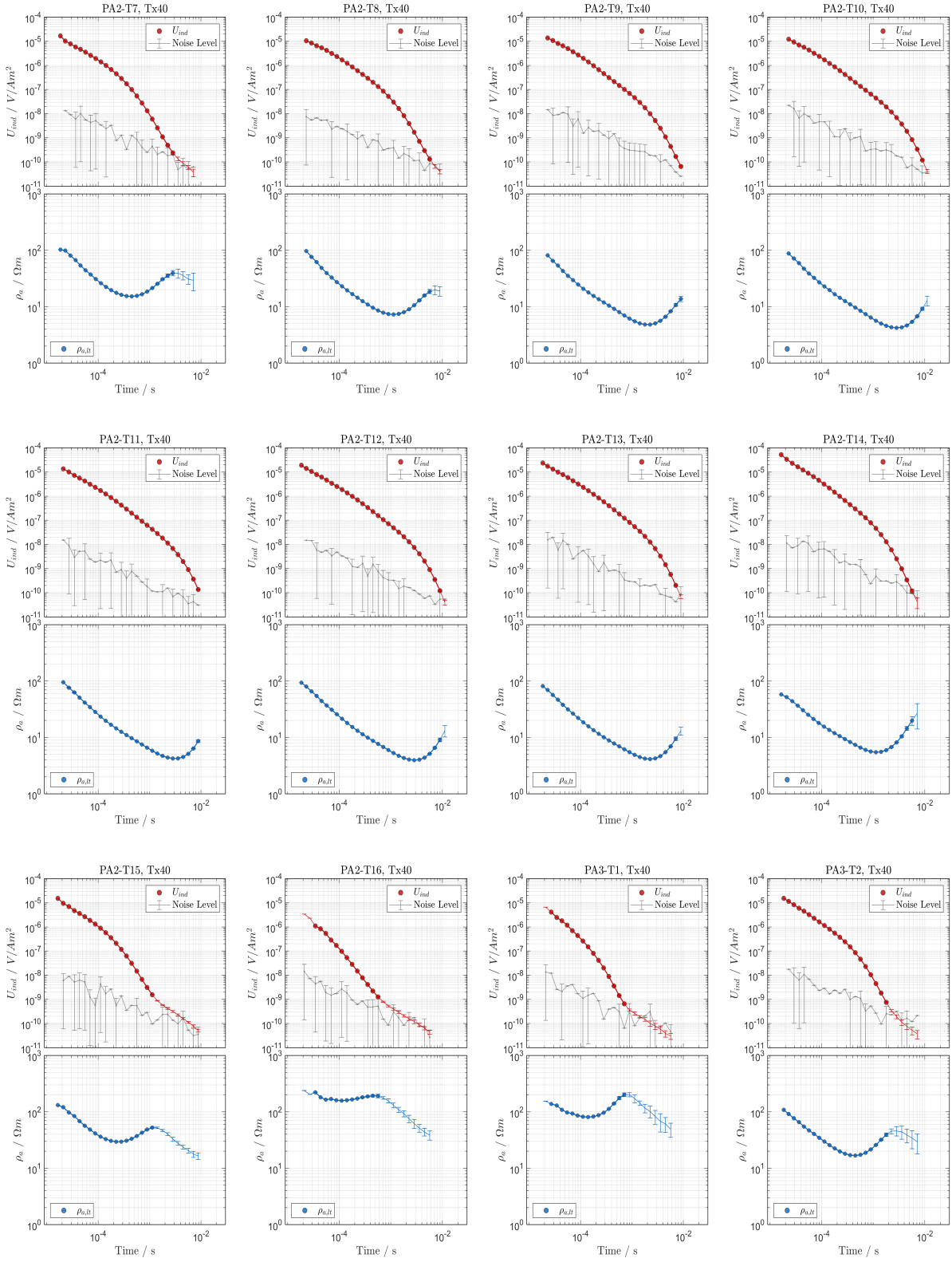
PA2-T7, Tx40
PA2-T8, Tx40
PA2-T9, Tx40
PA2-T10, Tx40
PA2-T11, Tx40
PA2-T12, Tx40
PA2-T13, Tx40
PA2-T14, Tx40
PA2-T15, Tx40
PA2-T16, Tx40
PA3-T1, Tx40
PA3-T2, Tx40
U_{ind}
Noise Level
U_{ind} / V/Am^2
ρ_a / Ωm
$\rho_{a,lt}$
Time / s

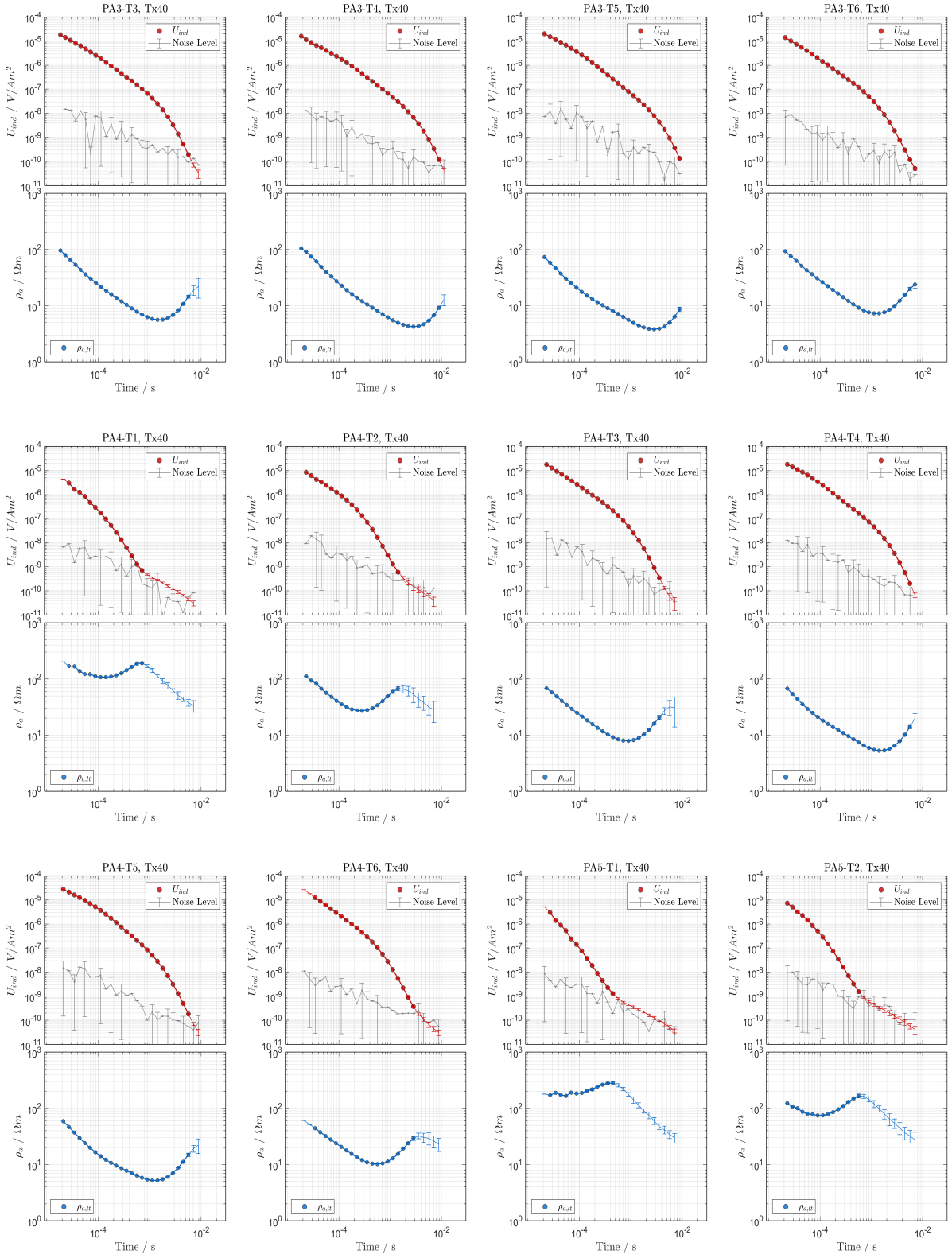
PA3-T3, Tx40
PA3-T4, Tx40
PA3-T5, Tx40
PA3-T6, Tx40
PA4-T1, Tx40
PA4-T2, Tx40
PA4-T3, Tx40
PA4-T4, Tx40
PA4-T5, Tx40
PA4-T6, Tx40
PA5-T1, Tx40
PA5-T2, Tx40
U_{ind}
Noise Level
U_{ind} / V/Am^2
ρ_a / Ωm
$\rho_{a,lt}$
Time / s

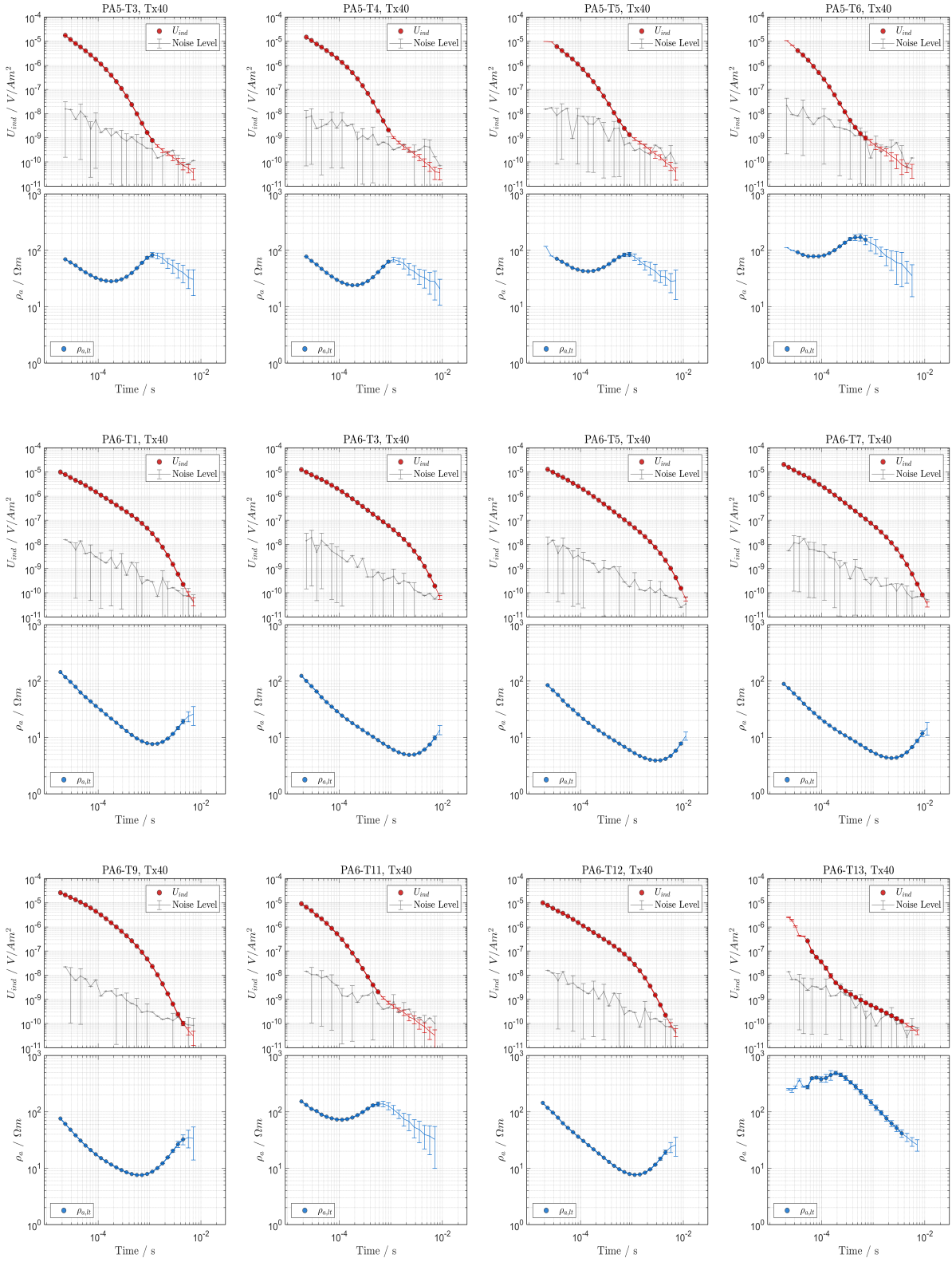
PA5-T3, Tx40
PA5-T4, Tx40
PA5-T5, Tx40
PA5-T6, Tx40
PA6-T1, Tx40
PA6-T3, Tx40
PA6-T5, Tx40
PA6-T7, Tx40
PA6-T9, Tx40
PA6-T11, Tx40
PA6-T12, Tx40
PA6-T13, Tx40
U_{ind}
Noise Level
U_{ind} / V/Am^2
ρ_a / Ωm
$\rho_{a,lt}$
Time / s

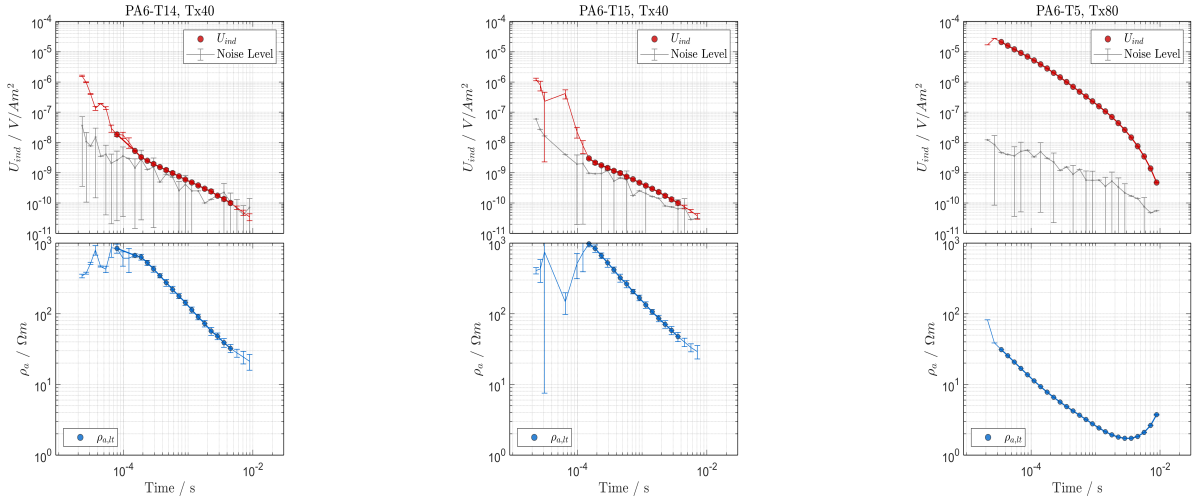

Figure A2.1: TEM field data of PAG clay pan. (a) The induced voltage and noise level in V/Am^2 and (b) late-time apparent resistivity in ohm-m.

A3 TEM field data of Paranal clay pan

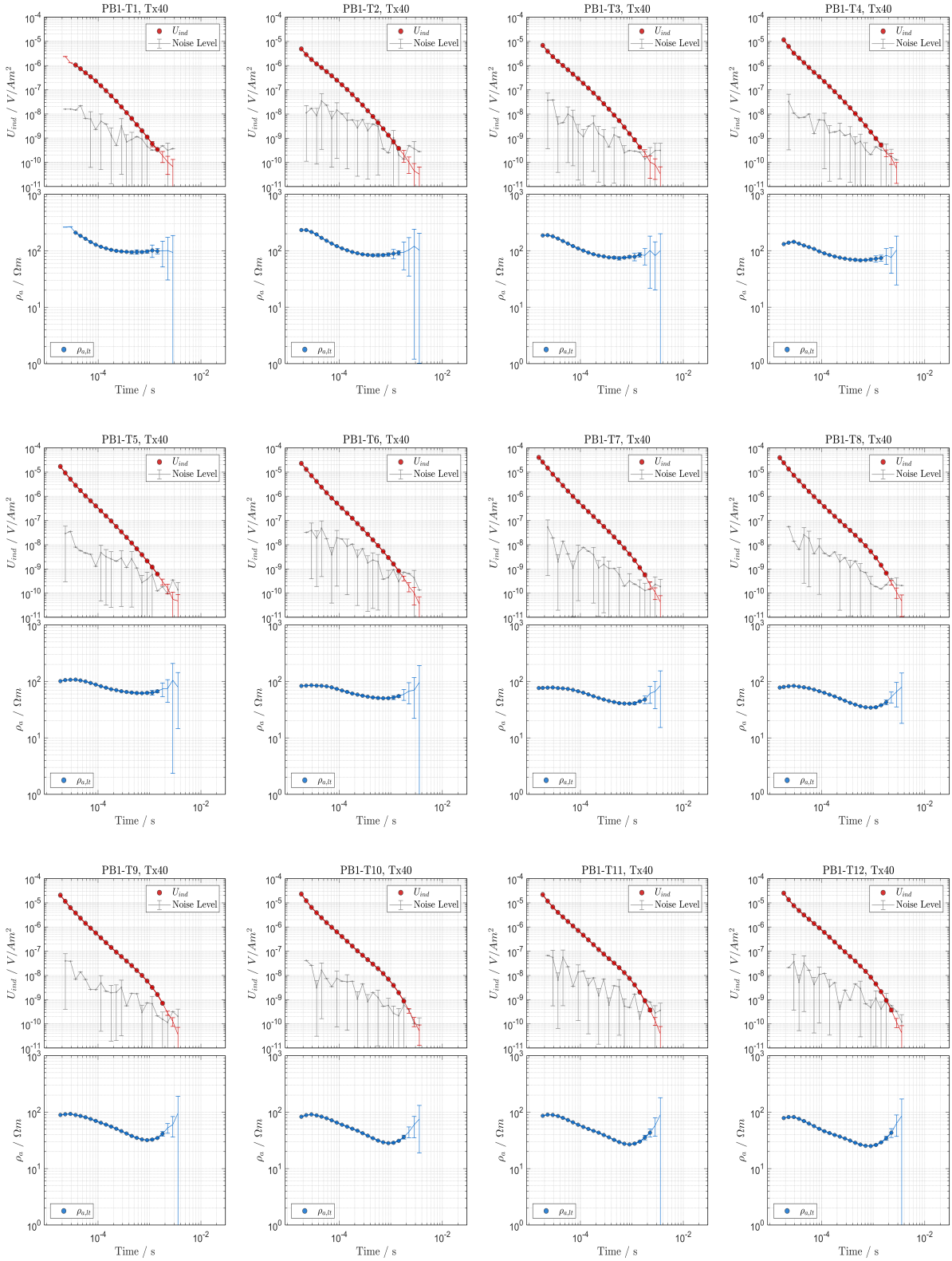

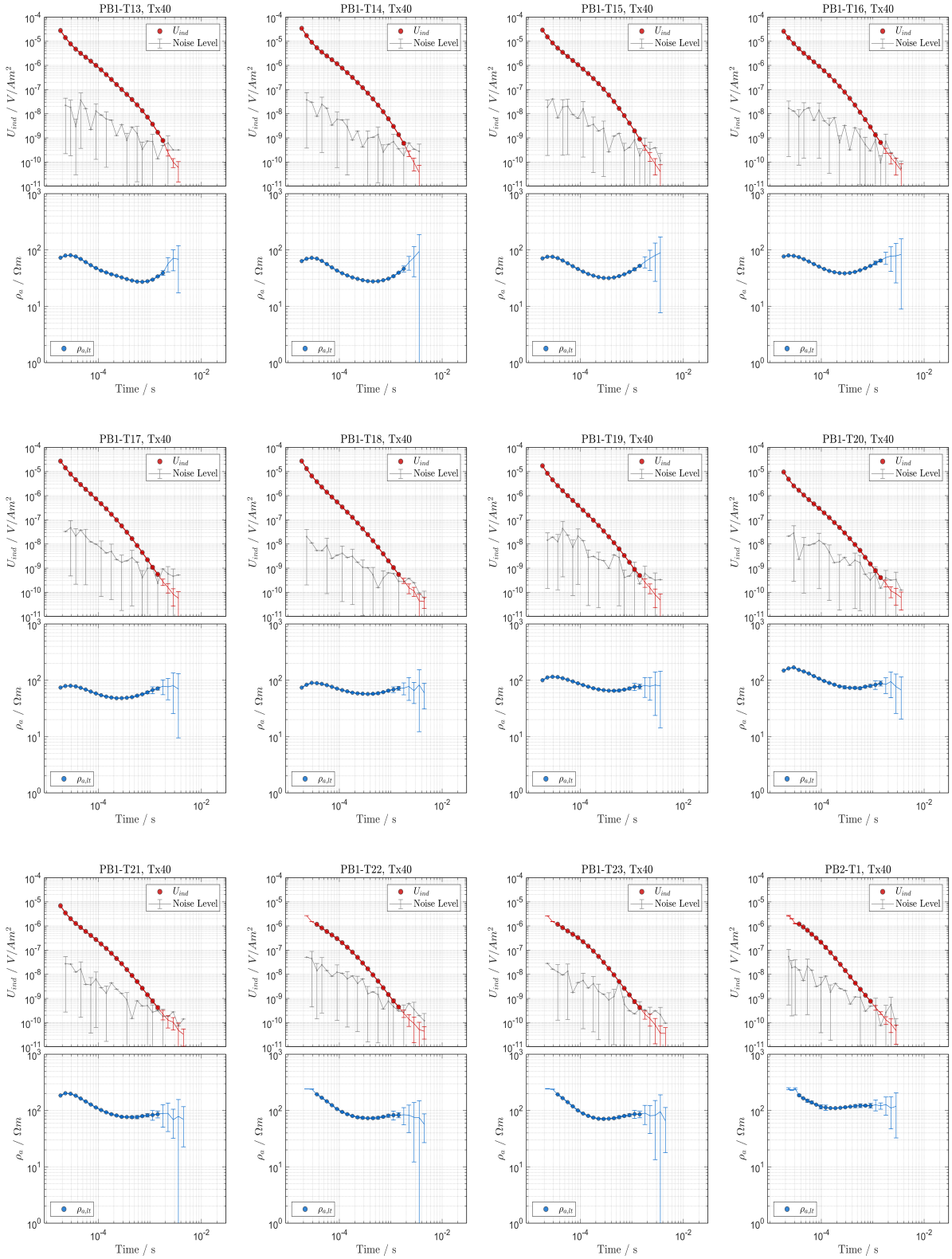
PB1-T13, Tx40
PB1-T14, Tx40
PB1-T15, Tx40
PB1-T16, Tx40
PB1-T17, Tx40
PB1-T18, Tx40
PB1-T19, Tx40
PB1-T20, Tx40
PB1-T21, Tx40
PB1-T22, Tx40
PB1-T23, Tx40
PB2-T1, Tx40
U_{ind}
Noise Level
U_{ind} / V/Am^2
ρ_a / Ωm
$\rho_{a,lt}$
Time / s

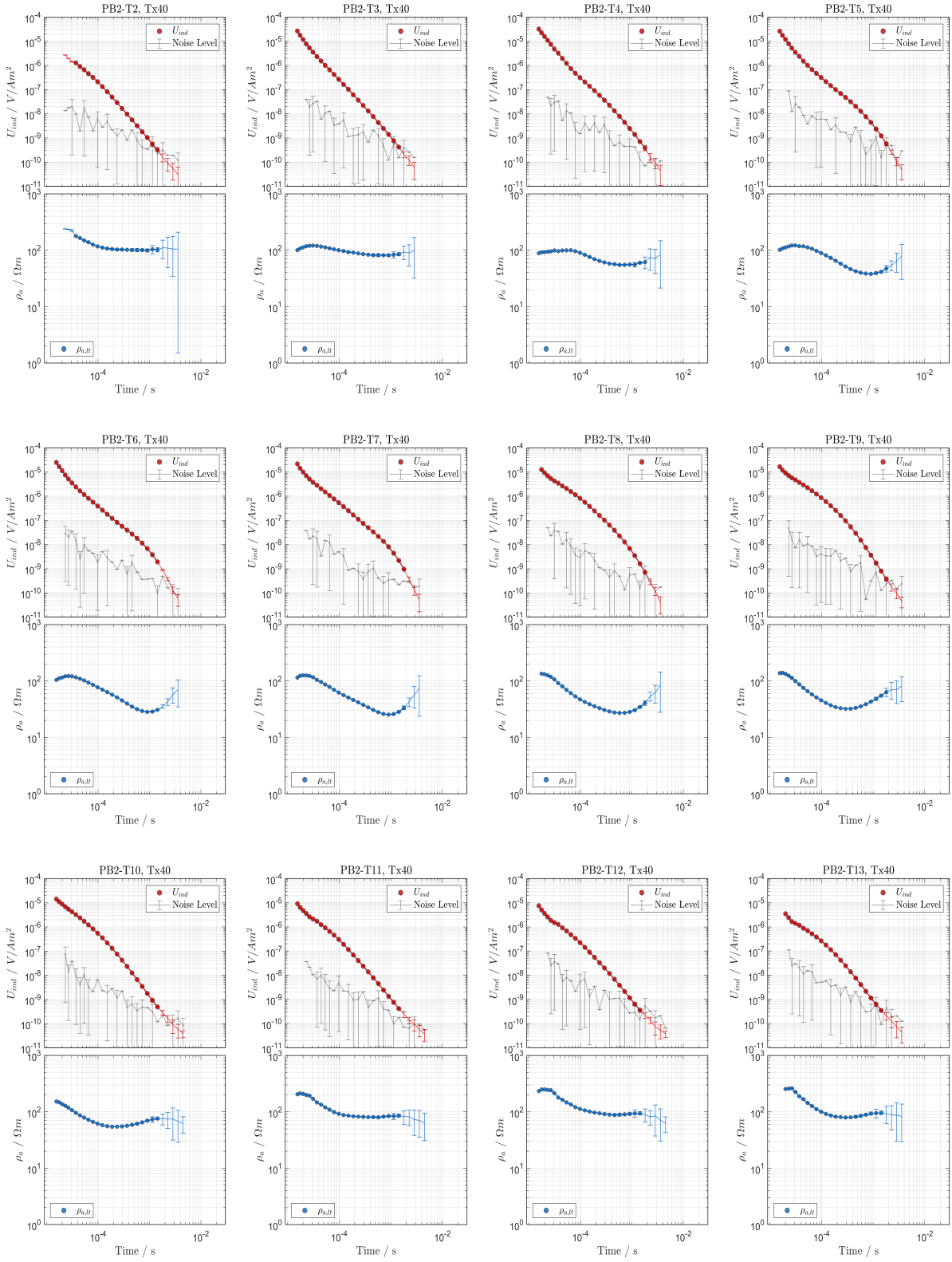
PB2-T2, Tx40
PB2-T3, Tx40
PB2-T4, Tx40
PB2-T5, Tx40
PB2-T6, Tx40
PB2-T7, Tx40
PB2-T8, Tx40
PB2-T9, Tx40
PB2-T10, Tx40
PB2-T11, Tx40
PB2-T12, Tx40
PB2-T13, Tx40
U_{ind}
Noise Level
U_{ind} / V/Am^2
ρ_a / Ωm
$\rho_{a,lt}$
Time / s

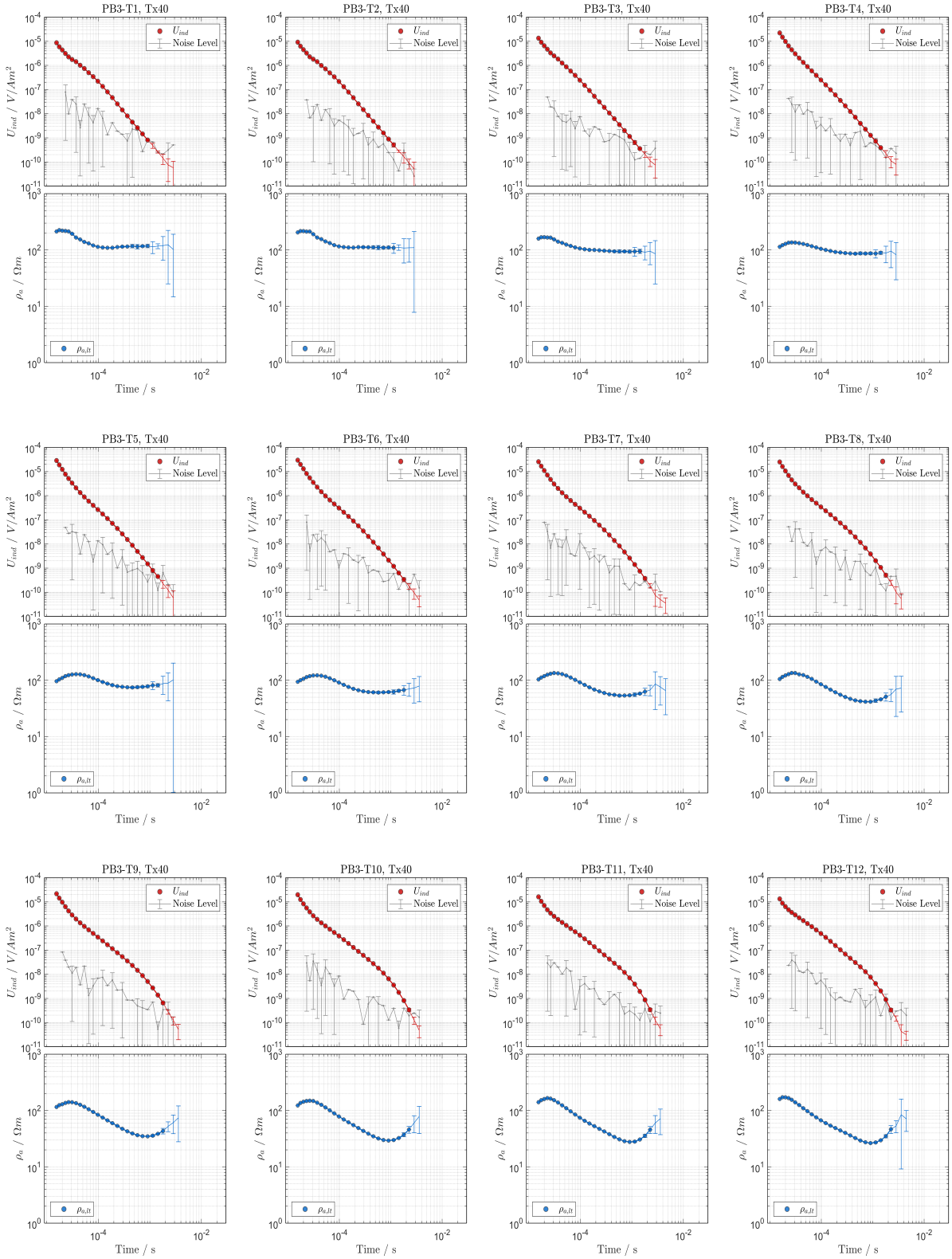
PB3-T1, Tx40
PB3-T2, Tx40
PB3-T3, Tx40
PB3-T4, Tx40
PB3-T5, Tx40
PB3-T6, Tx40
PB3-T7, Tx40
PB3-T8, Tx40
PB3-T9, Tx40
PB3-T10, Tx40
PB3-T11, Tx40
PB3-T12, Tx40
U_{ind}
Noise Level
U_{ind} / V/Am^2
ρ_a / Ωm
$\rho_{a,lt}$
Time / s

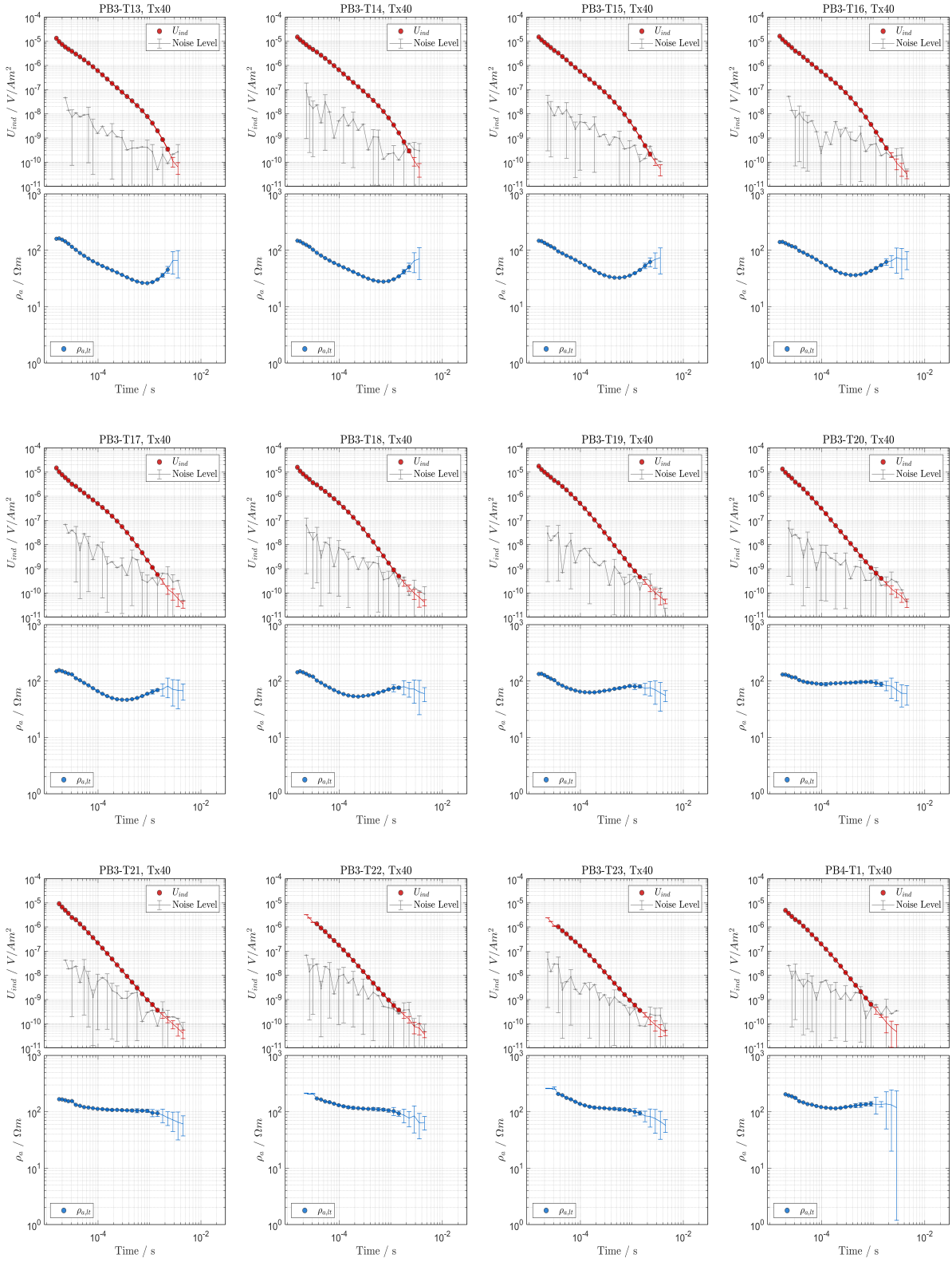
PB3-T13, Tx40
PB3-T14, Tx40
PB3-T15, Tx40
PB3-T16, Tx40
PB3-T17, Tx40
PB3-T18, Tx40
PB3-T19, Tx40
PB3-T20, Tx40
PB3-T21, Tx40
PB3-T22, Tx40
PB3-T23, Tx40
PB4-T1, Tx40
U_{ind}
Noise Level
U_{ind} / V/Am^2
ρ_a / Ωm
$\rho_{a,lt}$
Time / s

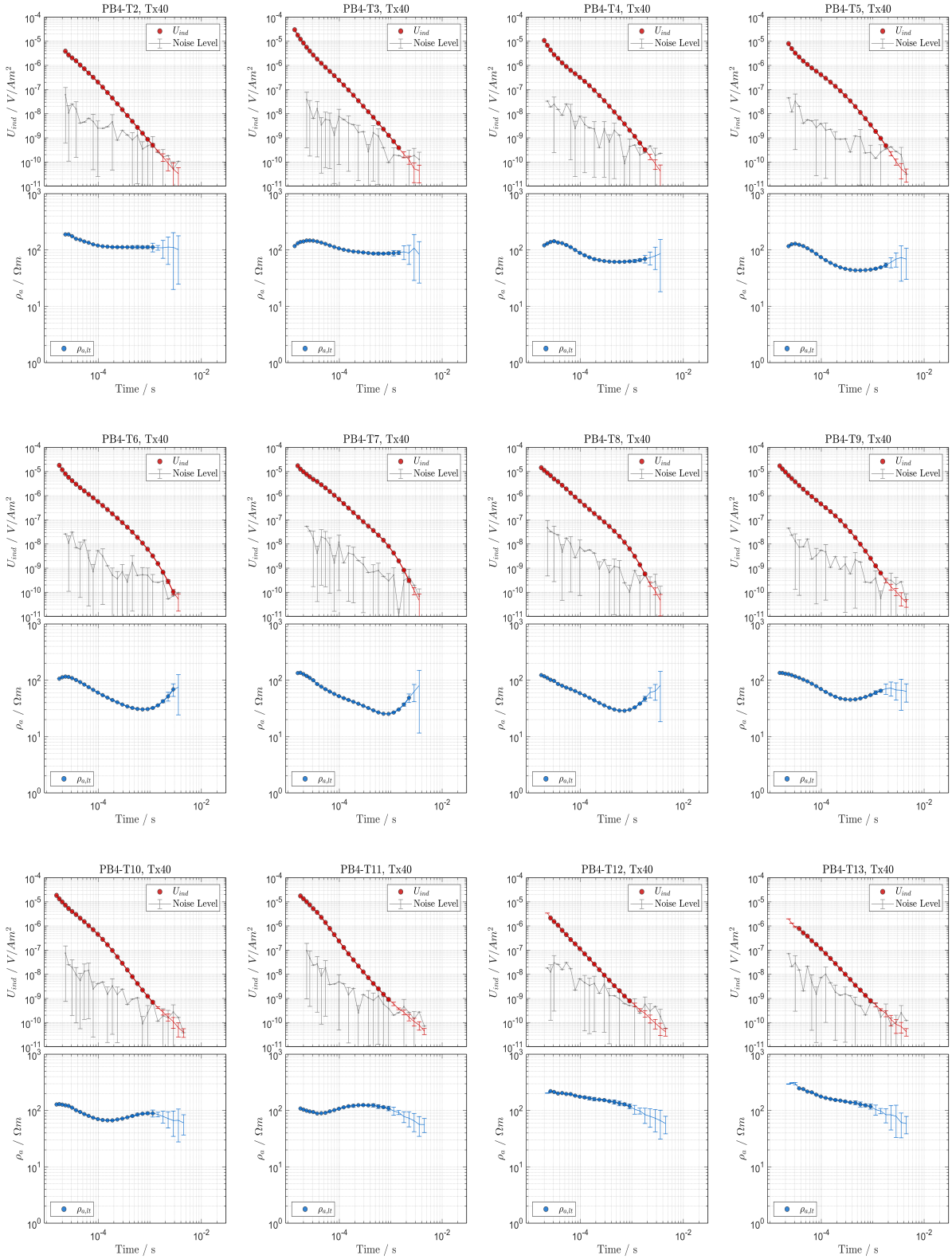
PB4-T2, Tx40
PB4-T3, Tx40
PB4-T4, Tx40
PB4-T5, Tx40
PB4-T6, Tx40
PB4-T7, Tx40
PB4-T8, Tx40
PB4-T9, Tx40
PB4-T10, Tx40
PB4-T11, Tx40
PB4-T12, Tx40
PB4-T13, Tx40
U_{ind}
Noise Level
U_{ind} / V/Am^2
ρ_a / Ωm
$\rho_{a,lt}$
Time / s

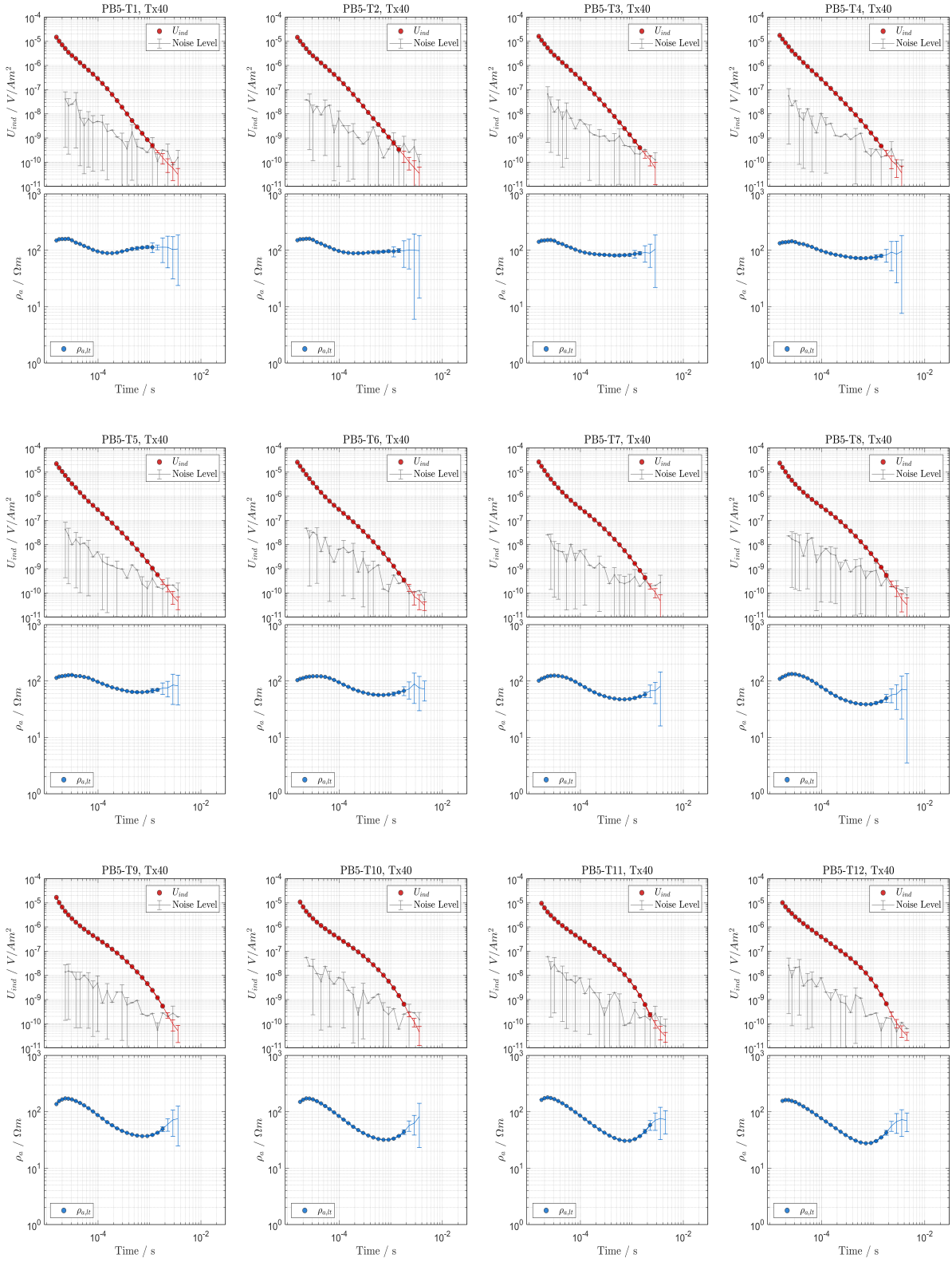
PB5-T1, Tx40
PB5-T2, Tx40
PB5-T3, Tx40
PB5-T4, Tx40
PB5-T5, Tx40
PB5-T6, Tx40
PB5-T7, Tx40
PB5-T8, Tx40
PB5-T9, Tx40
PB5-T10, Tx40
PB5-T11, Tx40
PB5-T12, Tx40
U_{ind}
Noise Level
U_{ind} / V/Am^2
ρ_a / Ωm
$\rho_{a,lt}$
Time / s

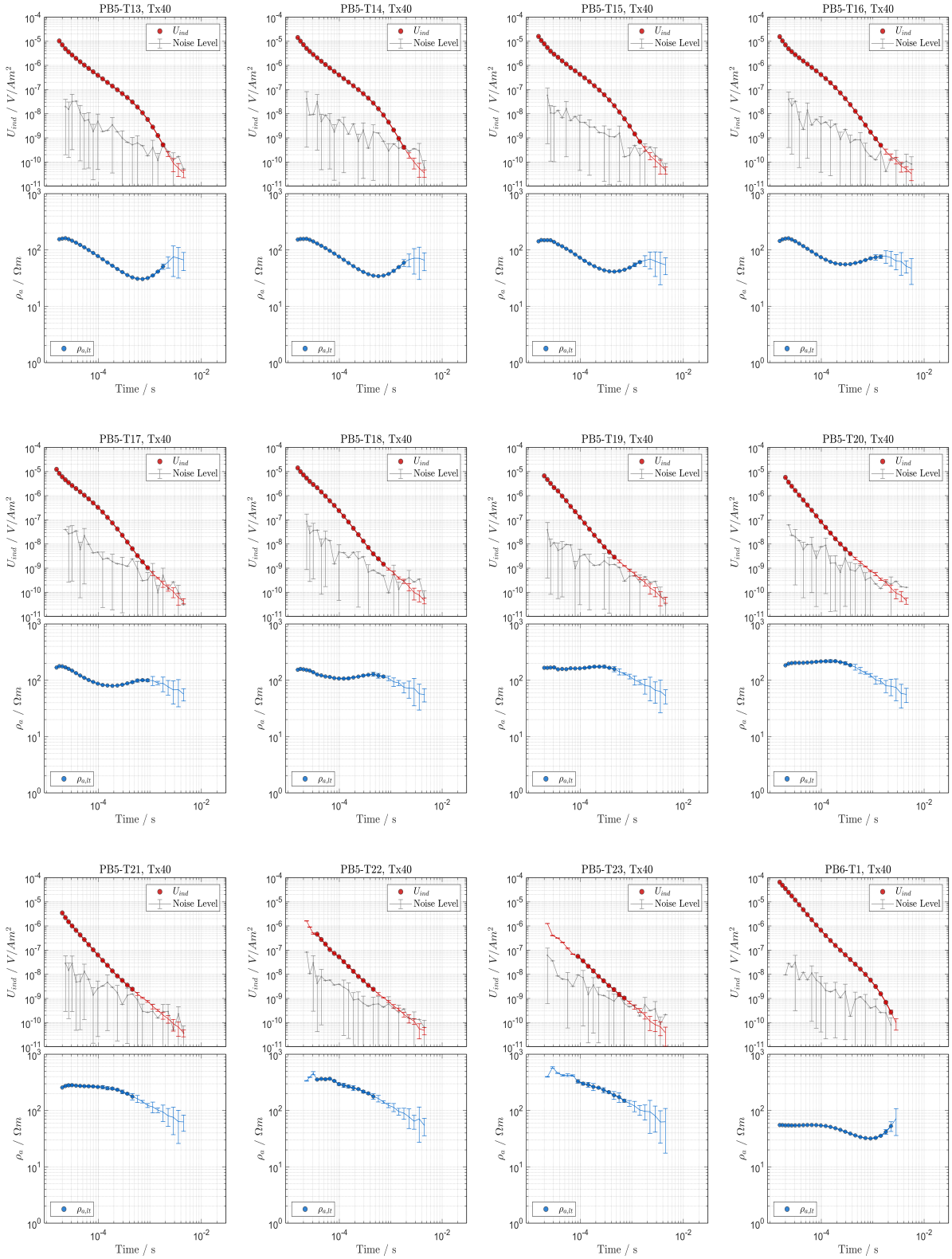
PB5-T13, Tx40
PB5-T14, Tx40
PB5-T15, Tx40
PB5-T16, Tx40
PB5-T17, Tx40
PB5-T18, Tx40
PB5-T19, Tx40
PB5-T20, Tx40
PB5-T21, Tx40
PB5-T22, Tx40
PB5-T23, Tx40
PB6-T1, Tx40
U_{ind}
Noise Level
U_{ind} / V/Am^2
ρ_a / Ωm
$\rho_{a,lt}$
Time / s

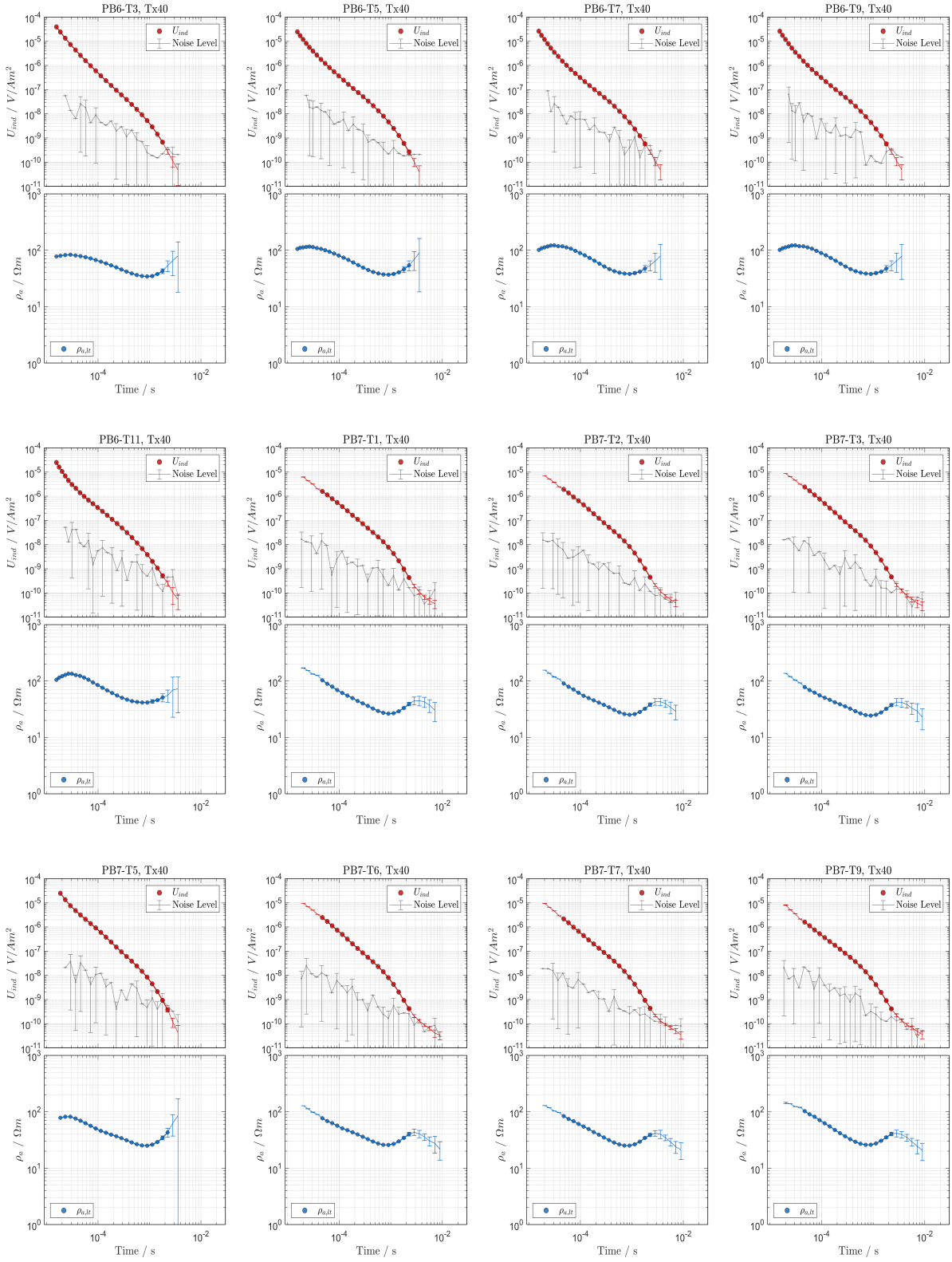
PB6-T3, Tx40
PB6-T5, Tx40
PB6-T7, Tx40
PB6-T9, Tx40
PB6-T11, Tx40
PB7-T1, Tx40
PB7-T2, Tx40
PB7-T3, Tx40
PB7-T5, Tx40
PB7-T6, Tx40
PB7-T7, Tx40
PB7-T9, Tx40
U_{ind}
Noise Level
U_{ind} / V/Am^2
ρ_a / Ωm
$\rho_{a,lt}$
Time / s

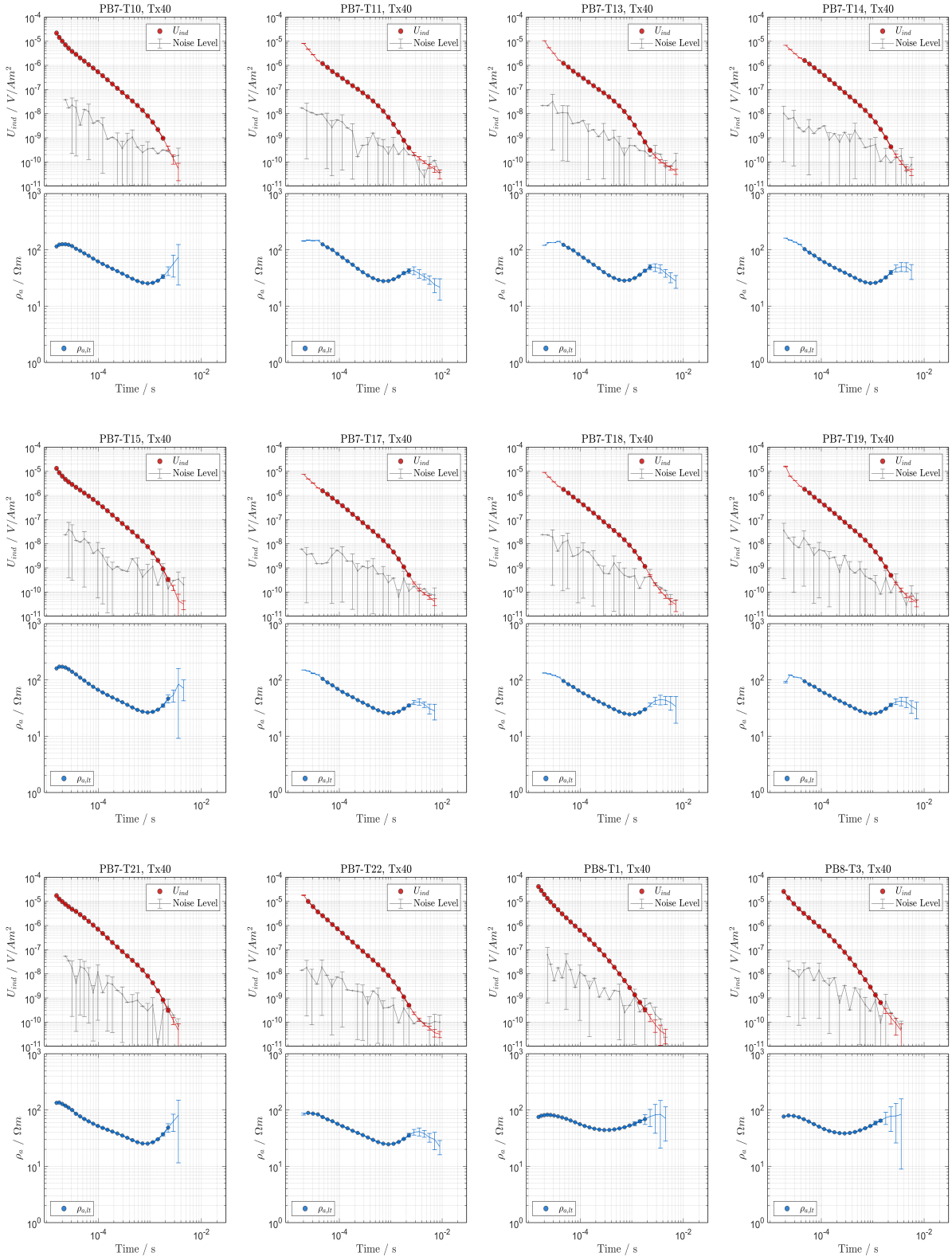
PB7-T10, Tx40
PB7-T11, Tx40
PB7-T13, Tx40
PB7-T14, Tx40
PB7-T15, Tx40
PB7-T17, Tx40
PB7-T18, Tx40
PB7-T19, Tx40
PB7-T21, Tx40
PB7-T22, Tx40
PB8-T1, Tx40
PB8-T3, Tx40
U_{ind}
Noise Level
U_{ind} / V/Am^2
ρ_a / Ωm
$\rho_{a,lt}$
Time / s

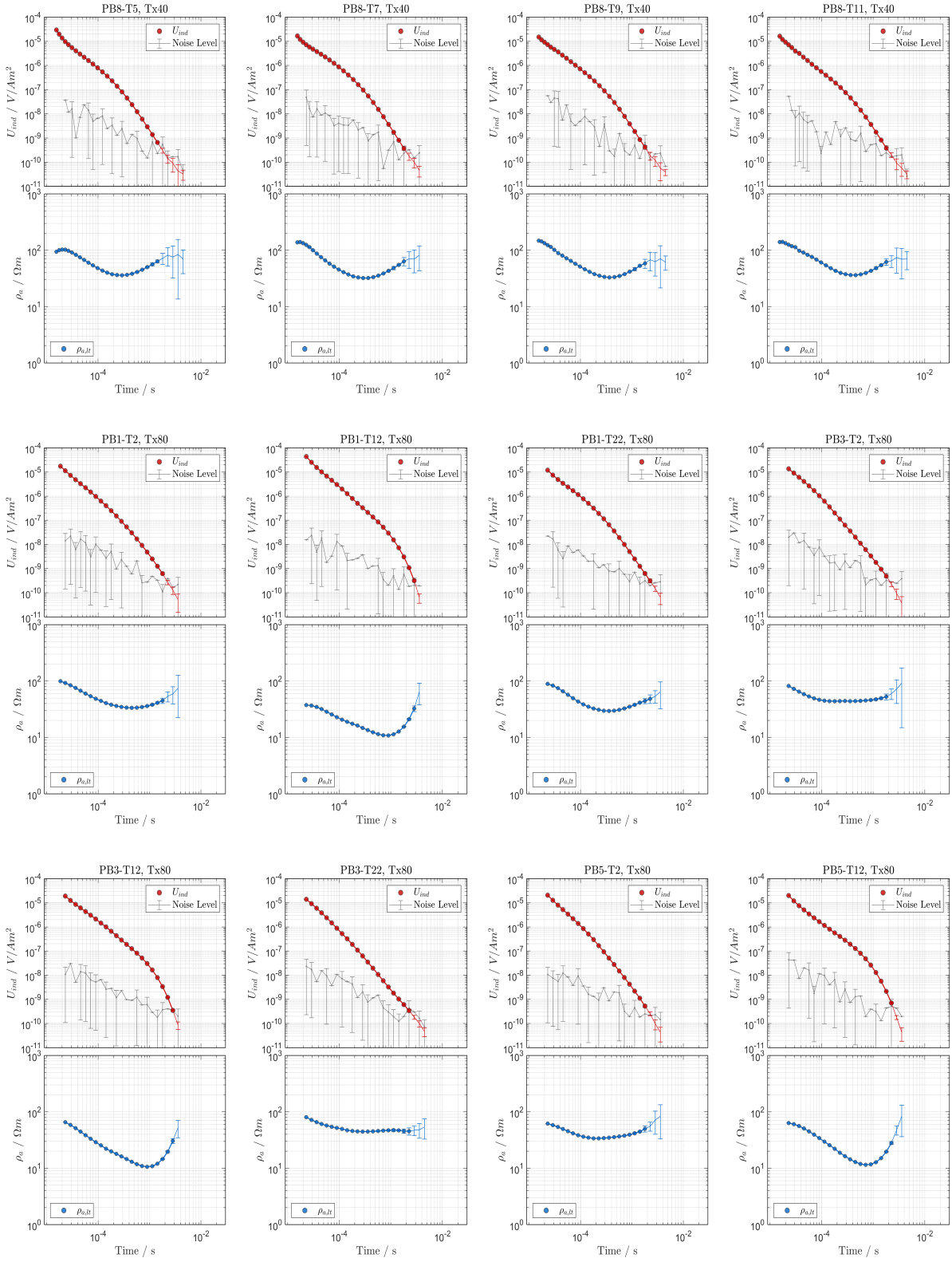
PB8-T5, Tx40
PB8-T7, Tx40
PB8-T9, Tx40
PB8-T11, Tx40
PB1-T2, Tx80
PB1-T12, Tx80
PB1-T22, Tx80
PB3-T2, Tx80
PB3-T12, Tx80
PB3-T22, Tx80
PB5-T2, Tx80
PB5-T12, Tx80
U_{ind}
Noise Level
U_{ind} / V/Am^2
ρ_a / Ωm
$\rho_{a,lt}$
Time / s

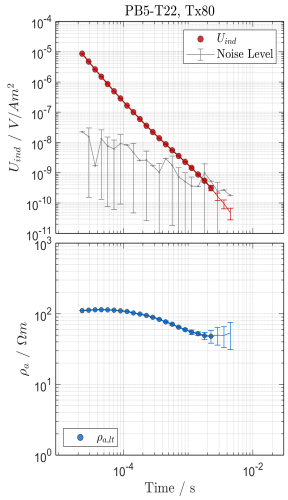

Figure A3.1: TEM field data of Paranal clay pan. (a) The induced voltage and noise level in V/Am^2 and (b) late-time apparent resistivity in ohm-m.

A4 1D TEM models of PAG clay pan

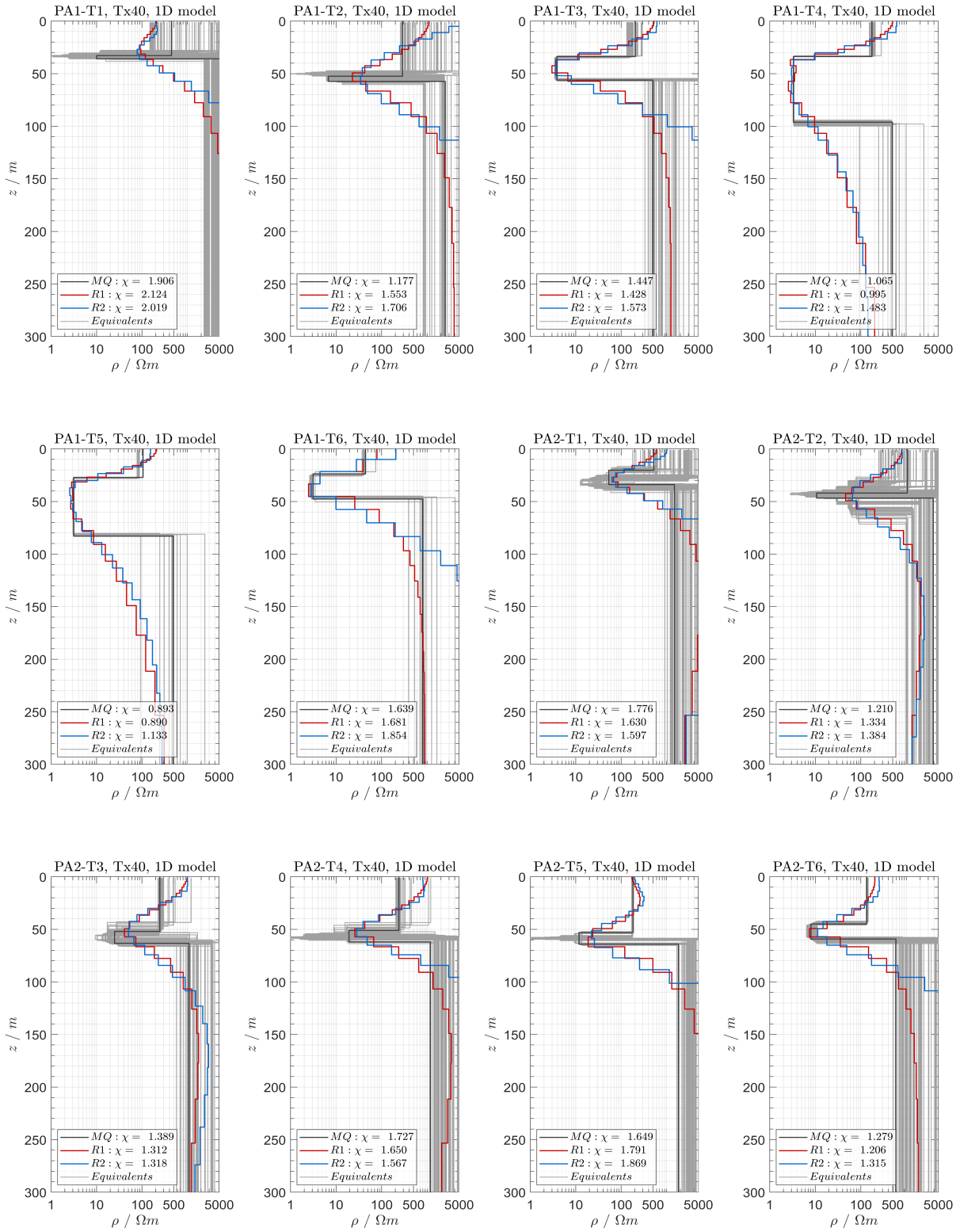

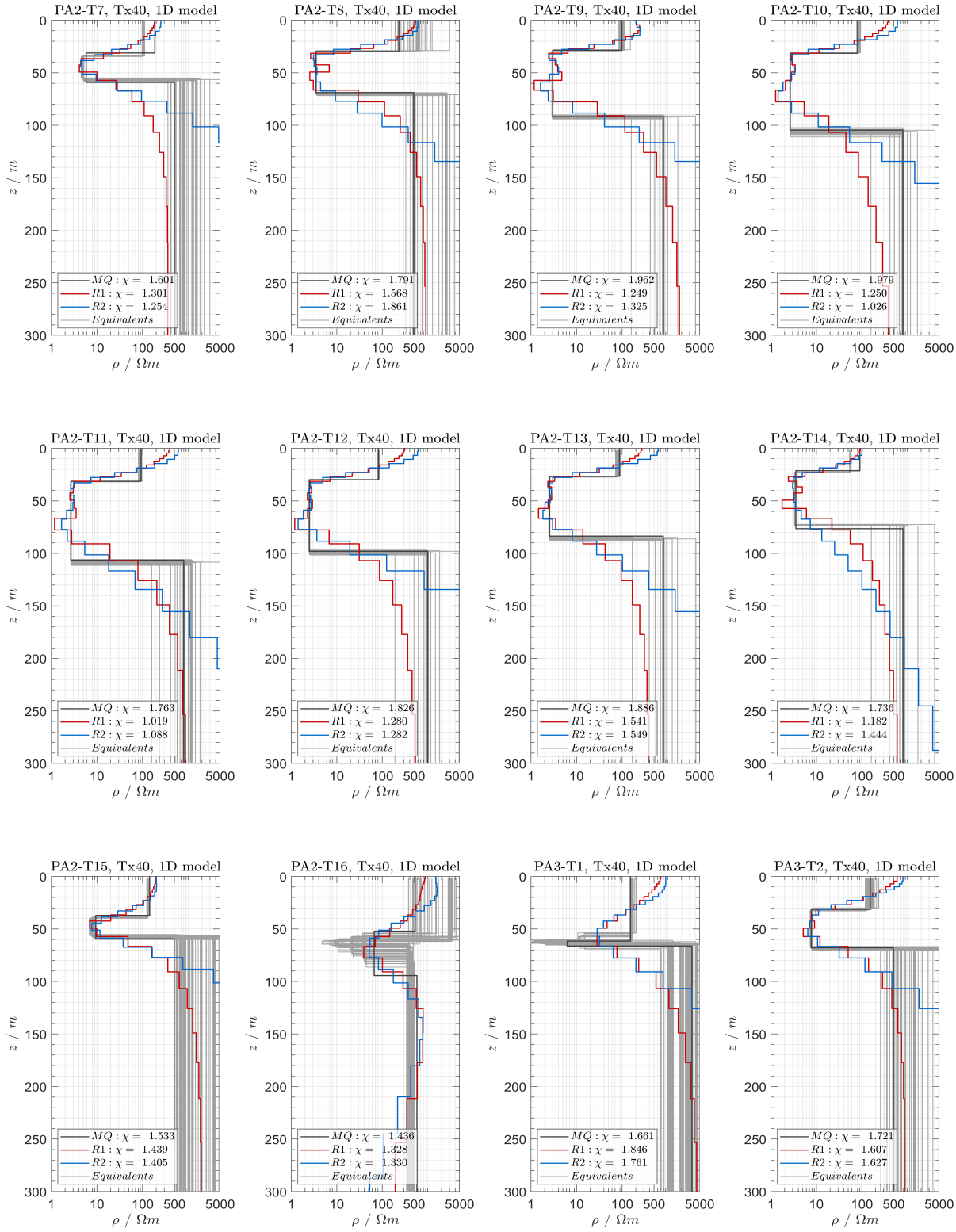
PA2-T7, Tx40, 1D model
MQ : χ = 1.601
R1 : χ = 1.301
R2 : χ = 1.254
Equivalents
PA2-T8, Tx40, 1D model
MQ : χ = 1.791
R1 : χ = 1.568
R2 : χ = 1.861
Equivalents
PA2-T9, Tx40, 1D model
MQ : χ = 1.962
R1 : χ = 1.249
R2 : χ = 1.325
Equivalents
PA2-T10, Tx40, 1D model
MQ : χ = 1.979
R1 : χ = 1.250
R2 : χ = 1.026
Equivalents
PA2-T11, Tx40, 1D model
MQ : χ = 1.763
R1 : χ = 1.019
R2 : χ = 1.088
Equivalents
PA2-T12, Tx40, 1D model
MQ : χ = 1.826
R1 : χ = 1.280
R2 : χ = 1.282
Equivalents
PA2-T13, Tx40, 1D model
MQ : χ = 1.886
R1 : χ = 1.541
R2 : χ = 1.549
Equivalents
PA2-T14, Tx40, 1D model
MQ : χ = 1.736
R1 : χ = 1.182
R2 : χ = 1.444
Equivalents
PA2-T15, Tx40, 1D model
MQ : χ = 1.533
R1 : χ = 1.439
R2 : χ = 1.405
Equivalents
PA2-T16, Tx40, 1D model
MQ : χ = 1.436
R1 : χ = 1.328
R2 : χ = 1.330
Equivalents
PA3-T1, Tx40, 1D model
MQ : χ = 1.661
R1 : χ = 1.846
R2 : χ = 1.761
Equivalents
PA3-T2, Tx40, 1D model
MQ : χ = 1.721
R1 : χ = 1.607
R2 : χ = 1.627
Equivalents
z / m
ρ / Ωm
0 50 100 150 200 250 300
1 10 100 500 5000

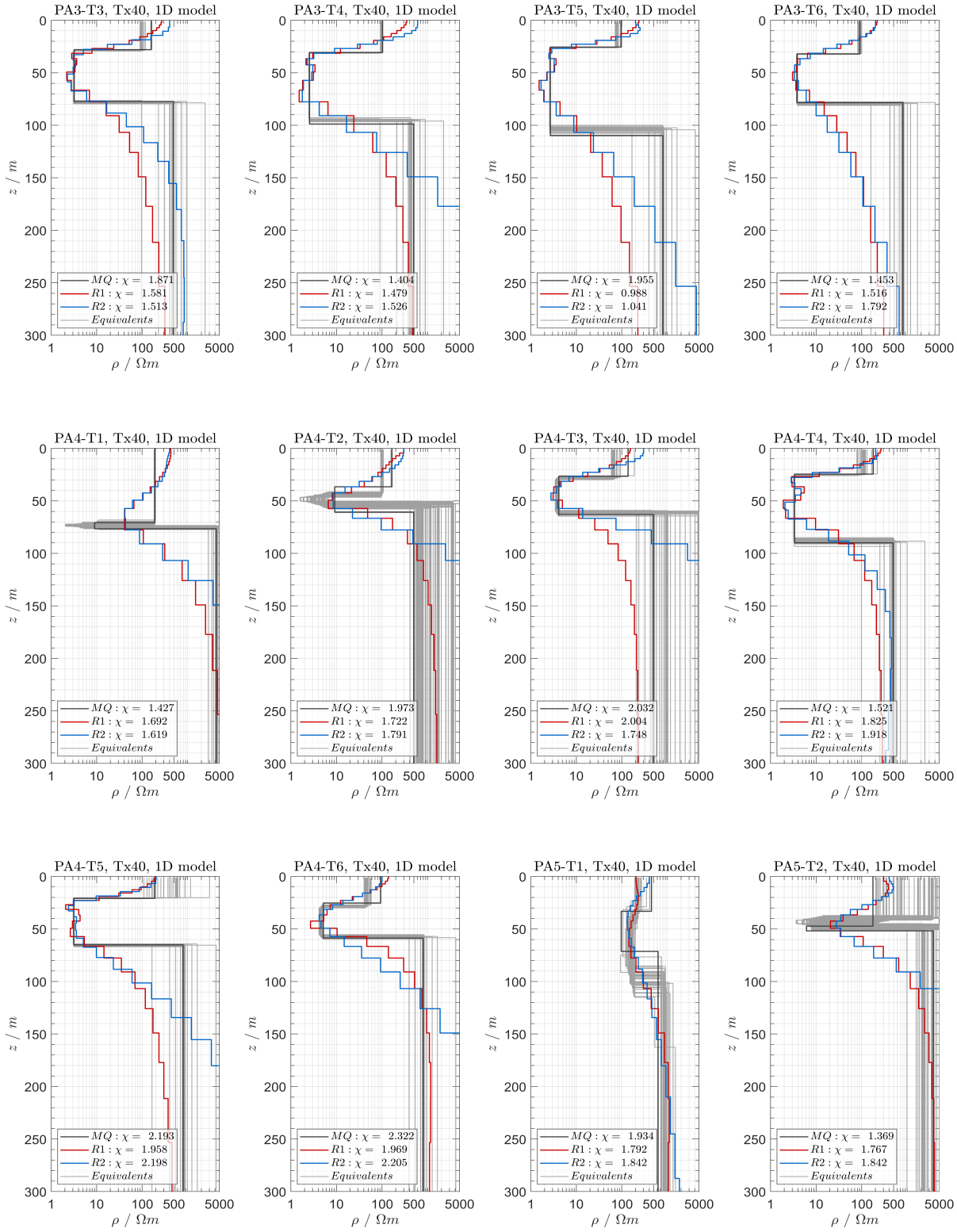
PA3-T3, Tx40, 1D model
MQ : χ = 1.871
R1 : χ = 1.581
R2 : χ = 1.513
Equivalents
PA3-T4, Tx40, 1D model
MQ : χ = 1.404
R1 : χ = 1.479
R2 : χ = 1.526
Equivalents
PA3-T5, Tx40, 1D model
MQ : χ = 1.955
R1 : χ = 0.988
R2 : χ = 1.041
Equivalents
PA3-T6, Tx40, 1D model
MQ : χ = 1.453
R1 : χ = 1.516
R2 : χ = 1.792
Equivalents
PA4-T1, Tx40, 1D model
MQ : χ = 1.427
R1 : χ = 1.692
R2 : χ = 1.619
Equivalents
PA4-T2, Tx40, 1D model
MQ : χ = 1.973
R1 : χ = 1.722
R2 : χ = 1.791
Equivalents
PA4-T3, Tx40, 1D model
MQ : χ = 2.032
R1 : χ = 2.004
R2 : χ = 1.748
Equivalents
PA4-T4, Tx40, 1D model
MQ : χ = 1.521
R1 : χ = 1.825
R2 : χ = 1.918
Equivalents
PA4-T5, Tx40, 1D model
MQ : χ = 2.193
R1 : χ = 1.958
R2 : χ = 2.198
Equivalents
PA4-T6, Tx40, 1D model
MQ : χ = 2.322
R1 : χ = 1.969
R2 : χ = 2.205
Equivalents
PA5-T1, Tx40, 1D model
MQ : χ = 1.934
R1 : χ = 1.792
R2 : χ = 1.842
Equivalents
PA5-T2, Tx40, 1D model
MQ : χ = 1.369
R1 : χ = 1.767
R2 : χ = 1.842
Equivalents
z / m
ρ / Ωm
0
50
100
150
200
250
300
1
10
100
500
5000

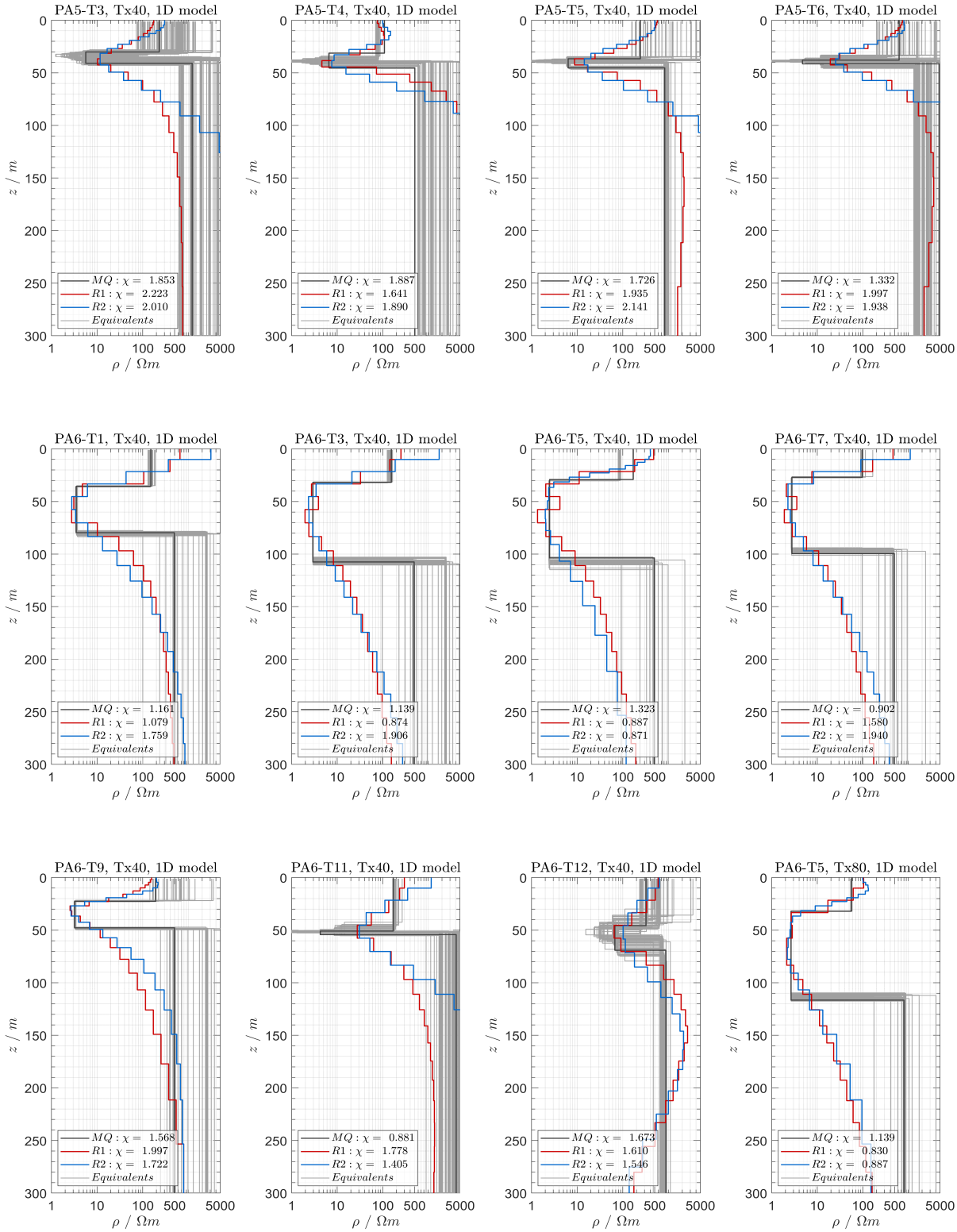

Figure A4.1: 1D models of PAG clay pan. Marquardt, Occam R1, Occam R2, and equivalent models. The corresponding χ is given in each legend.

A5 1D TEM models of Paranal clay pan

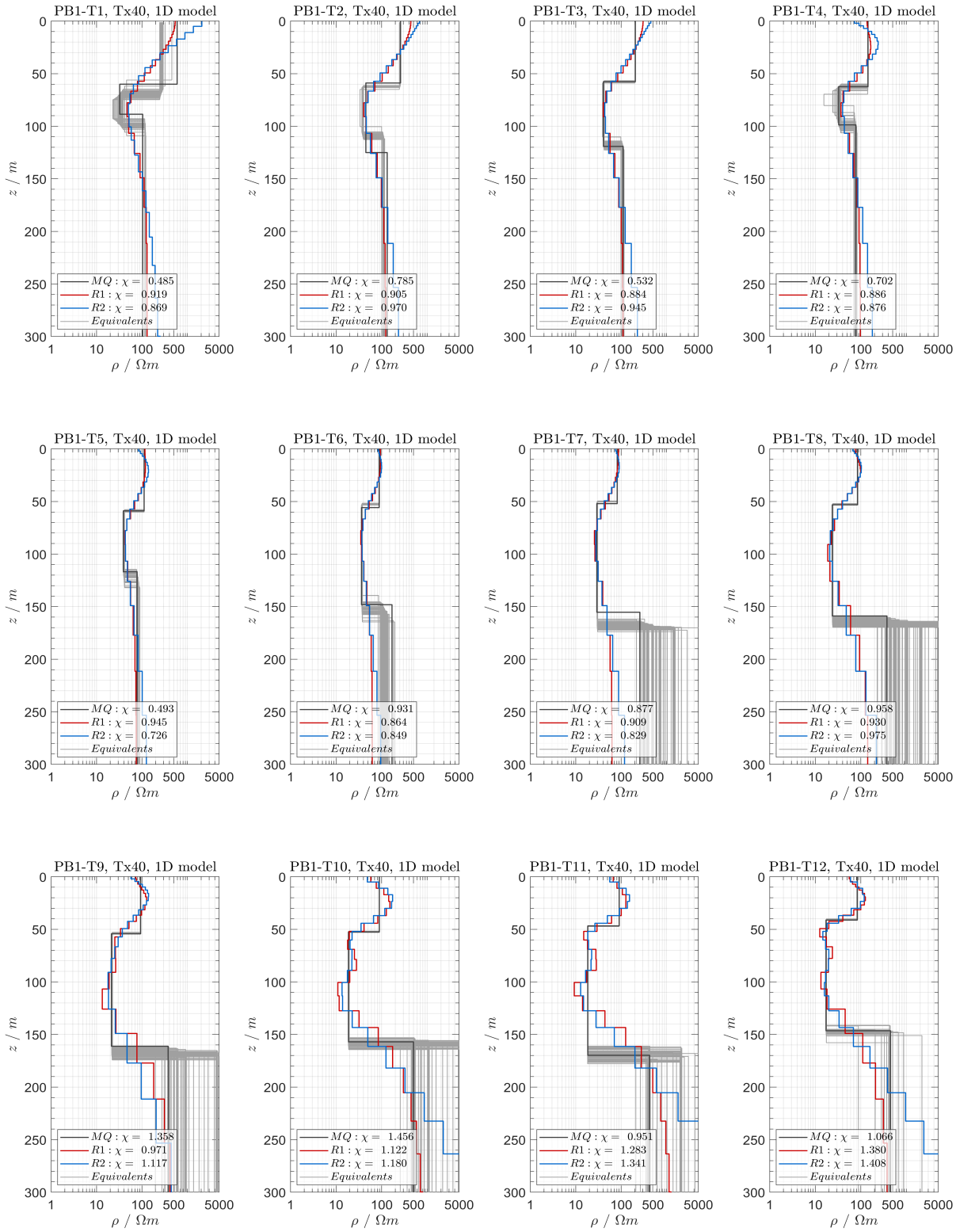

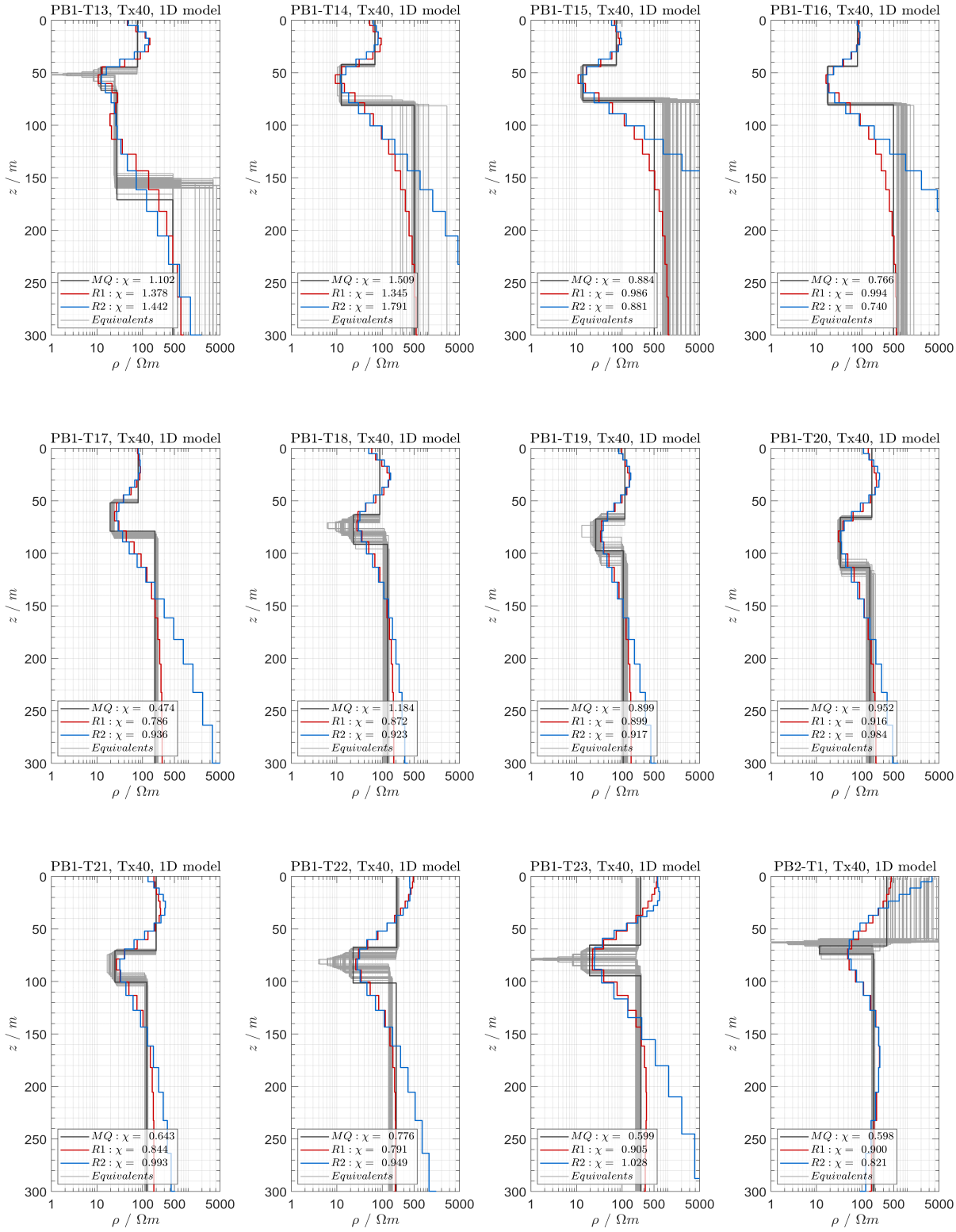
PB1-T13, Tx40, 1D model
MQ : χ = 1.102
R1 : χ = 1.378
R2 : χ = 1.442
Equivalents
PB1-T14, Tx40, 1D model
MQ : χ = 1.509
R1 : χ = 1.345
R2 : χ = 1.791
Equivalents
PB1-T15, Tx40, 1D model
MQ : χ = 0.884
R1 : χ = 0.986
R2 : χ = 0.881
Equivalents
PB1-T16, Tx40, 1D model
MQ : χ = 0.766
R1 : χ = 0.994
R2 : χ = 0.740
Equivalents
PB1-T17, Tx40, 1D model
MQ : χ = 0.474
R1 : χ = 0.786
R2 : χ = 0.936
Equivalents
PB1-T18, Tx40, 1D model
MQ : χ = 1.184
R1 : χ = 0.872
R2 : χ = 0.923
Equivalents
PB1-T19, Tx40, 1D model
MQ : χ = 0.899
R1 : χ = 0.899
R2 : χ = 0.917
Equivalents
PB1-T20, Tx40, 1D model
MQ : χ = 0.952
R1 : χ = 0.916
R2 : χ = 0.984
Equivalents
PB1-T21, Tx40, 1D model
MQ : χ = 0.643
R1 : χ = 0.844
R2 : χ = 0.993
Equivalents
PB1-T22, Tx40, 1D model
MQ : χ = 0.776
R1 : χ = 0.791
R2 : χ = 0.949
Equivalents
PB1-T23, Tx40, 1D model
MQ : χ = 0.599
R1 : χ = 0.905
R2 : χ = 1.028
Equivalents
PB2-T1, Tx40, 1D model
MQ : χ = 0.598
R1 : χ = 0.900
R2 : χ = 0.821
Equivalents
z / m
ρ / Ωm
0 50 100 150 200 250 300
1 10 100 500 5000

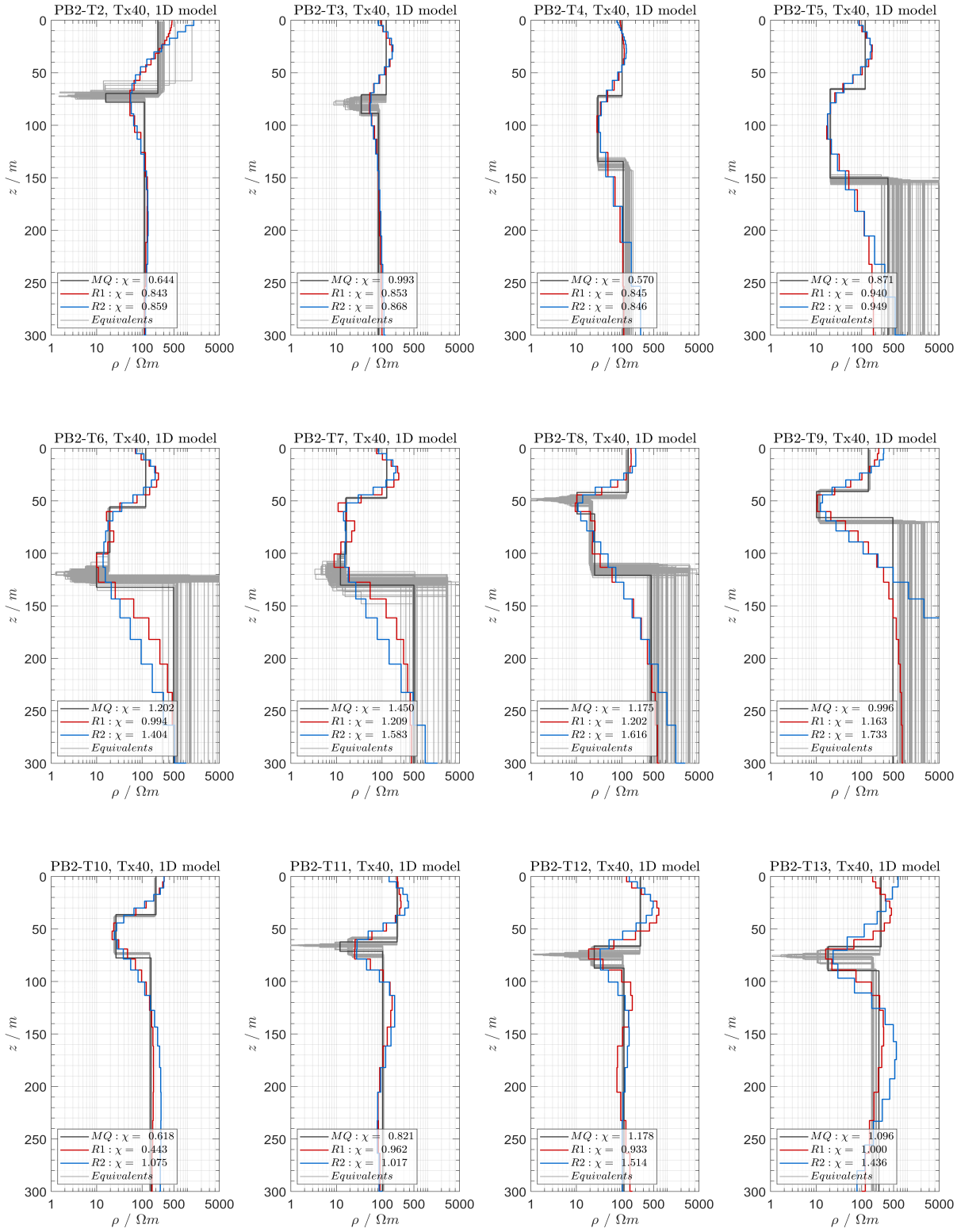
PB2-T2, Tx40, 1D model
MQ : χ = 0.644
R1 : χ = 0.843
R2 : χ = 0.859
Equivalents
PB2-T3, Tx40, 1D model
MQ : χ = 0.993
R1 : χ = 0.853
R2 : χ = 0.868
Equivalents
PB2-T4, Tx40, 1D model
MQ : χ = 0.570
R1 : χ = 0.845
R2 : χ = 0.846
Equivalents
PB2-T5, Tx40, 1D model
MQ : χ = 0.871
R1 : χ = 0.940
R2 : χ = 0.949
Equivalents
PB2-T6, Tx40, 1D model
MQ : χ = 1.202
R1 : χ = 0.994
R2 : χ = 1.404
Equivalents
PB2-T7, Tx40, 1D model
MQ : χ = 1.450
R1 : χ = 1.209
R2 : χ = 1.583
Equivalents
PB2-T8, Tx40, 1D model
MQ : χ = 1.175
R1 : χ = 1.202
R2 : χ = 1.616
Equivalents
PB2-T9, Tx40, 1D model
MQ : χ = 0.996
R1 : χ = 1.163
R2 : χ = 1.733
Equivalents
PB2-T10, Tx40, 1D model
MQ : χ = 0.618
R1 : χ = 0.443
R2 : χ = 1.075
Equivalents
PB2-T11, Tx40, 1D model
MQ : χ = 0.821
R1 : χ = 0.962
R2 : χ = 1.017
Equivalents
PB2-T12, Tx40, 1D model
MQ : χ = 1.178
R1 : χ = 0.933
R2 : χ = 1.514
Equivalents
PB2-T13, Tx40, 1D model
MQ : χ = 1.096
R1 : χ = 1.000
R2 : χ = 1.436
Equivalents
z / m
ρ / Ωm
0
50
100
150
200
250
300
1
10
100
500
5000

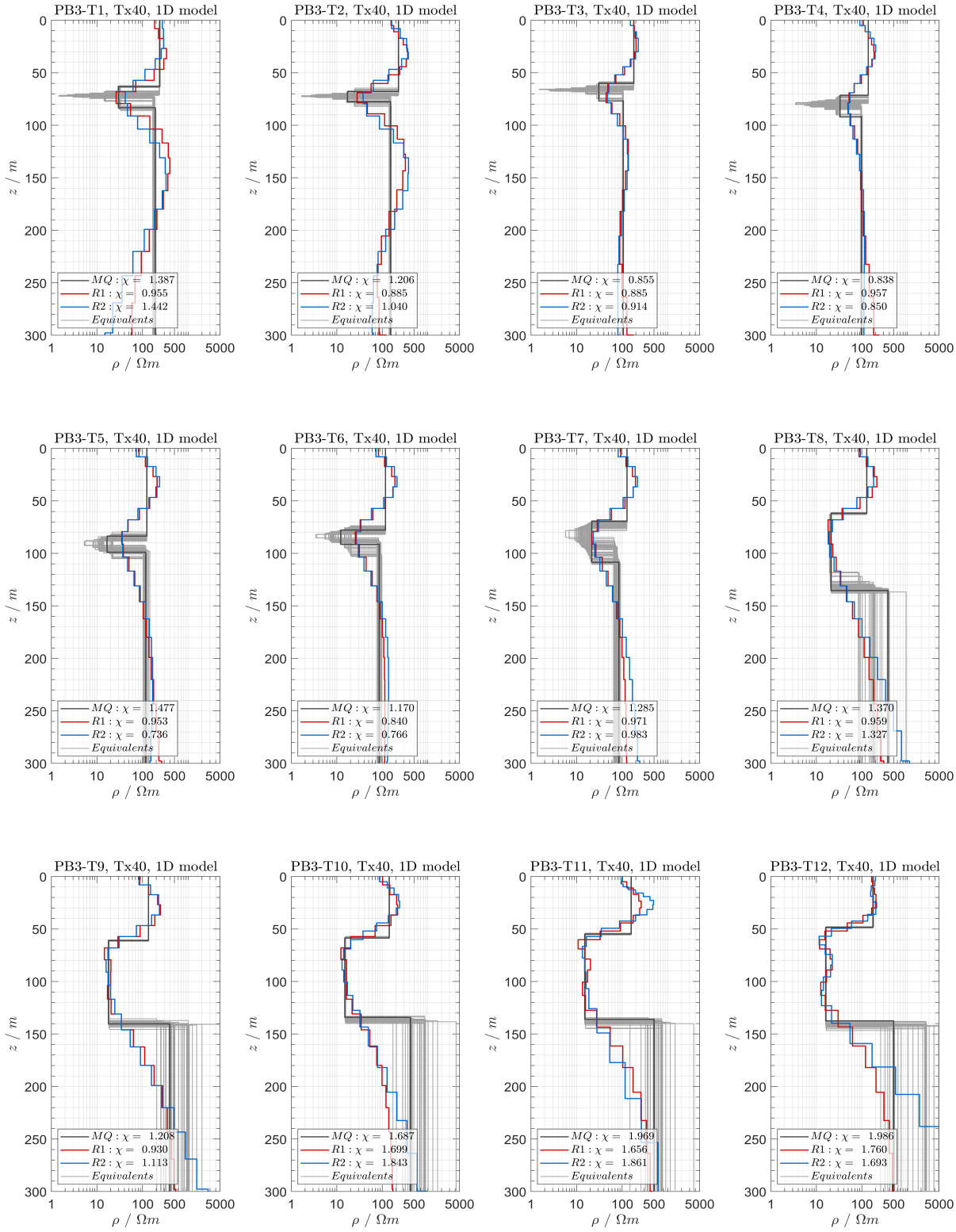
PB3-T1, Tx40, 1D model
MQ : χ = 1.387
R1 : χ = 0.955
R2 : χ = 1.442
Equivalents
PB3-T2, Tx40, 1D model
MQ : χ = 1.206
R1 : χ = 0.885
R2 : χ = 1.040
Equivalents
PB3-T3, Tx40, 1D model
MQ : χ = 0.855
R1 : χ = 0.885
R2 : χ = 0.914
Equivalents
PB3-T4, Tx40, 1D model
MQ : χ = 0.838
R1 : χ = 0.957
R2 : χ = 0.850
Equivalents
PB3-T5, Tx40, 1D model
MQ : χ = 1.477
R1 : χ = 0.953
R2 : χ = 0.736
Equivalents
PB3-T6, Tx40, 1D model
MQ : χ = 1.170
R1 : χ = 0.840
R2 : χ = 0.766
Equivalents
PB3-T7, Tx40, 1D model
MQ : χ = 1.285
R1 : χ = 0.971
R2 : χ = 0.983
Equivalents
PB3-T8, Tx40, 1D model
MQ : χ = 1.370
R1 : χ = 0.959
R2 : χ = 1.327
Equivalents
PB3-T9, Tx40, 1D model
MQ : χ = 1.208
R1 : χ = 0.930
R2 : χ = 1.113
Equivalents
PB3-T10, Tx40, 1D model
MQ : χ = 1.687
R1 : χ = 1.699
R2 : χ = 1.843
Equivalents
PB3-T11, Tx40, 1D model
MQ : χ = 1.969
R1 : χ = 1.656
R2 : χ = 1.861
Equivalents
PB3-T12, Tx40, 1D model
MQ : χ = 1.986
R1 : χ = 1.760
R2 : χ = 1.693
Equivalents
z / m
ρ / Ωm
0
50
100
150
200
250
300
1
10
100
500
5000

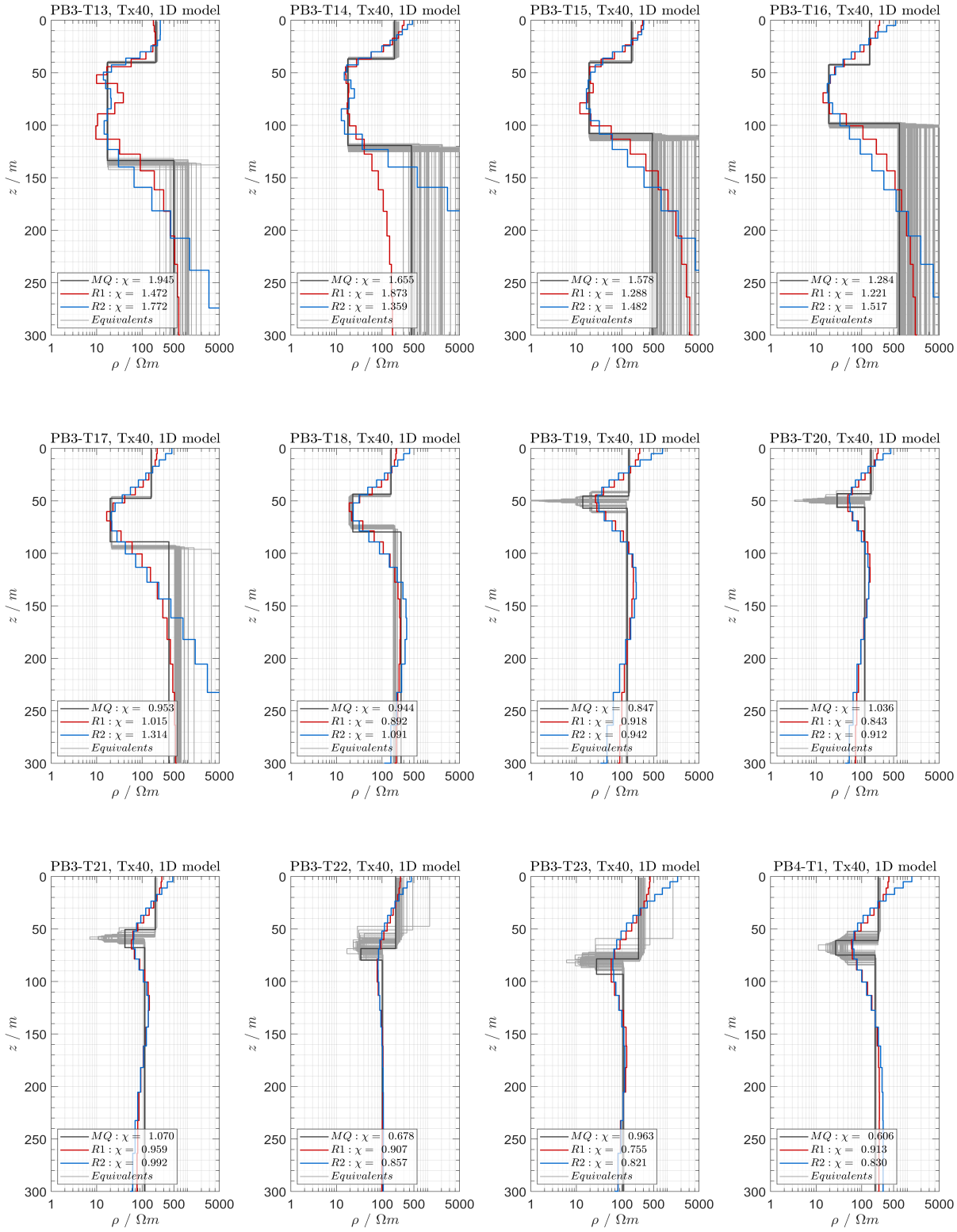
PB3-T13, Tx40, 1D model
MQ : χ = 1.945
R1 : χ = 1.472
R2 : χ = 1.772
Equivalents
PB3-T14, Tx40, 1D model
MQ : χ = 1.655
R1 : χ = 1.873
R2 : χ = 1.359
Equivalents
PB3-T15, Tx40, 1D model
MQ : χ = 1.578
R1 : χ = 1.288
R2 : χ = 1.482
Equivalents
PB3-T16, Tx40, 1D model
MQ : χ = 1.284
R1 : χ = 1.221
R2 : χ = 1.517
Equivalents
PB3-T17, Tx40, 1D model
MQ : χ = 0.953
R1 : χ = 1.015
R2 : χ = 1.314
Equivalents
PB3-T18, Tx40, 1D model
MQ : χ = 0.944
R1 : χ = 0.892
R2 : χ = 1.091
Equivalents
PB3-T19, Tx40, 1D model
MQ : χ = 0.847
R1 : χ = 0.918
R2 : χ = 0.942
Equivalents
PB3-T20, Tx40, 1D model
MQ : χ = 1.036
R1 : χ = 0.843
R2 : χ = 0.912
Equivalents
PB3-T21, Tx40, 1D model
MQ : χ = 1.070
R1 : χ = 0.959
R2 : χ = 0.992
Equivalents
PB3-T22, Tx40, 1D model
MQ : χ = 0.678
R1 : χ = 0.907
R2 : χ = 0.857
Equivalents
PB3-T23, Tx40, 1D model
MQ : χ = 0.963
R1 : χ = 0.755
R2 : χ = 0.821
Equivalents
PB4-T1, Tx40, 1D model
MQ : χ = 0.606
R1 : χ = 0.913
R2 : χ = 0.830
Equivalents
z / m
ρ / Ωm
0
50
100
150
200
250
300
1
10
100
500
5000

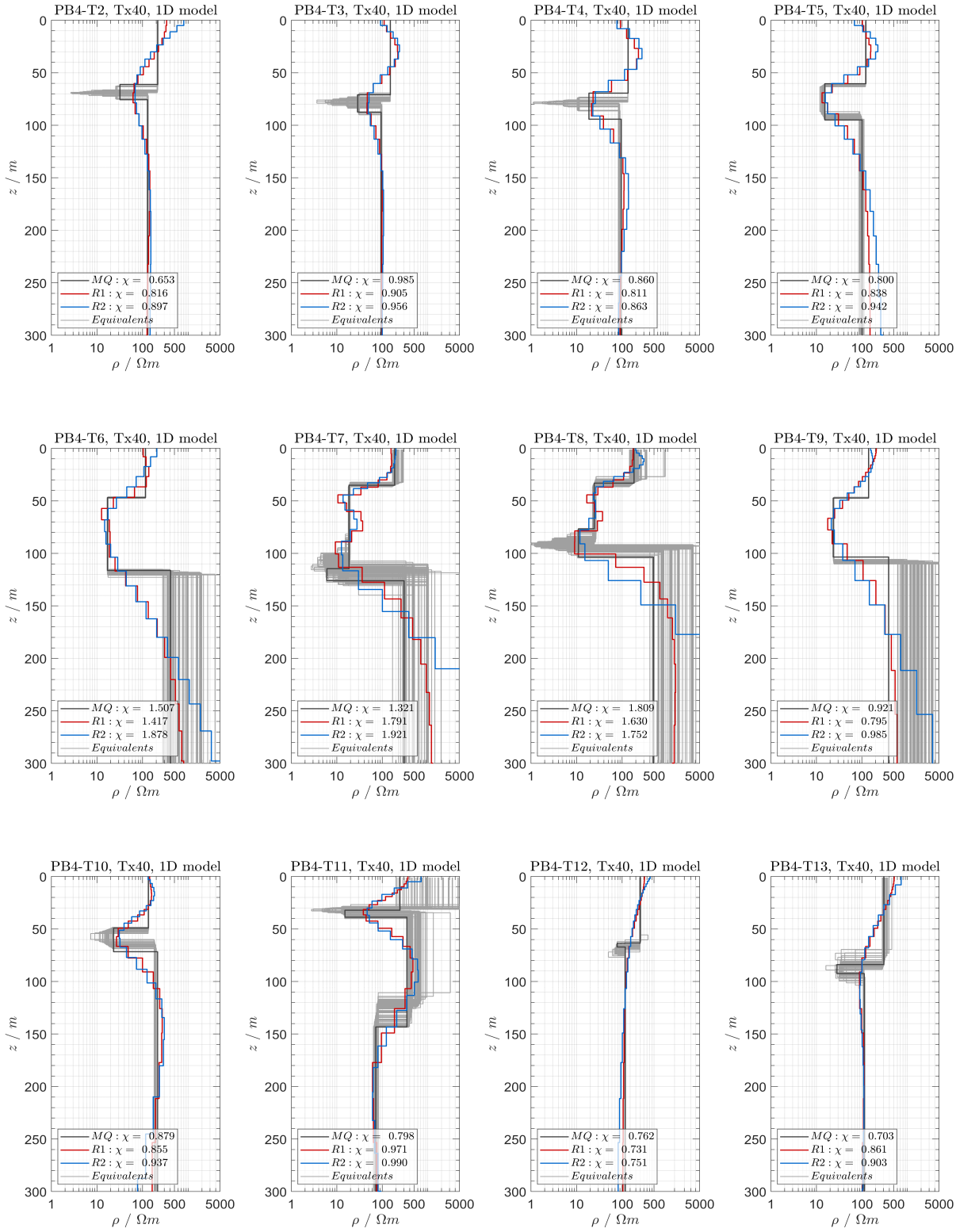
PB4-T2, Tx40, 1D model
MQ : χ = 0.653
R1 : χ = 0.816
R2 : χ = 0.897
Equivalents
PB4-T3, Tx40, 1D model
MQ : χ = 0.985
R1 : χ = 0.905
R2 : χ = 0.956
Equivalents
PB4-T4, Tx40, 1D model
MQ : χ = 0.860
R1 : χ = 0.811
R2 : χ = 0.863
Equivalents
PB4-T5, Tx40, 1D model
MQ : χ = 0.800
R1 : χ = 0.838
R2 : χ = 0.942
Equivalents
PB4-T6, Tx40, 1D model
MQ : χ = 1.507
R1 : χ = 1.417
R2 : χ = 1.878
Equivalents
PB4-T7, Tx40, 1D model
MQ : χ = 1.321
R1 : χ = 1.791
R2 : χ = 1.921
Equivalents
PB4-T8, Tx40, 1D model
MQ : χ = 1.809
R1 : χ = 1.630
R2 : χ = 1.752
Equivalents
PB4-T9, Tx40, 1D model
MQ : χ = 0.921
R1 : χ = 0.795
R2 : χ = 0.985
Equivalents
PB4-T10, Tx40, 1D model
MQ : χ = 0.879
R1 : χ = 0.855
R2 : χ = 0.937
Equivalents
PB4-T11, Tx40, 1D model
MQ : χ = 0.798
R1 : χ = 0.971
R2 : χ = 0.990
Equivalents
PB4-T12, Tx40, 1D model
MQ : χ = 0.762
R1 : χ = 0.731
R2 : χ = 0.751
Equivalents
PB4-T13, Tx40, 1D model
MQ : χ = 0.703
R1 : χ = 0.861
R2 : χ = 0.903
Equivalents
z / m
ρ / Ωm
0 50 100 150 200 250 300
1 10 100 500 5000

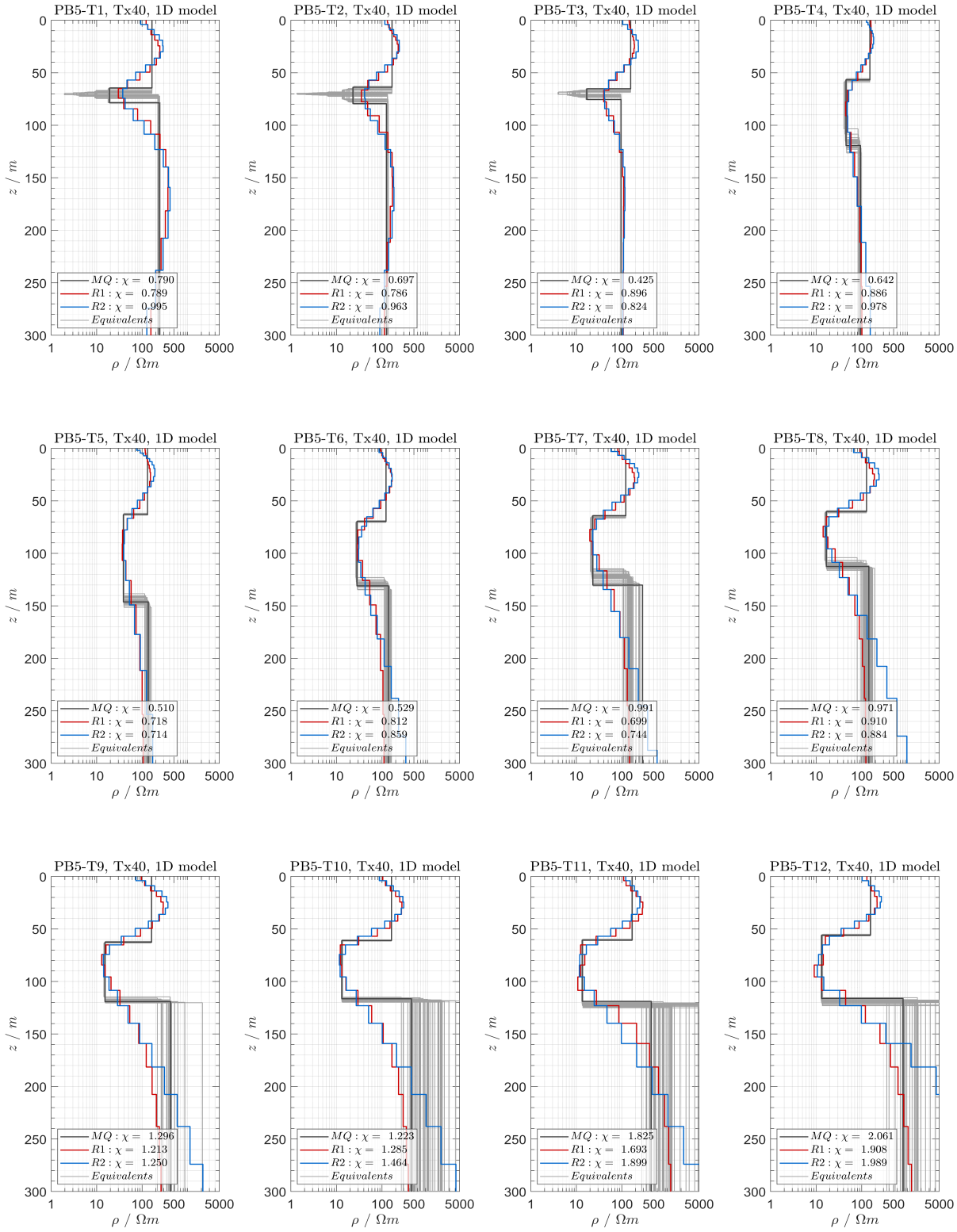
PB5-T1, Tx40, 1D model
MQ : χ = 0.790
R1 : χ = 0.789
R2 : χ = 0.995
Equivalents
PB5-T2, Tx40, 1D model
MQ : χ = 0.697
R1 : χ = 0.786
R2 : χ = 0.963
Equivalents
PB5-T3, Tx40, 1D model
MQ : χ = 0.425
R1 : χ = 0.896
R2 : χ = 0.824
Equivalents
PB5-T4, Tx40, 1D model
MQ : χ = 0.642
R1 : χ = 0.886
R2 : χ = 0.978
Equivalents
PB5-T5, Tx40, 1D model
MQ : χ = 0.510
R1 : χ = 0.718
R2 : χ = 0.714
Equivalents
PB5-T6, Tx40, 1D model
MQ : χ = 0.529
R1 : χ = 0.812
R2 : χ = 0.859
Equivalents
PB5-T7, Tx40, 1D model
MQ : χ = 0.991
R1 : χ = 0.699
R2 : χ = 0.744
Equivalents
PB5-T8, Tx40, 1D model
MQ : χ = 0.971
R1 : χ = 0.910
R2 : χ = 0.884
Equivalents
PB5-T9, Tx40, 1D model
MQ : χ = 1.296
R1 : χ = 1.213
R2 : χ = 1.250
Equivalents
PB5-T10, Tx40, 1D model
MQ : χ = 1.223
R1 : χ = 1.285
R2 : χ = 1.464
Equivalents
PB5-T11, Tx40, 1D model
MQ : χ = 1.825
R1 : χ = 1.693
R2 : χ = 1.899
Equivalents
PB5-T12, Tx40, 1D model
MQ : χ = 2.061
R1 : χ = 1.908
R2 : χ = 1.989
Equivalents
z / m
ρ / Ωm
0
50
100
150
200
250
300
1
10
100
500
5000

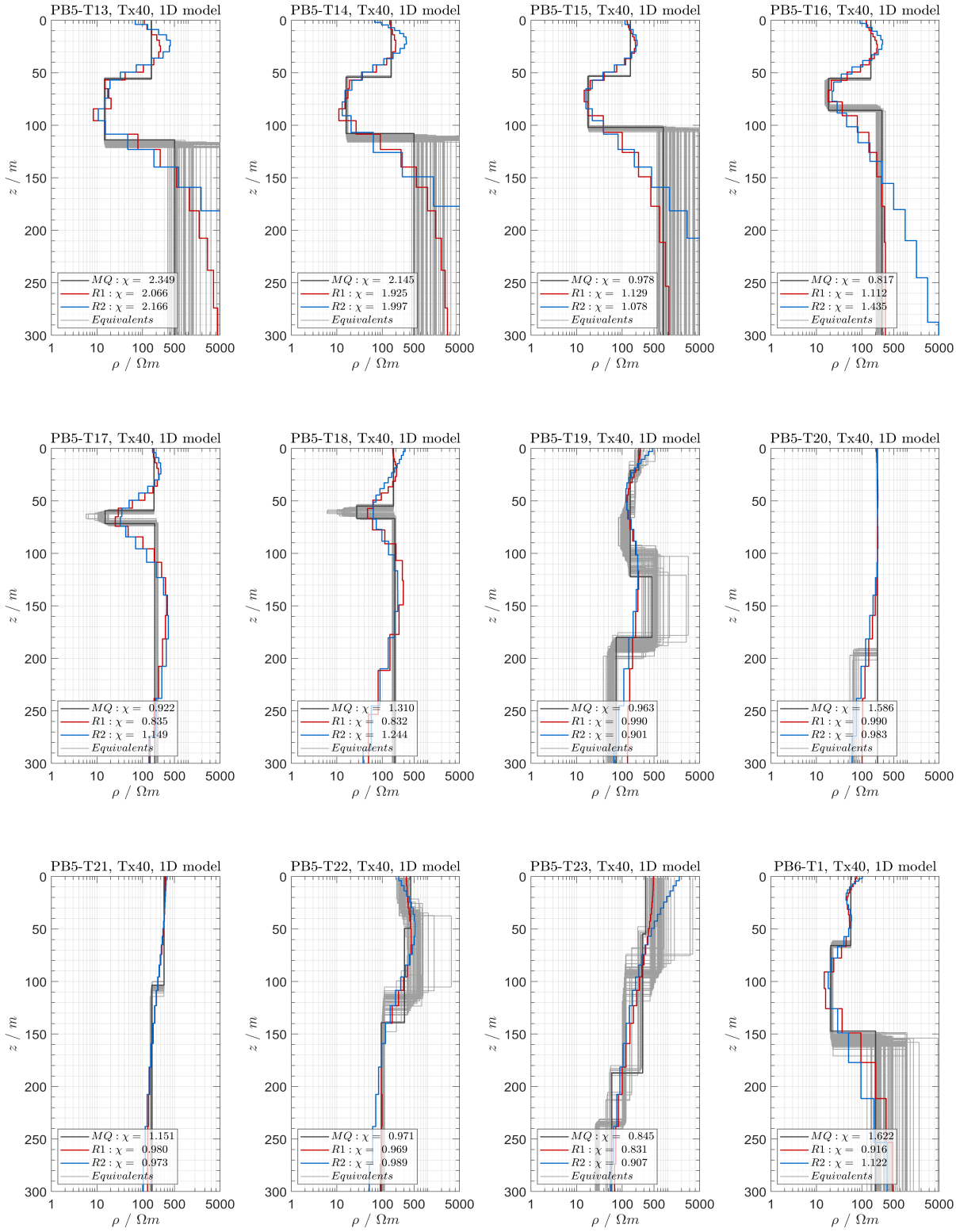
PB5-T13, Tx40, 1D model
MQ : χ = 2.349
R1 : χ = 2.066
R2 : χ = 2.166
Equivalents
PB5-T14, Tx40, 1D model
MQ : χ = 2.145
R1 : χ = 1.925
R2 : χ = 1.997
Equivalents
PB5-T15, Tx40, 1D model
MQ : χ = 0.978
R1 : χ = 1.129
R2 : χ = 1.078
Equivalents
PB5-T16, Tx40, 1D model
MQ : χ = 0.817
R1 : χ = 1.112
R2 : χ = 1.435
Equivalents
PB5-T17, Tx40, 1D model
MQ : χ = 0.922
R1 : χ = 0.835
R2 : χ = 1.149
Equivalents
PB5-T18, Tx40, 1D model
MQ : χ = 1.310
R1 : χ = 0.832
R2 : χ = 1.244
Equivalents
PB5-T19, Tx40, 1D model
MQ : χ = 0.963
R1 : χ = 0.990
R2 : χ = 0.901
Equivalents
PB5-T20, Tx40, 1D model
MQ : χ = 1.586
R1 : χ = 0.990
R2 : χ = 0.983
Equivalents
PB5-T21, Tx40, 1D model
MQ : χ = 1.151
R1 : χ = 0.980
R2 : χ = 0.973
Equivalents
PB5-T22, Tx40, 1D model
MQ : χ = 0.971
R1 : χ = 0.969
R2 : χ = 0.989
Equivalents
PB5-T23, Tx40, 1D model
MQ : χ = 0.845
R1 : χ = 0.831
R2 : χ = 0.907
Equivalents
PB6-T1, Tx40, 1D model
MQ : χ = 1.622
R1 : χ = 0.916
R2 : χ = 1.122
Equivalents
z / m
ρ / Ωm
0
50
100
150
200
250
300
1
10
100
500
5000

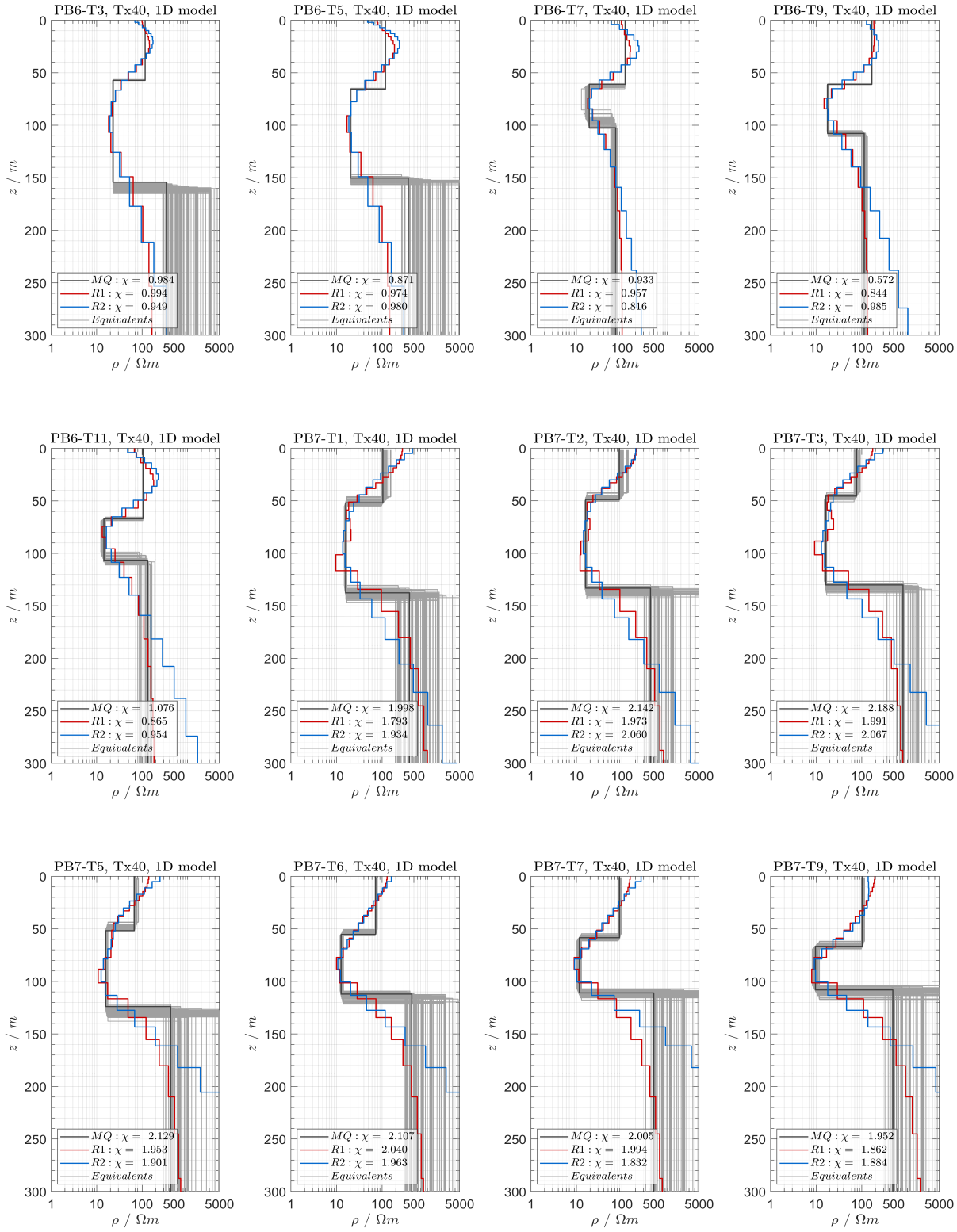
PB6-T3, Tx40, 1D model
MQ : χ = 0.984
R1 : χ = 0.994
R2 : χ = 0.949
Equivalents
PB6-T5, Tx40, 1D model
MQ : χ = 0.871
R1 : χ = 0.974
R2 : χ = 0.980
Equivalents
PB6-T7, Tx40, 1D model
MQ : χ = 0.933
R1 : χ = 0.957
R2 : χ = 0.816
Equivalents
PB6-T9, Tx40, 1D model
MQ : χ = 0.572
R1 : χ = 0.844
R2 : χ = 0.985
Equivalents
PB6-T11, Tx40, 1D model
MQ : χ = 1.076
R1 : χ = 0.865
R2 : χ = 0.954
Equivalents
PB7-T1, Tx40, 1D model
MQ : χ = 1.998
R1 : χ = 1.793
R2 : χ = 1.934
Equivalents
PB7-T2, Tx40, 1D model
MQ : χ = 2.142
R1 : χ = 1.973
R2 : χ = 2.060
Equivalents
PB7-T3, Tx40, 1D model
MQ : χ = 2.188
R1 : χ = 1.991
R2 : χ = 2.067
Equivalents
PB7-T5, Tx40, 1D model
MQ : χ = 2.129
R1 : χ = 1.953
R2 : χ = 1.901
Equivalents
PB7-T6, Tx40, 1D model
MQ : χ = 2.107
R1 : χ = 2.040
R2 : χ = 1.963
Equivalents
PB7-T7, Tx40, 1D model
MQ : χ = 2.005
R1 : χ = 1.994
R2 : χ = 1.832
Equivalents
PB7-T9, Tx40, 1D model
MQ : χ = 1.952
R1 : χ = 1.862
R2 : χ = 1.884
Equivalents
z / m
ρ / Ωm

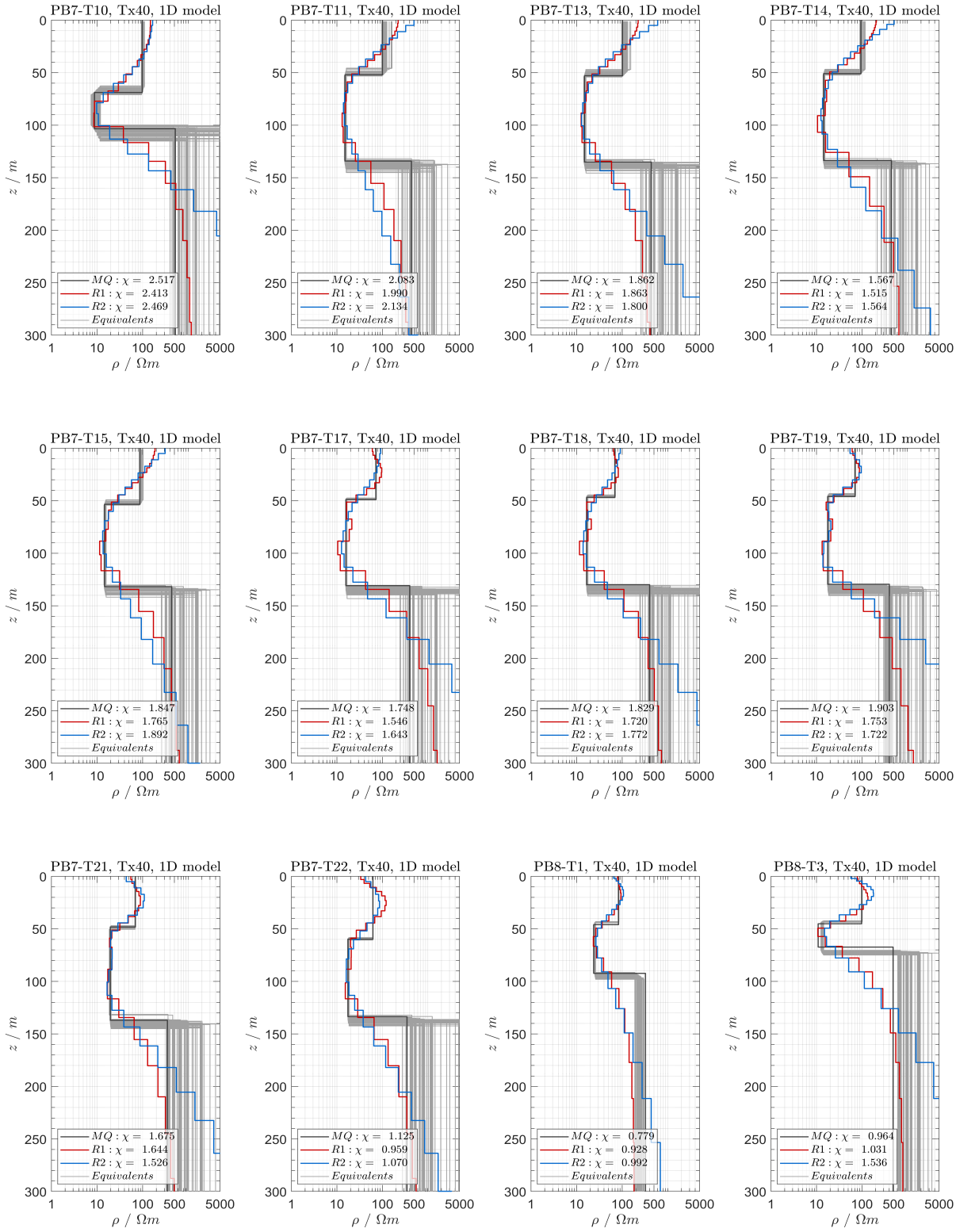
PB7-T10, Tx40, 1D model
MQ : χ = 2.517
R1 : χ = 2.413
R2 : χ = 2.469
Equivalents
PB7-T11, Tx40, 1D model
MQ : χ = 2.083
R1 : χ = 1.990
R2 : χ = 2.134
Equivalents
PB7-T13, Tx40, 1D model
MQ : χ = 1.862
R1 : χ = 1.863
R2 : χ = 1.800
Equivalents
PB7-T14, Tx40, 1D model
MQ : χ = 1.567
R1 : χ = 1.515
R2 : χ = 1.564
Equivalents
PB7-T15, Tx40, 1D model
MQ : χ = 1.847
R1 : χ = 1.765
R2 : χ = 1.892
Equivalents
PB7-T17, Tx40, 1D model
MQ : χ = 1.748
R1 : χ = 1.546
R2 : χ = 1.643
Equivalents
PB7-T18, Tx40, 1D model
MQ : χ = 1.829
R1 : χ = 1.720
R2 : χ = 1.772
Equivalents
PB7-T19, Tx40, 1D model
MQ : χ = 1.903
R1 : χ = 1.753
R2 : χ = 1.722
Equivalents
PB7-T21, Tx40, 1D model
MQ : χ = 1.675
R1 : χ = 1.644
R2 : χ = 1.526
Equivalents
PB7-T22, Tx40, 1D model
MQ : χ = 1.125
R1 : χ = 0.959
R2 : χ = 1.070
Equivalents
PB8-T1, Tx40, 1D model
MQ : χ = 0.779
R1 : χ = 0.928
R2 : χ = 0.992
Equivalents
PB8-T3, Tx40, 1D model
MQ : χ = 0.964
R1 : χ = 1.031
R2 : χ = 1.536
Equivalents
z / m
ρ / Ωm
0 50 100 150 200 250 300
1 10 100 500 5000

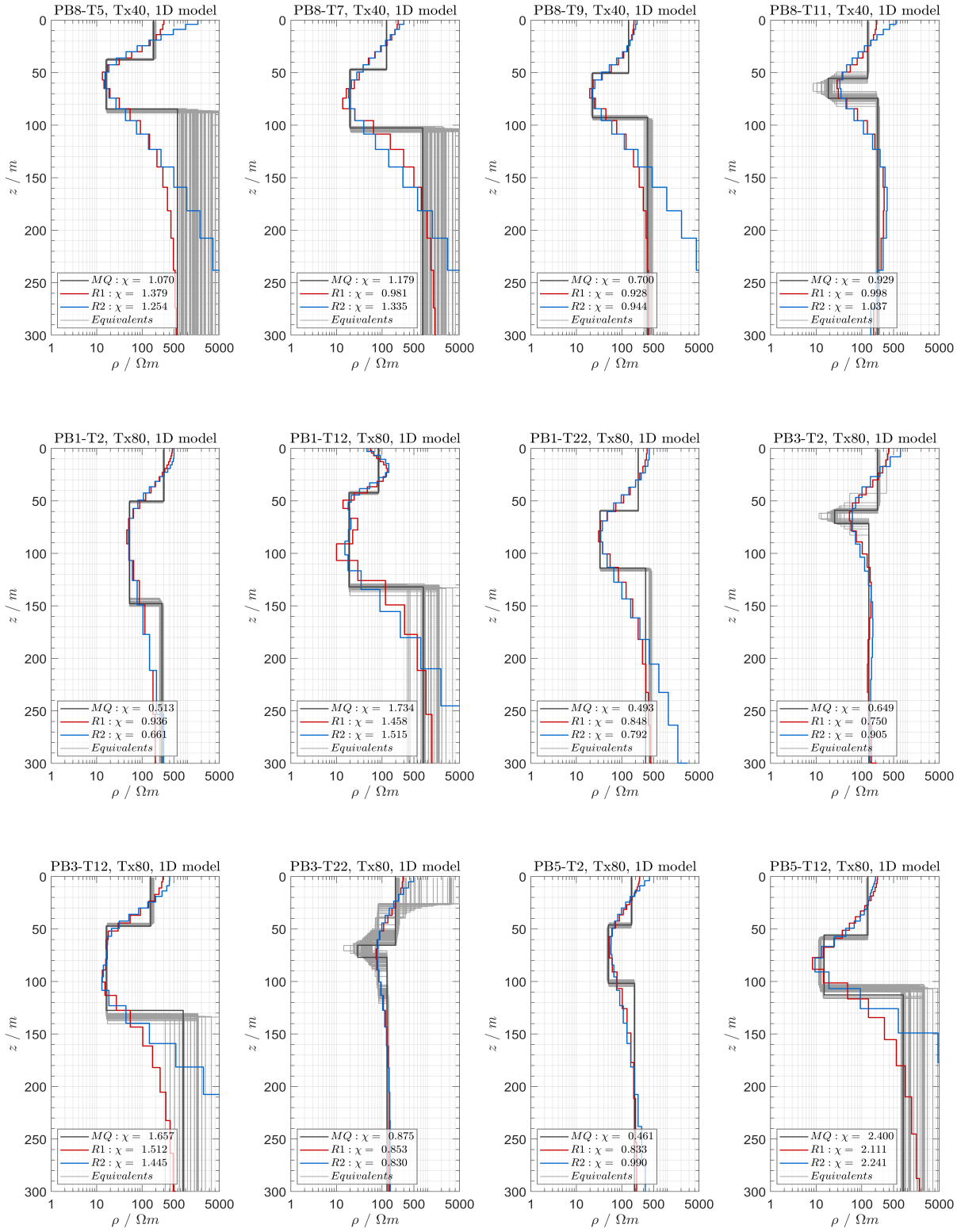
PB8-T5, Tx40, 1D model
MQ : χ = 1.070
R1 : χ = 1.379
R2 : χ = 1.254
Equivalents
PB8-T7, Tx40, 1D model
MQ : χ = 1.179
R1 : χ = 0.981
R2 : χ = 1.335
Equivalents
PB8-T9, Tx40, 1D model
MQ : χ = 0.700
R1 : χ = 0.928
R2 : χ = 0.944
Equivalents
PB8-T11, Tx40, 1D model
MQ : χ = 0.929
R1 : χ = 0.998
R2 : χ = 1.037
Equivalents
PB1-T2, Tx80, 1D model
MQ : χ = 0.513
R1 : χ = 0.936
R2 : χ = 0.661
Equivalents
PB1-T12, Tx80, 1D model
MQ : χ = 1.734
R1 : χ = 1.458
R2 : χ = 1.515
Equivalents
PB1-T22, Tx80, 1D model
MQ : χ = 0.493
R1 : χ = 0.848
R2 : χ = 0.792
Equivalents
PB3-T2, Tx80, 1D model
MQ : χ = 0.649
R1 : χ = 0.750
R2 : χ = 0.905
Equivalents
PB3-T12, Tx80, 1D model
MQ : χ = 1.657
R1 : χ = 1.512
R2 : χ = 1.445
Equivalents
PB3-T22, Tx80, 1D model
MQ : χ = 0.875
R1 : χ = 0.853
R2 : χ = 0.830
Equivalents
PB5-T2, Tx80, 1D model
MQ : χ = 0.461
R1 : χ = 0.833
R2 : χ = 0.990
Equivalents
PB5-T12, Tx80, 1D model
MQ : χ = 2.400
R1 : χ = 2.111
R2 : χ = 2.241
Equivalents
z / m
ρ / Ωm
0
50
100
150
200
250
300
1
10
100
500
5000

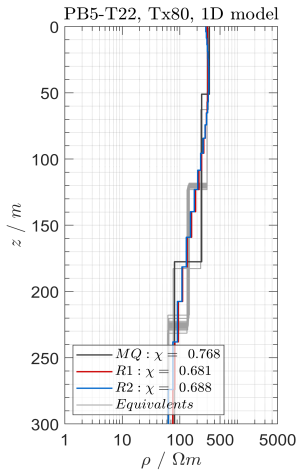

Figure A5.1: 1D models of Paranal clay pan. Marquardt, Occam R1, Occam R2, and equivalent models. The corresponding χ is given in each legend.

A6 Comparison Tx-40 and Tx-80 at PAG clay pan

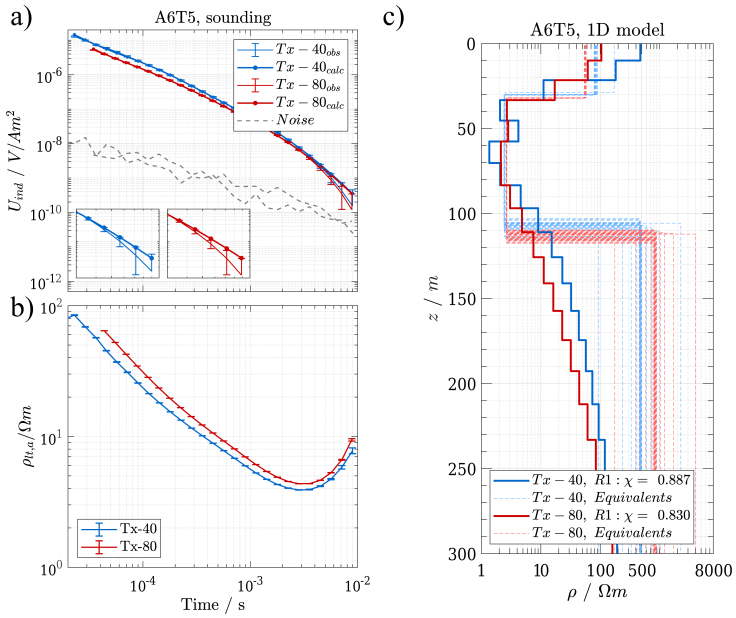

Figure A6.2: Tx-40 and Tx-80 soundings at station A6T5. (a) Observed and calculated induced voltage (U_{ind}). The stacked noise level in dashed grey. (b) late time apparent resistivity ($\rho_{lt,ap}$). (c) Occam R1 inversion and equivalent models derived from Marquardt approach at A6T5 using Tx-40 and Tx-80. The χ value is given in the legend of each model.

A7 Profiles PAG clay pan

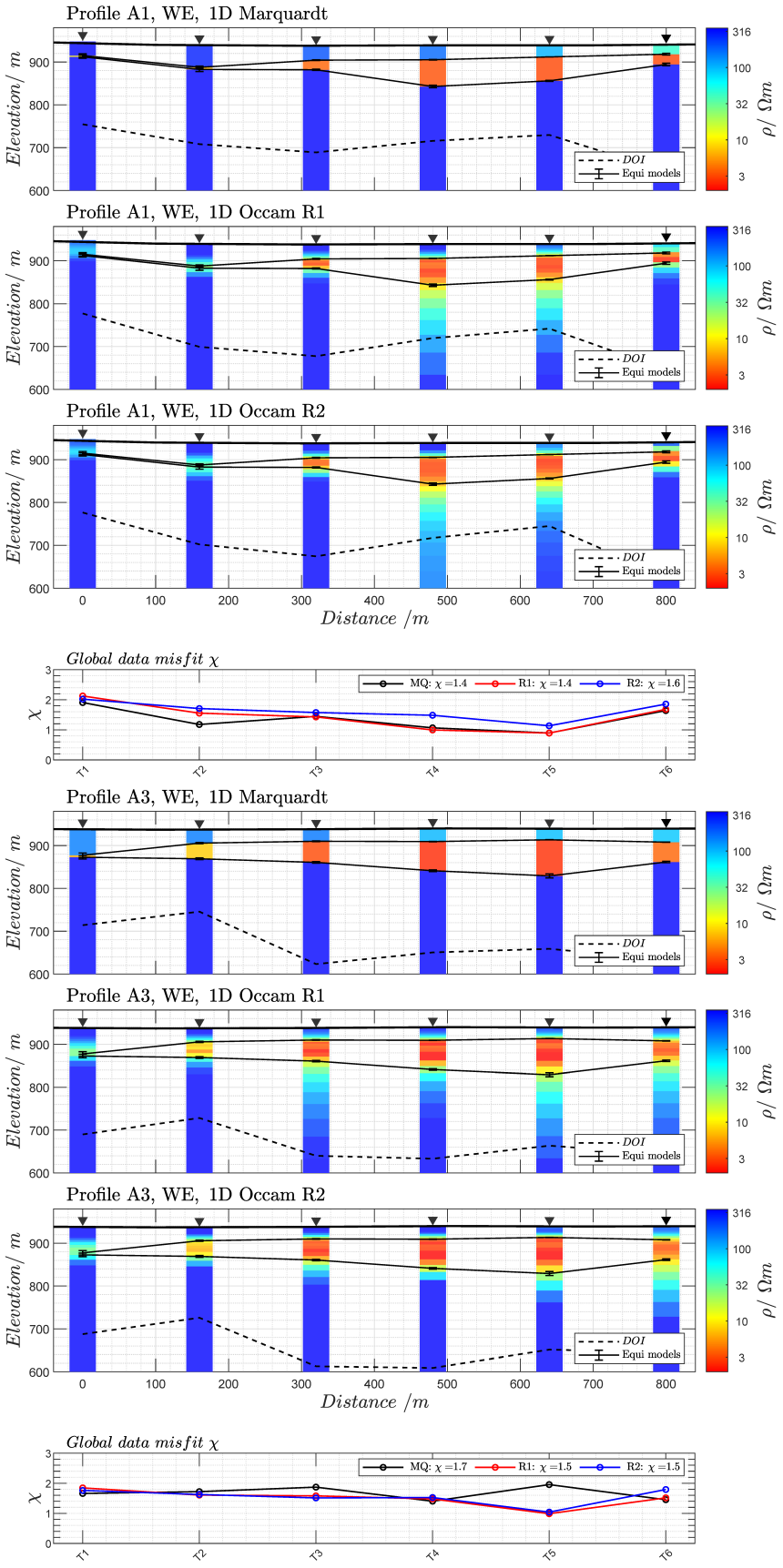

Figure A7.3: 1D stitched inversion results using (a) Marquardt, (b) Occam R1 and (c) Occam R2 models for profiles A1 and A3 in the PAG clay pan. Stations are illustrated by black triangles. The DOI is plotted as a dashed line. The depth range of the upper and basement obtained by the equivalent models are displayed as error bars. (d) Global data misfit χ of each approach along the profile.

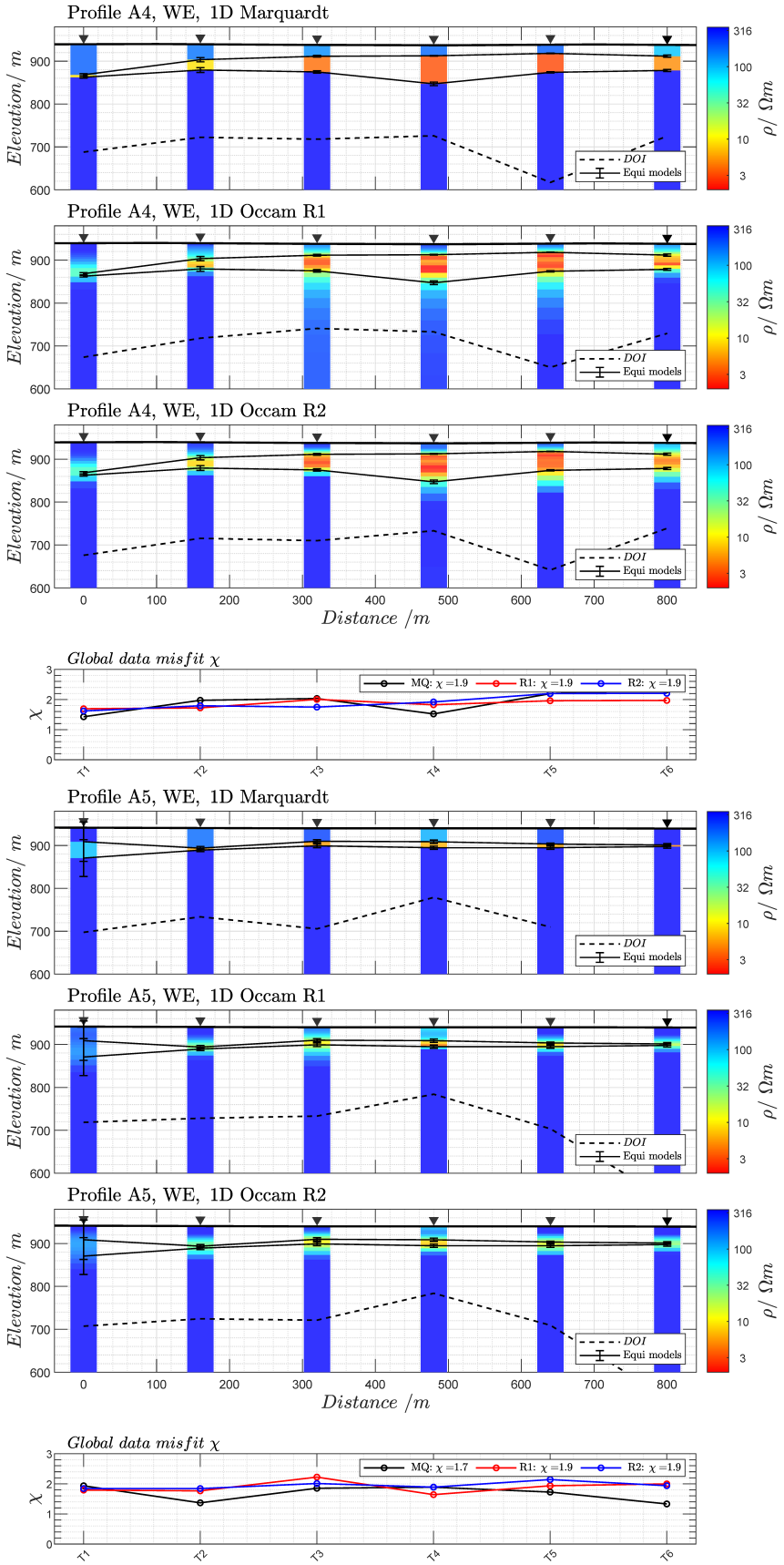

Figure A7.4: 1D stitched inversion results using (a) Marquardt, (b) Occam R1 and (c) Occam R2 models for profiles A4 and A5 in the PAG clay pan. Stations are illustrated by black triangles. The DOI is plotted as a dashed line. The depth range of the upper and basement obtained by the equivalent models are displayed as error bars. (d) Global data misfit χ of each approach along the profile.

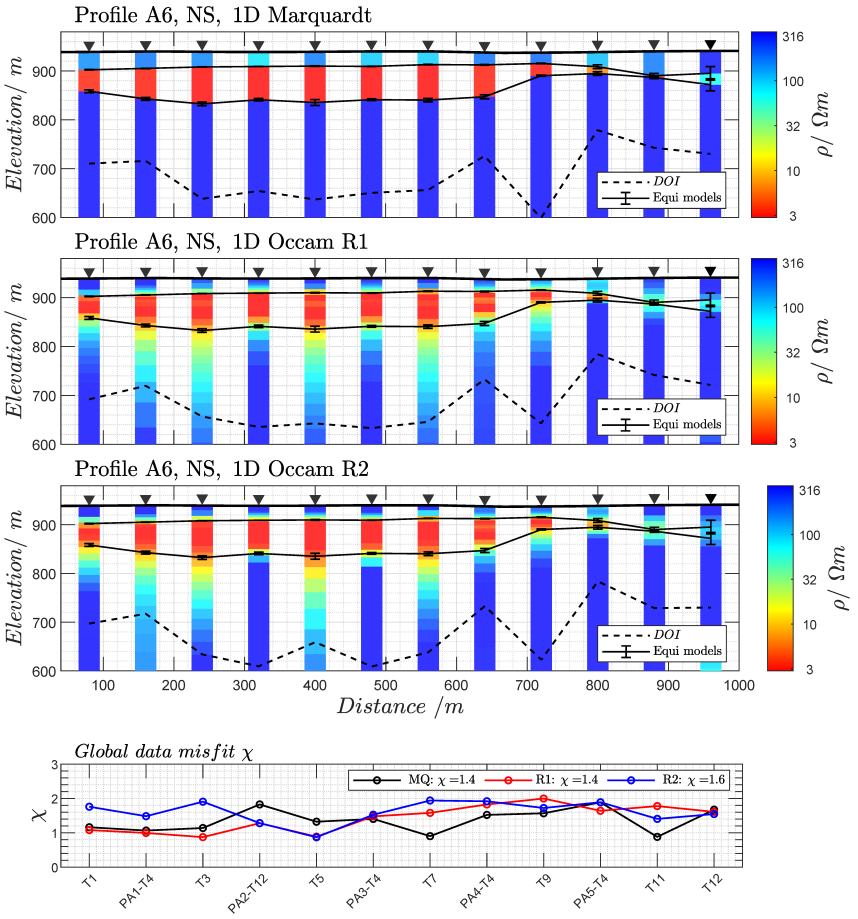

Figure A7.5: 1D stitched inversion results using (a) Marquardt, (b) Occam R1 and (c) Occam R2 models for profile A6 in the PAG clay pan. Stations are illustrated by black triangles. The DOI is plotted as a dashed line. The depth range of the upper and basement obtained by the equivalent models are displayed as error bars. (d) Global data misfit χ of each approach along the profile.

A8 Profiles Paranal clay pan

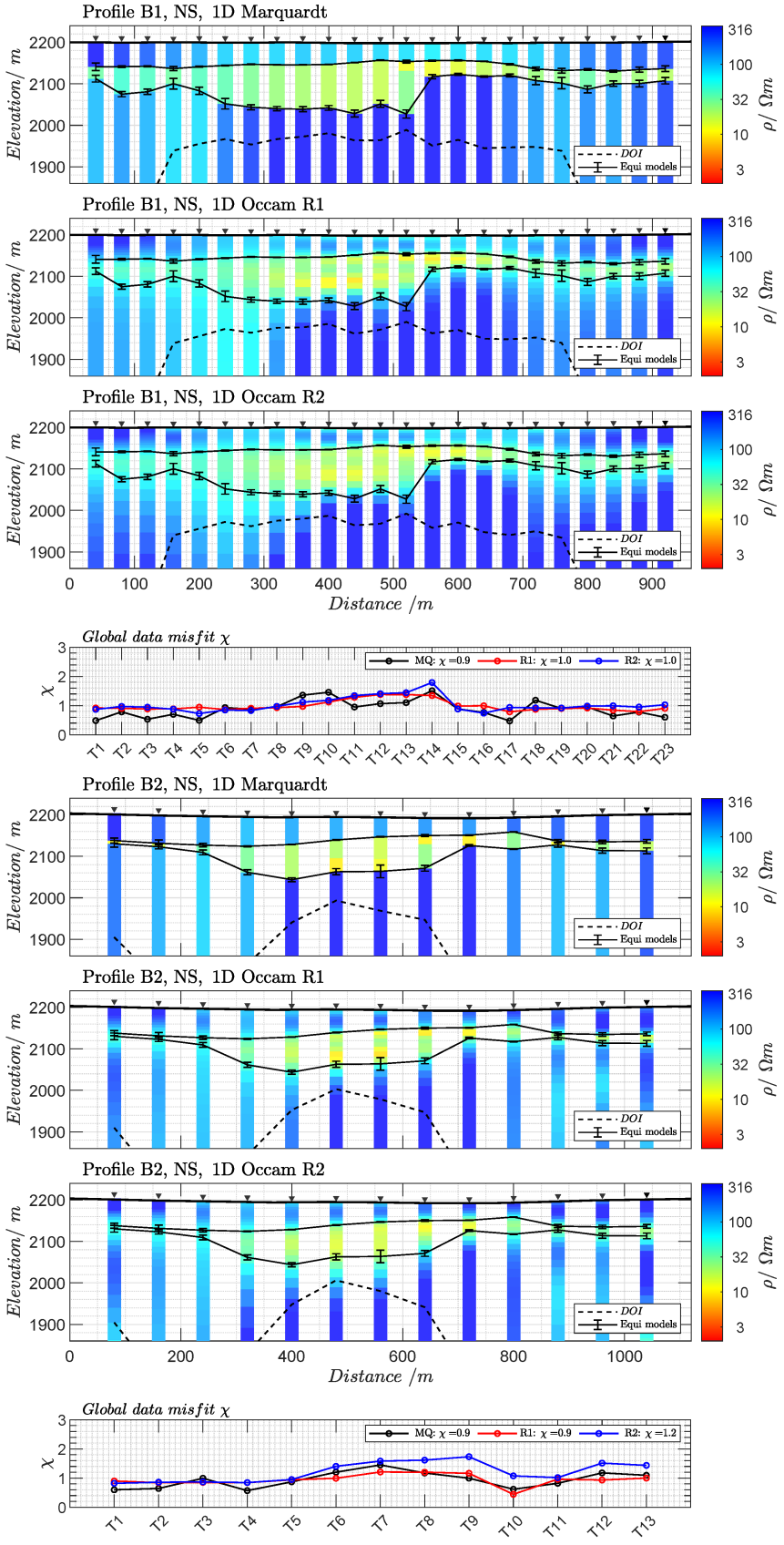

Figure A8.6: 1D stitched inversion results using (a) Marquardt, (b) Occam R1 and (c) Occam R2 models for profiles B1 and B2 in the Paranal clay pan. Stations are illustrated by black triangles. The DOI is plotted as a dashed line. The depth range of the upper and basement obtained by the equivalent models are displayed as error bars. (d) Global data misfit χ of each approach along the profile.

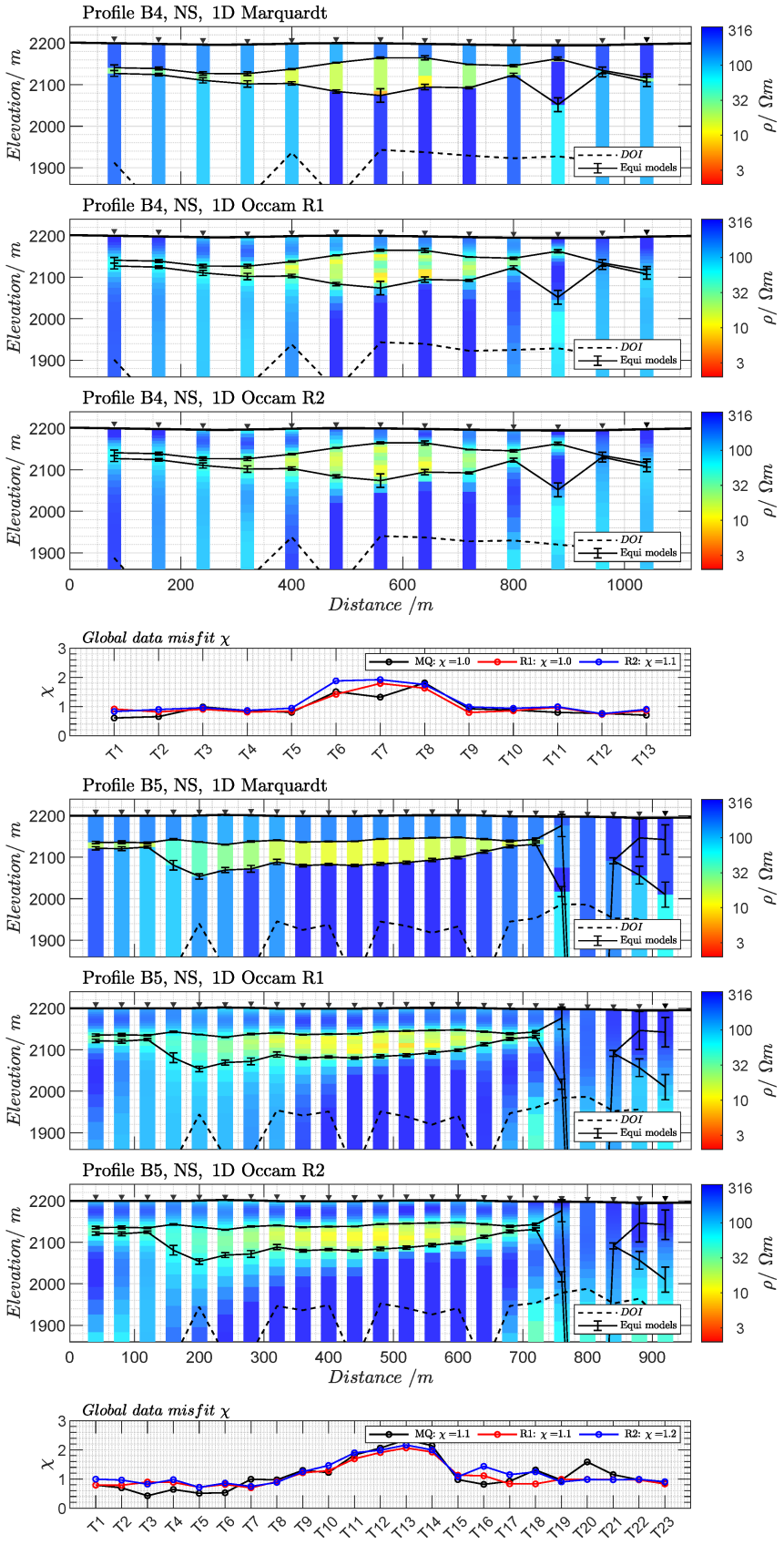

Figure A8.7: 1D stitched inversion results using (a) Marquardt, (b) Occam R1 and (c) Occam R2 models for profiles B4 and B5 in the Paranal clay pan. Stations are illustrated by black triangles. The DOI is plotted as a dashed line. The depth range of the upper and basement obtained by the equivalent models are displayed as error bars. (d) Global data misfit χ of each approach along the profile.

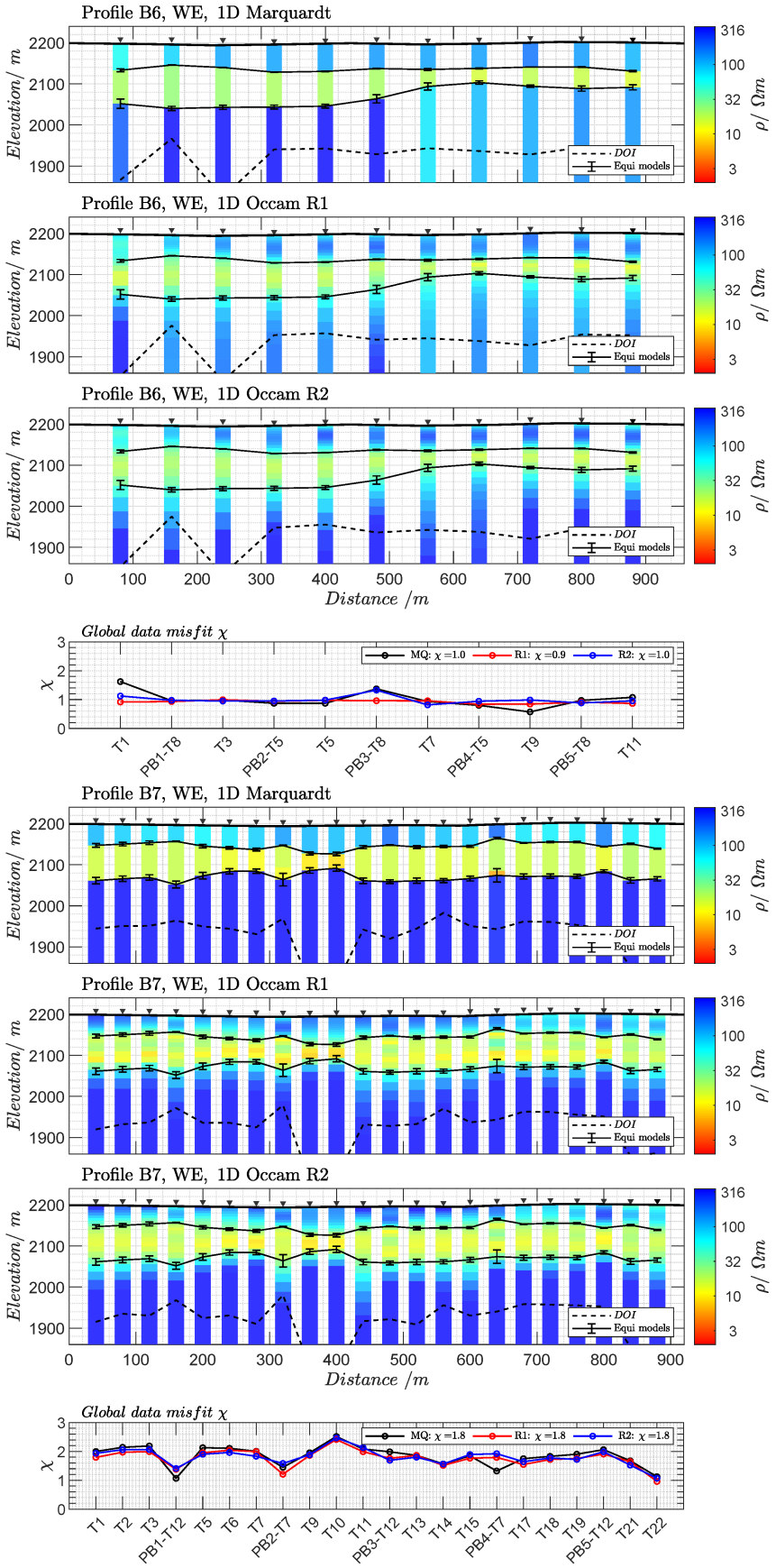

Figure A8.8: 1D stitched inversion results using (a) Marquardt, (b) Occam R1 and (c) Occam R2 models for profiles B6 and B7 in the Paranal clay pan. Stations are illustrated by black triangles. The DOI is plotted as a dashed line. The depth range of the upper and basement obtained by the equivalent models are displayed as error bars. (d) Global data misfit χ of each approach along the profile.

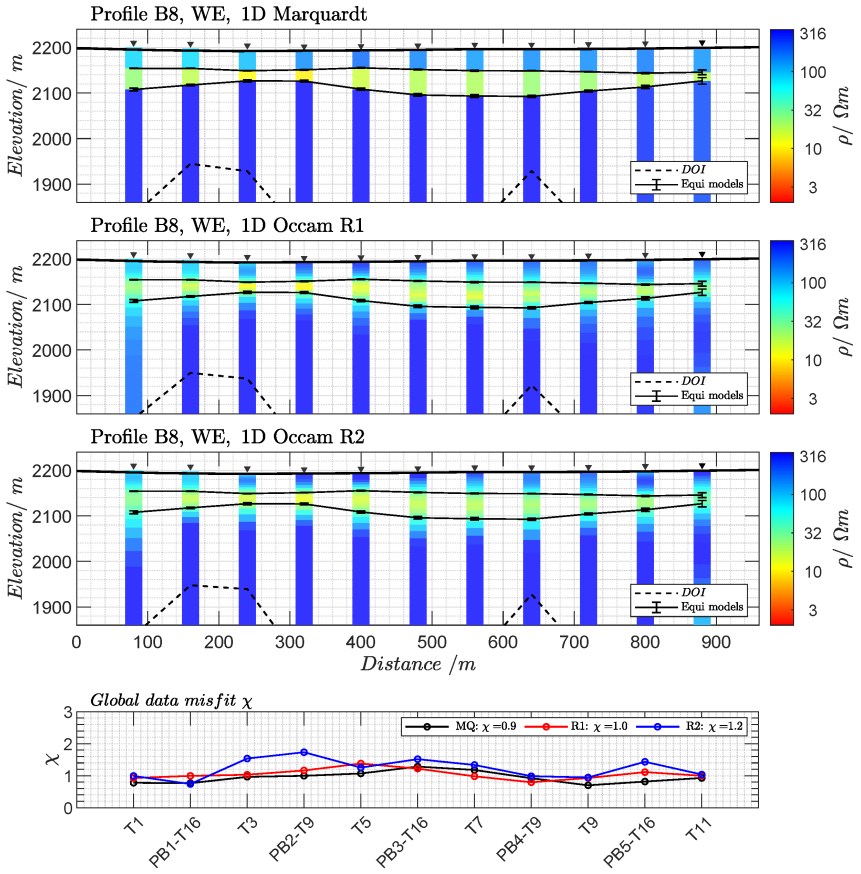

Figure A8.9: 1D stitched inversion results using (a) Marquardt, (b) Occam R1 and (c) Occam R2 models for profile B8 in the Paranal clay pan. Stations are illustrated by black triangles. The DOI is plotted as a dashed line. The depth range of the upper and basement obtained by the equivalent models are displayed as error bars. (d) Global data misfit χ of each approach along the profile.

A9 TEM 3D Inversion

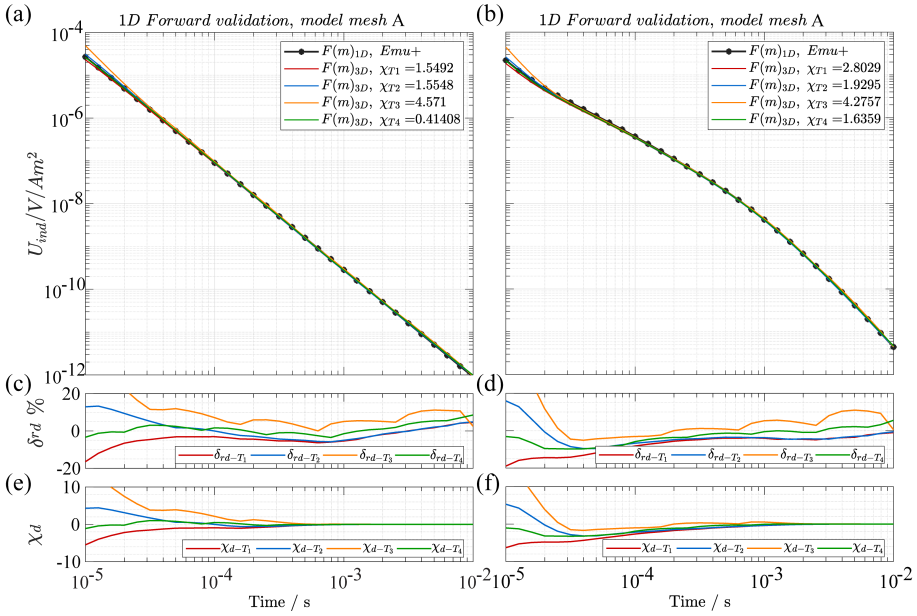

Figure A9.10: Comparison between the 1D semi-analytical solution and the 3D forward response using the Coarse model mesh for (a) a homogeneous half-space of 200Ωm and (b) a 3-layer case model. Different time-stepping setting parameters are tested and are displayed in each case. The corresponding relative differences δ_{rd} in percentage and the error-weighted relative difference χ_{rd} are displayed below each plot.

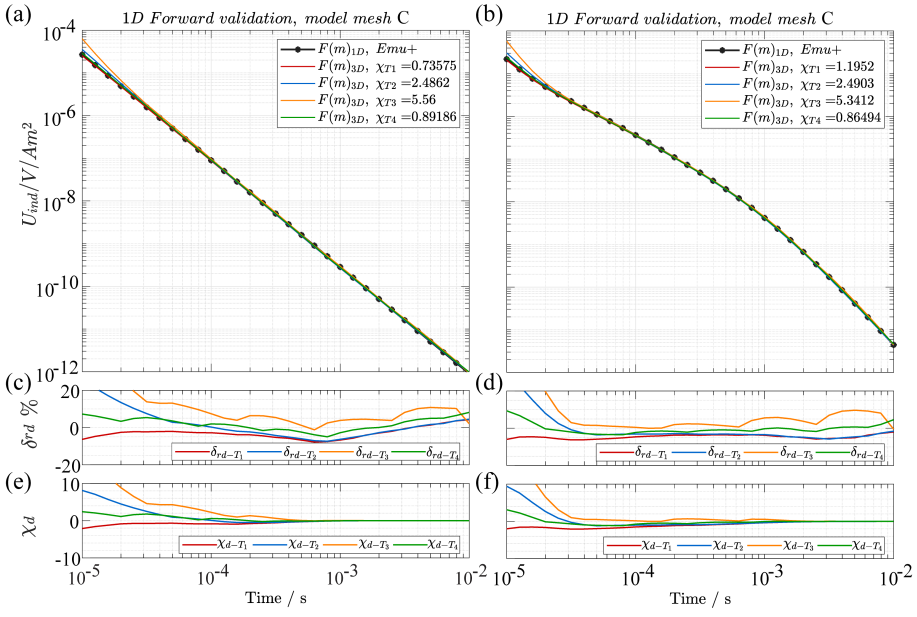

Figure A9.11: Comparison between the 1D semi-analytical solution and the 3D forward response using the Fine model mesh for (a) a homogeneous half-space of 200Ωm and (b) a 3-layer case model. Different time-stepping setting parameters are tested and are displayed in each case. The corresponding relative differences δ_{rd} in percentage and the error-weighted relative difference χ_{rd} are displayed below each plot.

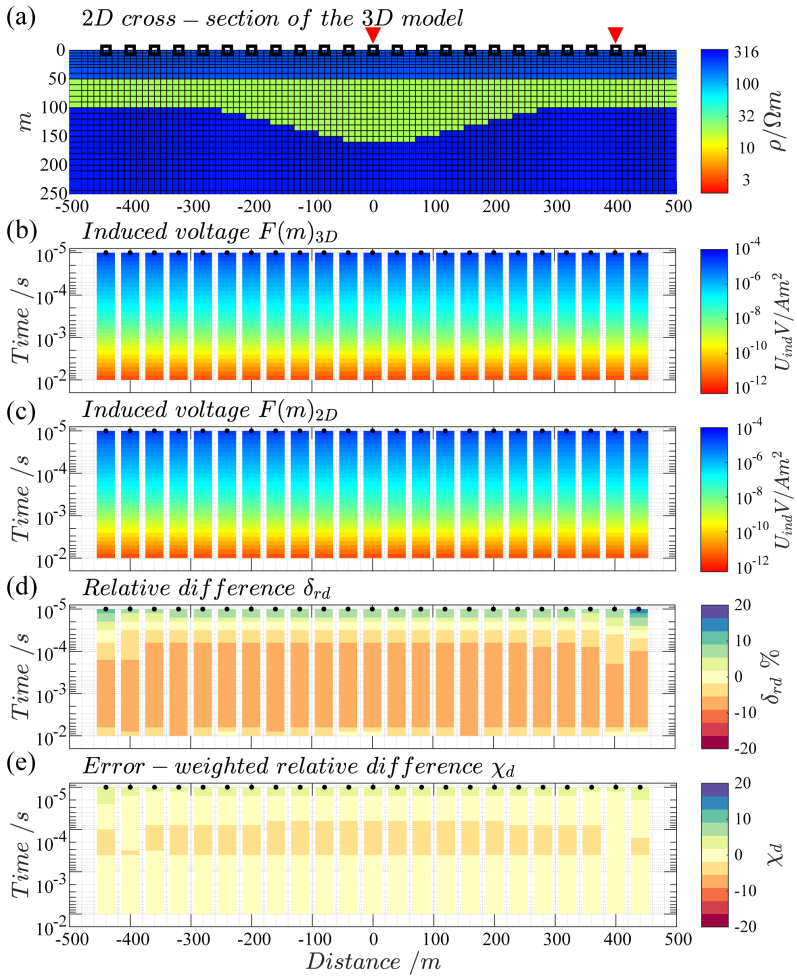

Figure A9.12: Comparison between the 2D synthetic and the 3D forward response using the Fine model mesh. (a) 2D cross-section of the 3D finite model with $N_x \times N_y \times N_z = 70 \times 37 \times 43$ cells. Red triangles show the position for stations T12 (center) and T22 (edge). (b) Induced voltage U_{ind} of the 3D forward modeling algorithm. (c) Induced voltage U_{ind} of the 2D synthetic response. (d) Relative differences δ_{rd} and (e) Error-weighted relative differences δ_{rd} between $F(m)_{3D}$ and $F(m)_{2D}$ synthetic responses.

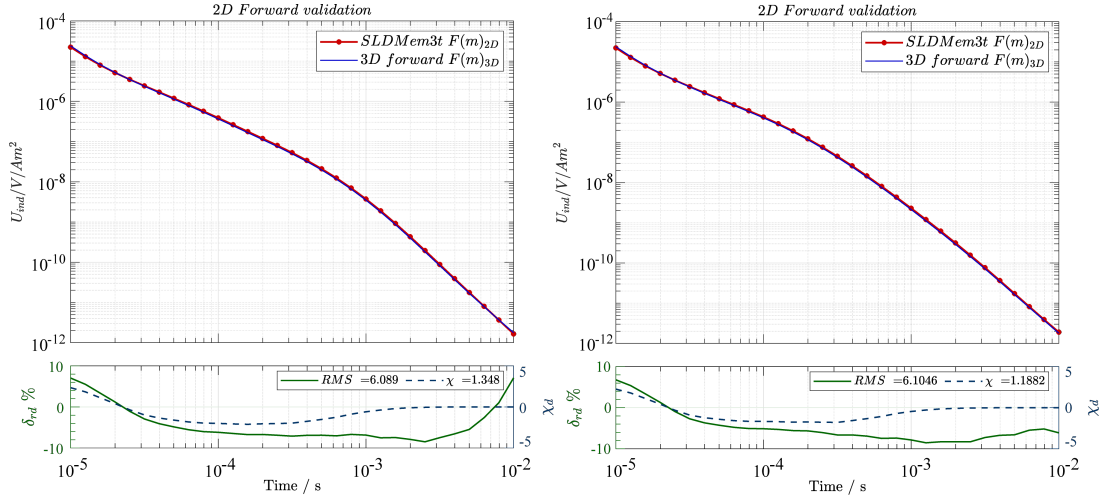

Figure A9.13: Transient comparison between the 2D synthetic and the 3D forward response using the Fine model mesh for the station (a) T12 at the center and (b) T20 at the edge of the profile. Below each comparison, the relative differences (to the left in green) and the misfit (to the right in blue) between the responses is displayed.

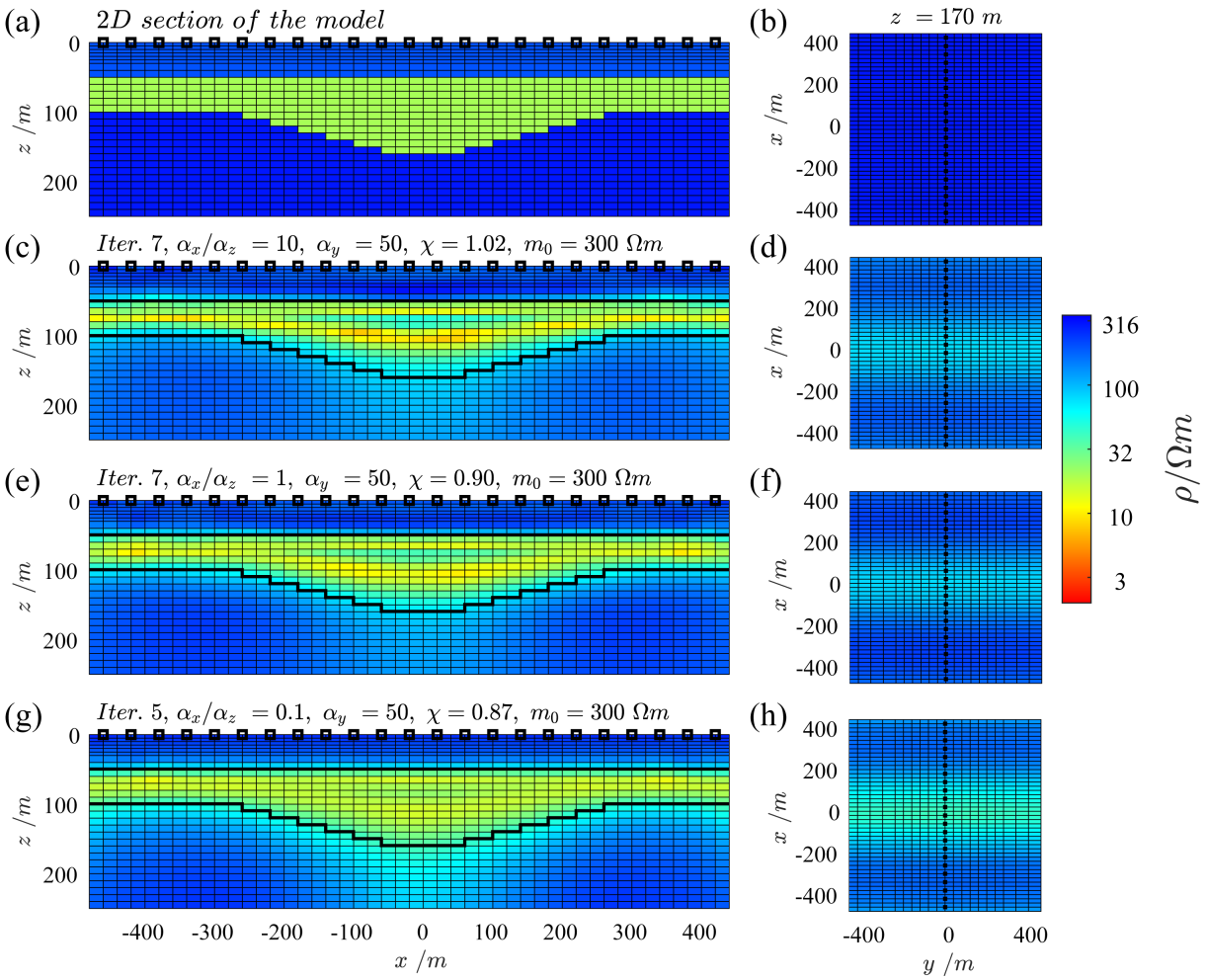

Figure A9.14: Influence of the ratio α_x/α_z. (a) 2D cross-section and (b) plan view at $z = 170$ m of model mesh used to derive the synthetic responses. In the same order, corresponding inversion results using (c, d) $\alpha_x/\alpha_z = 10$, (e, f) $\alpha_x/\alpha_z = 1$, and (g, h) $\alpha_x/\alpha_z = 0.1$. The shape of the conductor based on the model mesh is highlighted in black line. Black squares denote the source locations. In all the attempts, the smoothness in x- and z- direction is set up to $\alpha_{x,z} = 0.5$ and a initial model of $m_0 = 300\ \Omega$m is utilized. The number of iterations used and the χ value are given on each attempt.

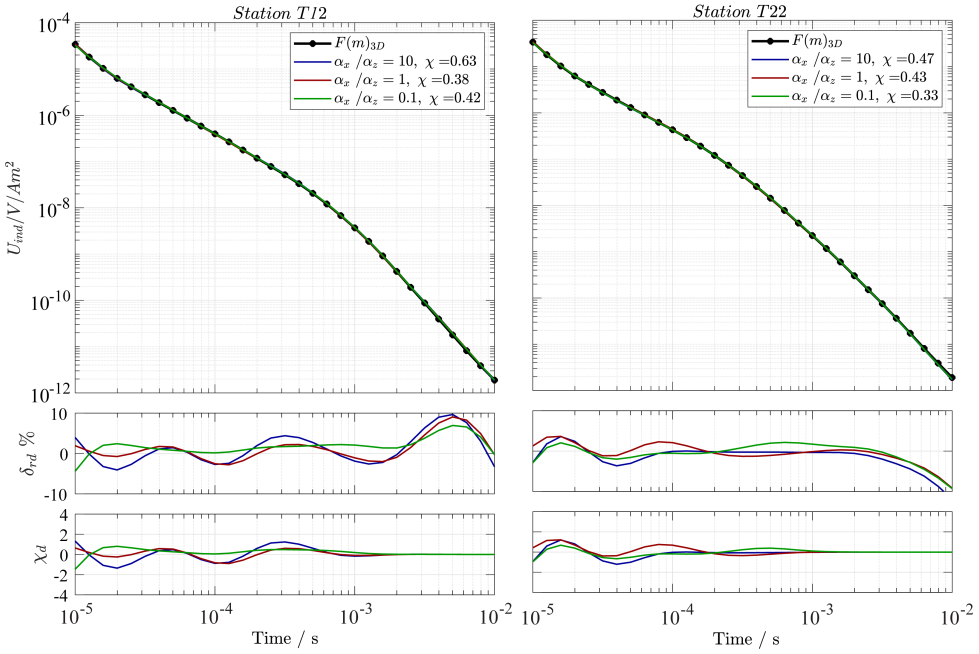

Figure A9.15: Calculated transients of T12 and T22 using $\alpha_x/\alpha_z = 10, 1, 0.1$. The relative differences and the misfit (error-weighted) between the synthetic and calculated responses are displayed below.

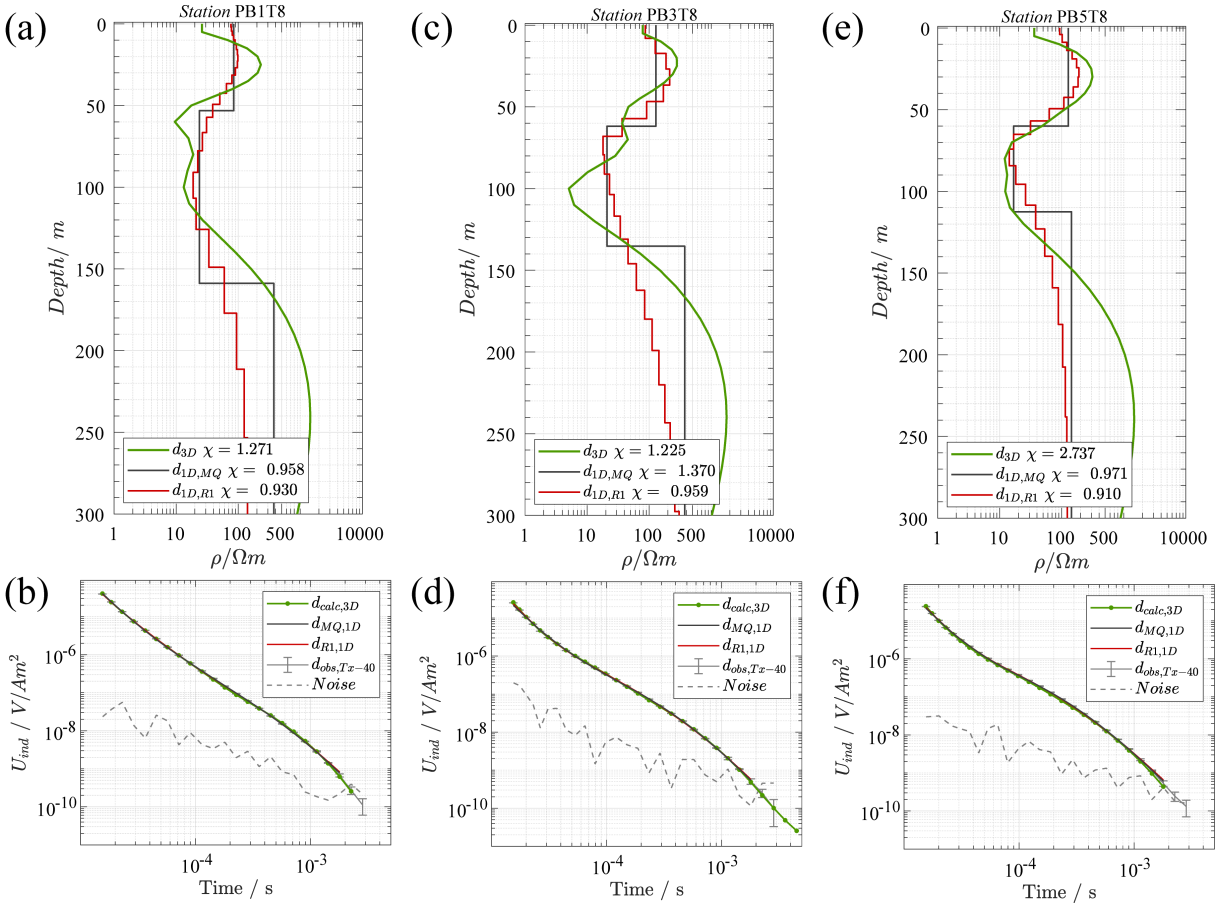

Figure A9.16: Comparison between the 1D models and resistivity distribution of the obtained 3D inversion for the stations (a) PB1T8, (b) PB3T8, (c) PB5T8. The Marquardt and Occam R1 1D inversion is displayed in black and red color. (b, d, f) below each 1D model, the observed and calculated TEM data for each inversion approach. The stacked noise level of each sounding is plotted as a dashed grey line.

Acknowledgments

I would like to express my deepest appreciation to

Prof. Dr. Bülent Tezkan for the supervision of this thesis. I am enormously thankful for allowing me to study in the Applied Geophysics working group. His advice and positive attitude in challenging moments in the past years supported me in reaching the end of this research.

Prof. Dr. Andreas Hördt, for appraising this thesis and encouraging discussion at the EMTF 2019.

Dr. Pritam Yogeshwar encouraged me since I contributed my first poster to the 23rd EMIW in Thailand in 2016. I could not have undertaken this journey without his fructiferous discussions about electromagnetics. He has contributed tremendously to my research, and I have learned much from him. His advice and friendship were great support over the past years.

Dr. Volker Wennrich, for those enriching geological discussions. He persuaded me a lot to keep working in an interdisciplinary environment. Furthermore, I am also grateful to Dr. Julia Diederich-Leicher, for helpful discussions and all the support in the organization of the field campaign.

Dr. Yajun Liu and Dr. Ronghua Peng for all the successful collaboration and provision of the time-domain 3D modeling and inversion algorithm. In addition, for their support and fruitful discussions during the past years.

I fully appreciate the support of the National Agency for Research and Development (ANID)/Scholarship Program/DOCTORADO BECAS CHILE-DAAD/2018 - 62170003 and from DAAD (funding program number 57395809).

Dr. Stefan Buske, Christoph Büttner, Peggy Gödickmeier, and Lukas Ninnemann for providing the active seismic data set and for the successful collaboration and support in the field campaign. I am grateful for the provision of the seismic equipment provided by the Geophysical Instrument Pool Potsdam (GIPP). And also, thanks to Dr. Jan Domagala from the SERNAGEOMIN for his fruitful geological discussions and for providing such unique knowledge about the Paranal clay pan and its regional context.

I would like to extend my sincere thanks to CRC 1211 team. Special thanks to Prof. Dr. Tibor Dunai and Prof. Dr. Martin Melles for promoting an integral interdisciplinary atmosphere and for all the support given during my doctorate stage.

Dr. Karin Boessenkool and Dr. Hannah Hartung, for all the organization and administrative support given by the GSGS and the IRTG, many of my issues were quickly solved.

Dr. Stefan Borowski and HPC team for supporting me in using the 3D algorithm in CHEOPS. They were always super helpful and friendly.

The DESMEX-II is funded by the Federal Ministry of Education and Research (BMBF) under grant 033R130CN to provide the Occam server.

Andreas Busse, for supporting all technical issues and assisting in using the Ageo institute servers.

Dr. Daniel Díaz, for many helpful discussions and advice and for providing the TEM and magnetometer devices from the Department of Geophysics of the University of Chile.

Sebastián Carrasco, Dr. Wiebke Möerbe, Dr. Alexander Grayver, Dr. Cai Ji, and Alex Carr for taking the time to proofread this thesis.

I want to thank all my colleagues at the IGM: Hannah, Shiva, Wiebke, Sophia, Stephan, Stefan, Cai Ji, Sacha, Kendra, Elif, Burak, Till, Ismael, and Sebas for all the push of motivation in the final phase of writing this thesis and for keeping such a friendly atmosphere.

This endeavor would not have been possible without my family core, Mami, Papi, Bane, Beli, Borito, Seba, Nadine, Andrés, and Molly. Despite the 14,000 km distance separating us, the family support was always there, and I am grateful to help me reach my dreams. I love you all so much! In addition, my deep gratitude to my partner, my life-route companion, *el pololi*, for such unquestioning support, for being with me all the time, and for all the effort we made to achieve our challenging dreams. And our lovely Geo, for such a unique cat-love while writing this manuscript.

I am deeply indebted to the Chilean friends that I met in Cologne. I have no words for Cata, Pipe, Maxi, and Anto for always being there when I needed it and adopting me as a family member without doubting. Marco, Natasha, Cami R., Domi, Max, Mariana, Francis, and Cami E., Lucía, Daniel, Ambrosio, for all the moments with such a Chilean spirit that helped my mental health.

Thanks to all the people I met during this period, in one way or another, they helped me to create a new and better version of myself. I have learned much about science, experienced many unforgettable moments, and overcame very stressful phases.

Gracias totales!

Erklärung zur Dissertation

Hiermit versichere ich an Eides statt, dass ich die vorliegende Dissertation selbstständig und ohne die Benutzung anderer als der angegebenen Hilfsmittel und Literatur angefertigt habe. Alle Stellen, die wörtlich oder sinngemäß aus veröffentlichten und nicht veröffentlichten Werken dem Wortlaut oder dem Sinn nach entnommen wurden, sind als solche kenntlich gemacht. Ich versichere an Eides statt, dass diese Dissertation noch keiner anderen Fakultät oder Universität zur Prüfung vorgelegen hat; dass sie - abgesehen von unten angegebenen Teilpublikationen und eingebundenen Artikeln und Manuskripten - noch nicht veröffentlicht worden ist sowie, dass ich eine Veröffentlichung der Dissertation vor Abschluss der Promotion nicht ohne Genehmigung des Promotionsausschusses vornehmen werde. Die Bestimmungen dieser Ordnung sind mir bekannt. Darüber hinaus erkläre ich hiermit, dass ich die Ordnung zur Sicherung guter wissenschaftlicher Praxis und zum Umgang mit wissenschaftlichem Fehlverhalten der Universität zu Köln gelesen und sie bei der Durchführung der Dissertation zugrundeliegenden Arbeiten und der schriftlich verfassten Dissertation beachtet habe und verpflichte mich hiermit, die dort genannten Vorgaben bei allen wissenschaftlichen Tätigkeiten zu beachten und umzusetzen. Ich versichere, dass die eingereichte elektronische Fassung der eingereichten Druckfassung vollständig entspricht.

Teilpublikationen:

Blanco-Arrué, B., Yogeshwar, P., Tezkan, B., Mörbe, W., Díaz, D., Farah, B., Buske, S., Ninneman, L., Domagala, J.P., Diederich-Leicher, J.L., Gebhardt, A.C., Wennrich, V. (2022). *Exploration of sedimentary deposits in the Atacama Desert, Chile, using integrated geophysical techniques.* Journal of South American Earth Sciences, 115, 103746. doi.org/10.1016/j.jsames.2022.103746

Köln, Januar 2023, Bárbara Nataly Blanco Arrué